

X-Ray and Photoelectron Spectroscopy of the Structure,
Reactivity, and Electronic Structure of Semiconductor
Nanocrystals

by

Kimberly Sue Hamad

S.B. (Massachusetts Institute of Technology) 1994

A dissertation submitted in partial satisfaction of the
requirements for the degree of

Doctor of Philosophy

in

Chemistry

in the

GRADUATE DIVISION

of the

UNIVERSITY OF CALIFORNIA, BERKELEY

Committee in charge:

Professor A. Paul Alivisatos, Chair

Professor Gabor Somorjai

Professor Paul McEuen

Spring 2000

The dissertation of Kimberly Sue Hamad is approved:

Chair

Date

Date

Date

University of California at Berkeley

Spring 2000

Abstract

X-Ray and Photoelectron Spectroscopy of the Structure, Reactivity, and Electronic Structure of Semiconductor Nanocrystals

by

Kimberly Sue Hamad

Doctor of Philosophy in Chemistry

University of California at Berkeley

Professor A. Paul Alivisatos, Chair

Semiconductor nanocrystals are a system which has been the focus of interest due to their size dependent properties and their possible use in technological applications. Many chemical and physical properties vary systematically with the size of the nanocrystal and thus their study enables the investigation of scaling laws. Due to the increasing surface to volume ratio as size is decreased, the surfaces of nanocrystals are expected to have a large influence on their electronic, thermodynamic, and chemical behavior. In spite of their importance, nanocrystal surfaces are still relatively uncharacterized in terms of their structure, electronic properties, bonding, and reactivity. Investigation of nanocrystal surfaces is currently limited by what techniques to use, and which methods are suitable for nanocrystals is still being determined. This work presents experiments using x-ray and electronic spectroscopies to explore the structure, reactivity, and electronic properties of semiconductor (CdSe, InAs) nanocrystals and how they vary with size. Specifically, x-ray absorption near edge spectroscopy (XANES) in conjunction with multiple scattering simulations affords

information about the structural disorder present at the surface of the nanocrystal. X-ray photoelectron spectroscopy (XPS) and ultra-violet photoelectron spectroscopy (UPS) probe the electronic structure in terms of hole screening, and also give information about band lineups when the nanocrystal is placed in electric contact with a substrate. XPS of the core levels of the nanocrystal as a function of photo-oxidation time yields kinetic data on the oxidation reaction occurring at the surface of the nanocrystal.

This is dedicated to my parents, Delfin and Electa

TABLE OF CONTENTS

| | | |
|-------|---|----|
| 1 | INTRODUCTION | 1 |
| 1.1 | References | 8 |
| 2 | SYNTHESIS OF SEMICONDUCTOR NANOCRYSTALS | 10 |
| 2.1 | Introduction..... | 10 |
| 2.2 | Motivation..... | 11 |
| 2.3 | General synthesis method..... | 11 |
| 2.4 | Synthesis details..... | 14 |
| 2.4.1 | II-VI (CdSe)..... | 14 |
| 2.4.2 | III-V (InAs)..... | 15 |
| 2.4.3 | InAs/CdSe core-shell nanocrystals | 17 |
| 2.5 | Preparation of samples for photoelectron spectroscopy | 19 |
| 2.6 | References | 21 |
| 3 | EXPERIMENTAL APPARATUS FOR PHOTOELECTRON SPECTROSCOPY | 22 |
| 3.1 | Pressure | 22 |
| 3.2 | Electron energy measurement..... | 23 |
| 3.3 | Photon sources | 24 |
| 3.4 | Sample manipulation | 26 |
| 3.5 | Sample intro | 26 |
| 3.6 | Temperature..... | 27 |
| 3.7 | Beamline hookup | 29 |
| 4 | PHOTOELECTRON SPECTROSCOPY | 30 |
| 4.1 | Motivation..... | 30 |
| 4.2 | Core levels in photoemission | 33 |
| 4.3 | Mapping the density of states (DOS)..... | 35 |
| 4.4 | Surface sensitivity..... | 36 |
| 4.5 | UPS vs. XPS | 38 |
| 4.6 | References | 40 |
| 5 | USING XPS AND UPS TO MEASURE THE DENSITY OF STATES IN NANOCRYSTALS..... | 41 |
| 5.1 | Introduction..... | 41 |
| 5.1.1 | What is expected for nanocrystals in terms of size evolution? | 41 |
| 5.1.2 | Information from PES on nanocrystals | 42 |
| 5.2 | Experimental: subtraction technique | 44 |
| 5.3 | Valence DOS for nanocrystals as a function of size and surfactant | 50 |
| 5.4 | DOS measured with UPS | 53 |
| 5.4.1 | Experimental method for nanocrystals | 53 |
| 5.4.2 | Results for UPS..... | 55 |
| 5.5 | Conclusions and outlook | 58 |
| 5.6 | References | 59 |
| 6 | X-RAY AND PHOTOELECTRON SPECTROSCOPY OF NANOCRYSTALS ON METAL SUBSTRATES: SIZE DEPENDENT HOLE SCREENING..... | 60 |
| 6.1 | Introduction..... | 60 |

| | | |
|---------|--|-----|
| 6.2 | XPS Experimental | 60 |
| 6.3 | Results..... | 60 |
| 6.3.1 | Core level shifts with shell layer thickness | 63 |
| 6.3.2 | XPS linewidth changes as a function of nanocrystal size | 69 |
| 6.4 | Expected causes of shifts..... | 71 |
| 6.4.1 | Distribution of surface sites | 71 |
| 6.4.2 | Quantum size effects..... | 72 |
| 6.4.3 | Hole screening..... | 72 |
| 6.5 | Evaluation of the core level shift in terms of electromagnetics..... | 73 |
| 6.6 | Conclusions..... | 79 |
| 6.7 | References..... | 80 |
| 7 | ULTRA-VIOLET PHOTOELECTRON SPECTROSCOPY OF NANOCRYSTALS ON METAL SUBSTRATES: MEASURING BAND OFFSETS | 81 |
| 7.1 | Introduction..... | 81 |
| 7.1.1 | Semiconductor heterojunctions in nanocrystals: core/shell particles | 84 |
| 7.2 | Experimental for UPS..... | 88 |
| 7.2.1 | Extrapolation method for VBM and cutoff..... | 90 |
| 7.2.2 | General method for measuring heterojunction band offsets by UPS..... | 94 |
| 7.3 | UPS Results for nanocrystal/metal interfaces: shifts of valence band maximum..... | 95 |
| 7.4 | UPS Results for CdSe/CdS core shell nanocrystals | 100 |
| 7.5 | Discussion..... | 103 |
| 7.5.1 | Electromagnetic effect of the band lineup..... | 103 |
| 7.5.2 | Core-shell nanocrystals: core level shifts interpreted in terms of band offsets..... | 104 |
| 7.6 | Conclusions..... | 107 |
| 7.7 | References..... | 109 |
| 8 | KINETIC STUDY OF THE PHOTO-OXIDATION AND THERMAL DECOMPOSITION OF CdSe NANOCRYSTALS BY X-RAY PHOTOELECTRON SPECTROSCOPY | 111 |
| 8.1 | Introduction..... | 111 |
| 8.2 | Experimental..... | 113 |
| 8.3 | Results and Discussion..... | 116 |
| 8.3.1 | Model..... | 122 |
| 8.3.2 | Determination of the rate law | 125 |
| 8.3.3 | Interpretation of activation energies | 126 |
| 8.3.4 | Interpretation of Arrhenius parameters..... | 128 |
| 8.3.5 | TPD | 130 |
| 8.3.5.1 | Reaction order of the k_{23} reaction..... | 136 |
| 8.4 | Summary..... | 139 |
| 8.5 | References..... | 141 |
| 9 | SURFACE STRUCTURE OF SEMICONDUCTOR NANOCRYSTALS STUDIED BY XANES..... | 143 |
| 9.1 | Introduction..... | 143 |
| 9.1.1 | Surface reconstructions for bulk..... | 143 |
| 9.1.1.1 | Peierls distortion..... | 144 |
| 9.1.2 | X-ray absorption as a structural probe | 149 |
| 9.1.3 | EXAFS vs. XANES | 152 |
| 9.2 | Experiment | 154 |

| | | |
|---------|---|-----|
| 9.2.1.1 | 3p (M_3) absorption | 158 |
| 9.2.1.2 | XPS..... | 163 |
| 9.3 | Discussion..... | 164 |
| 9.3.1 | FEFF7 Simulations..... | 164 |
| 9.3.2 | Bulk reconstruction as model..... | 169 |
| 9.3.3 | Other possibilities for broadening..... | 175 |
| 9.3.4 | Quantum confinement effects..... | 178 |
| 9.4 | Core shell particles..... | 182 |
| 9.5 | Evaluation of results..... | 184 |
| 9.6 | References..... | 186 |

ACKNOWLEDGMENTS

Science progresses only with the united efforts of many people. I have been fortunate to work with a group of bright and enthusiastic co-workers during my time at Berkeley. This work would have never been accomplished without the generous assistance of others, and I am indebted to them for their time and labor. There is a lot of work that does not appear in this thesis for which others must be recognized. Unfortunately, space limits the number of people I can thank explicitly.

First, I would like to thank my advisor Paul Alivisatos for his guidance in my research throughout my career. Paul had given me the freedom to pursue projects of my own choosing at my own pace, and also demonstrated extreme patience when research encountered frustrating barriers. I have learned much from him as well as his research group, and I appreciate the many years of his support.

It is a pleasure to acknowledge the members of the Alivisatos group, both past and present. The group has always been a delight to work with, nurturing an environment of learning as well as fun, and I have enjoyed their company both in and out of the lab. They have made my experience at Berkeley an enjoyable one. I would especially like to acknowledge the elder students and postdocs for their magnanimity in showing me the ropes of pursuing research during my introduction into graduate school. In addition, I received a great deal of technical help from many members. Thanks to Richard Roth, my partner on the XPS/UPS experiments and the data of the XANES experiment, along with the upkeep of the XPS machine. Richard showed perseverance and determination during many nights of synchrotron runs and tedious XPS experiments, and constantly contributed ideas to our work as we were discovering new turns and numerous complications in the lab. As anyone studying nanocrystals must also synthesize them, I owe much to the highly talented

Xiaogang Peng for consultation of nanocrystal synthesis and his unfailing patience in teaching myself (and simultaneously many others) about the tricks and pitfalls of chemical synthesis. Thanks to Andrew Guzelian and Juanita Wickham for teaching me how to synthesize the III-V nanocrystals. Andrew and Janet Bowen Katari had showed me how to do my first XPS experiments in Building 66. I thank Jörg Rockenberger for considerable help with the FEFF simulations and the data analysis, as well as discussions regarding the XANES experiments. Thanks also to Juanita for assistance in programming and running the FEFF calculations, as well as discussions regarding XRD simulations and coordinating the results with XANES (the code in the appendix). Thanks also to Erik Scher for assistance in the XPS, UPS, and XAS experiments, and who will continue those in the future. Also, there are countless efforts by the rest of the group members which I cannot enumerate here.

I would like to thank Tony van Buuren of LLNL and the ALS, who was a knowledgeable source on x-ray and electron spectroscopies of nanocrystals. Tony assisted in the XANES runs and had also graciously given us beamtime on beamline 8.0 at the ALS and beamline 8.2 at SSRL for many challenging, all-night experiments that are not mentioned here. We also had a great deal of help from Christoph Bostedt and Melissa Grush. Thomas Möller of DESY at HASYLAB has also been an expert source of information on x-ray and electronic spectroscopy of clusters, and has been generous in his consultations, in addition to being extremely helpful in setting up the XPS machine and the first synchrotron runs.

ALS support staff and the researchers at beamline 6.3.2 and 8.0 were instrumental in making experiments work both online and offline, particularly in orchestrating the hookup of the spectrometer to 6.3.2. Thanks to Erik Gullikson, Andreas Stonas, Stan Mrowka, Jim Underwood, Mike Chang, the riggers and vacuum technicians, and most of all Operations

Manager Ray Thatcher for his tremendous efforts in seeing that everything proceeded smoothly.

Thanks to Eric Peterson, Paul Gherity, and Bruce Richardson, and all the people at Physical Electronics who helped in the design, construction, and startup of the photoelectron spectrometer. Thanks also to members of the McEuen, Somorjai, McCusker, Harris, Neumark, and Stacy groups who had lent equipment, volunteered time on machines, or had supplied helpful advice. Thanks also to the College of Chemistry administration, as well as the machine, electronics, wood, and glass shops, who have aided greatly in supplementing or repairing the various experimental apparatuses used. Thanks to Rita Tidwell, the administrative assistant for the Alivisatos group, for her efforts to make all the important things happen.

Thanks to all my friends who had made my stay in the Bay Area enjoyable. I have been lucky enough to meet a menagerie of characters that have kept the rollercoaster ride here fascinating and entertaining. Thanks to all the kind folks at KALX 90.7FM for maintaining such a marvelous radio station, and for help in volunteering my time for their cause. Special thanks to my companions and fellow classmates Martin Zanni and Niels Damrauer, whose friendship went far above and beyond the call of duty.

Finally, I thank my parents Delfin and Electa, and my sisters Giselle and Alyssandrea for their constant love and support during my life. I express my profound gratitude for their guidance and selflessness, and for supporting me all these years in pursuing my goals. Lastly, I would like to thank Mark Schifferli for his love, devotion, and his unwavering faith in me.

1 INTRODUCTION

In his famous 1959 lecture “There’s Plenty of Room at the Bottom,” [1] Feynmann described his vision of the numerous and fantastic possibilities if one could control objects of reduced dimensions. In doing so, he urged scientists to pursue the study of objects of dimensions that lay in between molecules and solids, which had been relatively unexplored at that time. What had been barely touched 40 years ago has rapidly developed into a field of its own.

The study of materials in the nanometer regime is partially fueled by the physics of the problem; size is another variable by which physical properties can be measured and consequently provides another avenue of knowledge about the thermodynamic, electronic, and chemical properties of solids. Furthermore, a new perspective is needed to understand objects of this size. Nanocrystals, possessing 10^2 - 10^4 atoms, are too large to be described atom by atom and too small to be able to be considered infinite solids. Therefore, the language of molecular orbital theory and solid state physics must somehow be combined in order to understand the fundamental properties of objects in this size regime.

The physical properties of nanocrystals can show dramatic changes as the size of the particle is changed. The most stunning example of this is the color of CdSe semiconductor nanocrystal samples which can be seen by eye and does not require a complicated experimental apparatus. A sample of 25Å particles is yellow in color, but for a 35Å sample of the same material the color is red. We can use a simple quantum mechanical model to describe this behavior. From the equations describing a particle in a 1-dimensional box, the Schrödinger equation is

$$\frac{d^2\psi}{dx^2} + \frac{2mE}{\hbar^2}\psi(x) = 0$$

$$0 \leq x \leq a$$

where the potential is zero inside the box and infinite everywhere else. For our purposes, the particle is the exciton, or electron hole pair that is generated upon absorption of a photon. The general solution of the above equation has wavefunctions of the form

$$\psi = B \sin(kR)$$

where k is defined as

$$k = \sqrt{\frac{2mE}{\hbar^2}}$$

and energy levels that can be described as

$$E_n = \frac{n^2 \hbar^2}{8mR^2}$$

$$n = 1, 2, 3, \dots$$

The energy levels are discrete (as dictated by the quantum number n) and dependent on the size of the box. The equation for the energy levels illustrates that as the size of the box is decreased, the energy level spacings increase, which is exhibited as the dramatic color change in the samples described above. This quantum behavior is observed if the de Broglie wavelength of the particle is on the order of the box length, and brings up the important point about relative length scales. If we are to investigate physical behavior as a function of size, in order to see any changes the length scale of that property must be on the order of the size of the particle. The absorption energy of nanocrystals is but one example of the interesting properties that change dramatically with size.

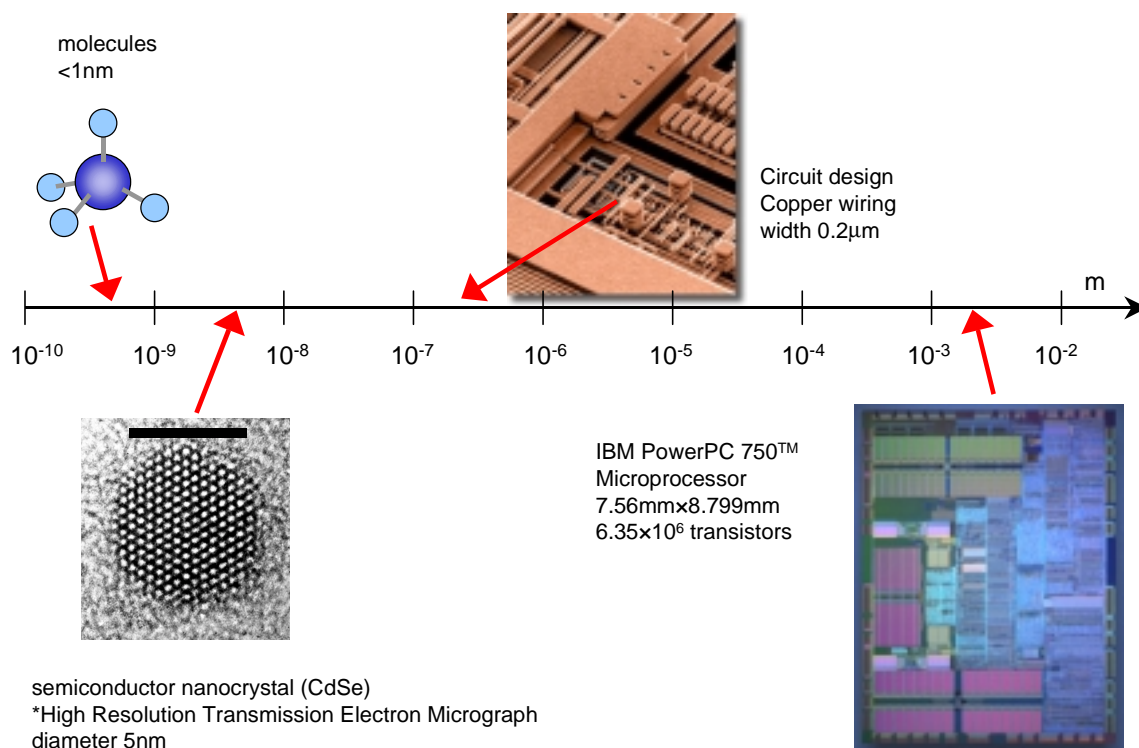


Figure 1-1 Scalebar indicating the size of computer chips, device features, the semiconductor nanocrystals that are the subject of study, and molecules.

In addition to understanding fundamental properties, nanocrystals are of interest to the computer industry by virtue of the size regime they occupy. Due to the increasing miniaturization of features in computer chips known as Moore's Law, electrical devices are rapidly approaching this size range. Figure 1 shows a scalebar indicating feature dimensions from macroscopic to microscopic. Wires on microprocessor chips have just reached a width of $0.20\mu\text{m}$ which enables the silicon industry to fit millions of transistors onto a millimeter sized chip. As features decrease in size, classical physics can no longer describe behavior and, as it was illustrated above, quantum mechanics must be invoked. Therefore, understanding the fundamental properties of nanocrystals is significant if computers are to use chips that have features in the nanometer size range. Furthermore, the techniques used to create features that are small are becoming more difficult to execute. Photolithography

has been used extensively to design small features but will reach its limit at $\sim 100\mu\text{m}$. If UV and x-ray photons are used, the dimensions may be reduced further into the nanometer regime. However, alternative routes to creating smaller dimension objects are becoming more attractive as they have the promise of accessing the regime below 100nm, which will soon become important.

Since its inception in the early 1980's, the study of nanometer sized objects has swiftly expanded into a broad field, with a wide variety of types of research. As aforementioned, nanocrystals provide a system in which to study the size dependence of fundamental physical and chemical properties. These include thermodynamic properties (solid-liquid and solid-solid phase transitions) [2, 3], metal-to-insulator transitions of individual dots and their assemblies[4] and electrical studies by means of effectively attaching electrodes to a nanocrystal and measuring the transport properties. Synthetic research in this area includes the exploration of new fabrication and processing techniques for nanocrystals [5, 6], as well as their assembly into higher order structures and complex arrangements. [7-10] In addition, because nanocrystals have many useful size dependent properties, they are potentially attractive in terms of industrial applications. The earliest possible industrial use of nanocrystals will be the TiO_2 nanocrystal-based solar cell of Graetzel and coworkers, which takes advantage of the high surface to volume ratio of the nanocrystals. In addition, size dependent photo- and electro-luminescence afford color tunable fluorescent labels for biology and light emitting diodes (LEDs) in which only one chemistry is necessary for processing [11-14].

One area of study for nanocrystals is the investigation of the surface. The surface of a nanocrystal is worth examining simply from the point of view of surface to volume ratios. As dimensions decrease, surface ratios increase by roughly $1/R$, where R is the particle

dimension. For a 28Å diameter CdSe nanocrystal, roughly half of the atoms are on the surface. In addition, many properties of nanocrystals are influenced by the surface. Thermodynamic properties are strongly dependent on the surface energy. The melting temperature of nanocrystals shows remarkable size dependence, which is largely due to the surface free energy. [3] Hysteresis curves for solid-solid phase transitions of nanocrystals show a marked change with different surfactants. [15] Surface states which lie in the gap of nanocrystals affect the optical transitions [16] and electronic accessibility. Although theoretical studies have begun to take into account explicitly surface effects [17-19], the question of how much the surface influences the optical transitions is still not known. Therefore, in order to have a complete picture of the physical properties of nanocrystals, characterization of their surface is necessary.

Nanocrystal surfaces have traditionally not been treated explicitly in the description of other physical properties. Frequently the treatment of nanocrystal surfaces involves oversimplified models such as a square potential barrier, a partially reflecting wall, or simply ignored due to the complexity in accounting for their properties. Furthermore, unexplained optical and electronic behavior of nanocrystals has often been attributed to surface traps, contributing to the picture of the surface as a defect. Studies of bulk two-dimensional surfaces have shown that surfaces and bulk are quite different physically and chemically; [20] more so, approximations as bulk cannot be used in the case of nanocrystals as the curvature is much greater.

As we will see in more detail later, chemical manipulation of nanocrystals is controlled by their surface chemistry. Colloidal nanocrystals are versatile by virtue of the fact that their surfactant can be exchanged, allowing their solubility in a variety of solvents or dispersion into polymers, crystallized by into a single crystal or in a host crystal. The handle

by which nanocrystals can be utilized and incorporated into useful devices is their surface chemistry.

Because nanocrystal surfaces influence many of their physical and chemical properties there is a need to study their surfaces in more detail. Very little is known about the electronic structure and bonding at the surface of a nanocrystal, and experiments that directly investigate nanocrystal surfaces are difficult to design. This thesis presents experiments focusing on the understanding the fundamental properties of nanocrystal surfaces, in particular their structure, reactivity, and how the interface between them and another bulk object affects their electronic structure in the hopes of bringing to light issues that influence other physical properties. By no means is this study comprehensive; rather, it presents only a few properties of nanocrystal surfaces that can be explored. However, it is an attempt at directly studying their surface which will hopefully be more understood in the future.

The experimental techniques used in this work to study nanocrystal surfaces are x-ray and electronic spectroscopy, which have a well-developed background. The spectroscopies that are used for this work are x-ray and ultra-violet photoelectron spectroscopy (XPS, UPS) which yield information about the chemical environment and electronic structure, and x-ray absorption near edge spectroscopy (XANES), which is used to probe the structural environment of atoms in a solid. These techniques are non-destructive and have been shown to yield meaningful information about chemical, electronic, and structural properties in a variety of materials, and thus are well suited for probing systems such as nanocrystals, which have not been fully characterized. These techniques will be applied to nanocrystals with the interest of studying their surface.

The outline of this work is the following. Chapter 2 will describe the method for synthesizing semiconductor nanocrystals. Chapter 3 will briefly describe the experimental apparatus used for XPS and UPS. Chapter 4 will discuss the technique of photoelectron spectroscopy. Chapter 5 describes a method to obtain the density of states of nanocrystals from XPS spectra. Chapters 6 and 7 are closely related and describe photoelectron experiments that probe size-dependent screening effects, measurement of the density of states, and band offsets for nanocrystals. Chapter 8 is a study of reactivity kinetics of the photo-oxidation of CdSe nanocrystals. Reactions with nanocrystals occur at the surface, and XPS can be used to study surface reactivity by its ability to obtain chemical state information. Structural studies of nanocrystal surfaces using XANES is described in Chapter 9. These experiments are performed with the goal of understanding the size dependence and how much of it is determined by the surface. Because the work in each of these chapters employs a different experimental technique or a variation of it, the methods will be described in their respective chapters.

1.1 References

- [1] R. Feynmann, (1959)Lecture.
- [2] S. H. Tolbert and A. P. Alivisatos, J. Chem. Phys. **102**, 4642 (1995).
- [3] A. N. Goldstein, C. M. Echer, and A. P. Alivisatos, Science **256**, 1425 (1992).
- [4] C. P. Collier, R. J. Saykally, J. J. Shiang, S. E. Henrichs *et al.*, Science **277**, 1978 (1997).
- [5] C. B. Murray, D. J. Norris, and M. G. Bawendi, J. Am. Chem. Soc. **115**, 8706 (1993).
- [6] X. Peng, J. Wickham, and A. P. Alivisatos, J. Am. Chem. Soc. **120**, 5343 (1998).
- [7] R. P. Sear, C. Sung-Wook, G. Markovich, W. M. Gelbart *et al.*, Phys. Rev. E **59**, R6255 (1999).
- [8] T. Vossmeier, S. Jia, E. Delonno, M. R. Diehl *et al.*, J. Appl. Phys. **84**, 3664 (1998).
- [9] G. P. Mitchell, C. A. Mirkin, and R. L. Letsinger, J. Am. Chem. Soc. **121**, 8122 (1999).
- [10] C. B. Murray, C. R. Kagan, and M. G. Bawendi, Science **270**, 1335 (1995).
- [11] V. L. Colvin, M. C. Schlamp, and A. P. Alivisatos, Nature **370**, 354 (1994).
- [12] M. C. Schlamp, X. Peng, and A. P. Alivisatos, J. Appl. Phys. **82**, 5837 (1997).
- [13] H. Mattoussi, L. H. Radzilowski, B. O. Dabbousi, B. O. Thomas *et al.*, J. Appl. Phys. **83**, 7965 (1998).
- [14] M. Bruchez, M. Moronne, P. Gin, S. Weiss *et al.*, Science **281**, 2013 (1998).
- [15] C.-C. Chen, A. B. Herhold, C. S. Johnson, and A. P. Alivisatos, Science **276**, 398 (1997).
- [16] M. G. Bawendi, P. J. Carroll, L. Wilson, and L. E. Brus, J. Chem. Phys. **96**, 946 (1992).
- [17] N. A. Hill and K. B. Whaley, J. Chem. Phys. **100**, 2831 (1994).

- [18] K. Leung and K. B. Whaley, J. Chem. Phys. **110**, 11012 (1999).
- [19] S. Pokrant and K. B. Whaley, European Physical Journal D **6**, 255 (1999).
- [20] G. A. Somorjai, *Chemistry in Two Dimensions: Surfaces* (Cornell University Press, 1982).

2 SYNTHESIS OF SEMICONDUCTOR NANOCRYSTALS

2.1 Introduction

The study of size-confined systems must include the synthesis as well as spectroscopy of the system. There are now various routes to produce systems in the nanometer size regime, ranging from molecular beam epitaxy (MBE) to solvent phase synthesis. In order to create well-designed structures in the nanometer size regime, one can approach it from large objects, the top down approach. The chemist, however, is accustomed to constructing molecules, which are systems assembled atom by atom. This is the bottom-up approach. Both methods have their respective advantages and disadvantages. However, as miniaturization increases, the top-down approach is becoming increasingly difficult and expensive to execute as conventional lithography will soon reach its limit in how small a structure it can write. The chemist's method to create nanocrystals in this size regime has the benefit that the product is soluble and therefore can be manipulated as a chemical reagent. Colloidal nanocrystals are much more flexible and versatile than MBE created or lithographically written dots. In addition, the production of nanocrystals has a high yield and turnover rate, and is extremely simple to carry out. From the point of view of the top-down methodology, solution synthesized nanocrystals are messy systems, with organic molecules on the surface which make the size and structure difficult to control. However, the degree of control in the synthesis of nanocrystals has advanced enormously in the last two decades, and at present control over composition and shape, as well as size and solubility, has reached a high degree.

In order to measure samples by photoelectron spectroscopy, the electrical contact must be made to the samples. Following the synthesis section, this chapter will describe the method used to accomplish this.

2.2 Motivation

As the purpose of studying nanocrystals is to understand size dependent physical and chemical properties, control of size in synthesis is crucial. All spectroscopic studies of nanocrystals are highly dependent on the monodispersity of the sample. Size distributions must be within reason in order to measure size dependent effects. Developments in nanocrystal synthesis have furthered research of their intrinsic properties. In addition, the choice of materials gives one freedom to study a variety of properties, such as magnetic, ferroelectric, structural, and optical behavior. The solution phase synthesis has been able to provide a wide variety of metals, semiconductors, and oxides.

2.3 General synthesis method

The synthesis of semiconductor nanocrystals has been well developed for II-VI semiconductors (CdSe, CdS, ZnSe, ZnS, CdTe) and III-V semiconductors (InP, InAs, GaAs) [1, 2]. The development of the pyrolytic route to making nanocrystals was one of the major advancements in the nanocrystal synthesis, and was the first type to produce samples with size distributions that were reasonable. Large quantities (≤ 1 gram) of nanocrystals can be produced in a few hours. The underlying strategy of this synthesis is the reaction of the molecular precursors instantaneously at high temperature in a coordinating solvent. Varying the concentrations of the reagents with respect to the reaction solution and growth time controls of the size of the particles.

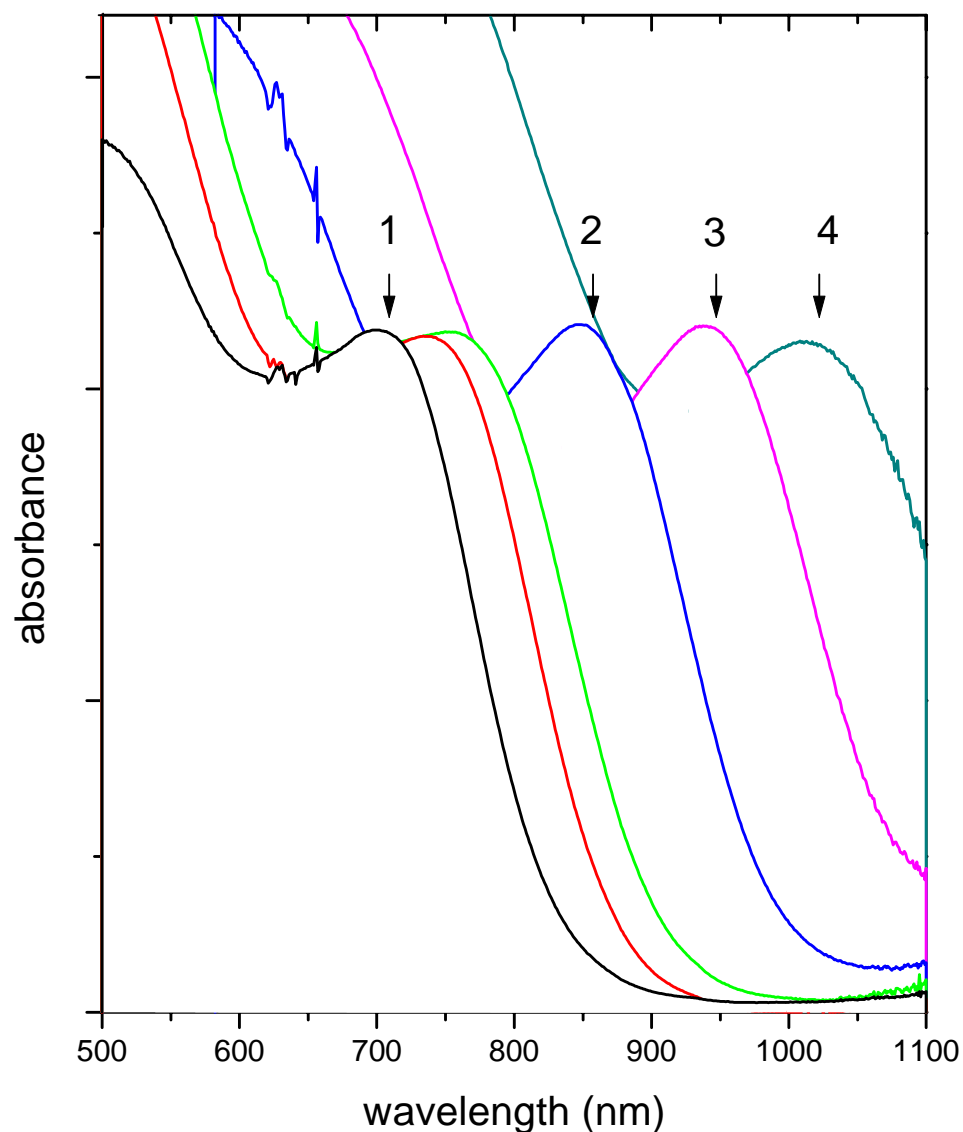


Figure 2-1 UV-vis absorption spectrum of InAs nanocrystals during growth. The numbers mark spectra taken immediately after an injection. The absorption feature shifts to longer wavelength (larger particle size) with both reaction time and with further injection of stock solution.

Evidence of the control of the size of the particle is evident from quantum confinement, which can be monitored by the optical absorption spectra. Recalling the particle-in-the-box model, the energy level spacing in a box is $\propto 1/R^2$, where R is the size of the box. Therefore, as the size of the particle is decreased, its absorption shifts to higher energy. Figure 1 shows the absorption spectra for a series of InAs nanocrystals. The

absorption feature for bulk InAs is at 0.36eV, or 1300nm and it is immediately evident that the nanocrystal absorption features exhibit quantum confinement. As the size of the particle decreases, the absorption edge shifts systematically to higher energy. The width of the absorption feature also indicates the size distribution of the sample.

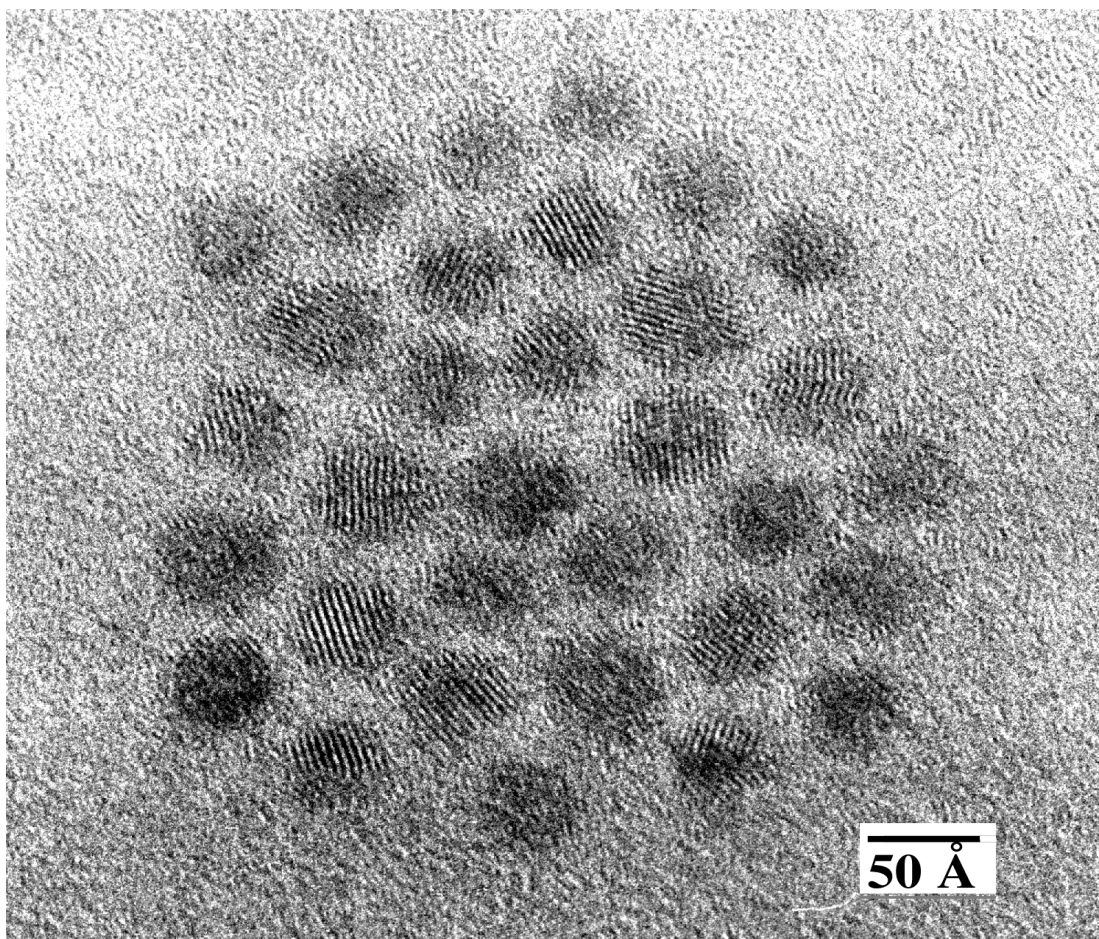


Figure 2-2 HRTEM of InAs nanocrystals on a carbon substrate. Courtesy of Andreas Kadavanich.

Characterization by high resolution transmission electron microscopy (HRTEM) and powder x-ray diffraction (XRD) shows that the particles are crystalline with the bulk lattice symmetry. Figure 2 shows a HRTEM of a field InAs particles. It is apparent that the sample is relatively monodisperse, with well-separated particles and not aggregates. The

presence of lattice fringes indicates the crystallinity of the particles. Not all particles show lattice fringes due to the random orientation on the grid.

The key advantage of the solution phase synthesis route is that the solvent becomes the surfactant to the particles. It caps the atoms on the surface, which prevents them from aggregating. The surfactant also enables the particles to be dissolved in a variety of solvents. It is the handle by which the particles are manipulated because it allows them to be dissolved in a variety of solvents and utilized as chemical reagents. The surfactant molecule can be removed or exchanged, allowing the nanocrystals to be put into a variety of solutions, dispersed into polymers, evaporated into thin films, organically linked to metal surfaces, crystallized into single crystals, and dried into powder form which can be redissolved. The surface of nanocrystals is the handle by which to control them, enabling their incorporation into devices such as light emitting diodes (LEDs), photovoltaics, and fluorescent labels for biological systems. Consequently, understanding the properties of their surface is of considerable practical significance.

2.4 Synthesis details

2.4.1 II-VI (CdSe)

Dimethyl cadmium is obtained commercially and transferred into a vial by a vacuum transfer under Ar at a pressure ≤ 20 mtorr. This removes impurities which have a higher vapor pressure than the pure compound. Pure Se metal is purchased under Ar and dissolved in tributyl phosphine in the glove box. The dimethyl cadmium is added such that the molar ratio between Cd:Se is 1:1. Size and shape control are the result of variations in the concentration. The solution should remain clear, indicating that the reagents have not reacted.

Trioctylphosphine oxide (90%) (TOPO) is degassed and heated under Ar to 360°C. The impurity in TOPO is crucial to the stabilization of the nanocrystals in solution [3]. The stock solution is injected immediately while the temperature is simultaneously lowered to the temperature for nanocrystal growth (300°C). Further injections will boost the size as well as improve the size distribution [2]. During the synthesis, the absorption spectrum is monitored to ensure that particle growth does not stop due to consumption of the reagents in solution. Once particle growth stops, Ostwald ripening begins, which is the growth of larger particles at the expense of smaller ones, an undesirable process as it increases the size distribution.

After the reaction is complete (either when the desired size is reached or the reagents are all consumed), the temperature is lowered and the nanocrystals are precipitated at room temperature with MeOH under Ar or air. The particles as synthesized are soluble in toluene, hexanes, and pyridine and can be stored as a solution or a powder indefinitely in dark and under Ar. The TOPO on the surface can be exchanged with another ligand or removed to change its solubility properties by refluxing with a labile ligand such as pyridine.

2.4.2 III-V (InAs)

The synthesis of III-V nanocrystals is based on the same principle of nucleation and growth of material. However, special precaution must be taken to avoid exposure to light and oxygen as the resulting materials (InP and especially InAs) are much more air sensitive than CdSe.

The molecular reagents for InAs are trimethylsilyl arsene (TMS As) and InCl_3 . TMS As is not commercially available and was synthesized by reducing As metal to As^{3-} . TMSCl is reacted with As^{3-} to form TMSAs. In all of the steps in the synthesis it is crucial to keep the reaction flasks air free.

As (metal) is refluxed in a mixture of NaK and anhydrous ethylene glycol dimethyl ether (diglyme) at 85°C. TMSCl which has been dried over CaH_2 is distilled (62°C) and added dropwise to the reaction flask with the temperature maintained at 50-55°C. The reaction is then refluxed overnight at 85°C. When cool, the reaction is filtered in a glove box to remove the salts that have formed (NaCl, KCl). The distillation pot is at LN2 temperatures and allowed to warm to room temperature, during which the diglyme is distilled off. TMSAs distills around 52°C as a clear product and is subsequently stored at 4°C in a glovebox.

The precursors are reacted in a flask of tri-*n*-octyl phosphine (TOP). Anhydrous TOP is distilled under vacuum to remove any of the oxide (TOPO). The InCl_3 is purchased and dissolved in distilled TOP by refluxing at 260°C under Ar. The amount of InCl_3 that is dissolved in the TOP is enough to make the solution saturated. Stock solution is made up so that the molar ratio of In:As is 1:1. Typically, the amount used is 1 ml TOP: InCl_3 with 0.144g TMSAs. The stock solution is prepared just before injection because the TMSAs and InCl_3 starts to react immediately, exhibited by the immediate color change of the solution from clear to yellow to red. The stock is rapidly injected into TOP at 300°C and the temperature is immediately lowered to 260°C, at which the particles are allowed to grow. Subsequent injections boost the size and also improve the size distribution as described for CdSe.

Because of the relatively poor size distribution and air sensitivity of the InAs particles, the particles are not precipitated out of solution in air. They are brought into a glove box, dissolved in a minimal amount of anhydrous toluene, and then size selectively precipitated. The solution for precipitation is 3:1 ethyl acetate: MeOH (by volume), though this ratio is altered to prevent the formation of an oil between it and the TOP/toluene

solution. The resulting precipitates are stored as a solution in anhydrous toluene in an inert atmosphere.

2.4.3 InAs/CdSe core-shell nanocrystals

Core-shell materials of InAs/CdSe were also prepared to a method similar to the one for CdSe/CdS [4-6] and InP/CdSe [7]. The InAs nanocrystals are dissolved and refluxed in TOP or anhydrous benzylamine in the temperature range of 110-260°C under Ar. The best results were obtained with benzylamine at 140°C. The time of the reflux is limited to a few hours as the particles tend to oxidize and the distribution broadens after a long period of time. CdSe stock solution is made in a 1:2 Cd:Se molar ratio in TBP, with the concentration much lower than in a CdSe synthesis (45mg Se : 120mg Me₂Cd : 12.3g TBP). The stock is injected into the nanocrystal reflux dropwise so as to allow complete dissolution. The volume of each injection is such that it completes one monolayer on the core. The optical absorption jumps on the order of 50 meV with each injection (Figure 3). The particles are precipitated out of the solution in air using MeOH and acetone, in varying concentrations to prevent oil formation with the TOP solution which inhibits size selection. In the case of benzylamine the particles are precipitated out with hexanes in air. Excess benzylamine is removed by washing with MeOH and reprecipitating with hexanes multiple times. Additional surfactant can be added to the CdSe surface by heating the nanocrystals in a solution of TOPO dissolved in butanol at 80°C for 1 hour.

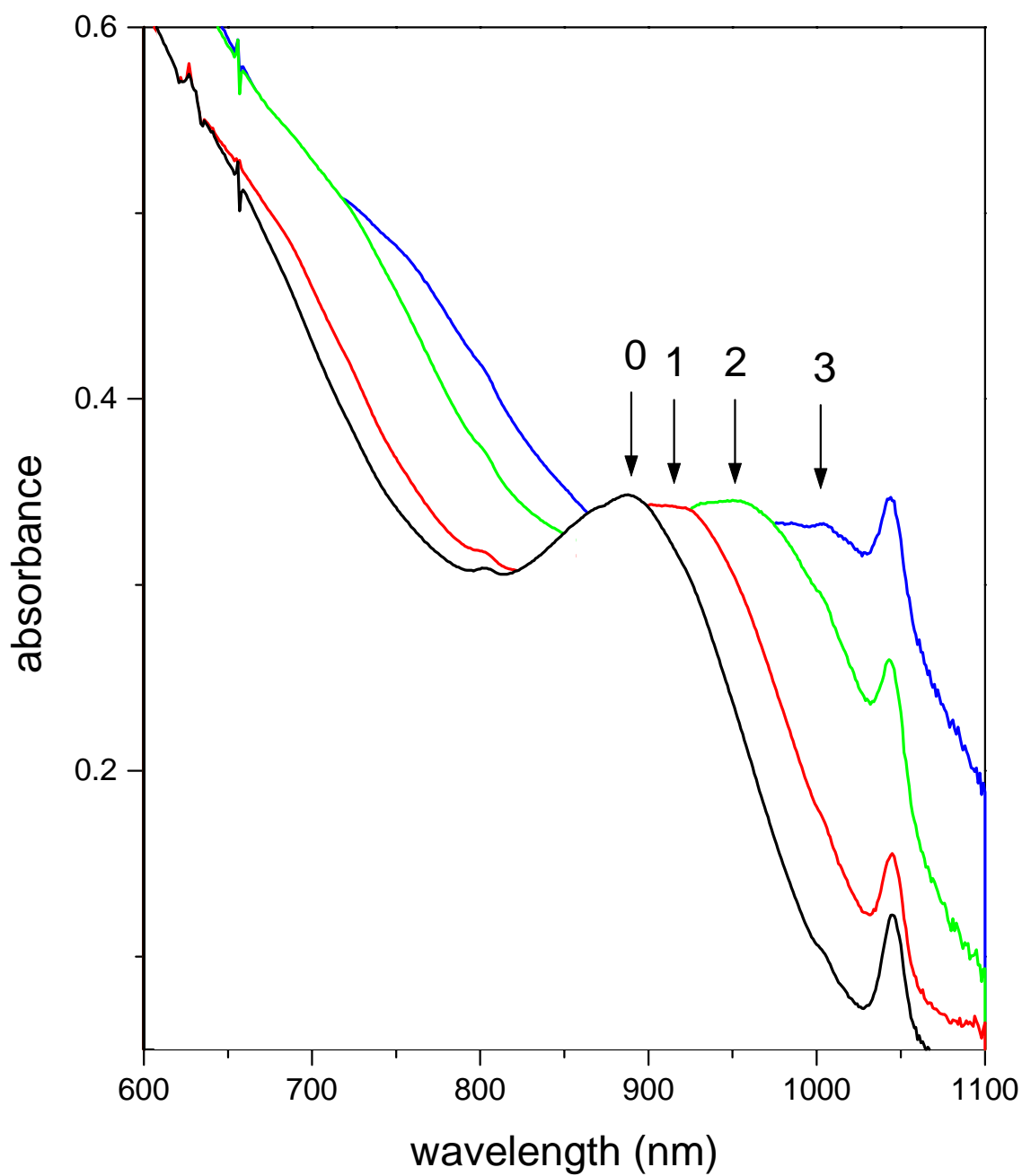


Figure 2-3 UV-vis absorption for InAs/CdSe core shell synthesis. The numbers mark the absorption spectra after injection of CdSe stock. The spectrum marked 0 is before any injections.

2.5 Preparation of samples for photoelectron spectroscopy

For PES the sample must have some way of refilling the electrons ejected in the photoemission process, so electrical contact must be made to the nanocrystals. This challenge has been overcome by an ingenious method of organically tethering the particles to a conducting surface[8, 9]. The proximity of the nanocrystal to a metallic substrate provides a means by which the charge can be dissipated in the nanocrystal. The organic linker is usually a dithiol (S-R-S), which has S ends that have a high affinity for Au. Because of this high affinity, the molecules form close-packed structures on the surface in which they are believed to be aligned perpendicularly to the substrate. The other end of the dithiol links to the nanocrystals. A schematic of the composite is shown in Figure 4. Au is evaporated onto cleaved mica in a vacuum evaporator and the substrate is subsequently annealed and plasma cleaned. They are submerged in an isopropanol solution of 1-6 hexanedithiol or 1-8 octanedithiol for 12 hours. The substrates are rinsed with isopropanol and dried in N₂ (g) before being submerged in nanocrystal solutions of toluene (for TOPO capped particles) or pyridine (in the case of TOPO stripped particles) for several hours. Nanocrystals have been successfully linked to Au, Ag, and indium tin oxide (ITO) by this method. The clusters can also be linked to semiconductor substrates such as Si by use of the molecule (3-mercaptopropyl) trimethoxysilane (HS(CH₂)₃Si(OCH₃)₃) in chloroform solutions. A field emission scanning electron microscopy image (FESEM) (Figure 5) of a CdSe/hexanedithiol/Au sample shows that the nanocrystals are deposited evenly on the Au surface without fusion or aggregation. Because the coverage of the nanocrystals on the substrates is less than a monolayer, the nanocrystals are in proximity to the metal surface which provides electrons to fill the hole created in the photoelectron process, so the samples

do not charge. This is important if the shifts of the core levels or valence bands are of interest.

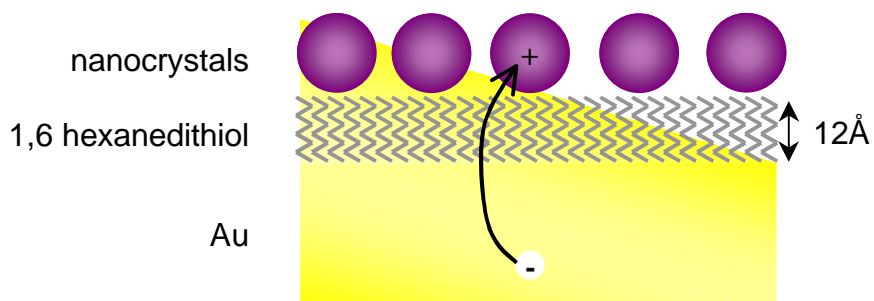


Figure 2-4 Schematic of the nanocrystals on dithiol/Au substrates. The hexanedithiol links the nanocrystals to the metal. Because of the proximity of the nanocrystals to the metal, the charge can be refilled.

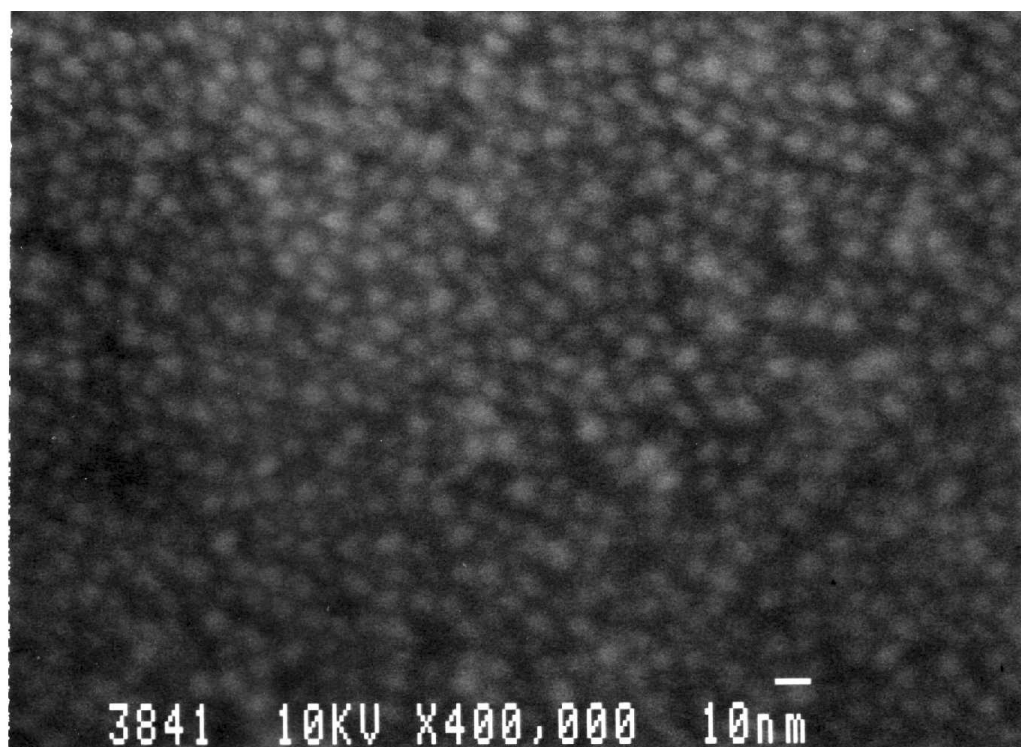


Figure 2-5 FESEM of 60Å CdSe nanocrystals on hexanedithiol/Au. The white spots are individual nanocrystals and the dark background is the hexanedithiol/Au substrate.

2.6 References

- [1] C. B. Murray, D. J. Norris, and M. G. Bawendi, J. Am. Chem. Soc. **115**, 8706 (1993).
- [2] X. Peng, J. Wickham, and A. P. Alivisatos, J. Am. Chem. Soc. **120**, 5343 (1998).
- [3] X. Peng, L. Manna, W. Yang, J. Wickham *et al.*, Nature **404**, 59 (2000).
- [4] X. Peng, M. C. Schlamp, A. V. Kadavanich, and A. P. Alivisatos, J. Am. Chem. Soc. **119**, 7019 (1997).
- [5] B. O. Dabbousi, J. Rodriguez-Viejo, F. V. Mikulec, J. R. Heine *et al.*, J. Phys. Chem. B **101**, 9463 (1997).
- [6] M. A. Hines and P. Guyot-Sionnest, J. Phys. Chem. **100**, 468 (1996).
- [7] U. Banin, 1999, personal communication.
- [8] V. L. Colvin, A. N. Goldstein, and A. P. Alivisatos, J. Am. Chem. Soc. **114**, 5221 (1992).
- [9] J. E. Bowen Katari, V. L. Colvin, and A. P. Alivisatos, J. Phys. Chem. **98**, 4109 (1994).

3 EXPERIMENTAL APPARATUS FOR PHOTOELECTRON SPECTROSCOPY

The x-ray photoelectron spectroscopy and TPD experiments described in this work were performed in a custom designed photoelectron spectrometer. This chapter describes the general features of the spectrometer in order to give light on its experimental capabilities. Because of the nature of the sample, certain apparatus that are found on common vacuum chambers may be omitted, such as ion sputterers (which would obliterate the nanocrystals) and electron diffraction systems (which require long range order). The architecture of the system (Figure 1) is designed with a main chamber for measuring electron spectroscopy and a second (or “prep”) chamber for measuring higher pressure experiments such as TPD. The sample can be brought through the two measuring chambers, which are isolated by a gate valve.

3.1 Pressure

The chamber is at ultra-high vacuum (UHV), with a base pressure as low as 1×10^{-10} torr but typically around 5×10^{-10} torr. The base pressure after UPS experiments is often as high as 5×10^{-9} torr due to the high pressure of the helium system (see below). The vacuum is achieved by roughing with a dry diaphragm pump and a turbomolecular pump, which then reaches a pressure that is feasible for an ion pump (1000l/s). The combination of the ion pumps with periodic use of the titanium sublimation pump achieves the pressures in the UHV regime. Additional pumping can be achieved cryogenically using the liquid nitrogen (LN2) pump.

3.2 Electron energy measurement

The electron detector is a hemispherical electron energy analyzer, with an energy resolution of 25meV. The energy selection is achieved by modulating the electrostatic potential between the two plates, thus allowing electrons of a specific energy to pass between the plates. Variation of the pass energy, or the energy to which the electrons are slowed down before the kinetic energy measurement, varies the resolution of the experiment. The higher the pass energy, the lower the resolution but the greater the signal that is detected. The detector is angle specific which allows mapping of momentum of the electron and can accept an electron distribution angle of $\pm 2^\circ$, $\pm 5^\circ$, or $\pm 7^\circ$.

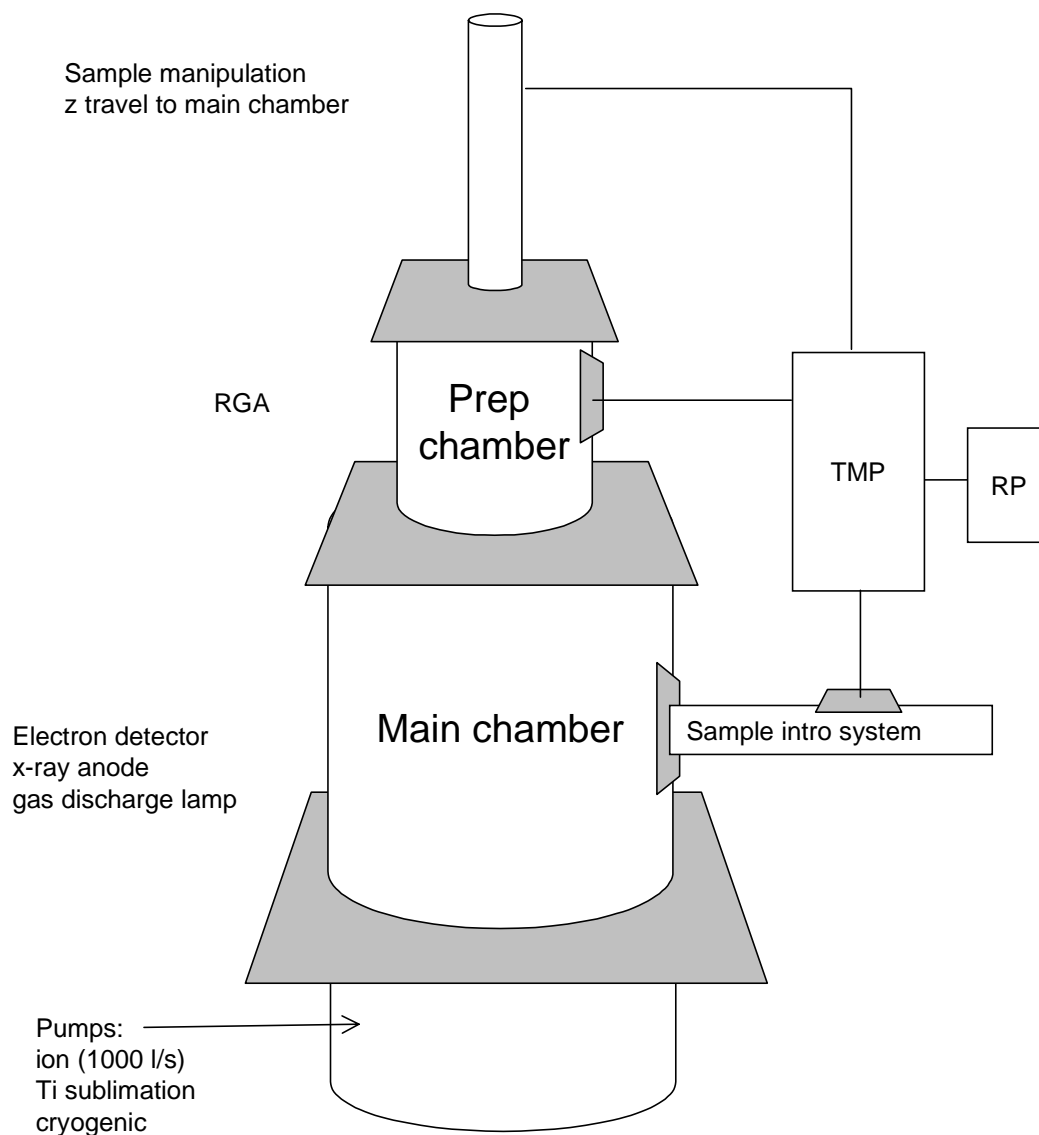


Figure 3-1 Schematic of the photoelectron spectrometer showing the architecture of the chambers. Valves are grey.

3.3 Photon sources

The chamber is equipped with a x-ray source and an ultraviolet source. The x-ray source is a dual anode (Mg or Al $K\alpha$) which emits light via the bombardment of the metal with electrons. The ultraviolet source is a gas discharge lamp which consists of a chamber where the electrical discharge occurs in an environment of a noble gas. In the case of He the

two lines of light that are emitted are 21.21eV and 40.8eV, which is the 2p-2s transition for the neutral and the singly ionized species, respectively. He I: He II intensity ratio is roughly 17:1 and varies with He pressure and voltage of the discharge. The typical operating voltage is 5kV and current is 25mA. Because the linewidth of the He line is $\sim 10\text{meV}$, the resolution makes it attractive as a photon source. Since no window transmits in this energy range, the light must be let into the UHV chamber by means of a capillary tube 1-2mm in diameter, which necessitates differential pumping. The pumping diagram for the UV lamp setup is shown in Figure 2. The lamp discharge is highly sensitive to contaminants, so the He used is of very high purity (at least 99.999%, though most often 99.9999% was used) and is run through a LN2 trap upstream of the discharge chamber. In addition, oil in the pumping system must be minimized so a dry scroll pump is used for the first stage and a sieve is used on the turbo/roughing pump station. Starting the lamp requires overpressuring the system to nearly atmospheric pressure (read on the thermocouple gauge) until the voltage “strikes” and then the pressure is lowered before the discharge dies. Pressure on the thermocouple gauge during operation of the lamp is $\sim 200\text{mtorr}$ and on the cold cathode gauge 8×10^{-6} torr. Pressure in the main chamber during a UPS experiment is $\sim 2 \times 10^{-8}$ torr.

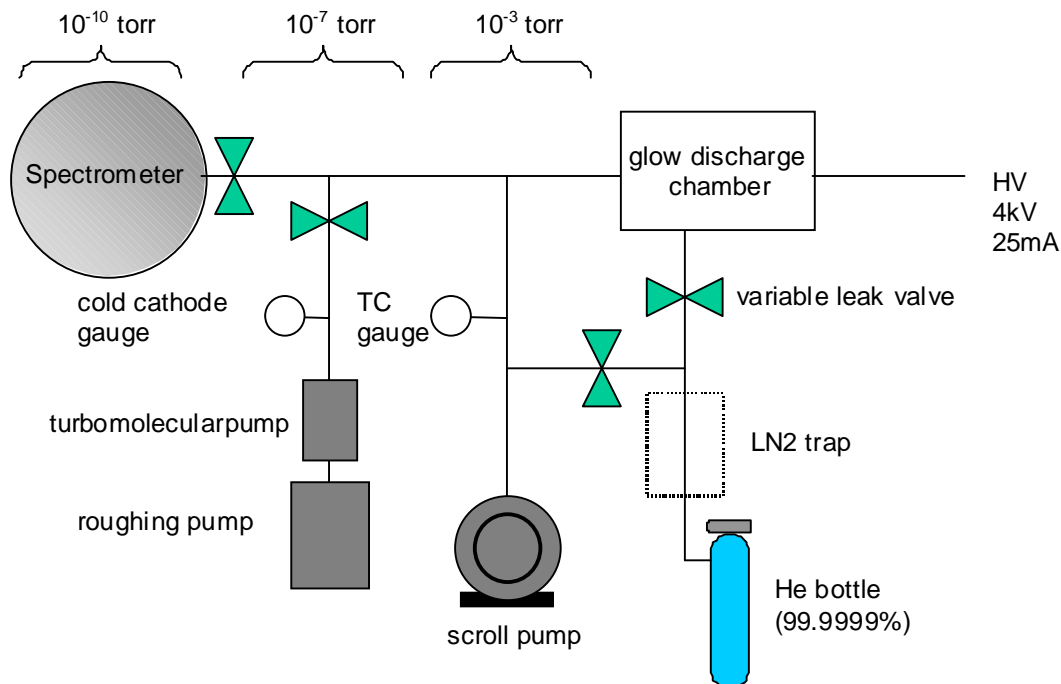


Figure 3-2 Pumping diagram for the He discharge lamp. Valves are denoted in green.

3.4 Sample manipulation

The sample manipulator was designed to allow for full sample translation and rotation so as to enable angle resolved photoemission experiments. Azimuthal and polar rotations are necessary for ARPES and XPD. Due to the teflon seals between the rotation stages, leaks are quite common with sample rotation so the seals are differentially pumped with a roughing pump and a 2 l/s ion pump. Because the sample must be brought through the upper chamber into the main chamber, the z travel must be 15" long, which makes the chamber very tall.

3.5 Sample intro

Study of nanocrystals as a function of size, surface capping group, and substrate requires the measurement of many samples unlike the study bulk surfaces in which experiments can be performed on a single sample that can be etched and re-used in vacuum

indefinitely. Therefore, sample changing must be both facile and rapid and not disturb the vacuum in the main chamber, as pump-down time is long. The sample introduction system consists of a load lock which can be brought to air and in a short amount of time pumped down to $\sim 10^{-7}$ torr, a pressure at which can be opened to the main measuring chamber.

Pressure in the main chamber during sample intro rises to $\sim 5 \times 10^{-9}$ torr. The sample intro system uses a swing arm to position it for either mounting the sample or to bring it into the main chamber (Figure 3). The motion control on the arm is by a magnetically coupled system, which reduces the possibility of leaks during motion. The transfer mechanism is achieved by the locking and unlocking of clips on the face and the base of the sample plate. In general, sample transfer can occur in about $\frac{1}{2}$ hour, including time for pump down of the load lock. The system also includes a vacuum “suitcase,” which permits introduction of samples without any exposure to air. The suitcase is relatively small ($\sim 4'' \times 12''$) and can be brought into a glove box, where the sample is put into the suitcase and the valve is shut. The suitcase is then attached to the load lock system and the sample can be then introduced into the main chamber.

3.6 Temperature

The sample plate on the manipulator can be cooled and heated. Cooling was achieved by thermal contact with a liquid nitrogen dewar mounted on a copper block in the chamber and allowed the temperature on the sample to go down to 180K. The sample heating was achieved radiatively by a filament directly behind the sample in a manipulator. The filament can also be placed at a potential to allow for electron beam heating, increasing the allowed temperature range to up to 500K. Temperature is measured by a thermocouple mounted directly on the sample plate. Contact with the

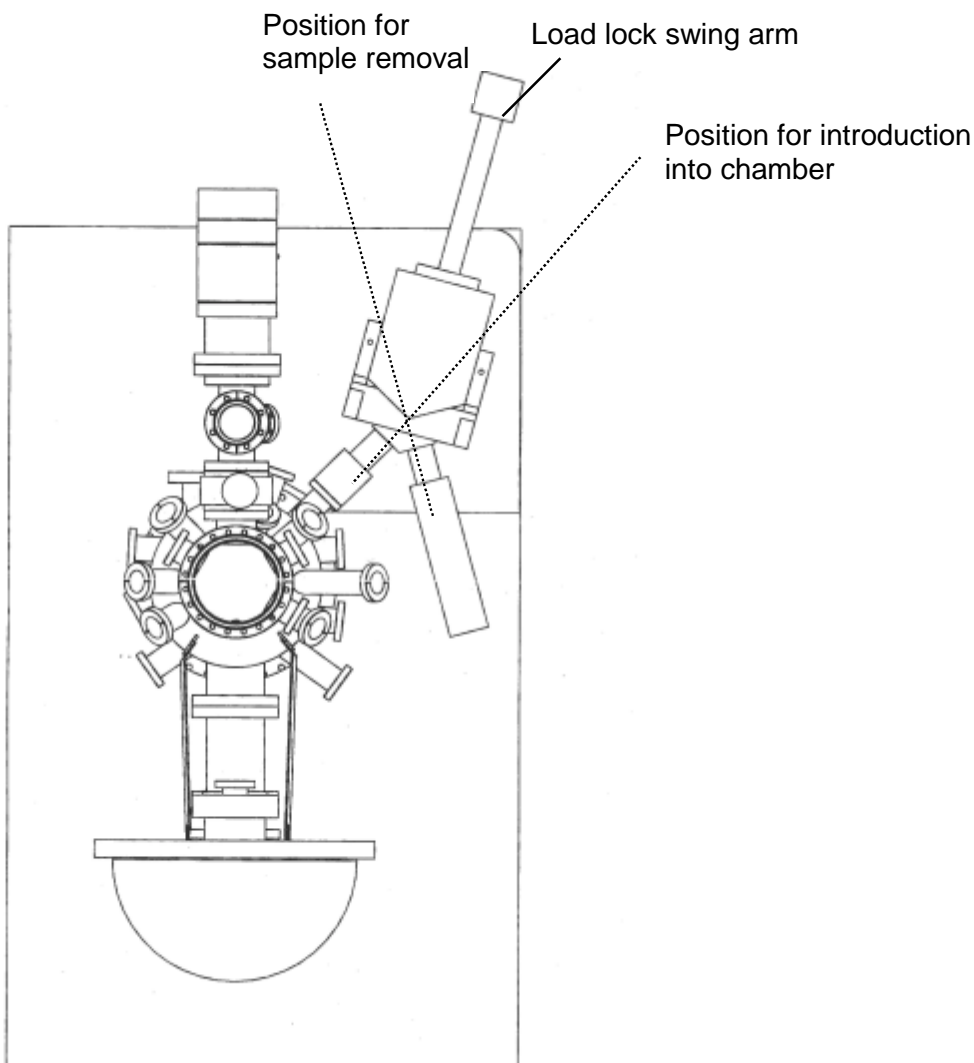


Figure 3-3 Top view of chamber showing the load lock assembly and the positions for sample transfer.

ends of the thermocouple on the sample with the outside temperature controller is via the clips of the sample plate upon mounting on the manipulator. The clips on the sample plate were manufactured out of chromel/alumel (Type K) so as the voltage drops were correct for accurate temperature measurements.

The sample plate can also be placed at a specific bias or at ground. The purpose of this is to be able to shift core level binding energy in a controllable manner, which allows accurate measurement of the low energy cutoff as well as diagnostic purposes.

The upper chamber is equipped with a quadrupole mass spectrometer capable of measuring down to 10^{-12} torr. The mass resolution is 0.25 amu, with a measurable range of 1-200amu. QMS systems are compact and therefore ideal for measuring gases on a UHV chamber.

3.7 Beamline hookup

Photoelectron spectroscopy experiments were also performed at the Advanced Light Source (ALS) for the goal of higher resolution and variable photon energy. The XPS chamber was attached to Beamline 6.3.2 beyond the endstation. The chamber was vertically raised ~ 6 feet to meet the height of the beam. Precision positioning and mechanical support of the chamber was achieved by use of a six-strut system, which allows variations of x, y, and z translation, along with pitch, yaw, and roll. Because the range of travel on a six-strut system is only ± 16 mm, the chamber had to be positioned very carefully before using the six-strut system. The beam was allowed into the chamber through a $< 1\text{mm}^2$ pinhole to prevent instantaneous filling of the chamber or the beamline endstation in the event of vacuum breakdown. The sample was aligned relative to the beam by aligning the sample with respect to the analyzer, the coordinates of which were known relative to the vacuum chamber. A HeNe laser defined the axis of detection in the chamber. A sample with phosphor (which fluoresces in x-rays) was placed in the detection axis and then the chamber was moved to coincide the beam with the detection axis.

4 PHOTOELECTRON SPECTROSCOPY

4.1 Motivation

As the size of a solid is made smaller, the continuous energy bands evolve into discrete levels or orbitals. Relative to the molecule and the infinite solid, the energy levels for the nanocrystal are not fully developed. One would like to understand how these bands evolve as a function of size of the system. Optical spectroscopy of nanocrystals probes how the conduction and valence band change together in quantum confinement, but how the conduction band and the valence band change separately must be measured by electronic spectroscopy. Photoelectron spectroscopy has proven to be a useful technique in investigating chemical state information and electronic structure about nanocrystals.

The following four chapters will describe two PES experiments that explore different properties of nanocrystals. The following chapter (Chapter 5) will describe PES experiments studying the chemical and electronic environment of nanocrystals by the core levels. In addition, PES is proportional to density of states and thus can be used to explore the change in the valence band structure and levels as a function of size and electronic environment. The following two chapters (Chapters 6 and 7) will describe experiments that find that the electronic structure of nanocrystals is influenced by the metal substrate onto which they are deposited. Interpretations in terms of hole-screening and band bending effects will be described, respectively. This chapter will also describe experiments using UPS to measure the band offsets for a nanocrystal/metal interface or within a core-shell nanocrystal. The final XPS chapter (Chapter 8) describes a study of the kinetics of a reaction occurring at the nanocrystal surface.

Photoemission was first observed in 1887 by Hertz, and described in the language of quantum mechanics by Einstein in 1905. PES has found its way into many fields as a spectroscopy in various forms, ranging from time-resolved studies of gas phase systems to examining band structures of solids. The potential of PES as a diagnostic tool was recognized by Kai Siegbahn in 1967 for its use as a chemical fingerprint (Electron Spectroscopy for Chemical Analysis, or ESCA) with the development of high resolution electron energy detectors and monochromatic x-ray sources. The chemical environment of an atom can be investigated by comparison of its core-level binding energies with a reference compound. As a result, XPS is widely available as an analytical tool.

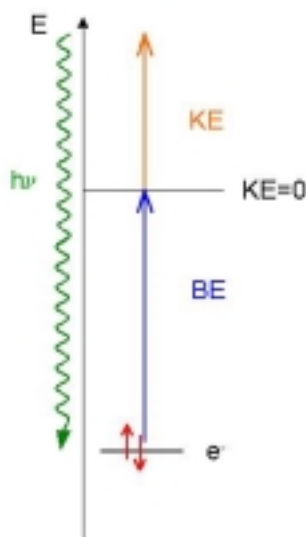


Figure 4-1 A energy level diagram for a photoemission experiment. A photon of known energy (green) is absorbed by a core electron (red), which is ejected with some kinetic energy (orange). By measuring the kinetic energy, the electron's binding energy can be deduced (blue).

The basic phenomenon of PES is the shining of monochromatic photons, usually in the x-ray or vacuum ultraviolet regime, on a solid. Electrons bound in the solid absorb the photons, and if the photon energy is high enough, the electron can be ejected from the solid into vacuum and be detected. Photoelectron intensity is measured as a function of kinetic

energy and lines in the intensity correspond to the atomic levels at certain binding energies in the solid. The momentum of the ejected electron is directly related to the momentum of the electron in its original state (in the solid), hence PES yields information about the electronic states of the solid. The basic phenomenon is illustrated in Figure 1.

The photoionization event for a system can be described as

$$M_0 + h\nu \rightarrow M_+^* + e^-$$

where M_0 is the isolated neutral, $h\nu$ the photon, M_+^* the positive ion in the excited state, and e^- the photoelectron with kinetic energy E_k . If $E_k \gg 0$, the electrostatic coupling between the e^- and M_+^* is small. The equation for the energy of the system before and after the photoionization event is

$$E_0 + h\nu = E_+^* + E_k$$

where E_0 is the total energy of the neutral in the ground state, $h\nu$ the energy of the photon, and E_+^* the total energy of the ionized system in the excited state. Therefore, the binding energy of a level is

$$\begin{aligned} E_B &= E_+^* - E_0 \\ &= h\nu - E_k \end{aligned}$$

It is crucial to note that the binding energy measured in an PES experiment is not the binding energy of the level of the neutral in the ground state but the energy difference between E_0 and E_+^* .

The ejection of the electron can be described in the simplified terms of the three step model. [1] Step (1) is the excitation of the electron upon photon absorption, step (2) is the transport of the electron to the surface of the solid, and step (3) is the emission of the electron from the solid into vacuum, where it can be detected. Because the electron

interacts strongly with the solid, it loses energy while it is traveling to the surface of the material, which will be explored further in section 4.4.

It is important to consider the nature of the final state M_+^* in a photoemission process. Upon ejection of a photoelectron, the system is left with a vacancy, or a hole which is a unit positive charge. The proximity of a positive charge in a deep core near the nucleus is energetically unfavorable, so the nearby electrons relax in order to screen the positive charges from each other. The electronic relaxation is on the order of 10^{-16} s, while nuclear geometric relaxation is approximately 10^{-13} s. Because the photoelectron takes about 10^{-15} s to leave the system, the photoelectron is sensitive to this electronic relaxation. Therefore, the photoelectron energy is affected by the screened hole along with any other electronic relaxation processes. Furthermore, the photoelectron spectrum is a measure of the system with a net positive charge and not of the neutral state.

4.2 Core levels in photoemission

If the electron originates from a deeply bound state or a core level, chemical information about the solid can be investigated. First, because the core levels appear at distinct binding energies, the presence of core levels gives a fingerprint of the elements in the solid. Secondly, the core levels often exhibit shifts in energy due to chemical environment. These are chemical shifts allow one to analyze the chemical environment of the atom. Chemical shifts for each element in the periodic table have been tabulated for various compounds. [2] The amount of the binding energy shift can often be quite large compared to the linewidth of the x-rays ($\sim 5\text{eV}$) and thus are easily recognizable. It is this feature of XPS which lends itself to chemical analysis.

The direction of the shift of the core level can be understood in terms of electrostatics. The energy of the core electron is affected by the attractive potential of the nucleus and the repulsive interaction with the surrounding electrons in the compound. If the chemical environment is changed, the valence electrons are redistributed and this change in electron density affects the binding energy of the core electrons. For example, oxidation of a compound involves the removal of electrons. Consequently, it becomes more difficult to remove another electron. As a result, oxidized forms of the elements shift to higher binding energy, on the order of a few eV.

The relative amount of a binding energy shift can be interpreted in terms of the electronegativity of the atoms involved. For example, Chapter 8 will describe experiments studying the oxidation of CdSe nanocrystals to produce CdSeO_{2,3}. The Se 3d core level spectra show dramatic changes with oxidation but the Cd 3d spectra do not. Because O and Cd have very different electronegativities, the binding energy of an electron on a Se atom bound to O is very different from one bound to Cd. On the other hand, the electronegativity of Se and O are quite similar, and thus the binding energy of a Cd atom bound to O is similar to one bound to Se. Therefore, it is expected that the chemical shift between CdSe and CdO is small, and indeed Cd does not show a well-separated oxide peak.

Core level shifts have also been found to come from structural changes. Due to the surface sensitivity of the technique, energetic differences in the core levels between a surface atom and its interior counterpart have been measured and found to be on the order of a few 100meV. For complex surfaces with multiple distinct atomic sites, the photoemission peaks are often decomposed into each of the atomic contributions. However, due to the limited resolution of an XPS experiment ($\geq 100\text{meV}$), the peak decomposition is often arbitrary and therefore unreliable.

Core level shifts may also arise from changes in the electronic structure of the material or relaxation processes. These shifts can yield information about the bonding of atoms in a solid and also electronic properties such as hole screening and band bending effects at an interface. XPS experiments used to investigate these effects in nanocrystals will be discussed in later chapters.

4.3 Mapping the density of states (DOS)

If the electron originates from the low binding energy region (0-10eV), the experiment probes the shallow valence states. The spectrum is broad due to the continuum of states in the occupied bands. Information about the band structure as well as interfacial properties such as band offsets can be attained. PES has been well established as one of the foremost techniques for mapping band structures and the density of occupied states [1]. It was the first technique to confirm band structure calculations for solids [3, 4]. As most of the important physical and chemical properties of solids are related to their valence electronic states, PES is a powerful technique for understanding fundamental behavior of materials.

The photoelectron spectrum is related to the density of states in a solid by

$$N(E) \propto N_0(E) T(E) S(E)$$

where the function $N_0(E)$ is the internal distribution of states as a function of energy (DOS of the solid), $T(E)$ is the transport function of the electron to the solid surface, and $S(E)$ is the threshold function of the solid. Both $T(E)$ and $S(E)$ vary without abrupt features as a function of energy. Therefore, the measured number of electrons as a function of energy $N(E)$ is directly proportional to the DOS of the solid.

4.4 Surface sensitivity

Because photoelectron spectroscopy involves measurement of the kinetic energy of electrons, it is a surface sensitive technique. This is easily understood by the fact that an electron ejected from a surface atom will encounter fewer atoms in its path out of the solid. Therefore, surface photoelectrons have a lower probability of undergoing inelastic scattering off neighboring atoms. The electron-solid interaction is strong, so there are a number of processes by which an electron can lose energy before it escapes the solid. Quantitatively, the depth from which an electron originates has a distinct energy dependence due to the combination of all the loss processes. Figure 2 shows a plot of the universal curve, which is a plot of this energy dependence. It describes the escape depth of an electron as a function of its kinetic energy. [1, 5-7] The points are measured for specific materials, but the general trend is observed for most solids, hence its “universal” label. It indicates that the scattering of the photoemitted electron will depend on its wavelength (or kinetic energy). The shape of the curve can be understood qualitatively as follows: at low or high kinetic energy, the interaction of the electron with the solid is weak and is scattered infrequently. This can be qualitatively argued by the wavelength of the photoelectron. At about 50 eV kinetic energy, the electron wavelength is closest in size to the core of an atom, thus scattering is frequent. As a result, a minimum occurs (at ~ 50 eV) at which the escape depth is extremely short (~ 5 - 10 \AA). It is at this kinetic energy that the electron measurement technique is the most surface sensitive.

The surface sensitivity of PES has made it instrumental in the study of bulk surfaces and interfaces. Surface scientists can exploit the finite escape depth to their advantage, which is exemplified in not only PES but also in low energy electron diffraction (LEED), electron energy loss spectroscopy (EELS), Auger electron spectroscopy (AES), and several other

techniques. However, it should be noted that the length scale that is surface sensitive for bulk systems is on the order of the size of the nanocrystal (10\AA). Therefore, a typical XPS measurement has an escape depth such that the experiment probes the entire nanocrystal, so XPS is not especially surface sensitive in the case of nanocrystals. For a photoemission measurement to probe only the surface of a nanocrystal, the escape depth must be on the order of 5\AA , which can be achieved by using lower energy photons from a synchrotron or a gas discharge lamp. Synchrotron experiments afford the possibility of tunable surface selectivity as kinetic energy of the photoelectron can be varied systematically.

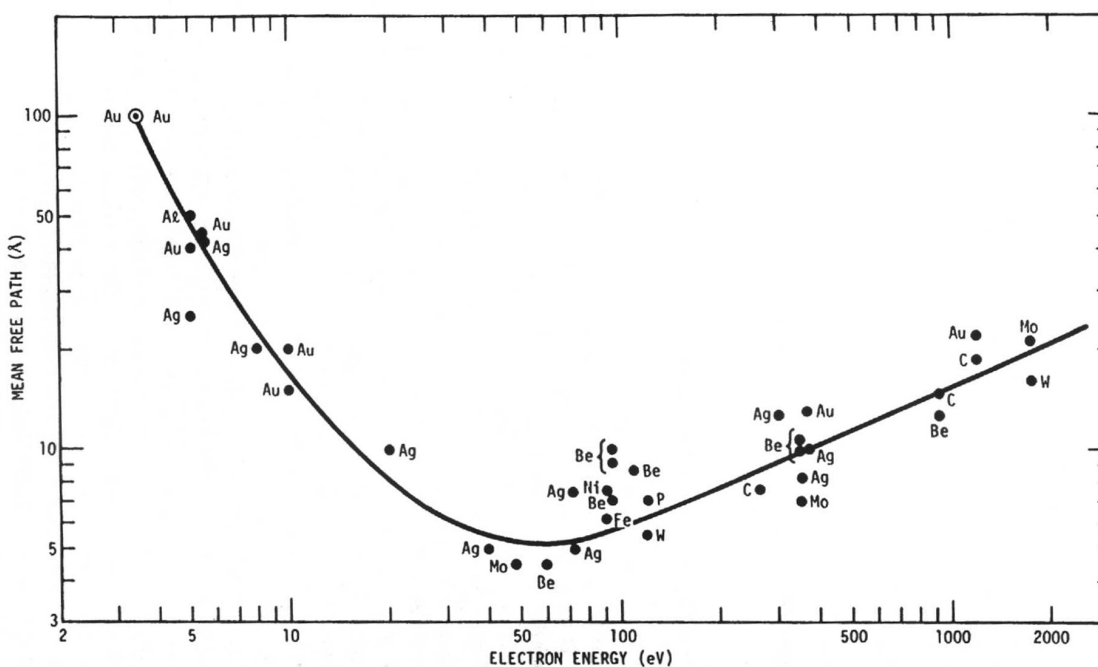


Figure 4-2 Mean free path of an electron (\AA) as a function of its kinetic energy (eV). Taken from [5, 6].

The other feature of studying surfaces using PES is that the surface sensitivity of the measurement demands clean surfaces. One studying bulk surfaces must take many precautions to insure that the surface is free of adsorbed molecules which may obscure the properties of the surface that are of interest. However, because of how they are synthesized,

nanocrystals inherently have a surfactant ligand, so clean surfaces are not always a possibility. The ligand can be removed from the nanocrystal by refluxing in certain solvents, but complete removal is not achievable. Moreover, since nanocrystals are made in solution, they are present many challenges in using electron spectroscopy to investigate their properties.

4.5 UPS vs. XPS

The valence band can be measured with either a high energy source (x-rays, or XPS) or a low energy source (ultraviolet radiation, or UPS). However, the two techniques differ in capability and also what they probe.

X-ray sources come in a variety of types but the most common is the x-ray tube (Mg or Al $K\alpha$). X-ray anodes produce light by electron bombardment of a metal, creating a vacancy on a core level. An electron from a higher level falls to fill the hole, emitting light of a specific energy. The x-ray linewidth is inversely proportional to the lifetime of the hole, so for the Mg $K\alpha$ transition which involves a deep hole (1s) the lifetime is very short.

The typical source for UPS is a helium lamp, which has a much higher resolution than the x-ray source (linewidth $\sim 10\text{meV}$). The higher resolution of the helium lamp is due to two factors. First, gas discharge lamps are the typical photon sources used for UPS and produce light from atomic transitions in the gas phase which have typical linewidths of $\sim 10\text{meV}$. Secondly, because the photon energy is lower, the pass energy on the detector can be set to a lower value, thus allowing a higher resolution measurement. One of the ramifications of the lower photon energy is increased surface sensitivity in UPS over XPS.

Since the kinetic energy of the photoelectron in a UPS experiment is typically in the range of 50eV, the mean free path or effective sampling depth is $\sim 5\text{\AA}$ according to the universal curve (Figure 1). This increased surface sensitivity also means that the experiment

is much more sensitive to contaminants. One major difficulty in measuring UPS spectra is determining whether or not one is measuring the material of interest or adsorbed molecules on the surface of the sample. This is an unfortunate obstacle for the nanocrystals scientist, as typical surface science techniques used to clean bulk surfaces (ion sputtering, baking, cleaving, etc.) cannot be applied to nanocrystals. However, it has been demonstrated successfully that UPS can be used to measure the band structure of electrically conducting polymers like PPV, which are commonly thought to be messy systems, due to being completely organic and synthesized in solution. [8]

In light of these issues, the following chapters will illustrate how PES can be applied to study the electronic structure and chemical state information of nanocrystals with particular interest in the surface. Experiments using PES to examine the density of states, electronic excited state properties, and chemical state information will all be described.

4.6 References

- [1] M. Cardona and L. Ley, *Photoemission in solids, volumes I and II* (Springer-Verlag, Berlin, New York, 1978).
- [2] J. F. Moulder, W. F. Stickle, P. E. Sobol, and K. D. Bomben, *Handbook of X-ray Photoelectron Spectroscopy* (Physical Electronics, Inc., Eden Prairie, 1995).
- [3] M. L. Cohen and J. R. Chelikowsky, *Electronic Structure and Optical Properties of Semiconductors* (Springer, Berlin, 1989).
- [4] P. Y. Yu and M. Cardona, *Fundamentals of Semiconductors: Physics and Materials Properties* (Springer-Verlag, New York, 1996).
- [5] G. A. Somorjai, *Chemistry in Two Dimensions: Surfaces* (Cornell University Press, 1982).
- [6] J. G. Tobin, in *Determination of Electronic and Optical Properties*, edited by B. W. Rossiter and R. C. Baetzold (John Wiley & Sons, Inc., 1993), Vol. VIII.
- [7] I. Lindau and W. E. Spicer, *Journal of Electron Spectroscopy and Related Phenomena* **3**, 409 (1974).
- [8] M. Löglund, W. R. Salaneck, F. Meyers, J. L. Brédas *et al.*, *Macromolecules* **26**, 3815 (1993).

5 USING XPS AND UPS TO MEASURE THE DENSITY OF STATES IN NANOCRYSTALS

5.1 Introduction

One of the primary goals of study size-confined systems is to understand the evolution of electronic structure with size. As a result, much effort has gone into measuring the electronic structure of nanocrystals by optical spectroscopy, which has been successful in yielding extremely sophisticated information about transitions at or near the energy gap. [1-3] However, XPS and UPS have the potential of acquiring information about the bands of a different nature, namely, the density of occupied states. This chapter describes experiments using these techniques to obtain the density of occupied states (DOS) in nanocrystals.

XPS measurements of bulk materials are performed with the goal of mapping band structure, which is a plot of the energy levels as a function of momentum, $E(\mathbf{k})$. It is this characteristic of XPS that first confirmed electronic band structure calculations of solids. [4] However, for nanocrystals, constructing an E vs. \mathbf{k} band diagram is not possible as \mathbf{k} is no longer a good quantum number due to the uncertainty imposed by the localization in real space ($\Delta x \cdot \Delta k = 1$). Therefore, for nanocrystals the relevant parameter which will be evaluated as a function of size is the density of states.

5.1.1 What is expected for nanocrystals in terms of size evolution?

How do electronic states vary as a function of size? If one considers the evolution of the occupied and unoccupied levels as a function of number of atoms in the system (N), the energy level spacing decrease as N increases until they form a continuum, or a band for $N = \infty$. A sketch of the occupied (blue) and unoccupied (gray) states as a function of the number of atoms in the system is shown in Figure 1. In the size regime between a few atoms

and infinity, the bands are centered on the atomic energy levels and their width is proportional to the amount of bonding interactions with their neighbors. As the size of the system is decreased, the nearest-neighbor interactions decrease and the band width of the conduction and valence bands narrows. Therefore, nanocrystals are expected to have narrower bands than in the bulk system, with the energy gap between them larger. The blue shift of the absorption feature in nanocrystals is direct evidence of the increase in the energy gap. Furthermore, bands for a cluster are not completely formed and still possess discrete states at the edges [5, 6] which also have been observed in optical spectroscopy.

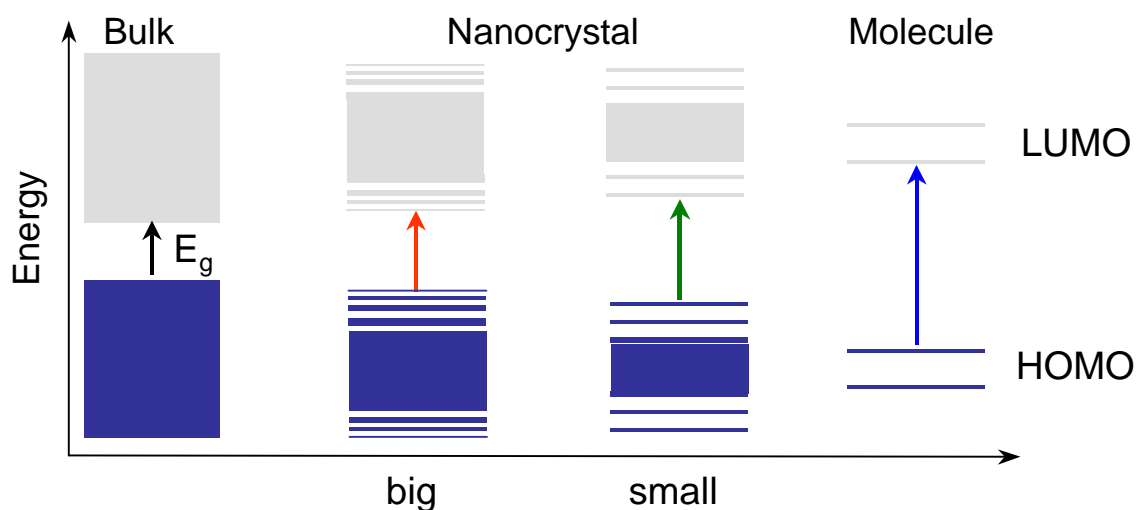


Figure 5-1 Schematic for the evolution of the density of occupied and unoccupied states as a function of size. The energy levels for molecule (right) are discrete and well separated, while for the bulk material (left) are a continuum and thus form bands. For nanocrystals (the two cases in between) the energy levels are discrete at the edges. As seen in optical measurements, the band gap in nanocrystals widens as the size of the particle decreases.

5.1.2 Information from PES on nanocrystals

Although optical spectroscopy can measure the amount that the band gap widens as a function the size, how much the valence band and conduction band shift individually cannot since an optical spectrum is a result of the transition from one to the other. PES

offers the advantage over optical spectroscopy that the angular momentum selection rules governing transitions do not apply. Because the electron is ejected and becomes a free electron, it has equal overlap with all initial electronic states in the solid. The other advantage of PES is that it employs high energy photon sources so it can access a larger energy range than optical spectroscopy (up to keV vs. 3.5eV) and thus can probe the entire valence band rather than just the edges. Therefore, photoelectron spectroscopy is useful for probing the occupied valence electronic states in nanocrystals. The equivalent technique for mapping the unoccupied states (conduction band) is inverse photoemission (IPES) in which a sample is bombarded with electrons and the resulting light emission is monitored. Since the valence states in a nanocrystal are expected to change with size, PES is useful for understanding size-dependent electronic structure in nanocrystals.

The individual shifts can be estimated from the change in the optical gap using the effective mass approximation. The energy as a function of the size of the particle (R) is described by

$$E(R) = E_g + \frac{\hbar^2 \pi^2}{2mR^2} \left(\frac{1}{m_e^*} + \frac{1}{m_h^*} \right) - \frac{1.8e^2}{\epsilon^* 4\pi\epsilon_0 R} - 0.248E_{Ry}^*$$

where m is the mass of the electron, m_e^* and m_h^* the effective masses of the electron and hole, respectively, and ϵ the dielectric constant of the particle (usually taken to be the bulk value). The first term is the bulk band gap. The second term is described as the kinetic energy term which describes the confinement of the electron and the hole as determined by their effective masses, and the third term describes the Coulomb interaction of the electron and the hole. The final term is the correlation energy which is often omitted due to its small contribution. Examining the kinetic energy term, the conduction band shift relative to the valence band shift should be on the order of the ratio of the effective masses of the hole to

the electron. For CdSe, m_h^* and m_e^* are 0.13 and 0.45, respectively, so this translates into a conduction band shift of 2/3 the optical band gap shift and a valence band shift of 1/3. Therefore, for a 25Å diameter nanocrystal which has an optical band gap of 2.3eV, the conduction band is shifted 1.5eV higher in energy and the valence band 0.8eV lower in energy (in the direction of higher binding energy).

Valence band evolution as a function of size has been successfully measured by photoelectron spectroscopy [7, 8] as well as soft x-ray fluorescence [9-11] in semiconductor nanocrystals as well as in size-confined systems such as porous silicon. The valence band edge shifts to higher binding energy relative to the bulk due in agreement with band gap widening. In addition, the valence band narrowing has been observed in metallic clusters due to increased localization of the electronic wavefunction. [7].

5.2 Experimental: subtraction technique

Because the nanocrystals must be deposited onto a substrate for proper photoemission measurements, the spectrum obtained in a photoelectron experiment is characteristic of both the nanocrystals and the substrate. This can be problematic if the substrate has sharp, intense features in the energy regimes in which the valence band of the nanocrystals is changing. Fortunately, it has been demonstrated that is possible to subtract the substrate signal out to observe the density of states of solely the nanocrystals and not the substrate. This technique has been used to obtain the Pt valence band density of states of supported Pt clusters separate from the spectrum of the graphite substrates [7].

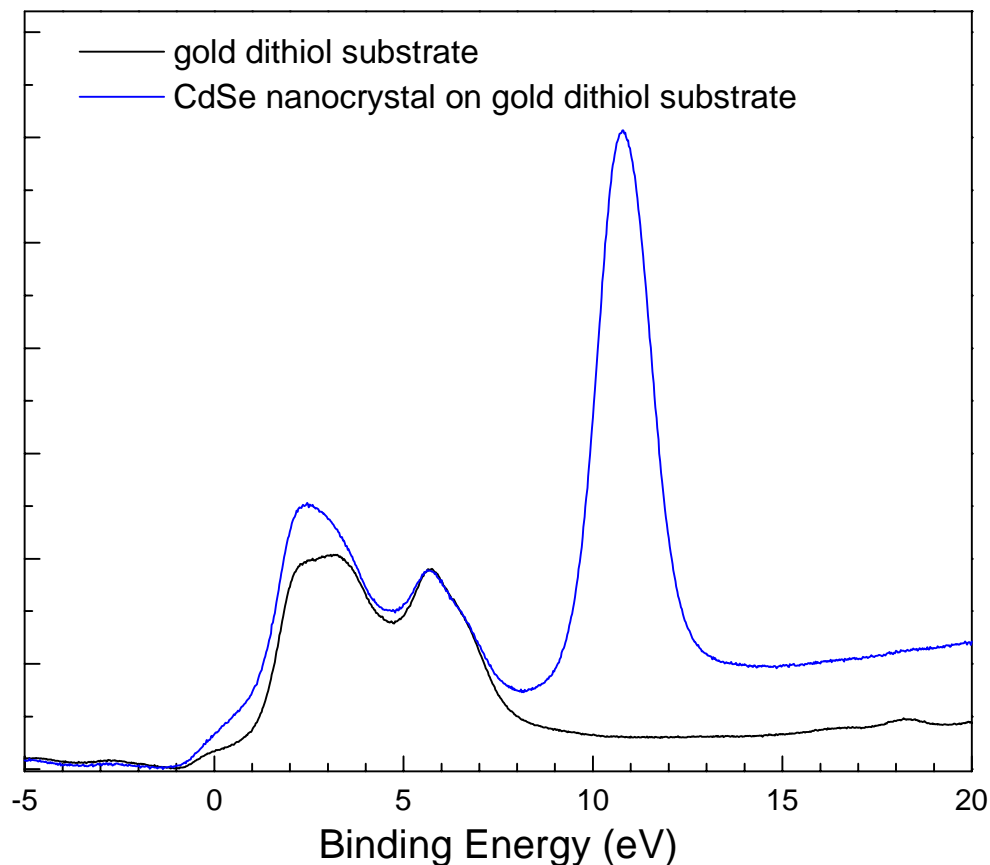


Figure 5-2 Valence band spectrum for a CdSe/dithiol/Au substrate (blue) and a dithiol/Au substrate (black). The substrate signal can be subtracted from the composite spectrum. The substrate spectrum is scaled to the intensity at the feature at 6eV.

Figure 2 shows schematic for CdSe nanocrystals on an Au substrate. A valence spectrum is taken for the Au/dithiol substrate with and without CdSe nanocrystals. The features 0eV-9eV in binding energy are the valence bands of both the Au and the nanocrystals. The high intensity narrow peak at 11eV is the Cd 4d core and is not a feature of the substrate. A spectrum of the Au/dithiol without nanocrystals is taken separately and subtracted from the nanocrystal/dithiol/Au spectrum, where the intensity of the substrate spectrum is scaled to match the Au feature at 6eV. Figure 2 shows the scaling of the Au blank (black) relative to the nanocrystal/dithiol/Au spectrum (blue) at the feature at 6eV. It

is assumed that this feature is due solely to the Au substrate, so in fact the intensity scaling is somewhat arbitrary.

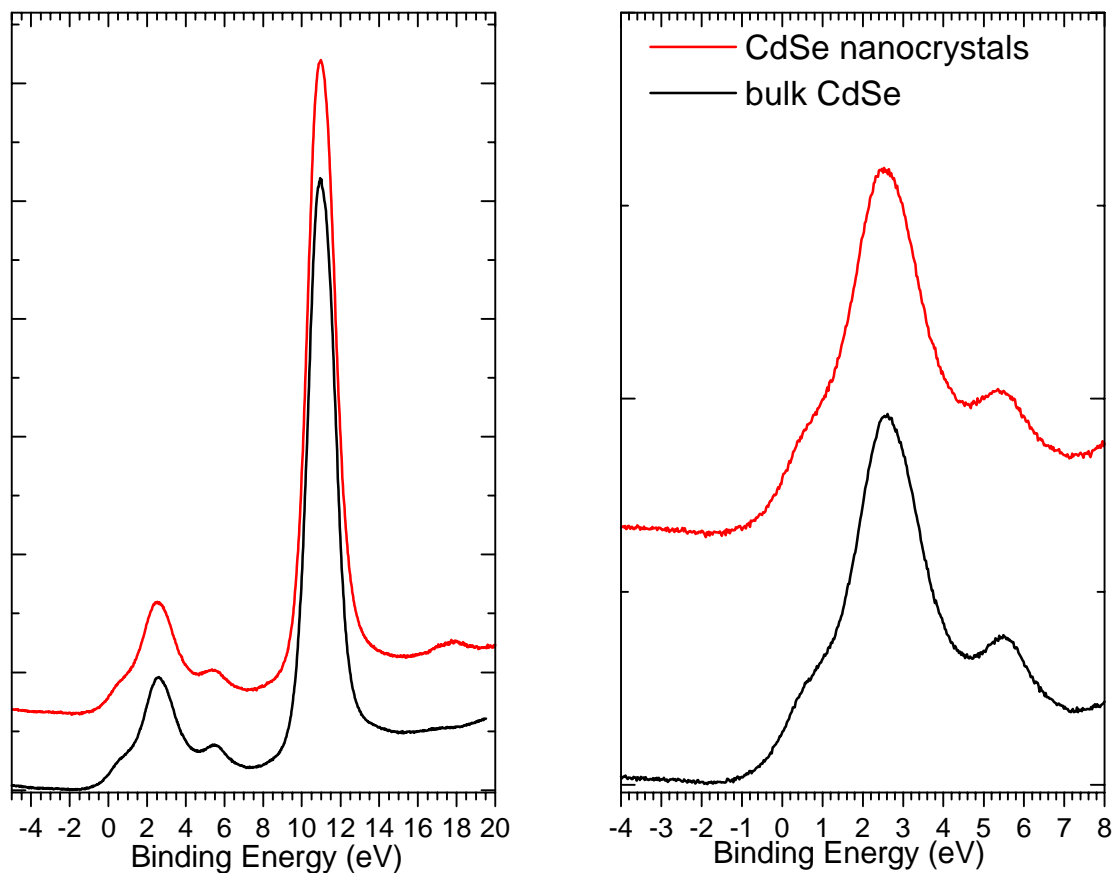


Figure 5-3 The nanocrystal valence DOS (red) after subtraction compared to bulk CdSe (black). The spectrum on the left shows the valence band and the Cd 4d core. The spectrum on the right is a closeup of the valence band region.

Nevertheless, the resulting difference spectrum (red) by using this feature to scale the substrate resembles the bulk CdSe spectrum (black), as shown in Figure 3. This subtraction technique illustrates that the spectra of the Au substrate and the nanocrystals are additive. If valence spectra are taken for two different coverages (low and high) (Figure 4, a and b) the difference between them when they are scaled to have the same intensity at a Cd only feature

(the Cd 4d core) is identical to the experimentally obtained spectrum for the Au/dithiol blank (Figure 4, c).

In order to get a reasonable difference spectrum, the original spectra must have high signal to noise, which necessitates high signal (kcps) and extended averaging (usually 750-1000 sweeps). Subtraction must not yield negative signals which is the result of improper scaling. In addition, the subtraction is facilitated by the relatively flat background at high electron kinetic energies.

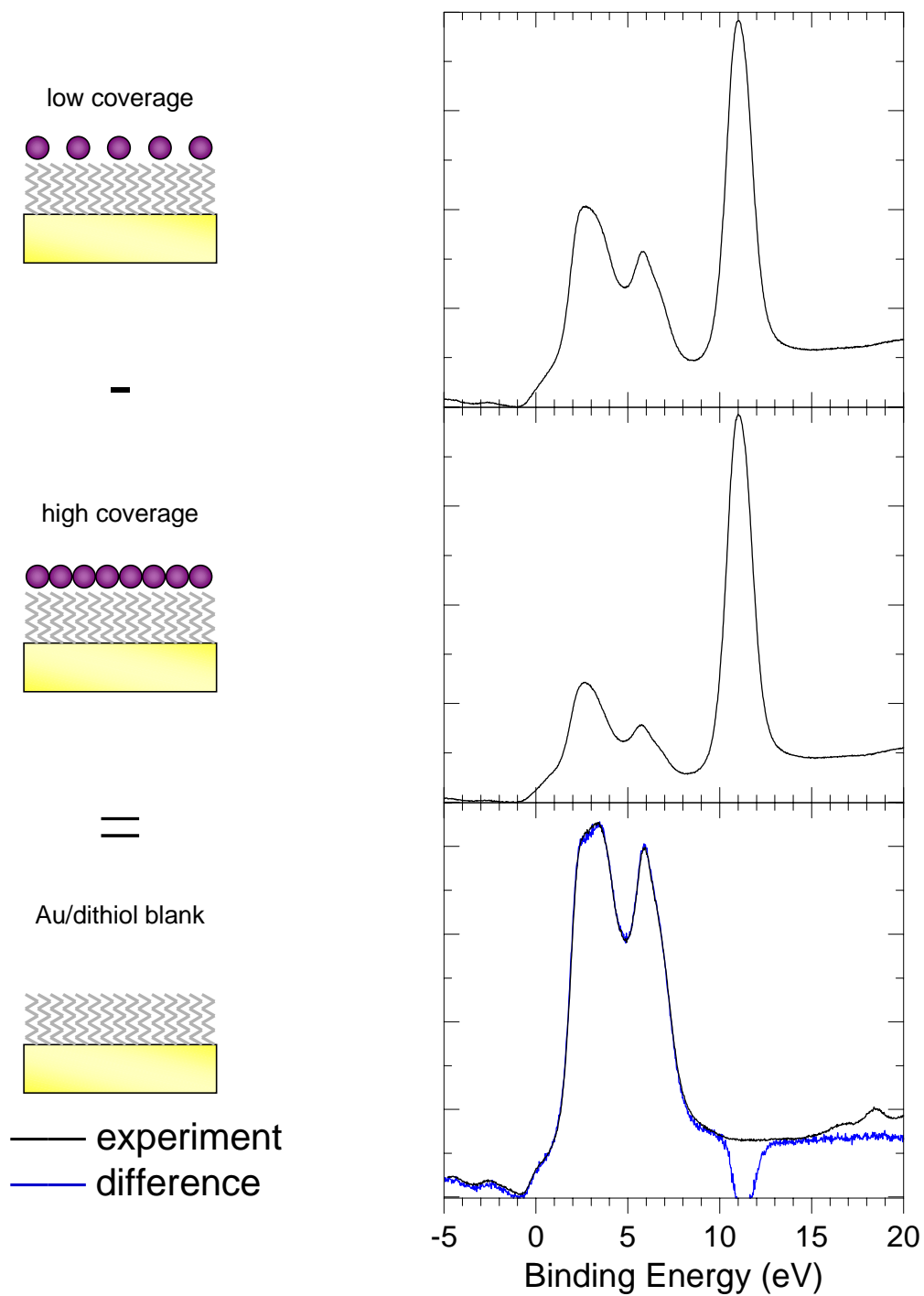


Figure 5-4 Illustration that the subtraction routine for the valence band spectrum is valid. The top spectrum is a valence band of CdSe/dithiol/Au of low coverage, and the middle spectrum is high coverage. If the spectrum are scaled to the Cd 4d intensity and the difference is taken, the spectrum matches the experimental result for the Au blank.

This subtraction procedure can be done if the nanocrystals are deposited onto ITO substrates with dithiol. In that case, the substrate has an In 4d core level at $\sim 17\text{eV}$ which is not present in the nanocrystal spectrum and the intensity scaling of the substrate is no longer arbitrary. ITO also has features that are less prominent in the valence region, which makes the background subtraction much less prone to artifacts. Figure 5 shows the XPS valence band spectra for a blank of ITO. The resulting difference spectrum for 60\AA CdSe nanocrystals is shown in Figure 6 and shows that the spectrum resembles that of nanocrystals on Au.

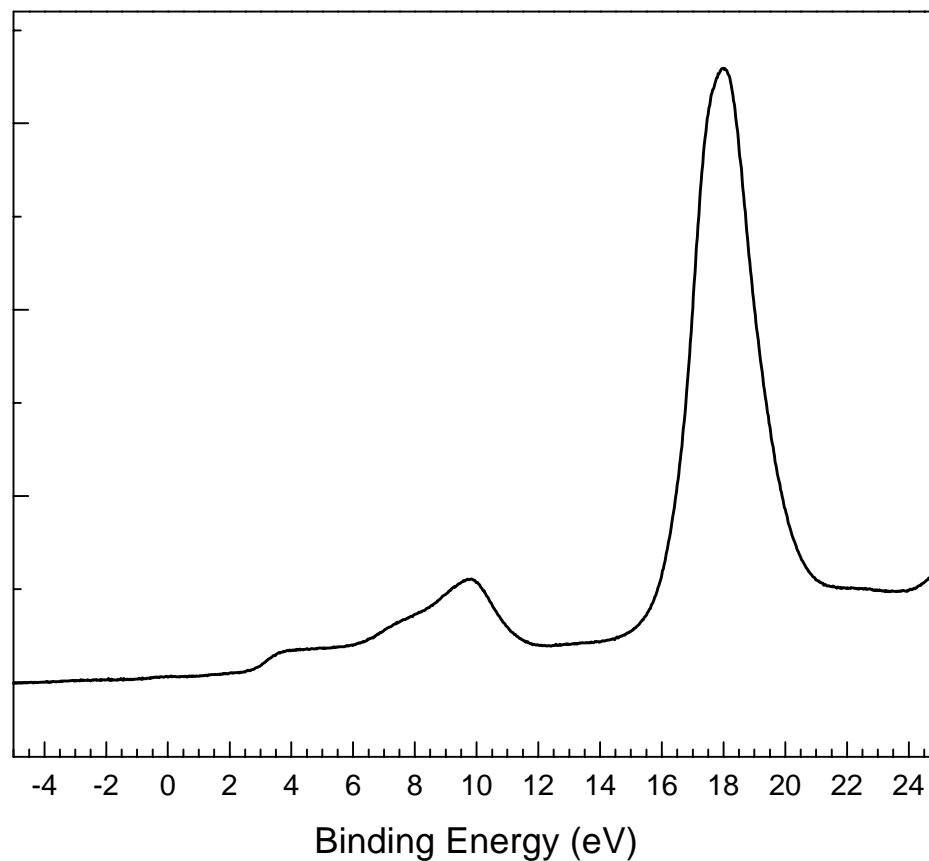


Figure 5-5 Valence band spectrum of ITO (indium tin oxide). The valence band is the feature that spans 0 to 11eV and the In 4d core is at $\sim 17\text{eV}$.

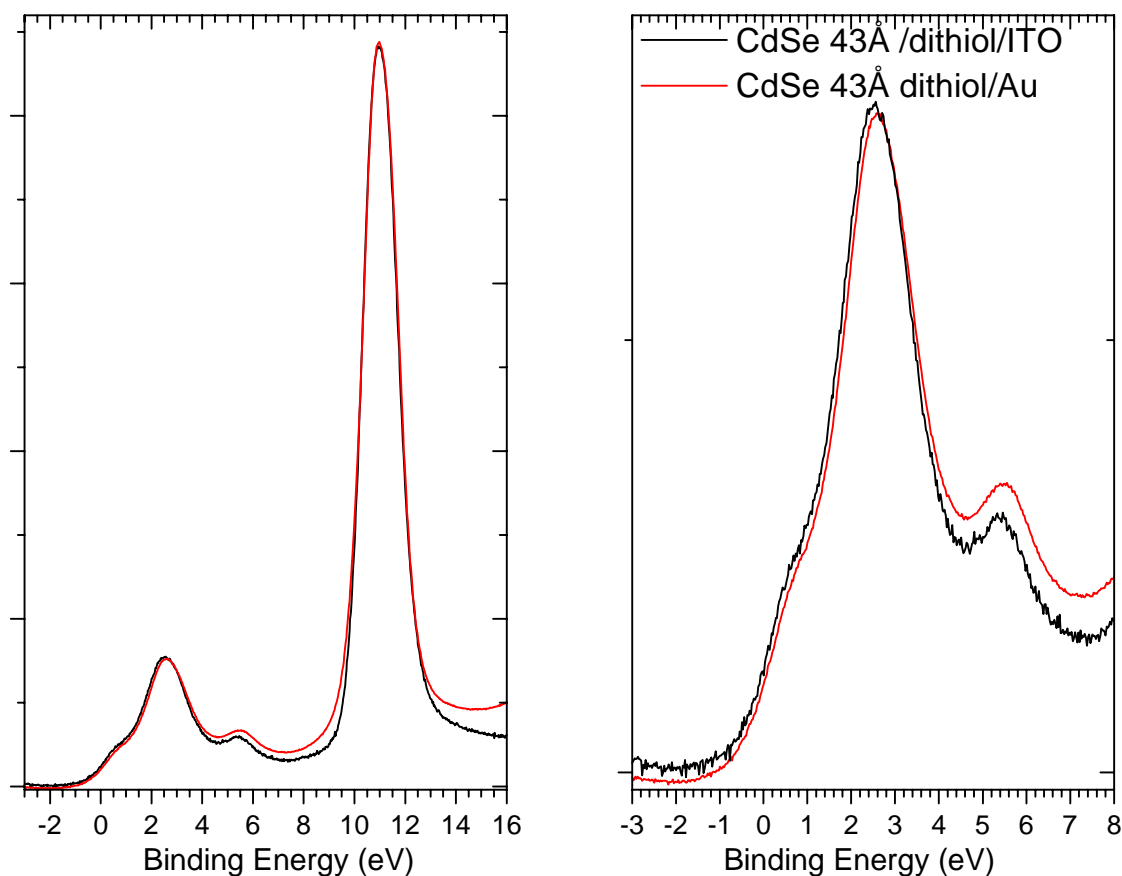


Figure 5-6 Valence band spectrum for 43Å CdSe nanocrystals on dithiol/Au (red) and dithiol/ITO (black). A closeup of the valence band region is shown on the right.

5.3 Valence DOS for nanocrystals as a function of size and surfactant

Figure 7 shows the DOS of CdSe nanocrystals 26, 43, and 60 Å in diameter after subtraction of the ITO substrate signal. The DOS of bulk CdSe is also shown. The shape of the DOS agrees with previous XPS experiments of bulk semiconductors as well as pseudopotential calculations from the band structure. [12-14] However, the DOS shows no noticeable change with size. Changing the ligand on the surface of the nanocrystal (TOPO vs. no ligand) also has negligible effect on the valence band spectrum, as shown in Figure 8. This is most likely due to the fact that the instrumental resolution is on the order of the x-ray linewidth, which is $\sim 700\text{meV}$.

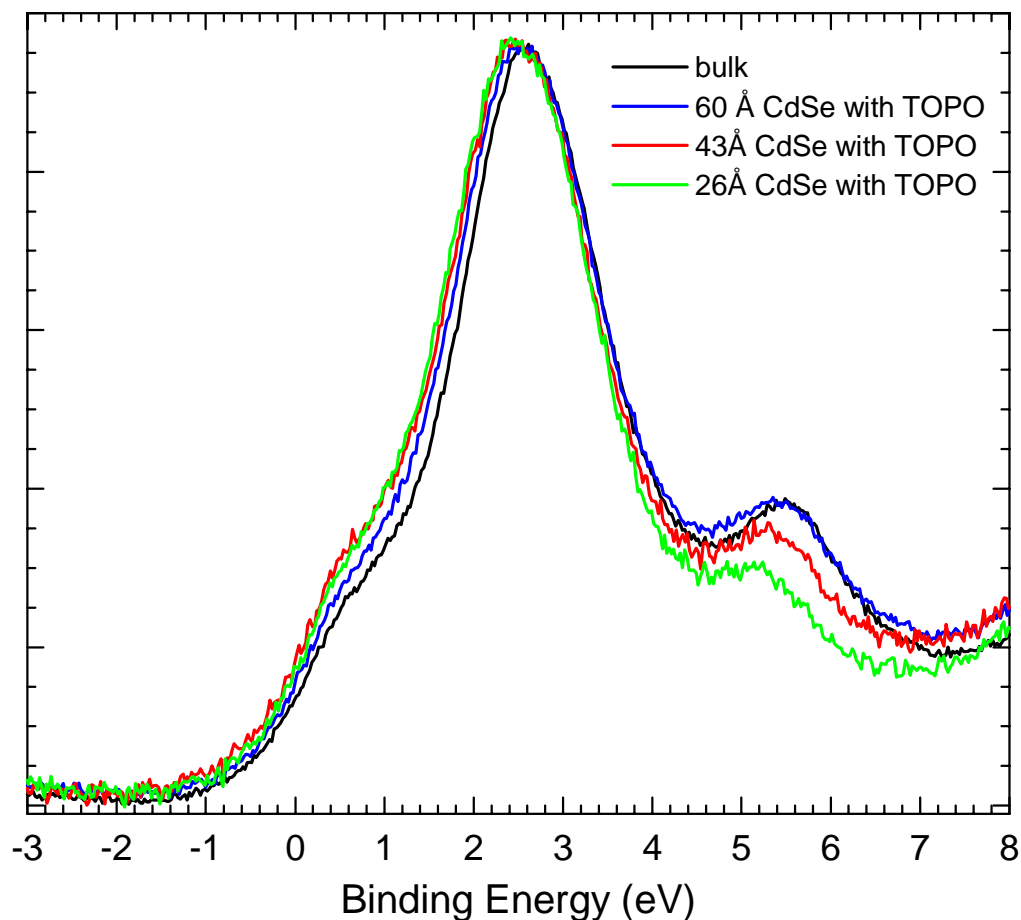


Figure 5-7 Valence band spectrum of TOPO capped CdSe nanocrystals of various sizes. The spectra show a weak size dependence.

Therefore, it is of interest to perform experiments with a higher resolution source if any size dependent effects are to be observed. Synchrotron radiation has a narrower linewidth, ~ 100 meV depending on the endstation. In addition to having extremely high brightness, synchrotron radiation has the added benefit of tunable photon energy, which allows one to probe different amounts of surface sensitivity due to tunable kinetic energy of the photoelectron. Experiments at beamline 6.3.2 at the Advanced Light Source using photon energies 70-200 eV have resulted in substrate spectra that are difficult to subtract. The reason for this is unknown, though it is probably due in part to the increasing

contribution of the inelastically scattered electrons to the background at low photon energies.

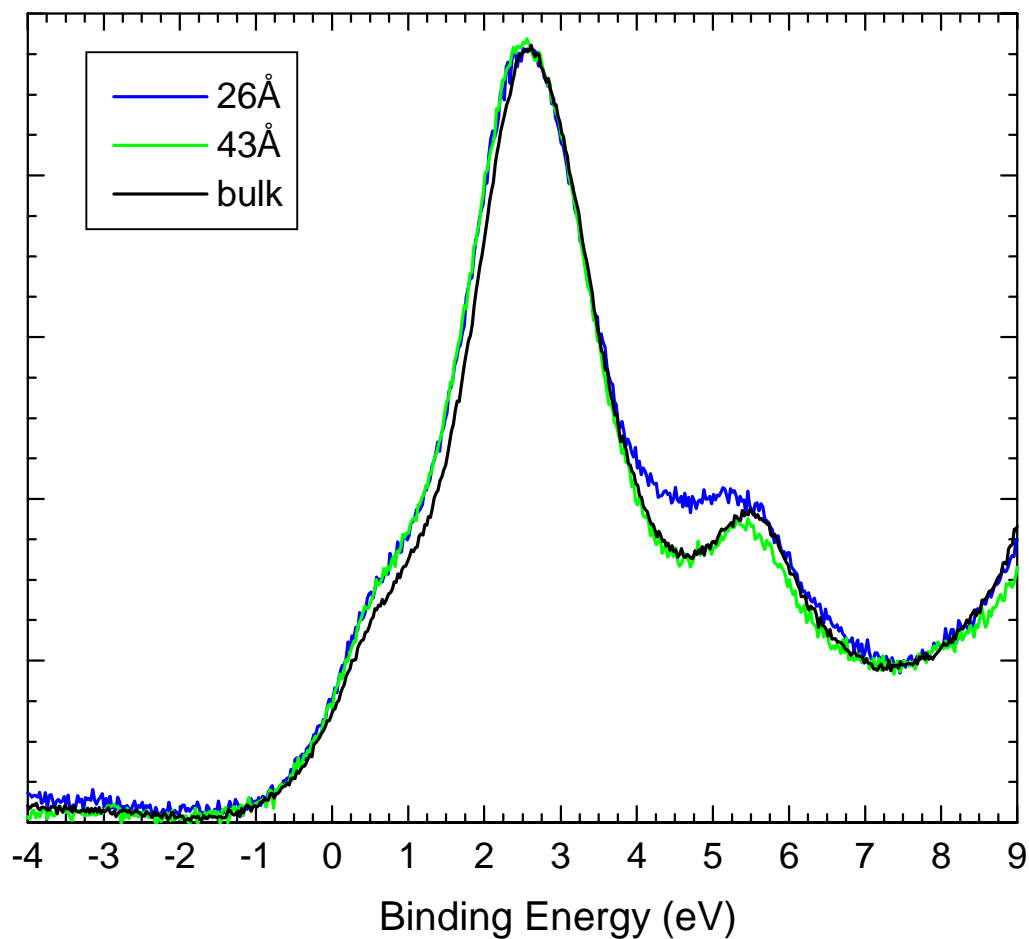


Figure 5-8 Valence band spectra taken with a Mg K α source for uncapped CdSe nanocrystals of two different sizes. The bulk spectrum is included for comparison.

5.4 DOS measured with UPS

5.4.1 Experimental method for nanocrystals

The other possibility for higher resolution is to perform UPS using a He discharge lamp. The sample form used for UPS is a nanocrystal thin film made from a solution either spin cast onto ITO or gold or linked by a self-assembled monolayer as described in chapter n. Samples had the organic surfactant removed (TOPO) as described in chapter 3.

For the first spectra taken (when the sample is first put into the chamber) the spectrum is mostly due to the organic material on the surface of the sample. This is evident from the high value for the IE. Upon irradiation with x-rays over several days (with either Al or Mg K α) the value decreases, until it eventually remains constant. It is believed that the x-rays removes the organic on the surface of the sample. Because organic molecules have large HOMO-LUMO separations, a spectrum dominated by their signal will have a high value for the IE. When the organic is removed, the semiconductor is exposed, and gives a lower IE. Figure 9 shows the He II valence band spectra for bulk CdSe which had been etched with HCl before introduction into the vacuum chamber. The first spectrum has a large broad feature at low binding energies which decreases in intensity as a function of increased irradiation time. This is confirmed by the appearance of the Cd 4d peak at ~ 14.5 eV BE as well as valence band features in both the He I and He II spectra with irradiation time (Figure 10). In addition, the C 1s peak intensity decreases with exposure to x-rays.

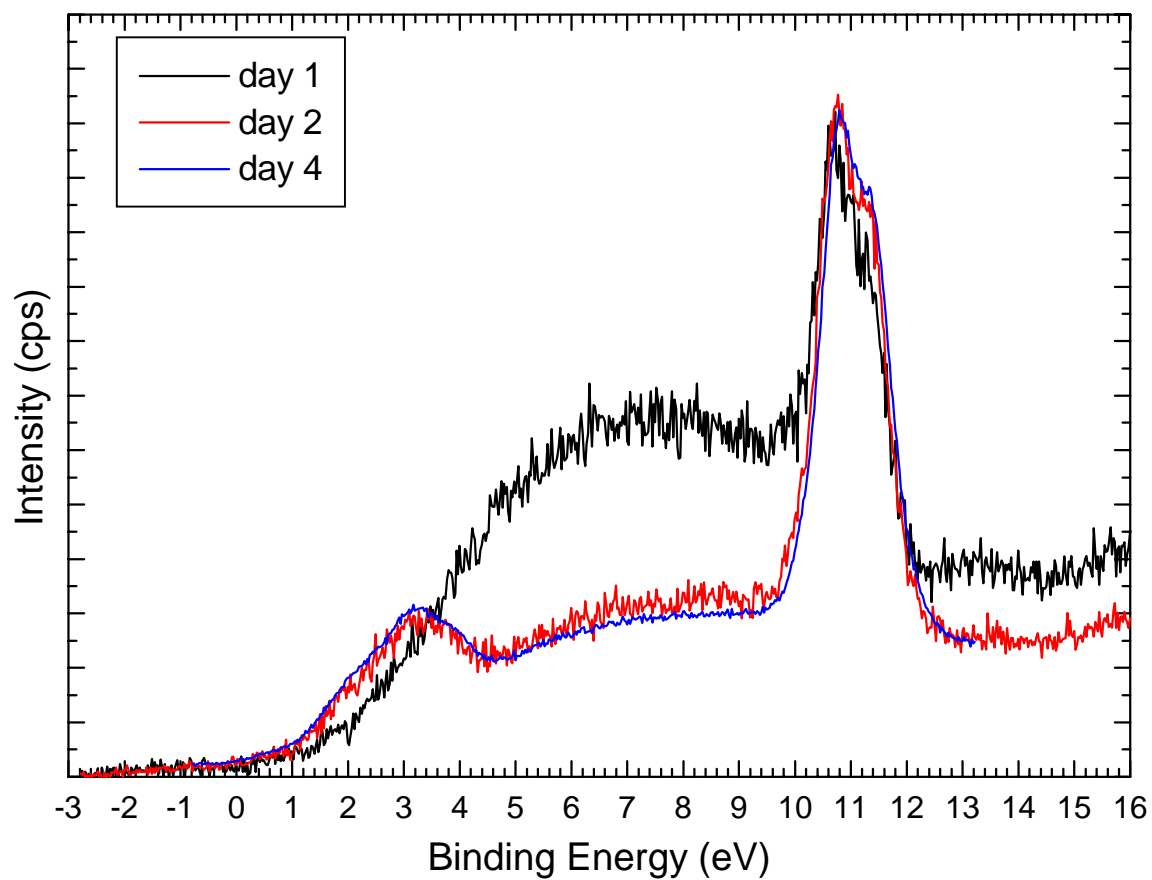


Figure 5-9 He II spectrum of bulk CdSe as a function of irradiation time in Al K α x-rays.

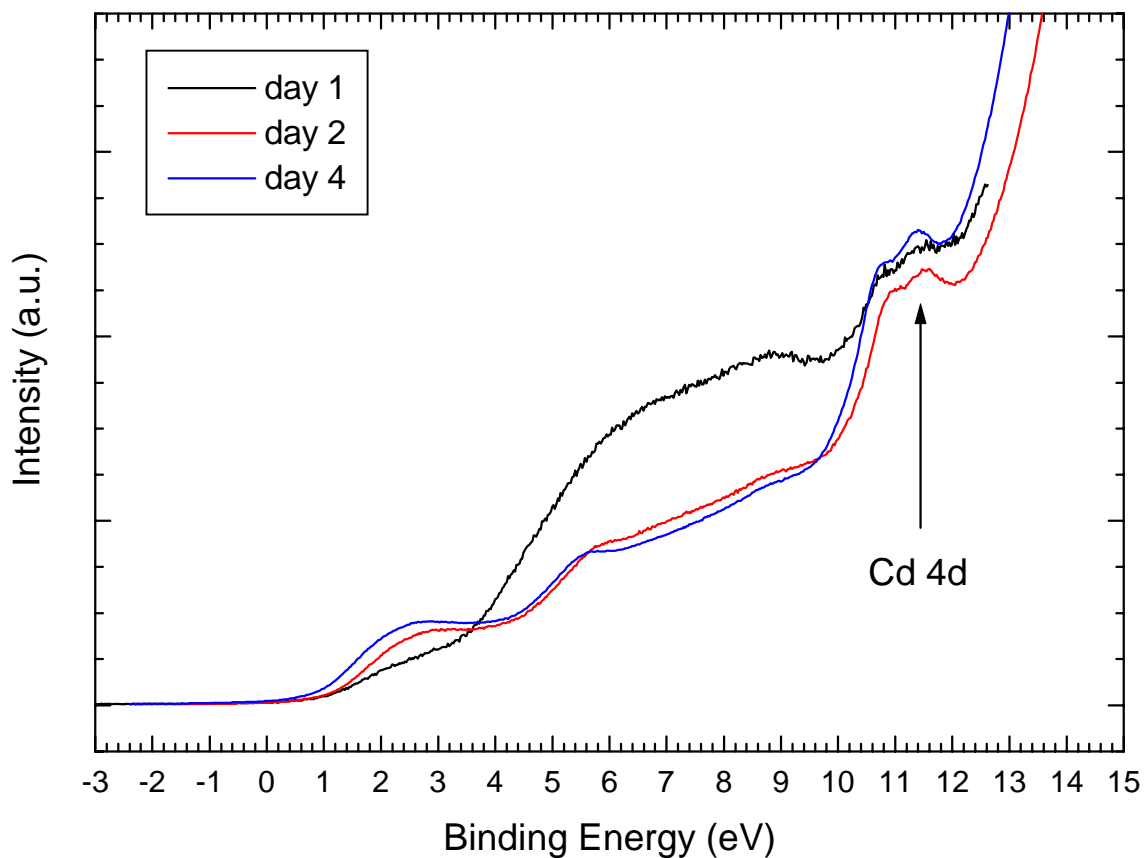


Figure 5-10 He I spectrum of bulk CdSe as a function of irradiation time in Al K α x-rays.

After a certain amount of time, the shape of the spectrum stops changing with x-ray time, and the signal is believed to be due to the nanocrystal alone. Typically it takes a sample at least 24 hours in the x-rays to reach this state. At this point the DOS of the sample can be examined.

5.4.2 Results for UPS

Figure 11 shows the valence band density of states for bulk CdSe and CdSe nanocrystals 43Å in diameter. It should be noted that the subtraction technique is much more difficult to employ on lower energy PES such as UPS or synchrotron radiation. This is

probably due to the increasing contribution of the inelastically scattered electrons to the background, which creates an upward slope in the spectrum.

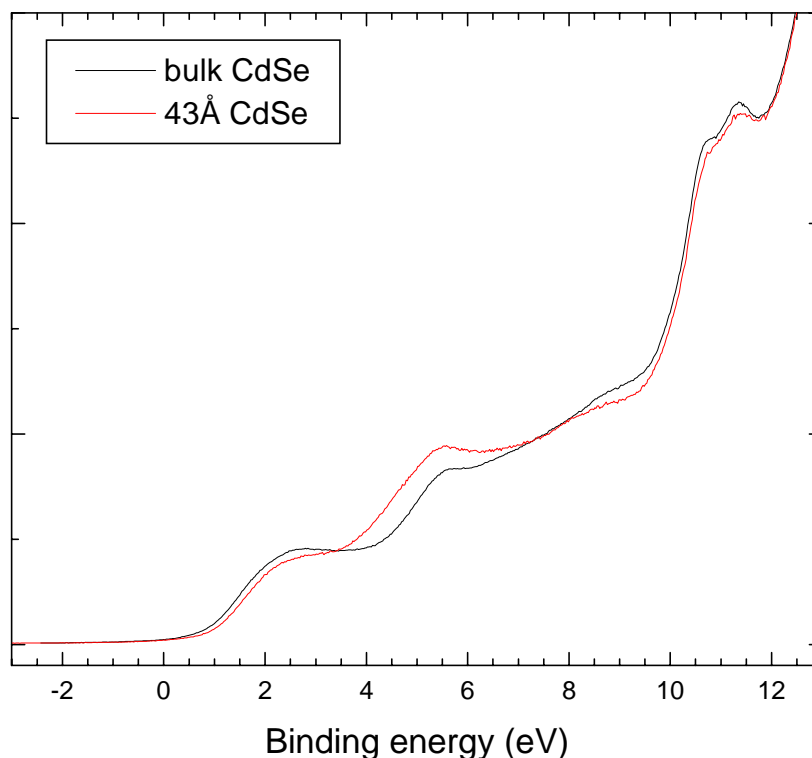


Figure 5-11 Valence band spectra of bulk CdSe and 43Å CdSe nanocrystals using He I radiation. The valence band is on a rising background due to the inelastically scattered electrons.

Upon examination of the valence band edge (Figure 12), the band edge shift of the nanocrystals is about 0.1eV to higher binding energy than bulk. The effective mass approximation predicts a shift of 1/3 of the change in the optical gap. For this size nanocrystals, the first absorption feature is centered at 597nm, which corresponds to a gap of 2.07eV. This is 0.35eV higher than the bulk band gap (1.72eV), and therefore the change in the valence band alone is expected to be 117meV, which is in rough agreement with the experimental result. In examination of the feature at roughly 5.5eV, the nanocrystal feature is shifted to lower binding energy, which is concurrent with band narrowing.

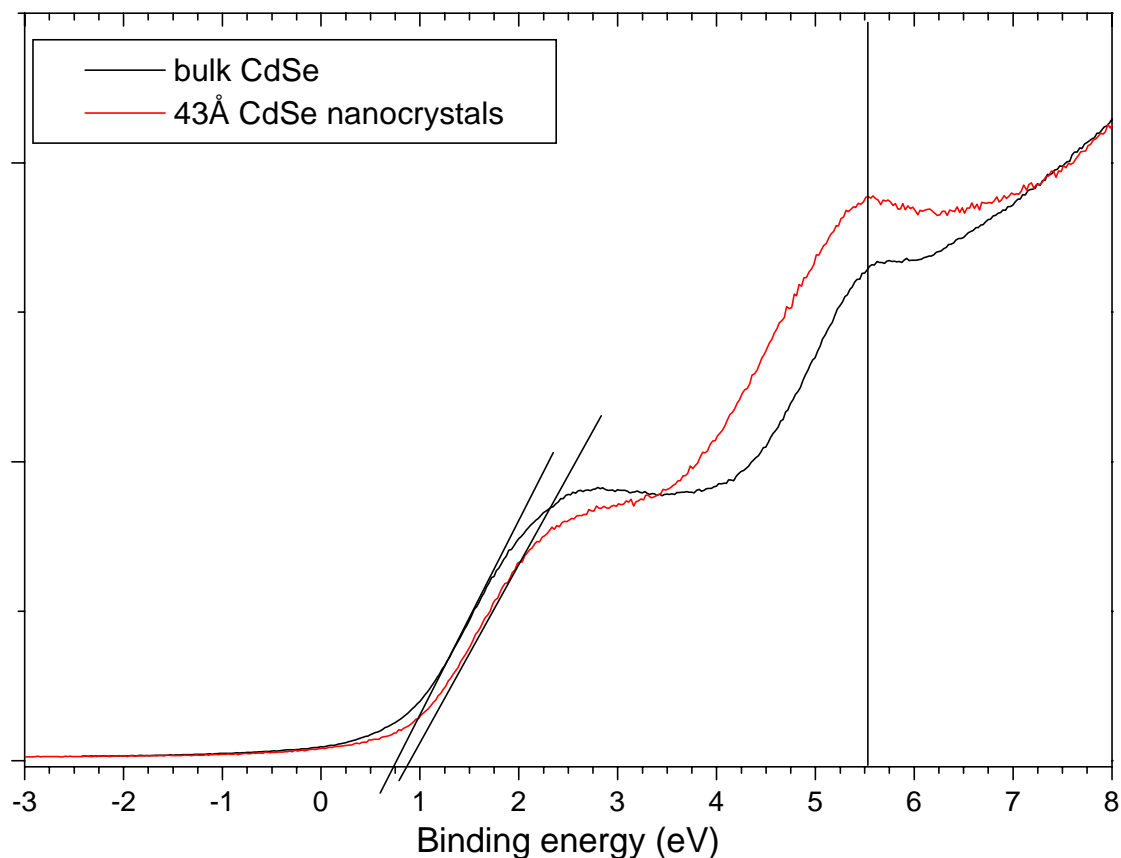


Figure 5-12 Valence band spectrum for bulk CdSe and 43Å nanocrystals taken with He I. The valence band edge for the nanocrystals is shifted to higher energy by ~ 100 meV, in agreement with the effective mass approximation. The feature at 5.5 eV is at a lower binding energy, exhibiting band narrowing.

However, the issue of the substrate influence remains. Because the nanocrystal photoelectron spectrum cannot be measured without a substrate, the effects of the substrate must also be taken into account. Band bending, which is dependent on the work function of the substrate, can change energy levels of a semiconductor. Chapters 6 and 7 focus on the influence of a substrate on the energy levels of the nanocrystal next to it.

5.5 Conclusions and outlook

Valence density of states of nanocrystals is measurable by x-ray photoelectron spectroscopy. Because the nature of the sample requires a substrate material, the substrate signal must be subtracted from the sample spectrum in order to view the valence DOS of only the nanocrystals. The spectra are additive and the obtained nanocrystal spectrum qualitatively resemble the bulk spectrum. However, the valence density of states taken by XPS shows no discretization or band narrowing as the size of the nanocrystal is decreased, which is most likely due to the fact that the changes expected are small compared to the resolution of the x-ray anodes used in the experiment. Spectra taken with He I and He II lines, which have a much smaller linewidth, show that the bands for nanocrystals are narrower than for bulk and that the band edge shifts to higher energy, in agreement with models for the density of states in confined systems.

5.6 References

- [1] S. Empedocles and M. Bawendi, Acc. Chem. Res. **32**, 389 (1999).
- [2] D. J. Norris, A. Sacra, C. B. Murray, and M. G. Bawendi, Phys. Rev. Lett. **72**, 2612 (1994).
- [3] U. Banin, J. C. Lee, A. A. Guzelian, A. V. Kadavanich *et al.*, Superlattices and Microstructures **22** (1997).
- [4] P. Y. Yu and M. Cardona, *Fundamentals of Semiconductors: Physics and Materials Properties* (Springer-Verlag, New York, 1996).
- [5] A. P. Alivisatos, Science **271**, 933 (1996).
- [6] M. G. Bawendi, M. L. Steigerwald, and L. E. Brus, Ann. Rev. Phys. Chem. **41**, 477 (1990).
- [7] W. Eberhardt, P. Fayet, D. M. Cox, Z. Fu *et al.*, Phys. Rev. Lett. **64**, 780 (1990).
- [8] V. L. Colvin, A. P. Alivisatos, and J. G. Tobin, Phys. Rev. Lett. **66**, 2786 (1991).
- [9] T. van Buuren, L. N. Dinh, L. L. Chase, W. J. Siekhaus *et al.*, Phys. Rev. Lett. **80**, 3803 (1998).
- [10] J. Luning, J. Rockenberger, S. Eisebitt, J. E. Rubensson *et al.*, Solid State Commun. **112**, 5 (1999).
- [11] J. Luning, 1998, Thesis.
- [12] L. Ley, R. A. Pollak, F. R. McFeely, S. P. Kowalczyk *et al.*, Phys. Rev. B **9**, 600 (1974).
- [13] L.-W. Wang and A. Zunger, Phys. Rev. B **53**, 9579 (1996).
- [14] *Landolt Börnstein New Series*.

6 X-RAY AND PHOTOELECTRON SPECTROSCOPY OF NANOCRYSTALS ON METAL SUBSTRATES: SIZE DEPENDENT HOLE SCREENING

6.1 Introduction

This chapter describes experiments investigating the electronic structure of semiconductor nanocrystals measured by XPS. The XPS data shows size dependent core level shifts which are the result of the influence of the metallic substrate onto which the samples are deposited. This set of experiments shows that the intrinsic properties of the nanocrystal alone are not separable from the nanocrystal in contact with a substrate in a PES measurement. This chapter will attempt to interpret the results in the picture of both the semiconductor-metal band offset in addition to a model that accounts for electromagnetic effects of the nanocrystal/organic/metal system and charge screening of the photocreated hole. A model taking into account electronic charge screening will be discussed.

6.2 XPS Experimental

XPS spectra were measured for the core levels In 3d, As 3d, and the substrate (Au 4f or Si 2p) with a pass energy of the electron analyzer set to 23.50eV so the resolution of the experiment was limited to the x-ray linewidth (0.7eV). Scans were over a 20eV range to allow for sufficient background before and after the photoelectron peaks. The core level spectra were fit using a commercial least squares fitting routine (Peakfit) using Voigt lineshapes.

6.3 Results

Figure 1 shows the In, As, and Au core levels for different sizes of nanocrystals on hexanedithiol/Au substrates. The In 3d and As 3d peaks shift to higher binding energy as

the size of the nanocrystal is decreased. However, the substrate peaks show no change, indicating that the binding energy shift is not due to sample charging. This shift is not a chemical shift due to oxidation as the nanocrystals show no evidence of being oxidized except for one sample; if the samples were oxidized the As 3d would show an additional peak due to the formation of As_2O_3 $\sim 5\text{eV}$ higher in binding energy. The In 3d core levels are the only cores for which this is easily measured, and this is due to the fact that the d levels tend to be narrower than other lines, and thus shifts of this core are more easily detected.

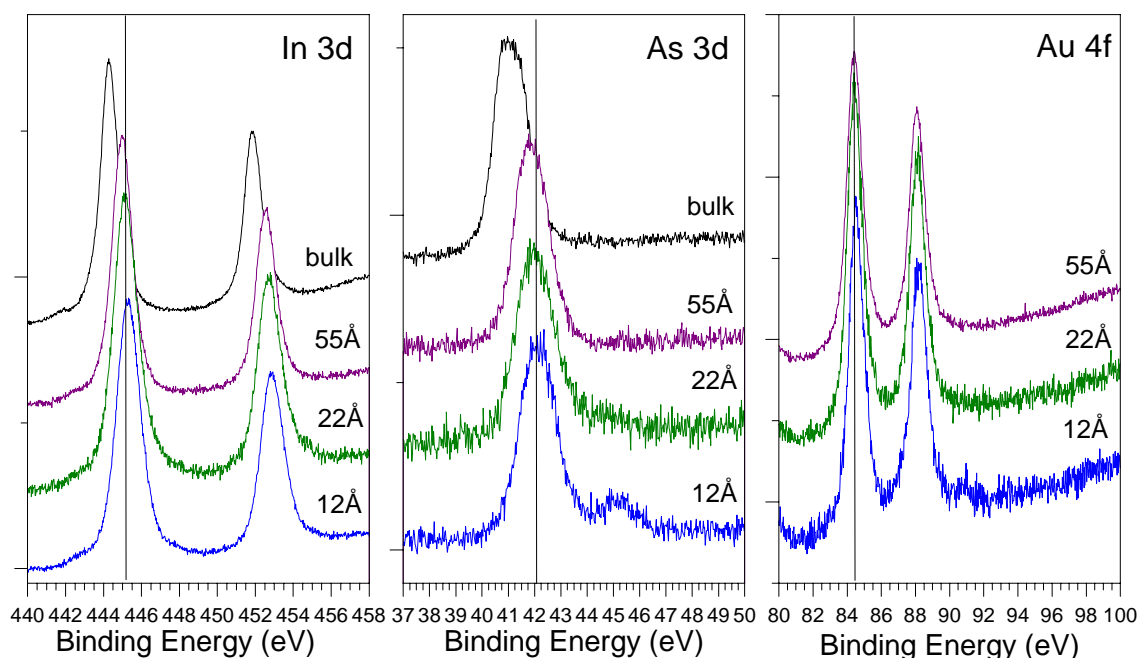


Figure 6-1 XPS spectra of the In 3d, As 3d, and Au 4f for InAs nanocrystals on hexanedithiol/Au substrates. The In and As cores shift to higher binding energy as the size of the nanocrystal is decreased. The Au cores exhibit no shift.

If the nanocrystals are deposited onto a different substrate such as Si (Figure 2) or deposited on an Au substrate with a longer linker (1,8-octanedithiol) (not shown) a similar effect is observed. This indicates that the binding energy shift is due to both the inherent properties of the nanocrystal as well as the substrate.

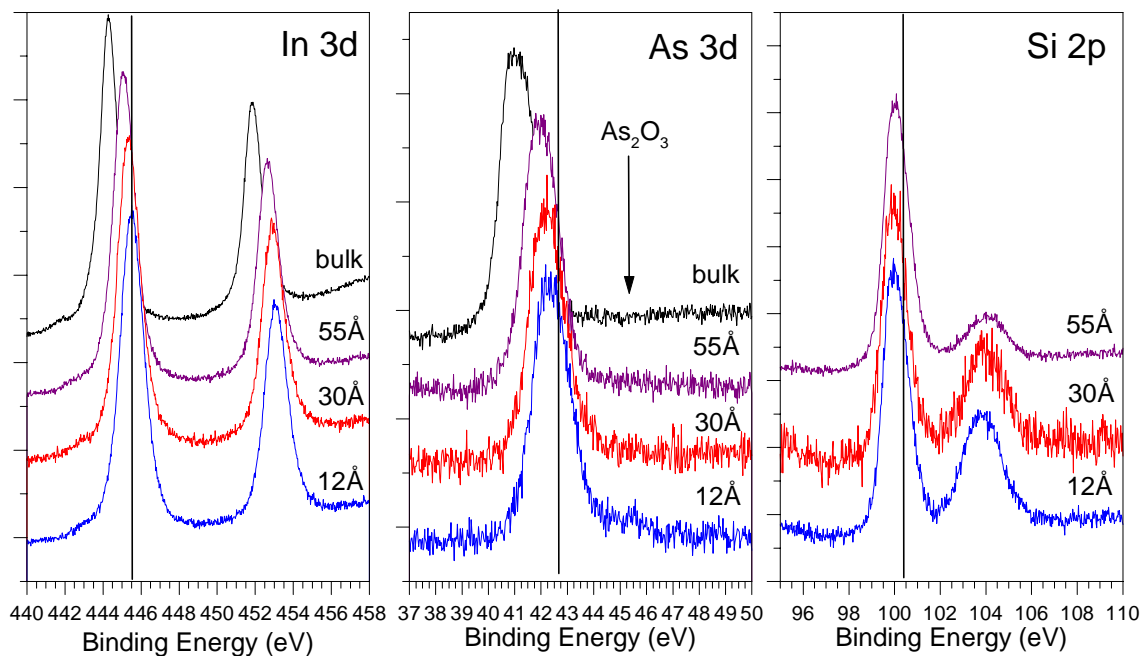


Figure 6-2 XPS spectra of the In 3d, As 3d, and Si 2p cores of InAs nanocrystals on MPS /SiO₂/Si substrates. The In and As cores shift to higher binding energy as the size of the nanocrystal is decreased. The Si 2p core exhibits no shift.

The amount of the binding energy shift for the In 3d cores on the three substrates is quantified in Figure 3. In order to remove any effects of substrate charging, the values are referenced to bulk as ΔBE_{rel} :

$$\Delta BE_{rel} = (BE_{In,nanocrystal} - BE_{Au}) - (BE_{In,bulk} - BE_{Au})$$

It should be emphasized here that the core levels are measured relative to the Fermi level of the substrate which is equal to that of the spectrometer. The In 3d core shifts a different amount depending on the substrate system. The largest shift observed is for the MPS/Si substrate, which is 0.36eV between the 12Å and 55Å diameter nanocrystals. The overall shift for the hexanedithiol/Au substrate is 0.29eV, while the octanedithiol/Au substrate is only 0.10eV.

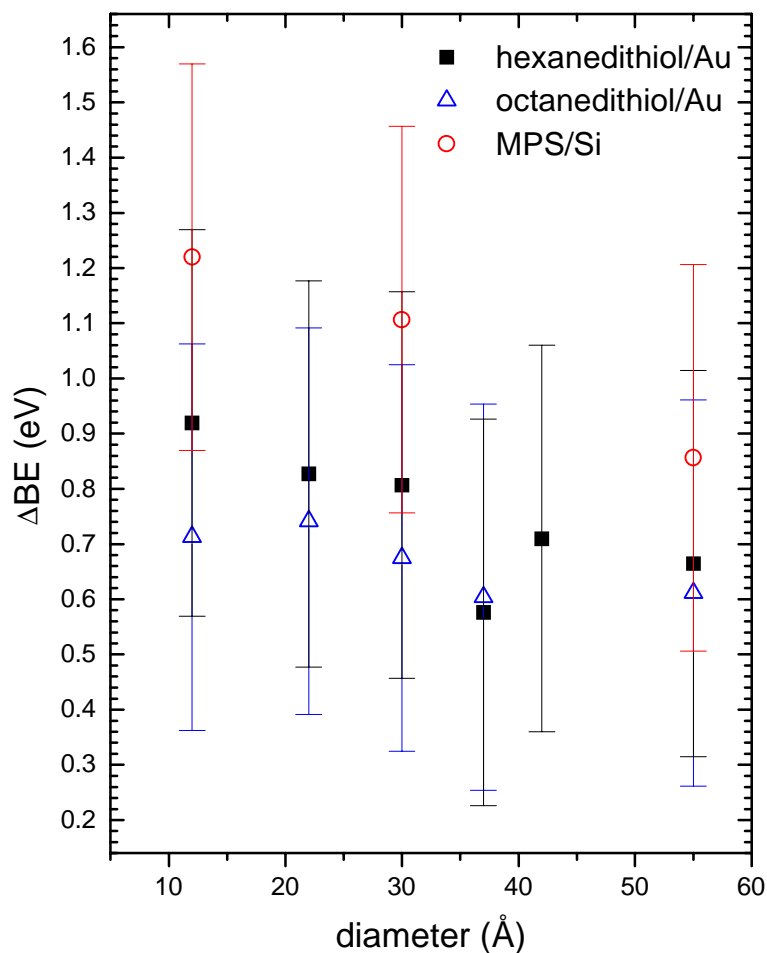


Figure 6-3 In 3d binding energy shifts relative to bulk for hexanedithiol/Au (squares), octanedithiol/Au (triangles) and MPS/Si (circles).

6.3.1 Core level shifts with shell layer thickness

In addition, the In 3d core level binding energy changes for a InAs/CdSe core/shell particle with varying CdSe shell thicknesses. InAs/CdSe core/shell particles were synthesized according to literature methods (see Chapter 2). Shell thickness was controlled by the number of times CdSe stock was injected, where each injection was calculated to add one monolayer of CdSe onto the InAs particles. The particles were deposited onto Au/mica substrates using hexanedithiol.

Figure 4 shows the In 3d core levels referenced to Au 4f_{7/2} for a 30Å diameter core as a function of shell thickness. As the shell is grown thicker, the binding energy shifts to lower energy, decreasing by 0.585eV from no shell (the InAs core) to a thick shell. A similar trend is observed for the As 3d core with a similar magnitude (0.625eV), Figure 5. In both cases the binding energy of the core level peak in the core/shell particle is higher than the bulk value: 359.88eV for In3d_{5/2}, -43.32eV for As 3d.

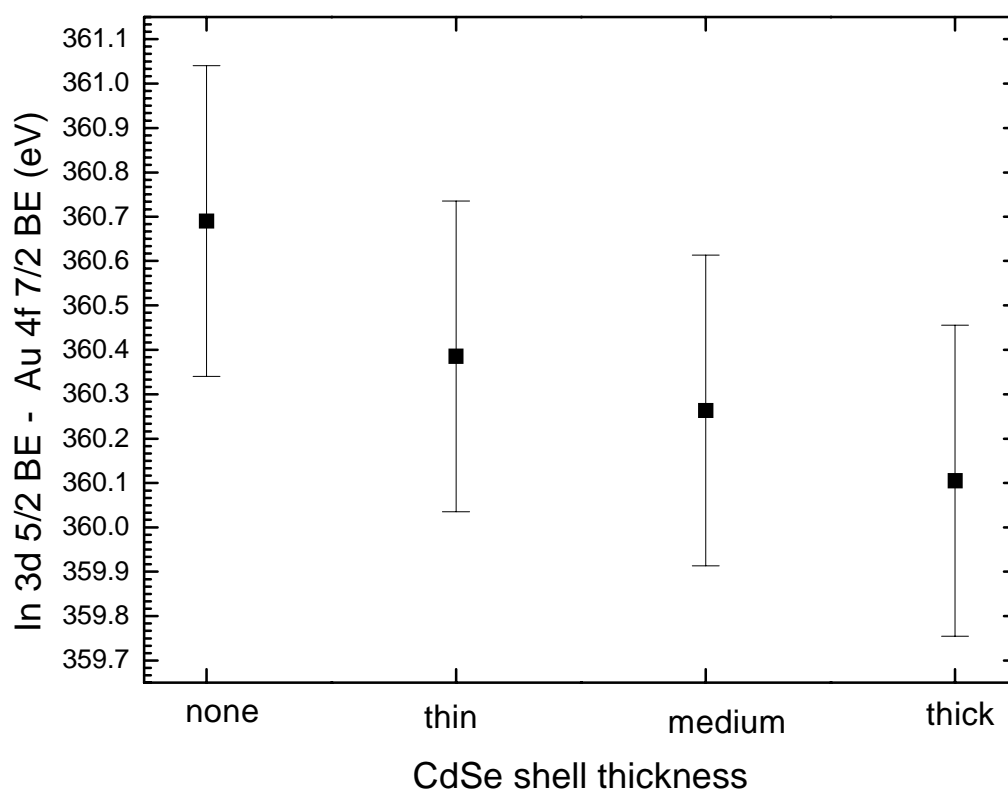


Figure 6-4 In 3d_{5/2} binding energy referenced to the Au 4f_{7/2} core level as a function of CdSe shell thickness in InAs/CdSe core/shell particles. The In 3d core shifts up to 0.585eV to lower binding energy as the shell thickness increases. The value of In 3d_{5/2} referenced to Au 4f_{7/2} for bulk InAs is 359.88eV (not shown on graph).

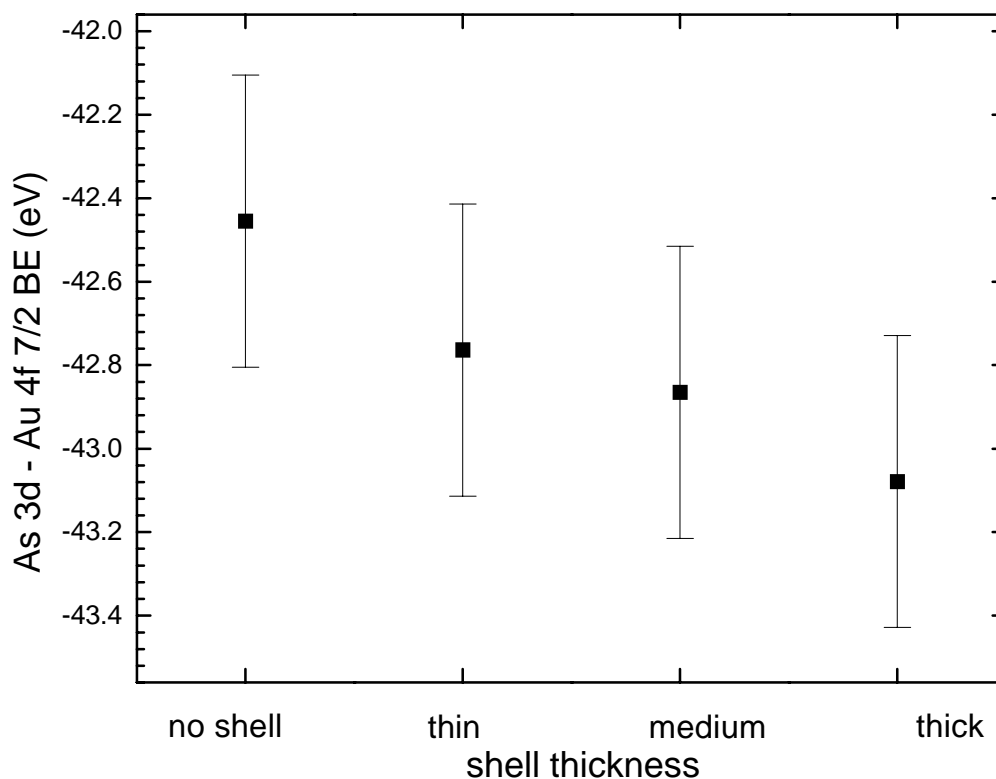


Figure 6-5 As 3d binding energy referenced to au 4f_{7/2} as a function of CdSe shell thickness in InAs/CdSe core/shell particles. The peak shifts up to 0.625eV to lower binding energy as the shell thickness is increased. The As 3d binding energy for bulk InAs referenced to au 4f_{7/2} is -43.32eV (not shown on graph).

The Cd 3d peak binding energy also changes as a function of shell thickness, though the magnitude is much less. Figure 6 shows the binding energy of the Cd 3d_{5/2} core referenced to Au 4f_{7/2} as a function of shell thickness for the same samples. The binding energy decreases by about 0.1eV as the shell is grown thicker. Again, the binding energy of this core level is higher than that of the bulk material (320.37eV referenced to bulk).

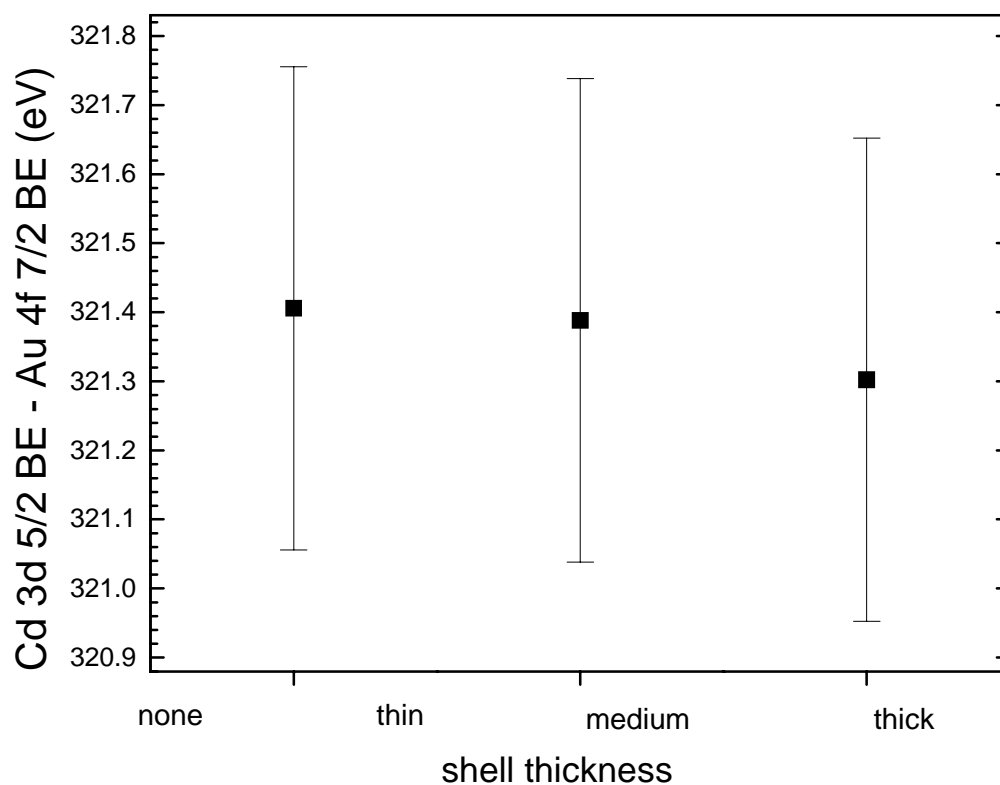


Figure 6-6 Cd 3d $_{5/2}$ binding energy referenced to Au 4f $_{7/2}$ as a function of shell growth in InAs/CdSe core/shell particles. The core shifts to lower binding energy as the shell is grown thicker (0.1eV).

Figure 7 summarizes the trend of the shifts as a function of nanocrystal size (a), length of organic linker (b), substrate material (c), and shell thickness of the CdSe overlayer (d).

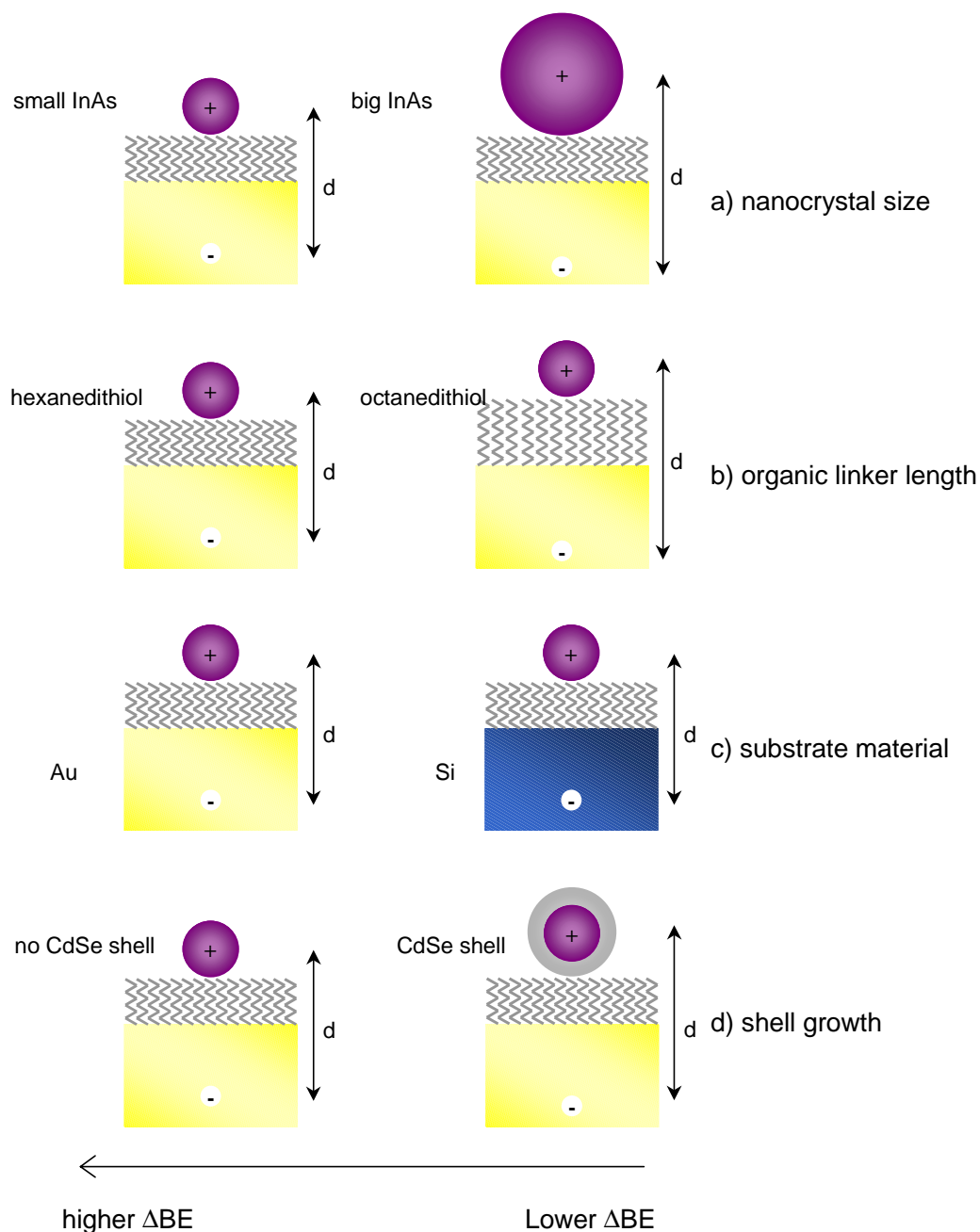


Figure 6-7 Schematic summarizing the amount of the binding energy shift as a function of nanocrystal size (a), length of the organic linker (b), and substrate type (c).

In this work, we have observed that InAs nanocrystals have exhibited a reproducible binding energy shift. These shifts are difficult to characterize in CdSe nanocrystals except using a higher resolution light source such as a synchrotron. Figure 8 shows the Cd 3d peaks for bulk CdSe and 25Å CdSe nanocrystals on a hexanedithiol/Au substrate using a

conventional x-ray source. It should be noted that CdSe nanocrystals of this size are the smallest diameter that can be routinely synthesized and handled at this time. The CdSe nanocrystals exhibit a shift to higher binding energy by 0.09 eV, accompanied by a linewidth broadening of 0.25 eV, which are smaller than the effects observed for the InAs nanocrystals. This is most likely due to the difference in the dielectric constants of the materials. InAs has a higher dielectric constant than CdSe (14.55 vs. 8), so electronic screening is more efficient in InAs. As a result, the screening properties which are expected to decrease with nanocrystal size are expected to change more with the size.

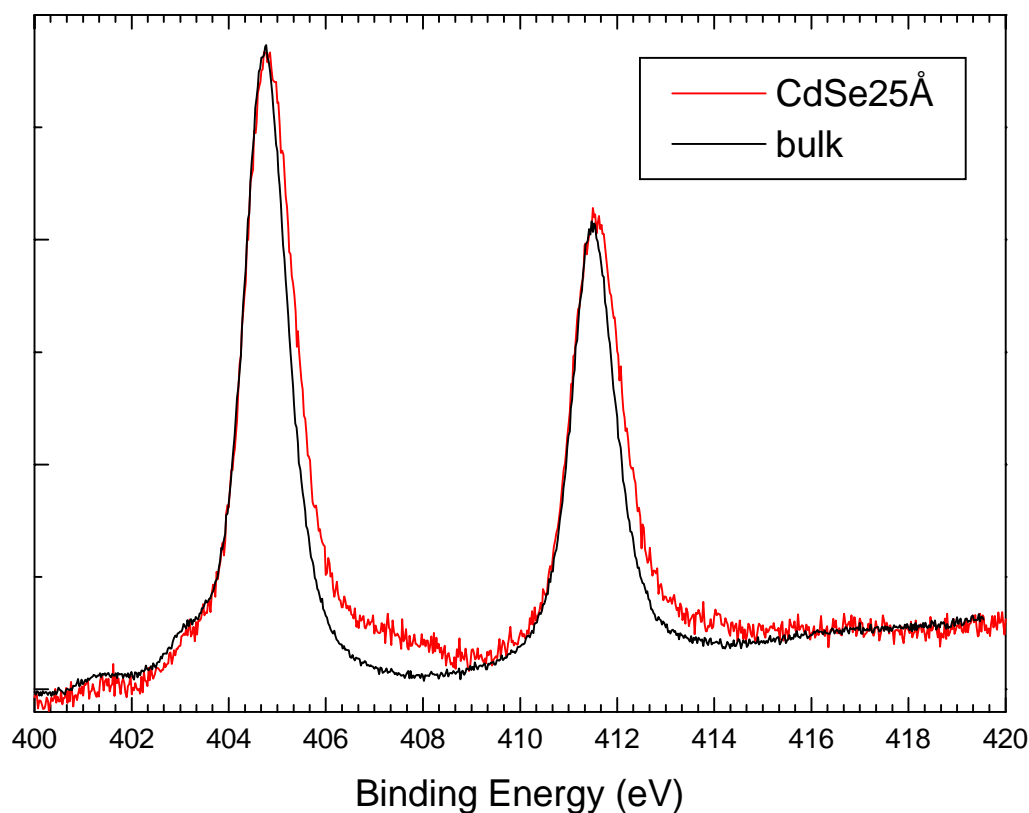


Figure 6-8 XPS spectra of Cd 3d cores for bulk CdSe (black) and CdSe nanocrystals 25 Å in diameter (red). The nanocrystal peaks are shifted to higher binding energy with a broader linewidth, though the overall change is smaller than for InAs.

6.3.2 XPS linewidth changes as a function of nanocrystal size

The other size dependent effect observed in the XPS core levels is a broadening.

Figure 9 is a plot of the FWHM of the In 3d core level obtained from the fitting routine as a function of nanocrystal diameter. The peak broadens about 0.250 eV as the size of the nanocrystal is decreased from 55 Å to 12 Å and appears to be relatively independent of the distance from the substrate and substrate material.

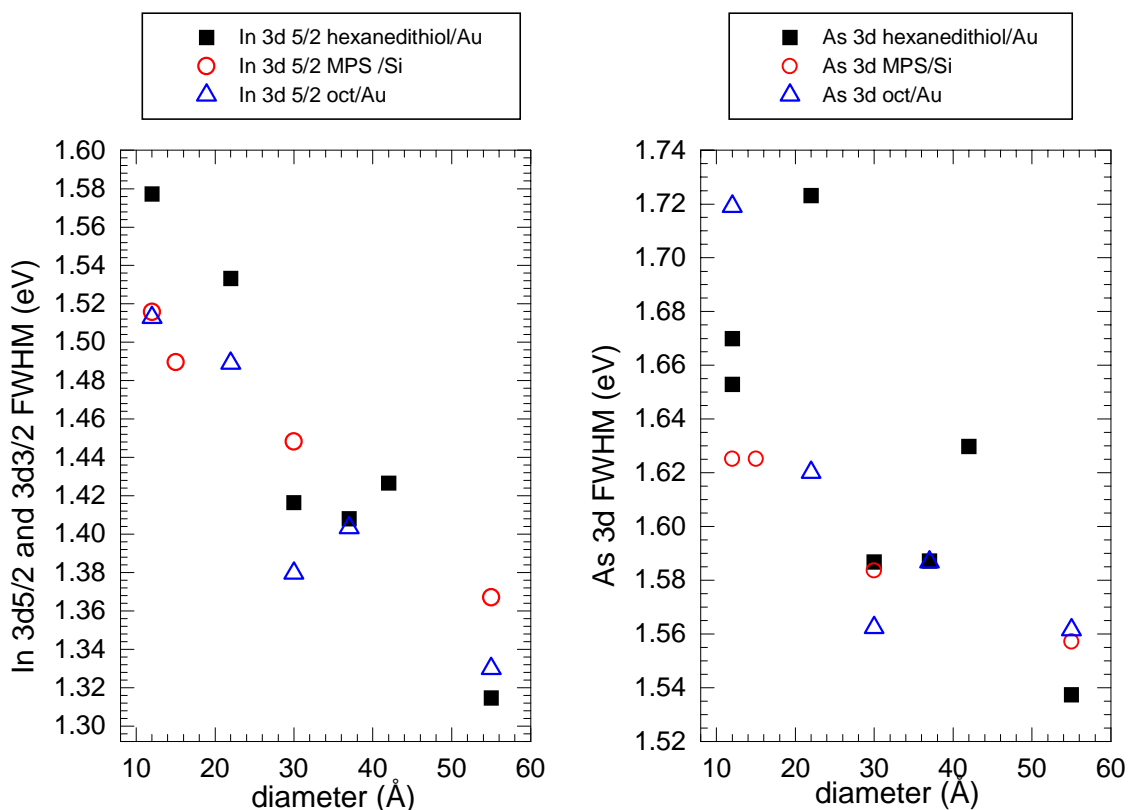


Figure 6-9 Core level width as a function of size for the In 3d_{5/2} and As 3d cores. The width increases as the size of the particle decreases and is relatively insensitive to the substrate material and length of the organic linker.

There are many possible explanations for a linewidth broadening as a function of decreasing particle size. If one considers a two-dimensional bulk surface, the electronic

environment of the surface atoms is different from the interior, thus generating a small shift of the XPS core level, known as a surface core level shift. Much work has been done on both metals [1] and semiconductors [2] to decompose photoelectron peaks into surface and interior contributions. Simple models accounting for the environment of the surface atom in terms of a Madelung potential have been found to be sufficient to describe these shifts.

In a nanocrystal, the surface peak would constitute a large contribution of the photoelectron signal. Furthermore, one expects a distribution of sites in a nanocrystal, which would result in a distribution of chemical shifts that would broaden the core level peak. So far, only the S 2p core level in very small CdS nanocrystals has exhibited size dependent effects which can be decomposed into varying contributions of the surface states [3, 4]. The S 2p core level is broad with multiple maxima due to different peak contributions and thus can be fit with a series of peaks representing bulk and surface contributions. Cd 3d cores have shown no observable shift as a function of size, even for nanocrystals having only ten Cd atoms. It is possible to fit the In 3d cores shown here to two photoelectron peaks representing bulk and surface sites that agree with surface to volume ratios. However, the fit can also be achieved with an arbitrary number of peaks with a variety of intensity ratios. Because the peaks do not show distinct core and surface contributions, it is not possible to make any conclusions about surface core level shifts in these particles.

The other possibility for the size dependent broadening of the FWHM is the lifetime of the hole. The linewidth of an XPS core level is inversely proportional to the lifetime of the hole. [5] However, extracting exact values for the lifetime is difficult due to additional broadening effects such as vibrational energy losses and chemical shifts[6, 7], as well as an asymmetry that is intrinsic to photoelectron lineshapes. The observed size dependence suggests that as the size of the particle is decreased, the lifetime of the hole decreases

(linewidth increases). This interpretation suggests that the smaller nanocrystals are more easily refilled than the larger ones. If one considers the correlation between binding energy shifts and linewidths [8], the trend is opposite: higher binding energies, which are indicative of lower electron density, are accompanied by narrower linewidths, because there are fewer electrons in the vicinity to quench the hole.

6.4 Expected causes of shifts

As was suggested beforehand, many factors affect the binding energy of core level and valence band positions in a photoelectron spectroscopy experiment. They can be attributed to initial state effects (intrinsic properties of the nanocrystal or nanocrystal/substrate system) or final state effects due to electronic relaxation and screening of the hole created in the photoelectron process). Below is a list of the effects which are expected to cause shifts in the energetic levels of nanocrystals in a XPS or UPS experiment.

6.4.1 Distribution of surface sites

As the nanocrystal is made smaller, the surface to volume ratio increases. Surface atoms are expected to have a core level binding energy that is slightly different from bulk due to their different environment ($\sim 100\text{-}500\text{meV}$). In semiconductors, the cations are expected to have shifts towards higher binding energy, whereas anions are expected to have shifts towards lower binding energy. Therefore, as the nanocrystal is made smaller, the surface contribution is expected to increase which would be exhibited in the photoelectron spectrum as a shift of the core level. Surface core level shifts are expected to affect all levels equally, including the valence band. This is an initial state effect.

6.4.2 Quantum size effects

The band gap widening and discretization of the valence and conduction states as discussed in Chapter 5 must also be considered. Quantum confinement affects only the valence band in a photoelectron experiment, the amount of which can be estimated from the effective mass approximation. This is also an initial state effect as it is due to the intrinsic properties of the nanocrystal. However, confinement should not affect the core levels as much as the valence levels they are deeply bound.

6.4.3 Hole screening

The creation of a positively charged hole near the positively charged nucleus is undesirable, so the electrons in the vicinity relax to screen the positive charge. Because the timescale of this relaxation is short, the photoelectron feels the effects of the screening and thus the binding energy is affected. This is a final state effect as the hole is created because of the photoelectron process.

In addition to screening, there are several electrostatic effects which must be taken into account, given the geometry of the system. The positive charge on the nanocrystal must be dispersed over the whole nanocrystal, which requires energy of approximately e^2/R , where e is the charge of an electron and R is the radius of the nanocrystal. This is the Coulomb charging energy. In addition, the positive charge on the nanocrystal can be stabilized by the formation of an image charge in the substrate, which reduces the Coulomb charging energy. If the timescale of these processes is shorter than the time to remove the electron, they are reflected in the binding energy of the measured photoelectron. If the observed trend in the linewidth is due to a lifetime effect, it supports this model of hole screening. If the hole is more energetically unfavorable, it will be quenched sooner, and so the lifetime of the hole will be shorter. This screening process is considered to be the most

plausible contribution to the observed core level shift, and thus will be explored in the following section.

6.5 Evaluation of the core level shift in terms of electromagnetics

What are the factors affecting the binding energy of a material? If one considers the core levels only, the binding energy in a metal written relative to the atomic level in vacuum (BE_{atom}) is

$$BE_{\text{metal}} = BE_{\text{atom}} - e\phi + E_{\text{hybrid}} - E_{\text{relax}}$$

where ϕ is the work function of the metal, $E_{\text{hybridization}}$ is the initial state effects from bond formation, and E_{relax} is the relaxation energy of the final state in the solid. For a spherical nanocrystal on a substrate, two additional terms must be included which describe the energy of the positively charged system due to the hole left behind. These terms are (1) the cost of dispersing the charge in a finite sized sphere (Coulomb charging energy) and (2) the energy gain involved in the formation of an image charge in the substrate in response to the hole in the nanocrystal:

$$BE_{\text{cluster}} = BE_{\text{atom}} - e\phi + E_{\text{hybrid}} - E_{\text{relax}} + E_{\text{Coulomb}} - E_{\text{image}}$$

The binding energy of the nanocrystal can then be described relative to the bulk value:

$$\Delta BE = BE_{\text{cluster}} - BE_{\text{metal}} = -e\Delta\phi + \Delta E_{\text{hybrid}} - \Delta E_{\text{relax}} + E_{\text{Coulomb}} - E_{\text{image}}$$

In addition, the values for the work function, $E_{\text{hybridization}}$, and $E_{\text{relaxation}}$ for a nanocrystal differ from those of the bulk metal. Both E_{Coulomb} and E_{image} contain values for the static dielectric constant of the nanocrystal. One can invoke a classical model from electrostatics

to describe E_{Coulomb} and E_{image} . For a metal sphere the energy cost of delocalizing a charge over a sphere of radius R is

$$E_{\text{Coulomb}} = e^2/2R$$

For a dielectric sphere, the term is reduced to

$$E_{\text{Coulomb}} = (e^2/2R) \cdot (1-\epsilon^{-1})$$

where ϵ is the dielectric constant of the sphere [9, 10]. The Coulomb charging energy is larger in metal clusters than in insulators, the former producing shifts on the order of 1eV for a 10Å diameter sphere. Because Coulomb charging is an energy cost, it reduces the photoelectron kinetic energy, effectively increasing its binding energy. For a diameter of 12Å, the model predicts a shift of +1.196eV for a metal sphere and 1.114eV for a semiconductor sphere with the InAs dielectric constant of 14.55.

It should be noted that dielectric constant is expected to be strongly size dependent for semiconductor nanocrystals. How the conduction electrons in a particle screen a positive charge is expected to be strongly dependent on the size of the system. For large particles, the system is nearly bulk like, and the electronic screening should be therefore more efficient than in smaller particles, where the electron density is low. Theoretical efforts have shown that the dielectric constant of nanocrystals is indeed size dependent, and decreases as the size of the particle decreases. For a Si nanocrystal 12Å in diameter a dielectric constant 1/2 the bulk value is predicted [11].

XPS is sensitive to the static dielectric constant of a material due to the nature of the final state of the system. In the photoelectron process, an electron is ejected from a core level, leaving a vacancy or a positively charged hole. Once the hole is created, the electrons in the vicinity of the hole relax to screen it from the positively charged nucleus. This extra-

atomic relaxation is a collective effect, and if the system is finite-sized can involve all the electrons in a cluster. [10] The amount of screening is dependent on the size and the dielectric constant of the material. Because the timescale of the electronic relaxation around the positively charged hole is fast ($\sim 10^{-16}$ s) relative to the escape of the photoelectron (10^{-15} s), the cluster remains charged within the lifetime of the hole. Therefore, an XPS spectrum measures the state of the ionized system. The binding energy measured reflects the relaxation energy of the final ionized state, and consequently the dielectric constant of the material. Direct correlation between the photoelectron binding energy and dielectric constant of a material has been measured.

Size dependent binding energy shifts in the XPS spectra of metal clusters [8, 12, 13] have been observed in numerous cases. The shift is well characterized and has been attributed to the size dependent Coulomb charging energy for a sphere. Description of the binding energy shift needs only a classical model utilizing the shape and geometry of the cluster, and does not require knowledge of the electronic structure of the cluster. Quantitative evaluation of the binding energy shifts in metal clusters has been well described by the Coulomb charging energy for a sphere, $e^2/2R$. [14] Analysis of photoelectron spectra from Ar(g) clusters demonstrates that binding energy shifts agrees with the model for a dielectric sphere, $e^2/2R \cdot (1-\epsilon^{-1})$ [9, 10], where ϵ is the dielectric constant for the particle and assumed to be the bulk value.

Image charge formation is a stabilization process, and thus reduces the Coulomb charge energy, effectively increasing the kinetic energy of the photoelectron (or decreasing its binding energy). Energy of image charge formation depends on the distance of the hole from the substrate as well as the dielectric constant of the substrate, nanocrystal, and organic linker. It should also depend on how well the hole is screened, which depends on the size of

the particle and shell growth. The need for a term describing the image charge energy in the description of the binding energy shift is confirmed by the fact that the amount of the binding energy shift changes when the substrate is changed from a metal to a semiconductor or the distance of the nanocrystal to the substrate is varied. The expression for E_{image} for a dielectric sphere next to a metal substrate with a dielectric layer in between has no simple analytical form, though intricate exact expressions have been derived. [15, 16] Qualitatively, the image charge stabilization should depend inversely on the distance of the cluster from the substrate, d , where d is the length of the spacer, and to a lesser degree on the static dielectric constants of the nanocrystal and the substrate.

Figure 10 shows the binding energy shift of the In 3d core for InAs nanocrystals on both hexanedithiol (squares) and octanedithiol/Au (triangles) substrates along with a model including only the Coulomb charging energy for a metallic sphere and a dielectric sphere with a bulk dielectric constant (14.55 for InAs). The model overestimates the energy shift at small R and underestimates the energy shift at large R . The difference between the two models is small. Evidently the model must include a term describing the image charge formation.

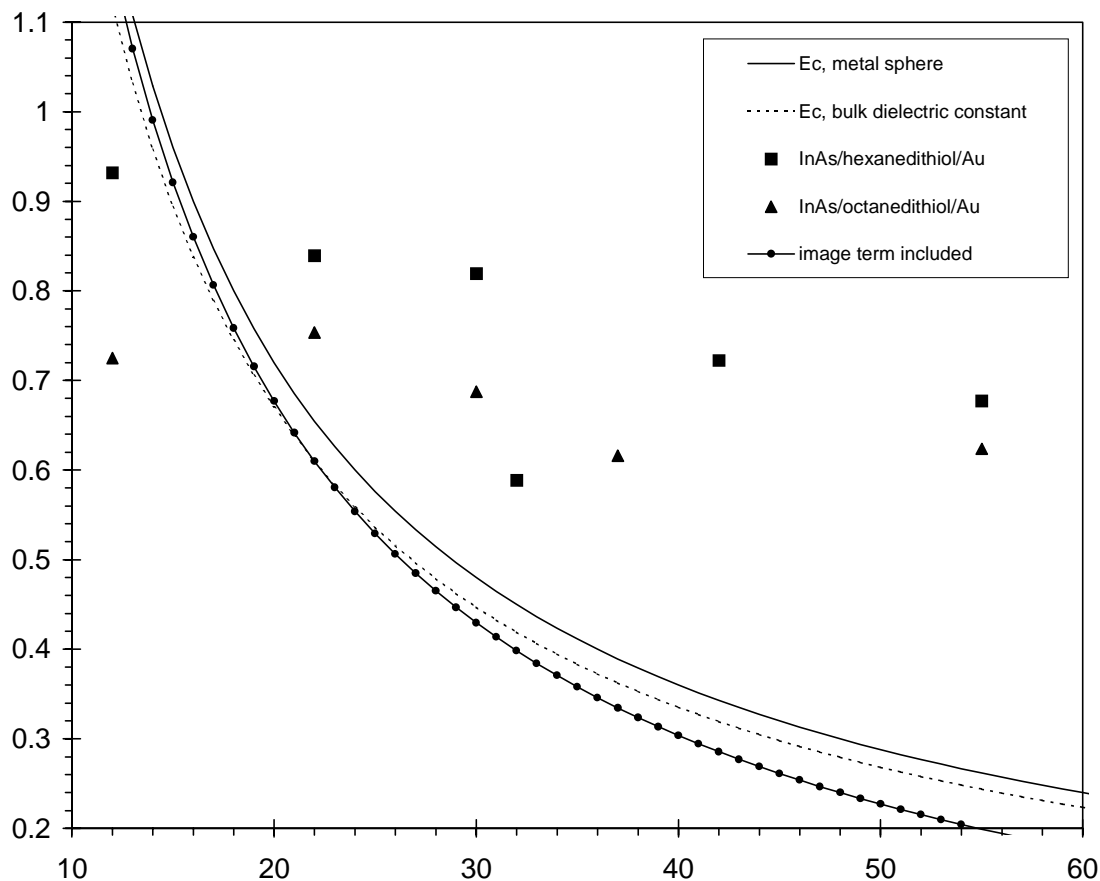


Figure 6-10 Binding energy shifts relative to bulk for hexanedithiol (squares) and octanedithiol (triangles) for InAs nanocrystals as a function of diameter. Models for the Coulomb charging energy of a metal sphere (line) and a semiconducting sphere with a dielectric constant of bulk InAs (dashed) are also included. A model including image charge formation for a metal sphere next to a plate is shown (line with circles).

Including the image charge formation for a metal sphere next to a metal slab is facilitated if one writes down the equations describing the capacitance of the system. The sphere is described as having a radius R and is at a distance d from the metal surface, where d is measured from the center of the sphere. The capacitance is written as

$$C = 4\pi\epsilon_0 R(1 + \beta^2 + \beta^3 + \beta^4 + \dots)$$

where

$$\beta = R/2d$$

The infinite series in β is necessary because the charge on the sphere induces an image charge in the metal, which induces another charge on the sphere, and so on. This series converges only if $R < d$, which is not the case for nanocrystals of the larger sizes. The charging energy U is

$$U = e^2/C$$

$$= e^2/R(1+\beta^2+\beta^3+\beta^4+\dots)$$

The functional form for this model is shown in Figure 8 (line with circles), and it also deviates from the experimental data at larger nanocrystal sizes.

Overall, the general trend is observed with this model but the evaluation does not account for the shift properly. This is mostly likely due to incompletely describing the capacitance of the nanocrystal/substrate system. A model fully describing this system is quite complicated as the image charge induces charges in not only the substrate but also the organic layer, and an infinite series for each of these interactions must be described.

Furthermore, reasonable values for the dielectric constants of all the materials involved must be used, which are not apparent for the case of the nanocrystal and the dielectric layer.

Evidently a model that is valid for $R > d$ including the dielectric constants of the organic layer and the nanocrystals needs to be invoked. Numerical simulations of the capacitance may offer solutions. In addition, a model that also accounts for the valence band shift is desirable. It is unclear as to how these electromagnetic effects would vary depending on whether the core or valence band is probed, along with which atom (anion or cation).

Variations in the lifetime of the hole could have an affect on the binding energy shift if the lifetime of the hole in the valence band is shorter than the timescale of photoelectron escape; in this case the image charge stabilization may play a lesser role.

6.6 Conclusions

The size dependent behavior of the photoelectron spectra of semiconductor nanocrystals is shown here to be dependent on the geometry and substrate materials of the nanocrystal/linker/substrate system. There are multiple explanations for these effects, some of which are expected to be dependent on each other. The two major contributions are expected to be the final state which involves screening of the photocreated hole and image charge formation in the metallic substrate, and the formation of space-charge barriers at the nanocrystal-metal interface. Constructing a model that describes the capacitance of the nanocrystal/substrate system describes the general trend of the binding energy shift, but shows quantitative errors which are most likely due to not accounting for the dielectric constant of the nanocrystals and the organic linkers. This model makes many assumptions, including that the charge is dispersed uniformly over the nanocrystal and that all the core levels are affected by the image charge equally. More sophisticated descriptions of the nanocrystal/linker/metal system may result in agreement with experimental data, and further experiments measuring the valence band offsets of nanocrystals and core/shell nanocrystals on the Si and thiol/gold substrates will help complete the data analysis.

The following chapter will describe UPS experiments of nanocrystals on metal substrates in terms of a model in which the metal influences the valence band levels of the nanocrystal. It will become evident that this description will be similar to the image charge model used here, and that the need for a model accounting for both the core levels and the valence levels.

6.7 References

- [1] D. M. Riffe, G. K. Wertheim, D. N. E. Buchanan, and P. H. Citrin, Phys. Rev. B **45**, 6216 (1992).
- [2] A. B. McLean, Surf. Sci. **220**, L671 (1989).
- [3] U. Winkler, D. Eich, Z. H. Chen, R. Fink *et al.*, Chem. Phys. Lett. **306**, 95 (1999).
- [4] J. Luning, 1998, Thesis.
- [5] R. W. Shaw Jr. and T. D. Thomas, Phys. Rev. Lett. **29**, 689 (1972).
- [6] N. Mårtensson and R. Nyholm, Phys. Rev. B **24**, 7121 (1981).
- [7] M. G. Mason, Phys. Rev. B **27**, 748 (1983).
- [8] V. Vijayakrishnan and C. N. R. Rao, Surf. Sci. Lett. **255**, L516 (1991).
- [9] J. Jortner, Z. Phys. D **24**, 247 (1992).
- [10] O. Björneholm, F. Federmann, F. Fössing, T. Möller *et al.*, J. Chem. Phys. **104**, 1846 (1996).
- [11] L.-W. Wang and A. Zunger, Phys. Rev. Lett. **73**, 1039 (1994).
- [12] S. B. Diczio and G. K. Wertheim, Comments Solid State Phys. **11**, 203 (1985).
- [13] G. K. Wertheim, S. B. DiCenzo, and D. N. E. Buchanan, Phys. Rev. B **33**, 538 (1986).
- [14] J. D. Jackson, *Classical Electrodynamics* (Wiley, New York, 1999).
- [15] J. Ståhlberg, U. Appelgren, and B. Jönsson, J. Coll. Interface Sci. **176**, 397 (1995).
- [16] H. Ohshima, J. Coll. Interface Sci. **198**, 42 (1998).

7 ULTRA-VIOLET PHOTOELECTRON SPECTROSCOPY OF NANOCRYSTALS ON METAL SUBSTRATES: MEASURING BAND OFFSETS

7.1 Introduction

This chapter will explore the behavior of the energy levels of a semiconductor nanocrystal when it is placed in contact with a metal. The previous chapter has demonstrated that a metal substrate can influence the core level binding energies due to the electromagnetic interaction of the hole created in the photoemission process. This chapter will show that the position of the valence band maximum is also dependent on the nanocrystal size, composition, and substrate material. Instead of interpreting the results in terms of a charge screening model as in the last chapter, a traditional band-bending model will be used.

The problem of energy levels for two metals in contact is one that has been well-studied both theoretically and experimentally. When two materials are put into electrical contact, an energy barrier is formed for either the hole or electron when it travels from one side to the other. For example, consider the situation in which a semiconductor is placed next to a conductor, or a metal oxide semiconductor (MOS) junction.

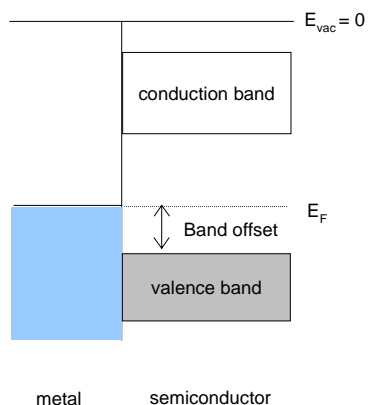


Figure 7-1 Band level diagram for a metal-semiconductor interface.

Figure 1 is a sketch of the conduction and valence bands of a semiconductor in contact with a metal where the vertical axis depicts energy and the horizontal axis real space. If an electron is to travel from the metal to the semiconductor, it must surmount an energy barrier from the Fermi level of the metal (E_F) to the conduction band of the semiconductor. Likewise, if a positively charged hole is to travel from the metal to the valence band of the semiconductor, it also must surmount an energy barrier. Therefore, it is apparent that how the bands for a heterojunction line up at the interface region of a material is an important problem for understanding the electronic transport properties of the whole system. [1] Values for the band offsets are quite important in the electronics industry, since the barriers for charge affect how a device operates. Furthermore, as device features become increasingly miniaturized, the total amount of the device that is interfacial is increasing, and therefore properties of interfacial areas become more important.

Interfaces can be a problem for a material if its reactivity is increased at an interface, such as at surface of a semiconductor with air. However, the electronic structure of interfaces can be used advantageously, and there are numerous examples of metal-semiconductor and semiconductor heterojunctions which exploit the specific energetics of the interface such as the transistor and the diode. Interest in band offsets has been prompted by developments in techniques used to grow high-quality, well-defined semiconductor layers. Control over layer growth enables tuning of the electronic properties of the system by growing heterojunctions of different materials or with different thicknesses. Therefore, one has another parameter by which materials can be designed to have specific desired properties. This “band-gap engineering” has realized applications such as the semiconductor laser and also improved systems like the LED and photovoltaic.

The first interface that will be explored here is the nanocrystal-metal interface. Nanocrystals have been incorporated into useful devices such as LEDs and photovoltaics in which they are spin cast onto a conducting surface or interspersed into a conducting polymer. [2-6] The quantity of interest is the relative position of the energy levels of the nanocrystal to the polymer or the metal electrode. An approximate band diagram for the LED is shown in Figure 2. [7] The materials utilized in the device are chosen carefully so that the way the bands line up works towards electron-hole recombination at the nanocrystal/polymer interface, producing light. Consequently, knowledge of the energy lineup is essential for designing a workable device.

Therefore, obtaining experimental values for the energy barriers at the interface is relevant for improving the performance of the device. This chapter will describe the measurement of band offsets at a nanocrystal-metal interface by ultraviolet photoelectron spectroscopy (UPS) with the goal of understanding how the electronic energy levels of the nanocrystal are influenced by a metallic substrate.

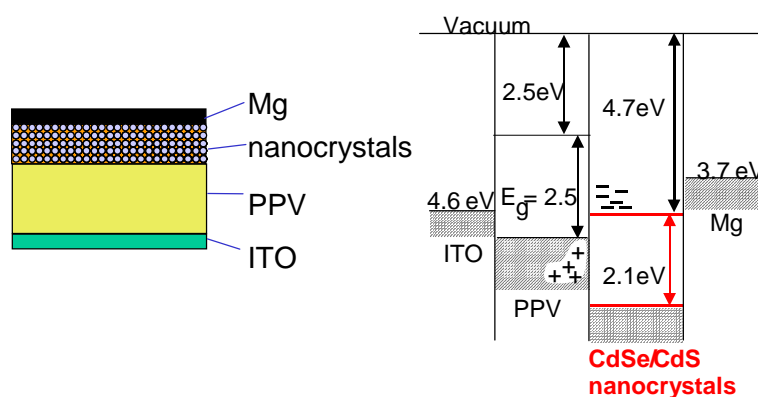


Figure 7-2 Real space diagram of a light emitting diode (LED) (left) and band level diagram (right). The LED is a bilayer device composed of the polymer paraphenylvinylene (PPV, yellow layer) and nanocrystal layers (red layers) sandwiched between ITO and Mg electrodes. The core-shell band levels relative to the polymer and electrodes are approximations based on theoretical IE values.

UPS has been effective in quantifying energy barriers for charge carriers in a heterojunction system. It is a natural choice for this task as it measures the density of states as a function of energy, and thus yields energetic positions of the valence band maximum. In the past when x-ray sources were more common, methods for obtaining the band offset using XPS were determined. [8, 9] It has been demonstrated that UPS can yield band offsets for less clean systems such as organic molecules [10] and also polymers [11] on metal interfaces. Alternative methods are electrochemistry or thermionic emission, both of which have been used successfully.

7.1.1 Semiconductor heterojunctions in nanocrystals: core/shell particles

The next interface that will be examined is the interface between two semiconductors. The two dimensional semiconductor heterojunction has been studied extensively as there are numerous examples of heterojunctions with useful properties as well as interesting physical characteristics.

The property that we would like to know is how the energy levels line up with respect to each other when two different semiconductors are put next to each other. The ionization energies of the materials can be used to predict the band offsets. Consider the two semiconductors in Figure 3a which are well separated in space. They have different band gaps, work functions, and ionization potentials. If they are brought into contact, the Fermi levels must be matched. Due to the band discontinuities at the interface, the bands bend in order to meet (Figure 3b). [12, 13]. The quantity of interest is the energy difference between the conduction and valence bands (Δ_{CB} and Δ_{VB}), as they describe the energy barrier that a charge carrier experiences when going from one side of the junction to the other.

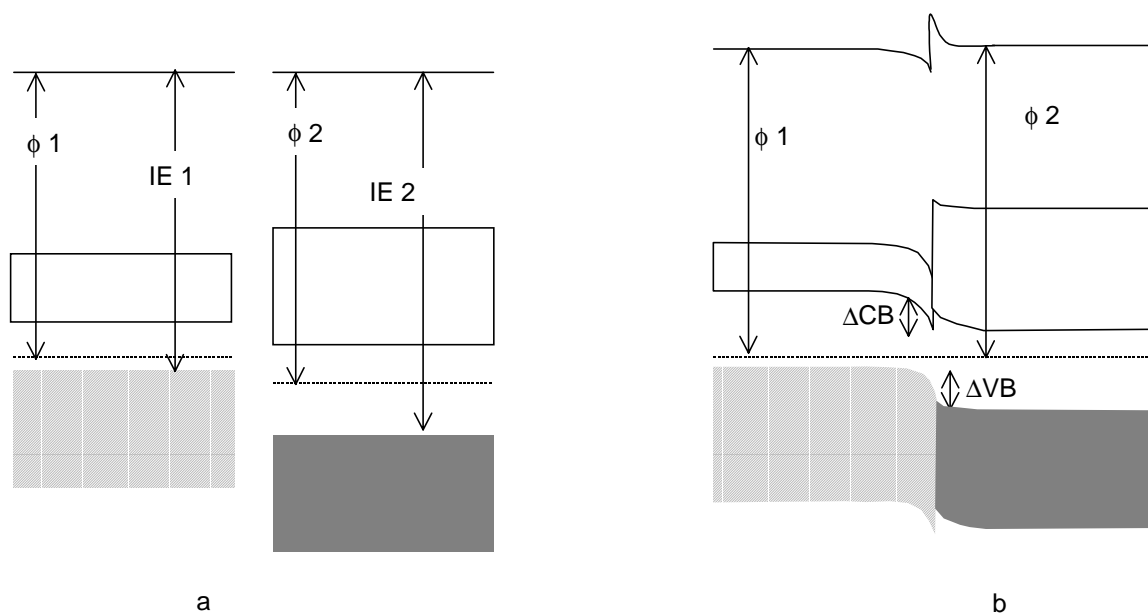


Figure 7-3 Schematic of a semiconductor heterojunction before (a) and after (b) electrical contact. ΔVB and ΔCB are the energy barriers at the valence band maxima and conduction band minima.

By judicious choice of the materials, band gap offsets can result in interesting electronic and optical properties of the resulting system. Esaki realized that superlattices made of alternating layers of two different semiconductors can have properties that are different from the individual semiconductors and which can be tuned by varying the layer thickness or materials implemented [14]. Complicated structures involving multiple semiconductors have brought about systems such as waveguides, photonic band gap materials, and blue LEDs. As a result, heteroepitaxy of semiconductors has been studied for several decades now and interesting physics along with novel applications are continuously being realized. For two-dimensional lattices, the use of molecular beam epitaxy (MBE) and metal-organic chemical vapor deposition (MOCVD) have been the primary techniques used to generate these structures.

However, discrepancies from the ionization potential technique described above have been found due to quantum dipoles or structural dipoles. Quantum dipoles are due to

the inherent properties of the two materials that make up the heterojunction. Structural dipoles are due to the structural characteristics of the interface, such as strain fields or defects. Not surprisingly, structural dipoles are highly dependent on the preparation conditions. Structural dipoles are not completely undesirable, as strain is one parameter by which to tune band offsets. For example SiGe alloys show electronic properties that change systematically with strain. [15].

The analog in nanocrystals for a two dimensional heterojunction are core shell nanocrystals in which an inorganic shell of a different material is grown on the surface of a nanocrystal, or a core shell particle. CdSe/ZnS [16-18] InP/CdSe, InAs/CdSe, [19] nanocrystals have been synthesized. In this case the layers grown are three-dimensional because they need to cover a spherical object. These have been successfully synthesized as core-shell nanocrystals such that the interfacial layer is heteroepitaxial, i.e., the atoms of the shell remain in registry with those of the core. CdSe with CdS is a good candidate for heteroepitaxial growth since the lattice mismatch between the two structures is less than 1% ($a_{\text{CdSe}} = 4.299\text{\AA}$, $a_{\text{CdS}} = 4.126\text{\AA}$).

As with two-dimensional heterojunctions, the choice of semiconductors that constitute the core/shell particle can result in electronic properties for one's advantage. Consider the CdSe/CdS band offset diagram for a nanocrystal (Figure 4). CdS (the blue region) has a larger bulk band gap than bulk CdSe (the white region) (2.1 vs. 1.72eV). If a layer of CdS is grown on top of the CdSe, the energy lineups for the conduction and valence band are a type I offset, or the case where the band gap for the smaller gap material (CdSe) is nested within the energy levels of the larger gap material. This offset results in confinement of the electron and the hole to the CdSe region. This has dramatic effects on the luminescence properties and chemical stability of the particles because the electron and hole

are confined in now three dimensions to the center of the nanocrystal. The luminescence is many fold times higher, approaching that of chemical dyes, because the probability of radiative recombination is enhanced due to increased electron-hole overlap. In addition, the particles are resistant to photo-oxidation since the hole cannot be trapped on the surface where it reacts with oxygen. Therefore, these particles are viewed as being nearly perfectly passivated; indeed, passivation by organic surfactants is incomplete due to steric hindrance of the ligands. [20]

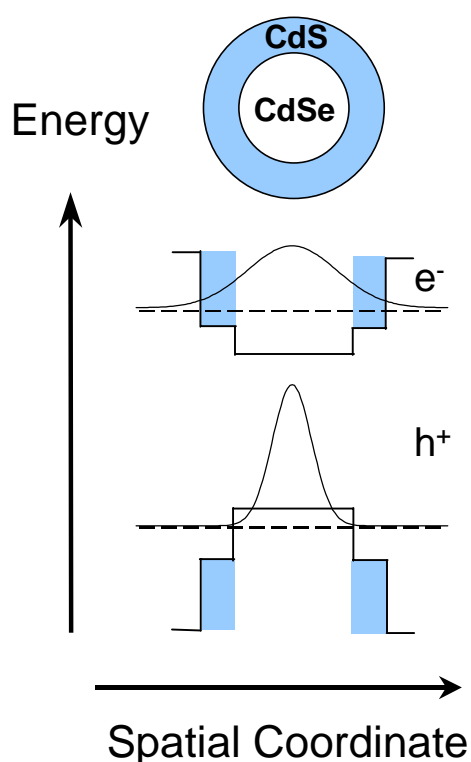


Figure 7-4 Energy level diagram for a core-shell CdSe/CdS nanocrystal. The wavefunctions for the electron and the hole are also indicated with approximate values for their energy values (dotted lines). Taken from [21].

Prediction of values for the band offset for core-shell nanocrystals using the ionization potentials of the materials is expected to not yield accurate results. The positions of the conduction band minimum and valence band maximum are shifted in energy due to

quantum confinement (as was shown in Chapter 4). More so, little is known about the structural quality of the interface. The shell may be epitaxially grown on the surface, but how much stress and strain at this curved interface is not easily characterized. The presence of strain fields may produce significant changes in the offset. Core-shell nanocrystals have a novel interface, and as a result are an interesting system to study both structurally and electronically. Therefore, an experimental value for the band offset at the CdSe /CdS interface is of interest.

7.2 Experimental for UPS

This section will describe how one obtains a value for the ionization energy (IE) of a material, which is defined as the minimum amount of energy to remove an electron from a material. For a semiconductor, this is the energy from the top of the valence band to the vacuum level, the latter of which is defined as the energy at which a free electron has zero kinetic energy.

Measuring the valence band maximum in a UPS experiment gives only the valence band relative to the E_F of the system, which is the Fermi level of the spectrometer because the sample is in electrical contact with the machine. Consequently, the vacuum level of the material is needed as a reference. This is achieved by measuring the low energy cutoff (E_{cutoff}) of the UPS spectrum which is essentially where $E_K = 0$ for the material.

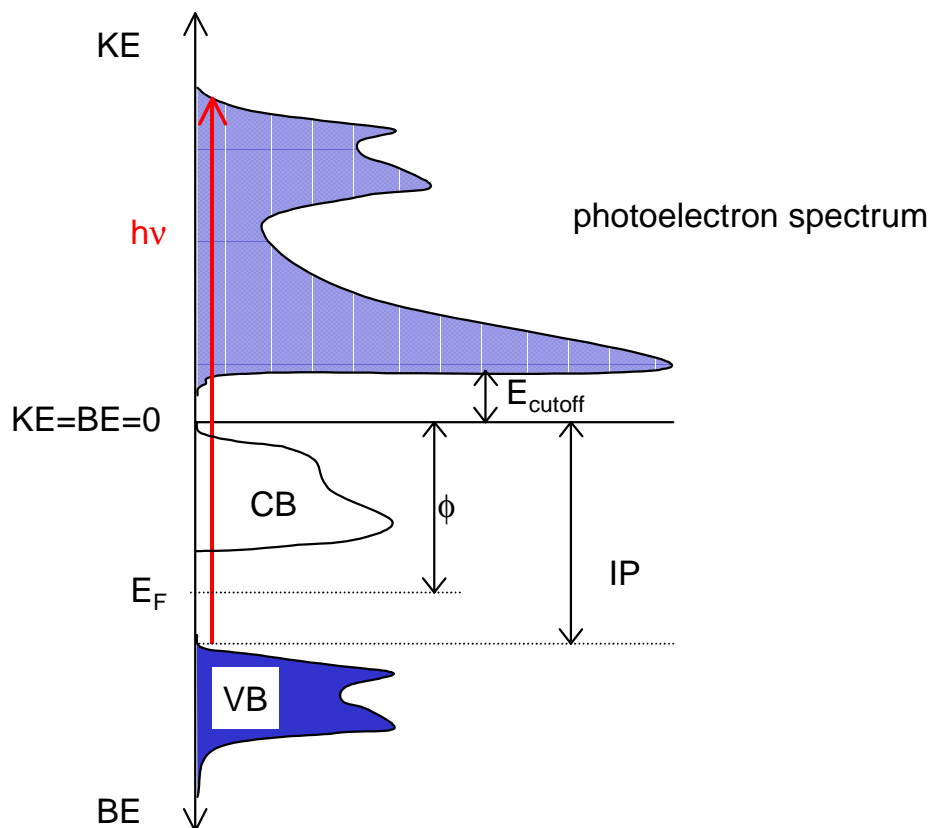


Figure 7-5. Schematic of the energy spectrum of a UPS experiment. The vacuum level is marked as 0. The spectrum measured is the intensity for $KE > 0$.

Figure 5 shows a schematic of a UPS spectrum with the valence band maximum and low energy cutoff marked. From the diagram it is evident that $h\nu - (E_{\text{VBM}} - E_{\text{cutoff}})$ is the ionization potential of the material. The other value of interest is the work function (ϕ) of a material, which is the energy difference between the vacuum level and E_F . Because E_F lies between the band gap in a semiconductor, $IE = E_{\text{VBM}}$ (relative to E_F) + ϕ . By substituting in the above formula for the IE from the spectroscopic features, one arrives at $\phi = E_{\text{cutoff}}$.

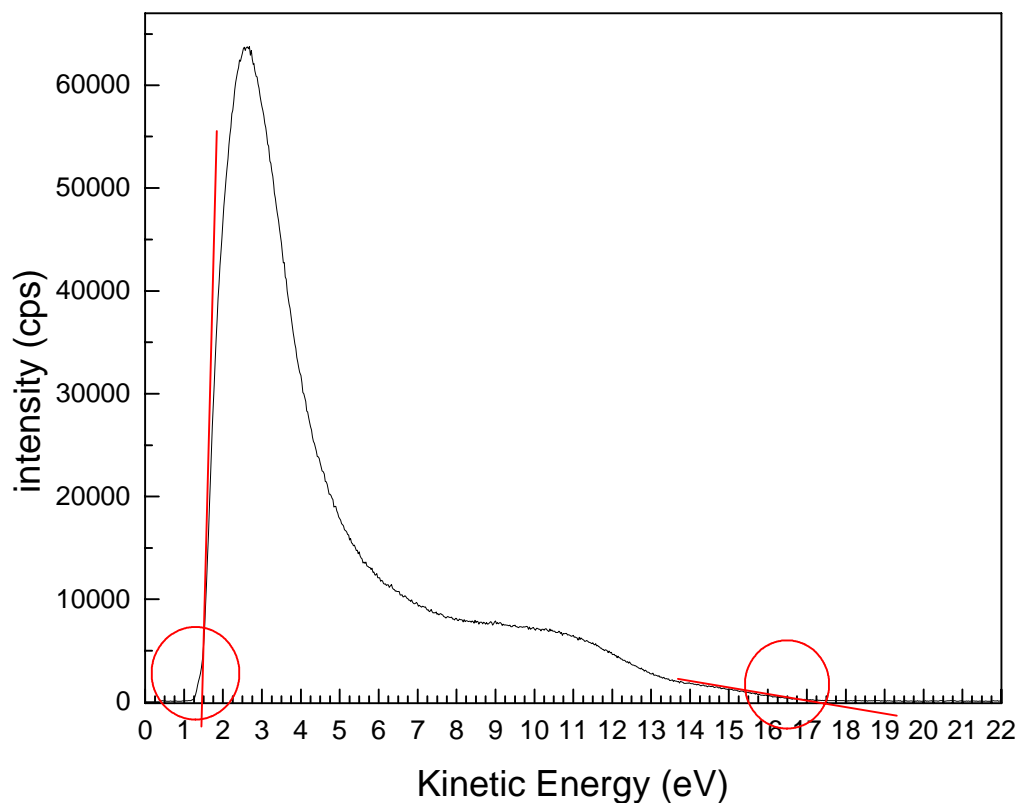


Figure 7-6 He I spectrum of a nanocrystal core shell on Au as a function of kinetic energy. The area in the circle on the left is the extrapolation for the E_{cutoff} , and the area at high kinetic energy is the extrapolation for the valence band edge.

7.2.1 Extrapolation method for VBM and cutoff

The method for obtaining a number for the cutoff or the valence band maximum from the spectrum is by drawing a line through the slope of the band and its intercept with a line drawn through the background, or zero level. Figure 6 shows the extrapolation of the cutoff and valence band maximum from a UPS spectrum using a He I line (21.2eV). The plot is intensity (electron counts/sec) as a function of kinetic energy. The spectrum ranges from 0-21.2eV, and the intensity is zero elsewhere. At the low kinetic energy regime is a large, high intensity feature that is due to the inelastically scattered electrons leaving the sample which drops due to the work function of the sample. Where the spectrum ends at

high kinetic energy is due to the top of the valence band (close to $KE = 21.21\text{eV}$). Often the sample is placed at a small bias (usually -5.000V) to shift the photoelectron spectrum to higher energy, so that the cutoff will not be influenced by low energy response functions of the spectrometer, which often leads to erroneous results. An alternative method is to use the inflection point of the spectrum, though extrapolation of a linear slope is more common. The uncertainty in extrapolating the value for the cutoff or valence band maximum by this technique is $\sim 100\text{meV}$. In the case of spectra with a great deal of noise or low signal, it is difficult to extrapolate accurately a line for the background. This is done for each material in the system (nanocrystal, metal) and a band lineup diagram can be constructed from IE and ϕ values.

The work functions for the substrates (Au, ITO) were also measured by UPS. Au evaporated onto cleaved mica was used. The sample was irradiated with x-rays for the same amount of time as the nanocrystal samples. Literature values for the work function of gold are 4.3eV , and from the UPS measurements here the average value obtained was the same within experimental error. ITO work function values were also obtained but literature values vary greatly (from 3eV to 7eV) [22] and depend heavily on manufacturing conditions. The average value obtained by the UPS measurements here (5.4 eV) was used as the ITO work function.

The samples must be exposed to x-ray radiation in order to remove the organic material adsorbed on the surface of the sample. This is critical because the organic material can give false values for the IE. The UPS spectrum changes drastically with the presence of organic material on the surface of the sample. The sample form used for UPS is a nanocrystal thin film made from a solution either spin cast onto ITO or gold or linked by a

self-assembled monolayer as described in Chapter 2. Samples had the organic surfactant removed (TOPO) as described in Chapter 2.

For the first spectra taken (when the sample is first put into the chamber) the spectrum is mostly due to the organic material on the surface of the sample. This is evident from the high value for the IE. Upon irradiation with x-rays over several days (with either Al or Mg $K\alpha$) the value decreases, until it eventually remains constant. It is believed that the x-rays removes the organic on the surface of the sample. Because organic molecules have large HOMO-LUMO separations, if the spectrum is dominated by their signal the value of the IE will be high. When the organic is blown off, the semiconductor is exposed, and gives a lower IE. Figure 7 shows the He II valence band spectra for bulk CdSe which had been etched with HCl before introduction into the vacuum chamber. The first spectrum has a large broad feature at low binding energies which decreases in intensity as a function of increased irradiation time. This is confirmed by the appearance of the Cd 4d peak at ~ 14.5 eV BE as well as valence band features in both the He I and He II spectra with irradiation time (Figures 7 and 8). In addition, the C 1s peak intensity decreases with exposure to x-rays.

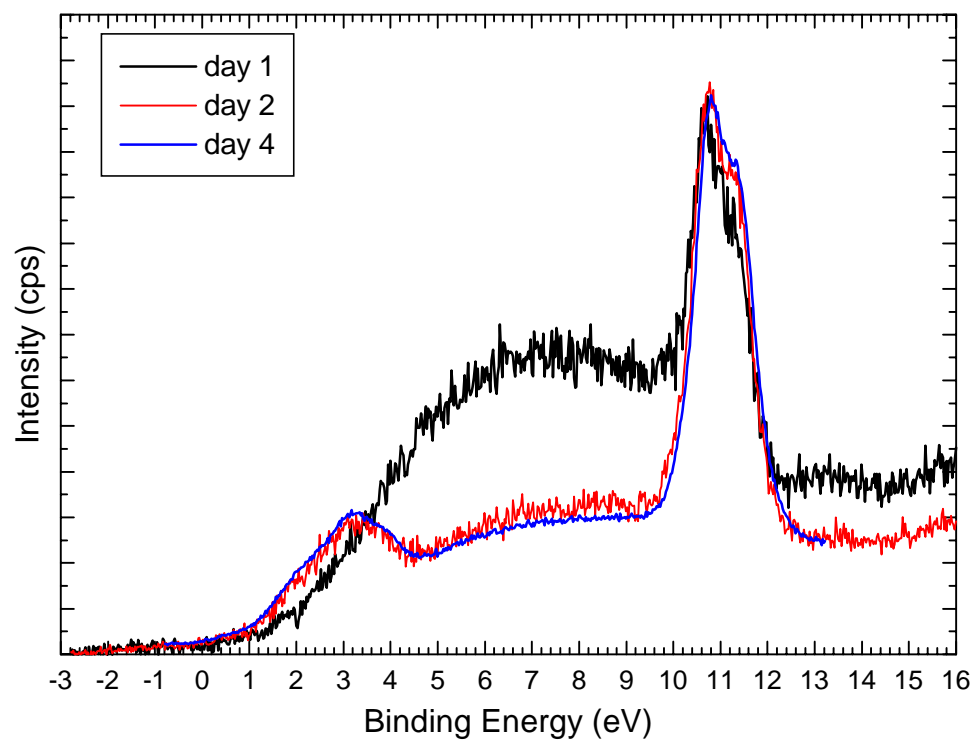


Figure 7-7 He II spectrum of bulk CdSe as a function of irradiation time in Al Ka x-rays.

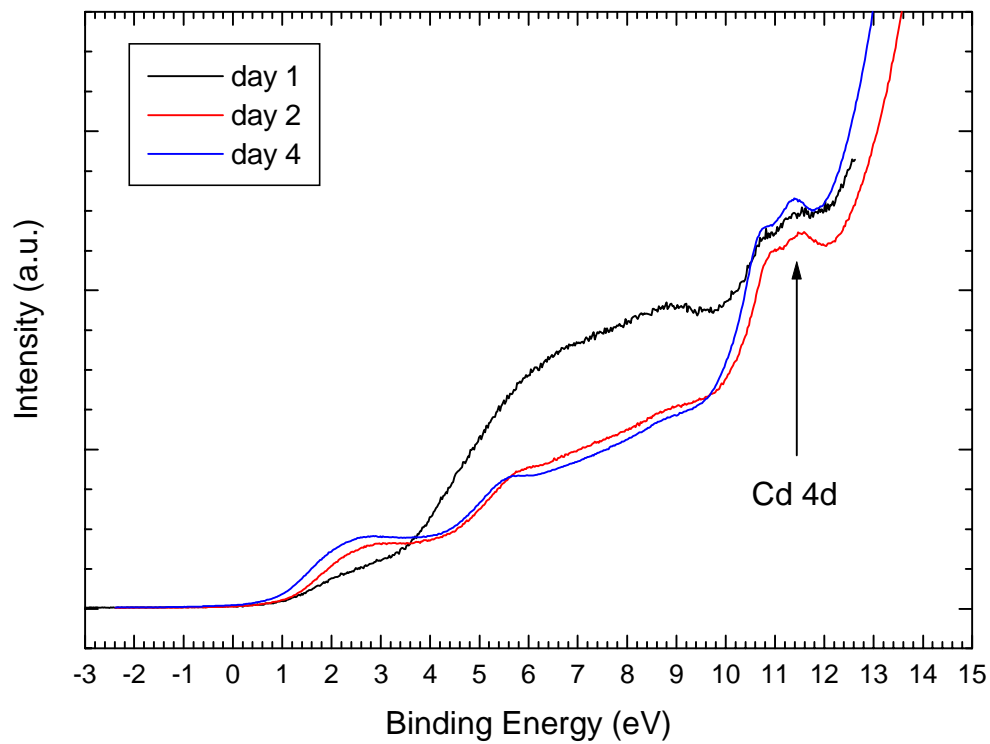


Figure 7-8 He I spectrum of bulk CdSe as a function of irradiation time in Al Ka x-rays.

After a certain amount of time, the shape of the spectrum stops changing with x-ray time, and the signal is believed to be due to the nanocrystal alone. Typically the spectrum stops changing in the low binding energy region after ~ 48 hours, but the low kinetic energy cutoff still changes for about 10 days. Once it reaches a state where it no longer changes, the values for the cutoff and valence band maximum and the DOS of the sample can be examined.

7.2.2 General method for measuring heterojunction band offsets by UPS

In the case of a junction of two semiconductors, the band offset is obtained by measuring first the ionization potential for the substrate semiconductor, then growing the second semiconductor on the surface and measuring the IE of the heterojunction. This has mostly been used on quantum wells grown by MBE or evaporation, which allows the measurement of band offset in situ [23, 24]. Because of the surface sensitivity of the measurement, only $\sim 5\text{\AA}$ of the 2nd layer is measured and not thus effects from the 1st layer can be excluded. Effects of band bending must also be accounted for, so core levels of each of the materials are also measured by XPS. Because band bending is effectively an electric field between the two materials, it affects all of the energy levels equally (cores levels, valence band, and low energy cutoff), and thus must be subtracted from the shifts of the valence bands that to isolate the band offset of the lineup. The valence band offset ΔVB is

$$\Delta VB = E_{\text{VBM}}(\text{CdS}) - E_{\text{VBM}}(\text{CdSe}) - (\text{bandbending}(\text{CdSe}) + \text{bandbending}(\text{CdS}))$$

where the first two terms is the difference in the valence band maxima and the term in brackets describes the band bending in the sample. The values for only band bending in a sample can be monitored by XPS of the core levels. The change in the conduction band, ΔCB , can be obtained if the band gaps of the materials are known:

$$\Delta CB = \Delta VB + E_g(\text{CdSe}) - E_g(\text{CdS})$$

The materials used in the core/shell particle, InAs and CdSe, were chosen due to the small lattice mismatch as well as the large difference in their band gaps, which possibly results in large valence band offsets which are easy to measure. CdSe: $E_g = 1.72\text{eV}$ CdS: $E_g = 2.1\text{eV}$ InAs: $E_g = 0.36\text{eV}$. Furthermore, from HRTEM images it is evident that the CdS shell growth is epitaxial on the CdSe surface. This is due to both the spherical geometry of the system coupled with a small lattice mismatch between the two systems. The synthesis of InAs/CdSe core shells is still being optimized, and whether or not the shell growth is truly epitaxial is still being investigated.

7.3 UPS Results for nanocrystal/metal interfaces: shifts of valence band maximum

A nanocrystal spectrum taken with He I is shown in Figure 9, plotted as intensity as a function of binding energy (eV). The feature at high binding energy is the low energy cutoff. The feature at 11eV is the Cd 4d core level, and the broad features at lower binding energy (0-8eV) are due to the valence bands of the nanocrystals. The features are in general similar to those of bulk (see Chapter 5). Figure 10 shows the same sample taken with He II where the Cd 4d core is more prominent.

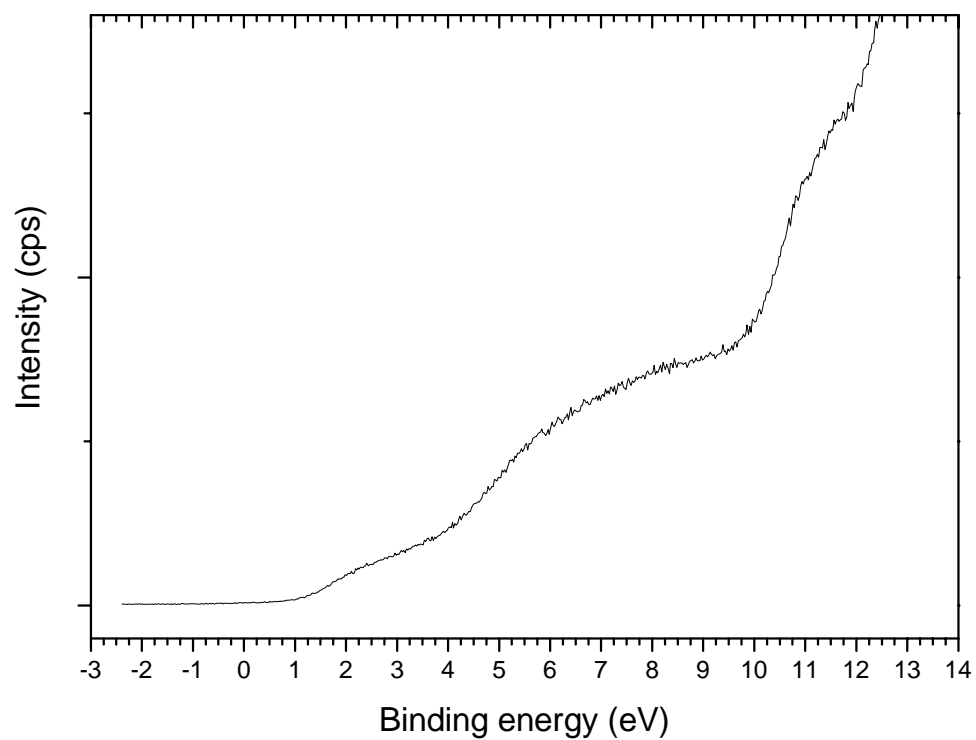


Figure 7-9 He I spectrum of 35Å diameter CdSe nanocrystal on ITO.

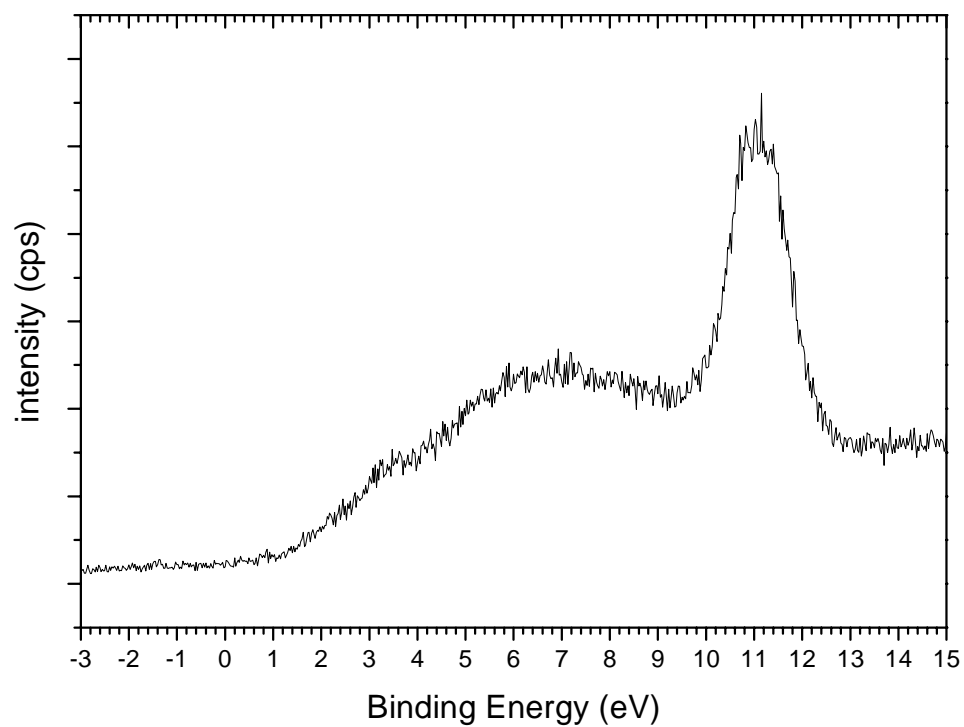


Figure 7-10 He II spectrum of 35Å nanocrystals on ITO.

Table 7-1 values for the valence band, conduction band, and work function (in eV) relative to the vacuum level for bulk and 35Å and 25Å CdSe nanocrystals on dithiol/Au.

| Diameter | Valence band maximum | Conduction band minimum | Work function |
|----------|----------------------|-------------------------|---------------|
| Bulk | 5.26 | 3.54 | 4.55 |
| 35Å | 5.92 | 3.75 | 5.2 |
| 25Å | 4.71 | 2.33 | 3.91 |

Table 1 shows the IE values for CdSe nanocrystals and bulk plotted relative to the vacuum level. The bulk values are measured from a single crystal. The nanocrystal IE is measured relative to an Au substrate which has a work function of 4.3Å. In all cases the position of the conduction band is inferred from the optical gap ($E_{CB} = E_{VB} - E_g$). As the nanocrystal is made smaller, the bands shift closer in energy towards the vacuum level. This is probably due to band bending at the nanocrystal-metal interface resulting in a pulling of the energy levels closer to the metal.

The energy positions of the edges of the valence and conduction bands relative to the E_F of the system are shown in Figure 18. It is evident that the band gap opening is not symmetric: between the 25Å and 35Å nanocrystal the conduction band shifts upwards 0.12eV while the valence band shifts downwards by 0.08eV. This total shift is roughly 2/3 to 1/3, as predicted by the effective mass approximation.

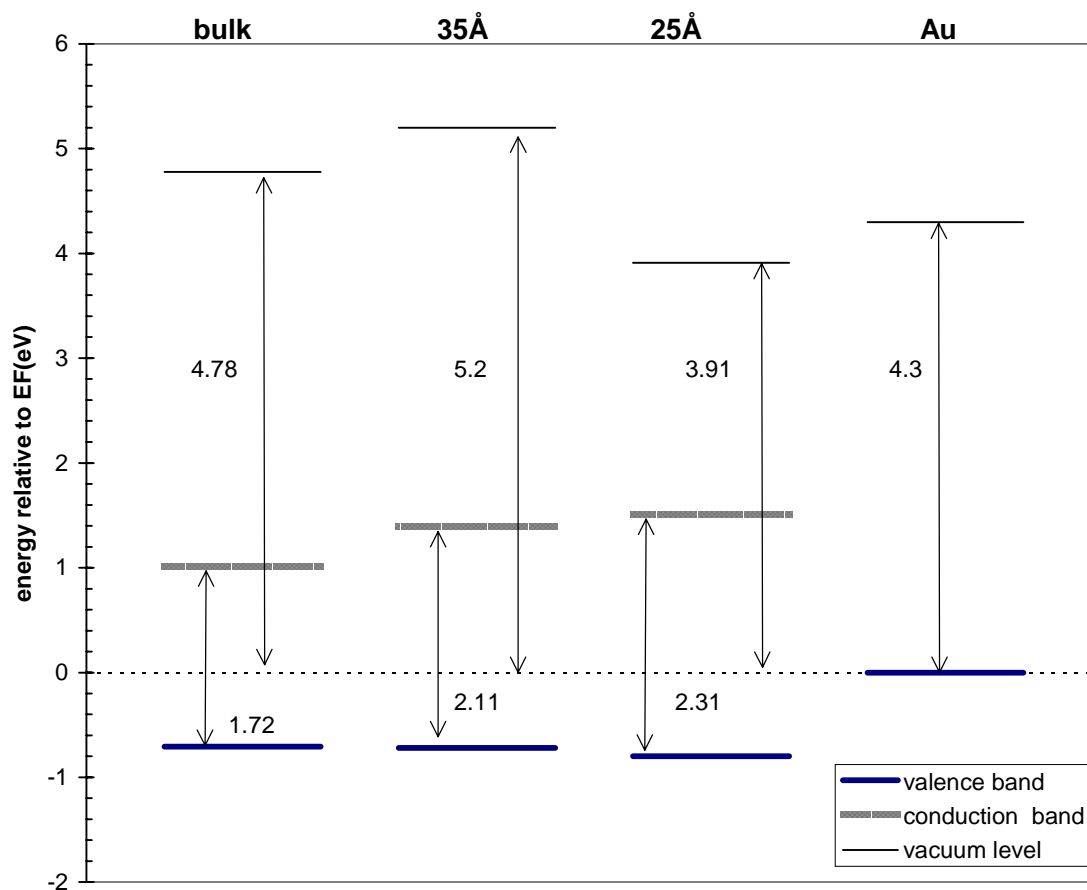


Figure 7-11 Valence and conduction band positions for bulk and CdSe nanocrystals on Au plotted relative to the Fermi level (dotted line).

The positions of the bands change if the nanocrystals are put onto a substrate with a different work function. Table 2 compares the values for Au vs. ITO substrates. Figure 19 is constructed from these values, showing the valence and conduction band positions relative to the E_F of the system. It is evident that for the higher work function material ITO the levels of the nanocrystal are pushed downwards by 0.83 eV and the vacuum level by 0.91 eV. This is due to the E_F being lower (or higher in binding energy) for ITO, which drags down the levels of the nanocrystals. In addition, the position of the E_F in the energy gap is changed by 0.83 eV. Therefore, it is apparent that the energy band positions in the

nanocrystal are dependent on the electronic properties of the substrate. The values obtained for the valence band offset of CdSe nanocrystals on ITO substrates agree with those determined from photocurrent measurements in CdSe nanocrystal/MEH-PPV (semiconducting polymer) photovoltaic devices.

Table 7-2 Values for the valence band, conduction band, and work function (in eV) relative to the ionization potential for 35Å CdSe nanocrystals deposited onto dithiol/Au and dithiol/ITO substrates.

| Sample | Valence band maximum | Conduction band minimum | Work function | Substrate work function |
|---------|----------------------|-------------------------|---------------|-------------------------|
| 35Å/Au | 5.92 | 3.81 | 5.2 | 4.3 |
| 35Å/ITO | 5.84 | 3.73 | 4.29 | 5.4 |

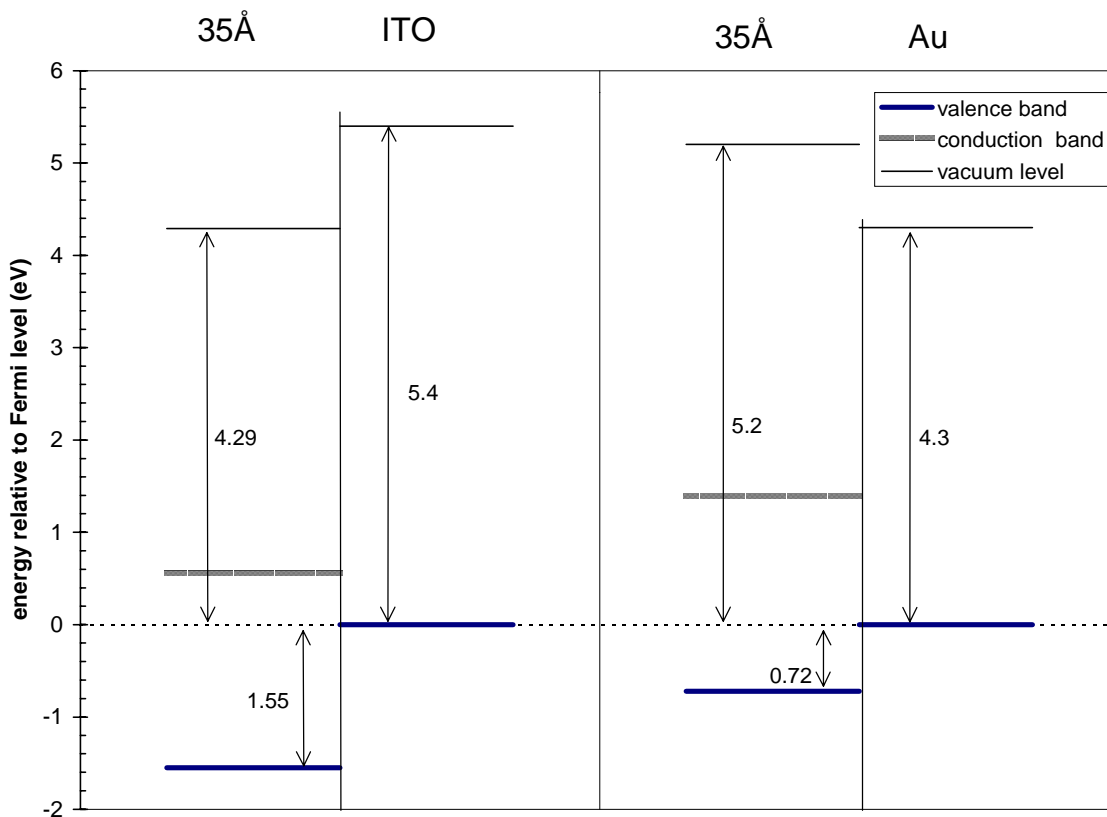


Figure 7-12 Valence and conduction band levels relative to the Fermi level for a 35Å on Au vs. ITO.

7.4 UPS Results for CdSe/CdS core shell nanocrystals

Table 3 shows the values for the conduction band, valence band, and work function relative to the vacuum level for a 25Å CdSe core and the same core with two different shell thicknesses of CdSe. Figure 13 are the positions of the valence and conduction bands relative to the Fermi level constructed from these values. The position of the conduction band for CdSe is inferred from the values for the energy gap for the nanocrystal. Band bending effects which would shift the core levels with shell growth was found to be negligible, though the Cd 3d cores are expected yield ambiguous results since it is present in both the shell and core. Therefore, the Se 3d and S 2p core must be used to estimate band bending and those are both quite broad, especially the S 2p. Exact band gap values for the

CdS is not known as there is no way to measure the band gap of the shell by itself. The bulk band gap value can serve as a lower limit and thus included in the sketch as a dotted line.

The effect of CdS shell growth is an increase in position of the valence band maximum, which is in agreement in the higher band gap material grown on the surface. The valence band shifts 0.99eV towards higher binding energy with the growth of a thin shell and stays constant with further shell growth. This energy barrier for the hole is great enough such that the hole remains trapped on the CdSe, concurrent with the high luminescence and high resistance to photo-oxidation of core/shell particles. With additional shell growth the position of the valence band maximum stays relatively constant, changing only 0.098eV.

Table 7-3 Values for the valence band, conduction band, and work function (in eV) relative to the ionization potential in core and core/shell nanocrystals with two different thicknesses. The CdSe core is 25Å in diameter in all samples.

| Sample | Valence band maximum | Conduction band minimum | Work function |
|-------------|----------------------|-------------------------|---------------|
| Core | 4.71 | 2.4 | 3.91 |
| Thin shell | 5.70 | 2.99 | 4.35 |
| Thick shell | 5.60 | 2.90 | 4.28 |

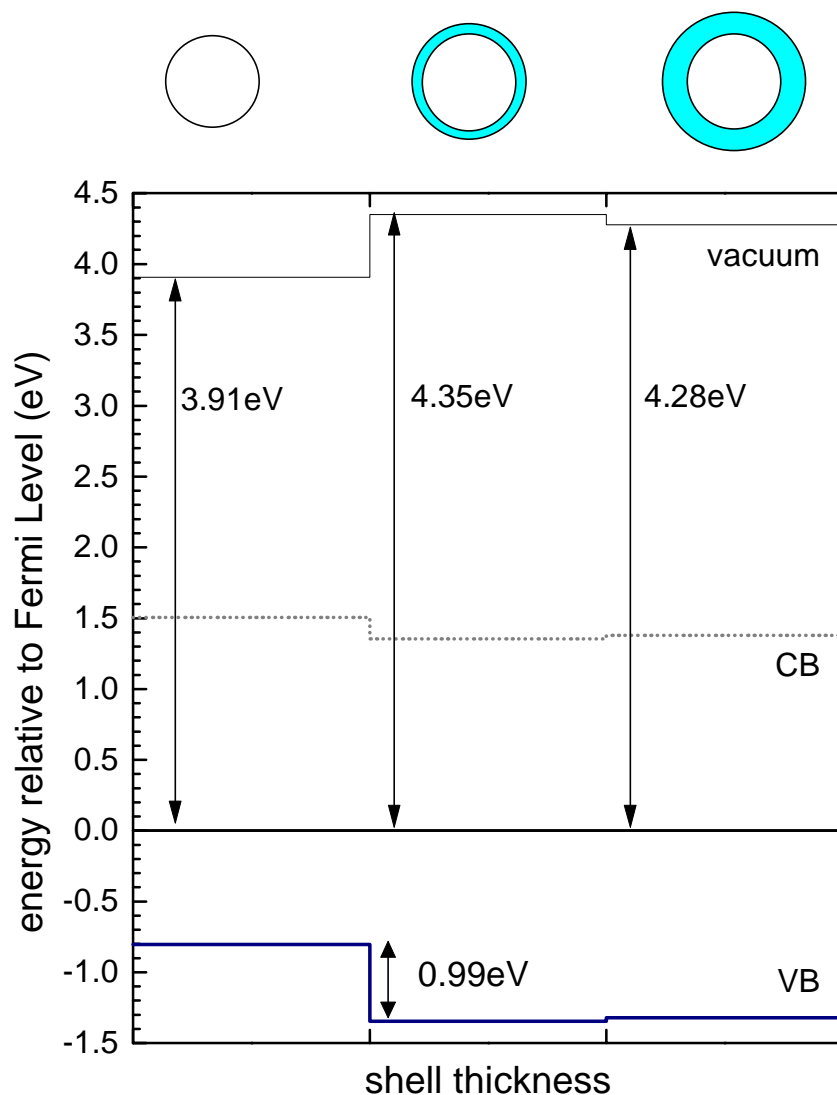


Figure 7-13 Valence and conduction band positions for core and core/shell particles of CdSe/CdS relative to the Fermi level. The valence band shifts 0.99eV to higher energy with shell growth.

Confinement of the electron is not known as the position of the conduction band cannot be inferred from optical absorption spectroscopy. By using the bulk values for CdS the conduction band position is relatively close in energy to that of the CdSe core; therefore, the electron may encounter a negligible barrier when going from the core to the shell.

Energetic values for the positions of the bands using a particle in a box model with a step potential for the CdSe/CdS interface also results in a larger barrier for the hole than for

the electron. The energy differences, though, are smaller: 0.51eV for the valence band and 0.27eV for the conduction band. However, this calculation assumes partially reflecting boundaries and deduces band offsets using only the ionization potentials of the materials.

7.5 Discussion

7.5.1 Electromagnetic effect of the band lineup

When a semiconductor nanocrystal is placed in electrical contact with a substrate, the energy levels of the nanocrystal are affected. This is due to the fact that the Fermi level of the system must be the same across the interface. The energy levels of the semiconductor bend in order to meet this requirement. This creates a space charge layer (where the energy levels are bent). Because it is effectively an electric field, it affects all levels, core and valence, equally. This is also an initial state effect as it is not due to the final state of the photoemission process. It is important to note that band bending can shift the levels of the semiconductor either upwards or downwards.

The valence band shifts vary for the nanocrystals as the substrate work function is changed due to the fact that the bands must bend in order to match the work function of the substrate material. The 35Å nanocrystal levels are pulled down by the ITO ($\phi=5.4\text{eV}$) and pulled up by the Au ($\phi=4.3\text{eV}$). The amount of band bending that occurs is dependent on the size of the nanocrystal. It is conceivable that it is more difficult to pull down the energy levels of the entire nanocrystal as the size is increased. Band bending for bulk semiconductors occurs over large length scales, much larger than a nanocrystal—on the order of 100nm, and it is not intuitive how this effect would scale with the size of a spherical object smaller than its length scale.

The previous chapter has shown that the core levels of InAs nanocrystals are pulled downwards (toward higher binding energy) when deposited on Au or Si substrates. This was qualitatively explained by screening of the hole by an image charge in the substrate. Here, we see that the effect of a space charge layer must also be accounted for. The question is how does hole screening vary as the binding energy of the level being probed decreases? Presumably, the screening of the valence band hole as was described in the previous chapter may also contribute to the valence band shifts. The screening of the valence band hole is likely to be very different from that of the core levels. Core level hole screening is a larger effect due to the fact it is close the nucleus. A valence band hole is far from the positively charged nucleus, and thus the relaxation effects are expected be weaker and slower. However, this screening is still expected to be a contributing factor to the valence band shift. The other question that arises is what are the relative contributions of the band bending and hole screening effects? In order to answer these questions, further experiments are necessary in which all the levels (valence and core) are measured on a variety of substrates, with different length organic linkers. Due to the fact that UPS measurements requires several days, the valence band spectra set presented here is not a complete one.

7.5.2 Core-shell nanocrystals: core level shifts interpreted in terms of band offsets

When a shell is grown onto the nanocrystals, the system becomes more complicated. The levels of the core are affected by both the shell as well as the metallic substrate. Furthermore, it is unclear how much of the shell and core the UPS measurements probe. The universal curve (Chapter 4) estimates the mean free path of the photoelectron to be about 5 Å, which would include only the shell in the 2 monolayer sample. However, this approximation is not accurate for non-planar solids. As a first approximation, the junction between the two semiconductors are considered here.

The experimental data shown in Figure 6-4 shows a shift of the In 3d core to lower binding energy as the CdSe shell is grown thicker. At first, it may be hypothesized that the shift in binding energy is indicative of the interface region in the core/shell particles.

Assuming that the surface of the cores is In rich, the In atom at the surface would experience a different environment due to coordination with Se atoms of the shell.

Electronegativity values for the four elements are given in Table 4. However, in terms of electronegativity the direction of the binding energy shift is in the opposite direction: Se is more electronegative than As and thus an In atom next to it would have a higher binding energy than one fully coordinated by As atoms. By the means of this same argument, no change is expected for the As atoms as the electronegativity of In is the same for Cd.

Table 7-4 Table of Pauling electronegativities for the elements in InAs/CdSe core/shell particles.

| | |
|----|-----|
| In | 1.7 |
| Cd | 1.7 |
| Se | 2.4 |
| As | 2.0 |

Shell growth apparently affects all the core levels in the core by roughly the same amount and in the same direction, which is the same effect as an electric field. Therefore, the data suggests that the electric field that is produced by the growth of the shell effectively pulls down the levels of the InAs. For illustrative purposes one can construct a band offset diagram for the bulk materials to get a qualitative picture of the band bending between InAs and CdSe (Figure 14). The work functions and ionization energies of the two materials are denoted in (a). The InAs work function is assumed to be in the middle of the gap since the work function value varies greatly depending on preparation conditions. [25] Since the gap

of InAs is small (0.36eV) this approximation should not introduce a significant amount of uncertainty. When the materials are put into electrical contact (b) the E_F must be aligned, which would create a large band discontinuity at the interface, estimated from this example to be ~ 1.09 eV for the valence bands (0.4 eV for the conduction band). Therefore, the bands bend in order to meet. [12] The amount of band bending is directly proportional to the doping density (N) in the semiconductors. From the experimental values for the In 3d and Cd 3d core level shifts, it is apparent that the band bending is greater in the InAs.

The In 3d shift to lower binding energy is concurrent with band bending that shifts the InAs levels upwards in energy, as depicted in the diagram in Figure 14. This value for band bending (0.6 eV) must be subtracted from the shift in the valence band maximum in order to obtain values for the valence band offset between the two materials. Measurements of the valence band maximum for the InAs/CdSe core/shell particles were not measured and unfortunately cannot be incorporated into the evaluation.

This model for the band level shifts is only hypothetical, and furthermore cannot be accurately predicted given the dependence of band offsets on strain, unknown doping density in the nanocrystals, and the influence of the substrate on the energy levels which is not quantified. The band bending model is evidently not as concrete as that predicted by image charge screening; nevertheless, it cannot be ruled out as a possible cause for the observed valence band shifts. Further experiments investigating the valence band shifts may provide insight about the nature of the core/shell interface as well as how the particle as a whole couples with the metallic substrate, which would allow a more sophisticated analysis of the energy levels at the interface.

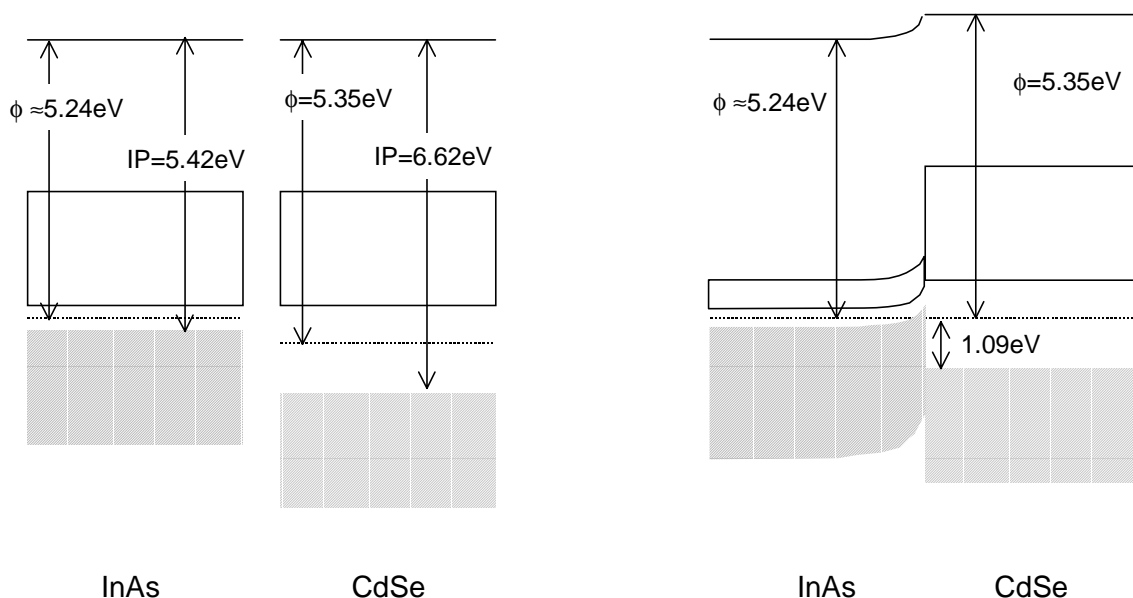


Figure 7-14 Schematic of the band positions for InAs and CdSe when they are separate (left) and for the InAs/CdSe heterojunction (right). The InAs bands are pulled upwards due to the discontinuity of the conduction bands at the interface.

7.6 Conclusions

This chapter in conjunction with the results from Chapter 6 shows that the energy levels of the nanocrystal are strongly influenced by the substrate onto which they are deposited. The valence band maximum can shift to either lower or higher binding energy, depending on the work function of the substrate. As the size of the nanocrystal is decreased, the position of the valence bands and the vacuum level are more strongly affected.

Interpreting the shifts in terms of a band offset picture can only qualitatively describe the levels of the semiconductor nanocrystal being changed when it is placed next to a metal. More sophisticated descriptions of the nanocrystal/linker/metal system may result in agreement with experimental data, and further experiments measuring the valence band offsets of nanocrystals and core/shell nanocrystals on the Si and thiol/gold substrates will help complete the data analysis.

Evidently the shifts of the energy levels are affected by both initial state effects--the electric field created from band bending to make the E_F lineup across the junction--as well as final state effects—the screening of the hole created in the photoemission process. A full set of experiments are necessary in which levels as a function of binding energy (from valence to deep core) are tracked for a variety of substrates and shell materials. From these experiments one would be able to formulate the relative contributions of initial and final state effects and thus determine the nature of the interaction of the nanocrystal with a bulk metal in its proximity.

7.7 References

- [1] W. Mönch, Surf. Sci. **299/300**, 928 (1994), and references within.
- [2] B. O. Dabbousi, M. G. Bawendi, O. Onitsuka, and M. F. Rubner, Appl. Phys. Lett. **66**, 1316 (1995).
- [3] M. C. Schlamp, X. Peng, and A. P. Alivisatos, J. Appl. Phys. **82**, 5837 (1997).
- [4] V. L. Colvin, M. C. Schlamp, and A. P. Alivisatos, Nature **370**, 354 (1994).
- [5] N. C. Greenham, X. Peng, and A. P. Alivisatos, Phys. Rev. B **54**, 17628 (1996).
- [6] D. E. Fogg, L. H. Radzilowski, B. O. Dabbousi, R. R. Schrock *et al.*, Macromolecules **30**, 8433 (1997).
- [7] M. Schlamp, 1998, Chemistry, University of California at Berkeley, Thesis.
- [8] J. R. Waldrop and R. W. Grant, Phys. Rev. Lett. **43**, 1686 (1979).
- [9] E. T. Yu, M. C. Phillips, J. O. McCaldin, and T. C. McGill, Journal of Vacuum Science Technology B **9**, 2233 (1991).
- [10] S. Narioka, H. Ishii, D. Yoshimura, M. Sei *et al.*, Appl. Phys. Lett. **13**, 1899 (1995).
- [11] M. Löglund, W. R. Salaneck, F. Meyers, J. L. Brédas *et al.*, Macromolecules **26**, 3815 (1993).
- [12] H. Ibach and H. Lüth, Solid-State Physics: An Introduction to Principles of Materials Science (Springer-Verlag, New York, 1995).
- [13] A. H. Nethercot, Phys. Rev. Lett. **33**, 1088 (1974).
- [14] L. Esaki and R. Tsu, IBM Journal of Research and Development **14**, 61 (1970).
- [15] A. P. Hitchcock, T. Tyliczszak, T. Aebi, J. Z. Xiong *et al.*, Surf. Sci. **291**, 349 (1993).
- [16] C. F. Hoener, K. A. Allan, A. J. Bard, A. Campion *et al.*, J. Phys. Chem. **96**, 3812 (1992).

- [17] M. A. Hines and P. Guyot-Sionnest, J. Phys. Chem. **100**, 468 (1996).
- [18] B. O. Dabbousi, J. Rodriguez-Viejo, F. V. Mikulec, J. R. Heine *et al.*, J. Phys. Chem. B **101**, 9463 (1997).
- [19] U. Banin, 1999, personal communication.
- [20] J. E. Bowen Katari, V. L. Colvin, and A. P. Alivisatos, J. Phys. Chem. **98**, 4109 (1994).
- [21] X. Peng, M. C. Schlamp, A. V. Kadavanich, and A. P. Alivisatos, J. Am. Chem. Soc. **119**, 7019 (1997).
- [22] Y. Park, V. Choong, Y. Gao, B. R. Hsieh *et al.*, Appl. Phys. Lett. **68**, 2699 (1996).
- [23] R. Schlaf, C. Pettenkofer, and W. Jaegerman, J. Appl. Phys. **85**, 6550 (1999).
- [24] R. S. List and W. E. Spicer, J. Vac. Sci. Tech. B **6**, 1228 (1988).
- [25] Landolt Börnstein New Series.

8 KINETIC STUDY OF THE PHOTO-OXIDATION AND THERMAL DECOMPOSITION OF CdSe NANOCRYSTALS BY X-RAY PHOTOELECTRON SPECTROSCOPY

8.1 Introduction

Colloidally synthesized nanocrystals can be dissolved in a variety of solvents and therefore can be manipulated easily and cheaply by standard wet chemical techniques. This has facilitated their incorporation into devices such as LEDs and photovoltaics [1-5]. The high surface to volume ratio for nanocrystals creates problems for processing since reactivity can increase by many orders of magnitude as the size is decreased. High surface to volume ratios are exploited by catalysis but this attribute can be problematic for the incorporation of nanocrystals into optical, electrical, and magnetic devices in which stability in ambient conditions is crucial. Therefore, understanding the reactivity of nanocrystals in light and oxygen is of practical significance. One would like to be able to know for how long nanocrystals are stable in air and light in laboratory conditions. This chapter describes experiments that use techniques that are common in studying bulk surfaces such as XPS and TPD (temperature programmed desorption) to characterize the kinetics of reactions that occur at the surface of nanocrystals. As aforementioned, the application of bulk surface spectroscopic techniques to nanocrystals is not straightforward, and as will be illustrated, special considerations must be made to account for the nanocrystal surfaces.

Size dependent reactivity has been studied extensively for small clusters in the gas phase composed of metals or noble gases in which the number of atoms in the cluster ranges from 1 to approximately 100. Non-monotonic trends of reactivity are observed due to occurrences of magic number clusters when either closed electronic shells or stable

geometrical arrangements occur. [6-8]. In light of the studies on gas phase clusters, we would like to study scaling laws for reactivity for semiconductor clusters above the size regime where magic numbers occur. This size regime has not been studied as extensively as noble gas or alkali metal clusters due to the difficulty of forming large clusters in the gas phase. The degree of precision with which one can study size dependent properties of nanometer size particles is considerably less than that of a typical gas phase experiment due to finite size distributions, and achievement of colloidal samples with monodispersity on the order of 5% is a recent accomplishment. In the nanometer size regime, the relevant parameter is the number of surface atoms, and it is expected that surfaces dominate the behavior as the size of the particle is decreased, while bulk values would be approached as the size is increased. The scaling laws governing reactivity in this size regime are expected to have monotonic trends, since magic number effects would be small perturbations. Jortner et al. predict that above a certain particle size, properties of the cluster follow smoothly with size [9]. The reaction studied here is photo-oxidation, which is relevant for understanding the stability of semiconductor particles in ambient conditions.

Studying the size dependent reactivity of semiconductor clusters brings forth complications that are not present in metal and noble gas clusters. Oxidation of binary semiconductors is often accompanied by a competing evaporation process that cannot be suppressed. In addition, evaporation of binary semiconductors often proceeds noncongruently [10]; that is, one component evaporates while the other component remains on the surface in a condensed form. For example, As_4 (g) evaporates from GaAs, leaving a layer of Ga (l) on the surface through which the As_4 (g) must diffuse through to evaporate [11] which complicates the analysis of the evaporation rates. In addition, evaporation rates have been found to be dependent on the stoichiometric ratio of the two components, and in

nanocrystals the stoichiometry is size dependent [12, 13]. Furthermore, semiconductor surfaces often reconstruct or form facets [14] in order to minimize dangling bonds; the exact shape of the particle is neither spherical nor polyhedral and therefore cannot be easily described in a simple model.

8.2 Experimental

CdSe nanocrystals with mean diameters of 28 Å, 43 Å, and 55 Å were synthesized according to literature techniques [15, 16]. In order to facilitate oxidation of the nanocrystals, the organic surfactant must be removed. Nanocrystals are synthesized with the surfactant tri-*n*-octyl phosphine oxide (TOPO) on the surface. It is important to emphasize that if particles with TOPO on the surface are exposed to oxidizing environments, the rate constants are up to 20 times smaller. Inorganically capped particles (CdS/CdSe "core-shells") [17, 18] are extremely photostable with rate constants for photo-oxidation estimated to be 3 orders of magnitude smaller. In order to observe oxidation on a reasonable timescale, the particles must be prepared in such a way that they are more vulnerable to photo-oxidation. Therefore, the surface of the nanocrystals must be bare. The nanocrystals were refluxed in dry pyridine for 2 to 3 hours at 115°C under an argon atmosphere, which removes up to 70% of the TOPO from the particle surface. The air free colloidal solutions were then immediately transferred under inert atmosphere into a nitrogen glove box. For an oxidation experiment, the nanocrystals were bound to a conducting substrate (ITO) by the organic linker 1,6 -hexanedithiol with coverage of < 1ML [12]. To drive off remnants of adsorbed pyridine, the samples were preheated for 1 hour at 180°C in the dark under nitrogen. Two samples were removed before the photo-oxidation process for the $t = 0$ measurement.

The components essential for the decomposition of semiconductor nanocrystals are oxygen and light of energy larger than the band gap of the particles. The light is necessary to create an electron-hole pair which provides holes to trap on the surface and react with oxygen. The nanocrystal/hexanedithiol/ITO samples were exposed to light and oxygen in a glass furnace oven. The amounts of oxygen and nitrogen were regulated from a tank > 95% in purity by mass flow controllers (in the range of 30-70 cm³/min), with a Xe lamp as the light source ($\lambda = 200\text{nm} - 1100\text{nm}$). Samples were removed at 10 time intervals over a period of three hours.

Because ITO is optically clear as well as metallic, it allows for measurement of both the optical spectrum and the photoelectron spectrum. Optical absorption was performed on an HP845X UV-visible diode-array spectrometer to determine the size and size distribution as a function of oxidation time. The nanocrystal monolayers on the ITO still exhibited a measurable absorption peak, though the signal was in general low and noisy.

The chemical state information was obtained by x-ray photoelectron spectroscopy (XPS) on in the spectrometer described in Chapter 3. Spectra were taken with the Mg K α (1253.6 eV) anode and the pass energy was set to 23.50eV. The Se:Cd ratio was found to vary for a given sample depending on the position, so for adequate statistics multiple scans were taken on a given sample. Figure 1 shows the Se 3d:Cd 3d peak area ratio for a single sample measured in different areas. The points marked by arrows indicate measuring the same spot on the sample. A standard deviation of 0.07 is observed. Therefore, three Cd 3d and Se 3d core level scans were measured and averaged for each sample. The scans were taken non-consecutively to improve statistics by avoiding measurement of the same sample spot. For each oxidation experiment a total of 60 scans were taken, with 6 data points for each time interval. Peaks were fit using a commercial fitting program (Peakfit, Jandel

Scientific) using Voigt lineshapes which are appropriate for x-ray lineshapes convoluted with a core level. The method used to prepare the data before fitting (sectioning, baseline subtracting, smoothing) was consistent throughout all the data sets. The background subtracted was linear, and the smoothing parameters used were from a Savistky-Golay algorithm.

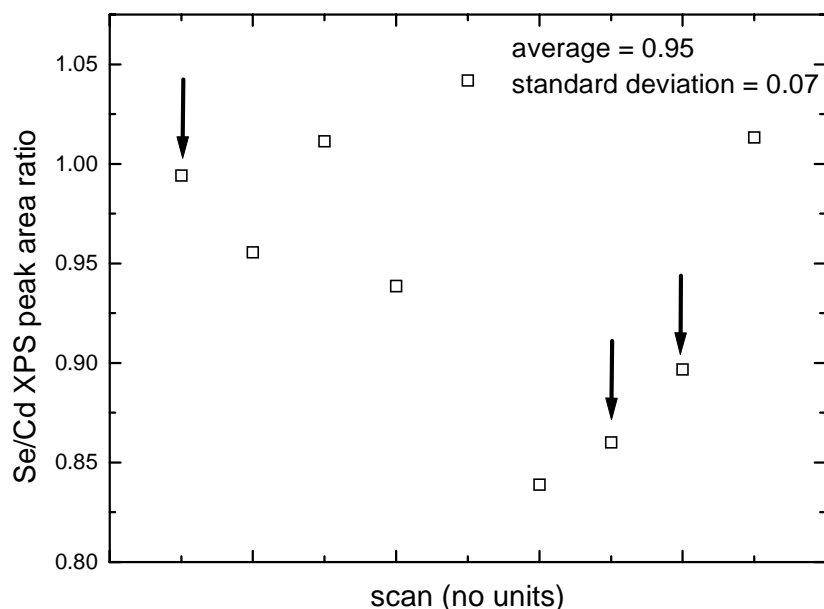


Figure 8-1 Raw Se:Cd XPS peak ratios for a single CdSe/dithiol/ITO sample taken in different areas. The arrows indicate the same spot on the sample.

Separate temperature-programmed desorption (TPD) experiments were implemented to measure the products of evaporation from pre-oxidized nanocrystals. Nanocrystal samples were prepared from pyridine or distilled 4-ethyl pyridine solutions and deposited onto Ta substrates (which are stable in the temperature range of the TPD experiments) without the use of hexanedithiol, which would complicate the mass spectrum considerably. Samples were pre-oxidized by heating at 80°C in air and under light for ~2 hours. The presence of oxidized Se was confirmed by XPS measurements at room temperature. The samples were brought into a separate chamber with a base pressure of

1×10^{-8} torr for temperature programmed desorption (TPD). Cooling was achieved by thermal contact with a liquid nitrogen dewar in the chamber, and electron bombardment on the back of the sample face was utilized to heat the samples. Temperature was read from a thermocouple junction spot welded to the sample face. The sample must be electrically isolated from the manipulator because temperature is read from the voltage drop across the thermocouple junction. Therefore, a special sample platen with ceramic spacers was used. For accurate values of temperature, the sample clips were made of chromel/alumel, which matched the materials in the thermocouple (type K). The sample temperature was ramped at a constant rate of 0.3, 1.0, or $1.7^{\circ}\text{C}/\text{sec}$ in the range of -50°C to 350°C through a feedback loop written to control the current through the filament on the sample manipulator. The evaporated products Se (g) (80 amu), Cd (g) (116 amu), and SeO_2 (g) (112amu) were monitored by a quadrupole mass spectrometer as a function of sample temperature (Stanford Research Systems). Temperature ramping rate was simultaneously monitored in every scan to confirm that it was linear. In order to prevent measuring the gases desorbing from the walls of the chamber in the vicinity of the RGA head, the cage around the RGA filament was wrapped with foil and the sample was placed as close as possible to the RGA head ($<0.5\text{in}$).

8.3 Results and Discussion

Figures 2a. and 2b. show a series of Se 3d peaks and Cd 3d photoemission peaks as a function of oxidation time. The peak areas are scaled to the Cd 3d areas. The scan in 0h is an unoxidized sample. The Se peak at longer oxidation times shows a chemical shift indicative of an oxidized form of SeO_2 (the peak at 59eV). [19] In addition, the area of the Se peak at 54eV decreases. The Cd peak shows no change with oxidation time.

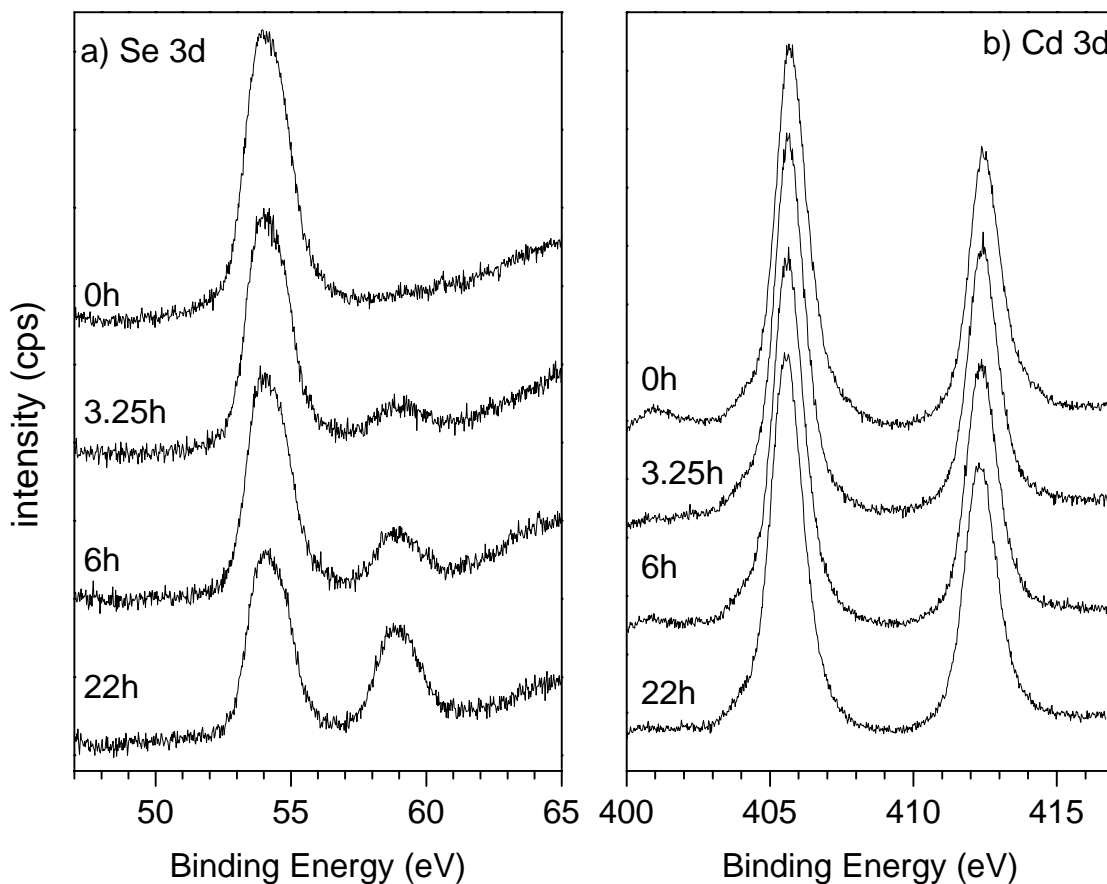


Figure 8-2 Se 3d and Cd 3d peaks in the photoelectron spectra of CdSe nanocrystals as a function of oxidation time. The Se peaks areas are normalized to the Cd 3d 3/2 peak areas. (a) is the unoxidized sample, (d) is the most oxidized sample. The Cd peaks show no dependence on oxidation time. The Se feature at 54 eV corresponds to Se bound to Cd, where the feature at 59 eV corresponds to an oxidized form of Se.

In Figure 3 the areas of the Se peaks normalized to the Cd peak areas are plotted as a function of oxidation time. The oxide peak at 59 eV (filled squares) increases from 0 at $t = 0$ h (see lower spectrum), while the Se peak at 55 eV (filled circles) decreases from its initial value. If the sum of the Se and Se oxide peaks are plotted (empty triangles) it is evident that a certain amount of Se is not accountable for in the XPS spectra. This can be attributed to

the evaporation of Se in the form of SeO_2 or Se_2 [20-22]. The amount of Se in the vapor form has been deduced from the difference of the total amount from its initial value (filled triangles).

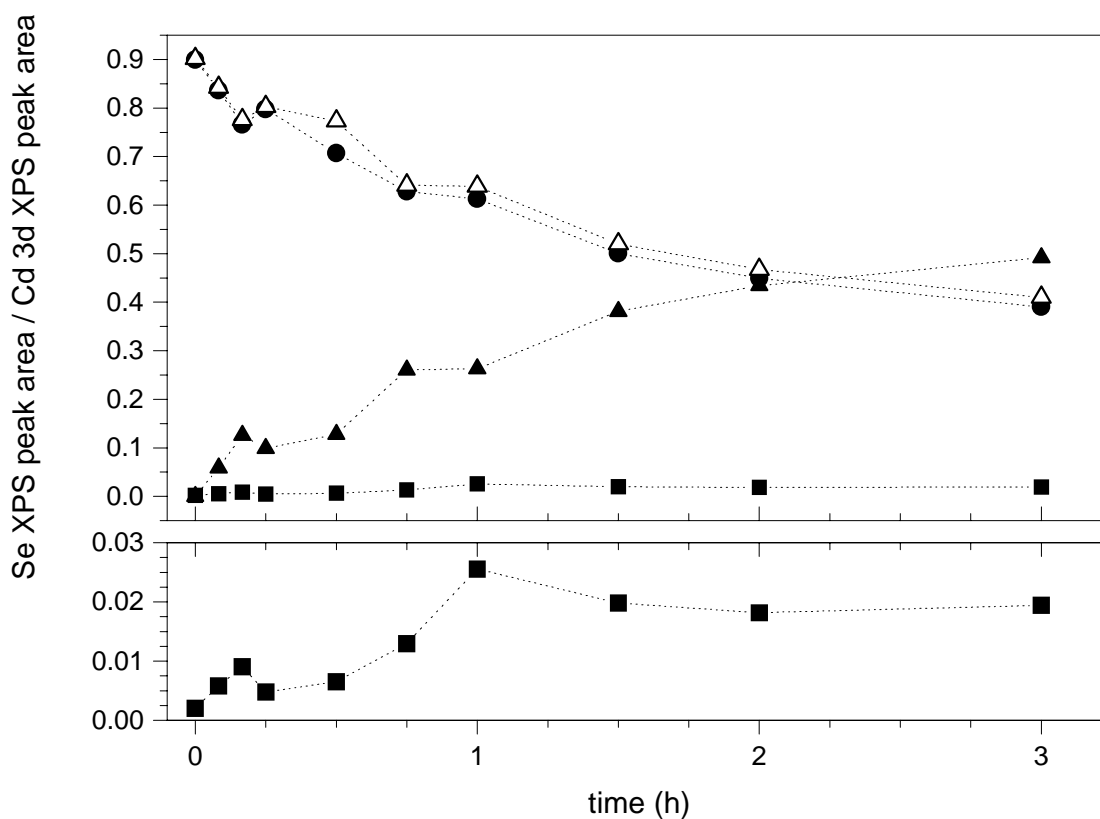


Figure 8-3 Se 3d (circles), oxide (squares) and total (empty triangles) peak areas normalized to Cd 3d areas as a function of oxidation time. The lower spectrum is a close-up of the Se oxide time trace. The evaporated amount of Se (filled triangles) is determined from the total amount of Se lost.

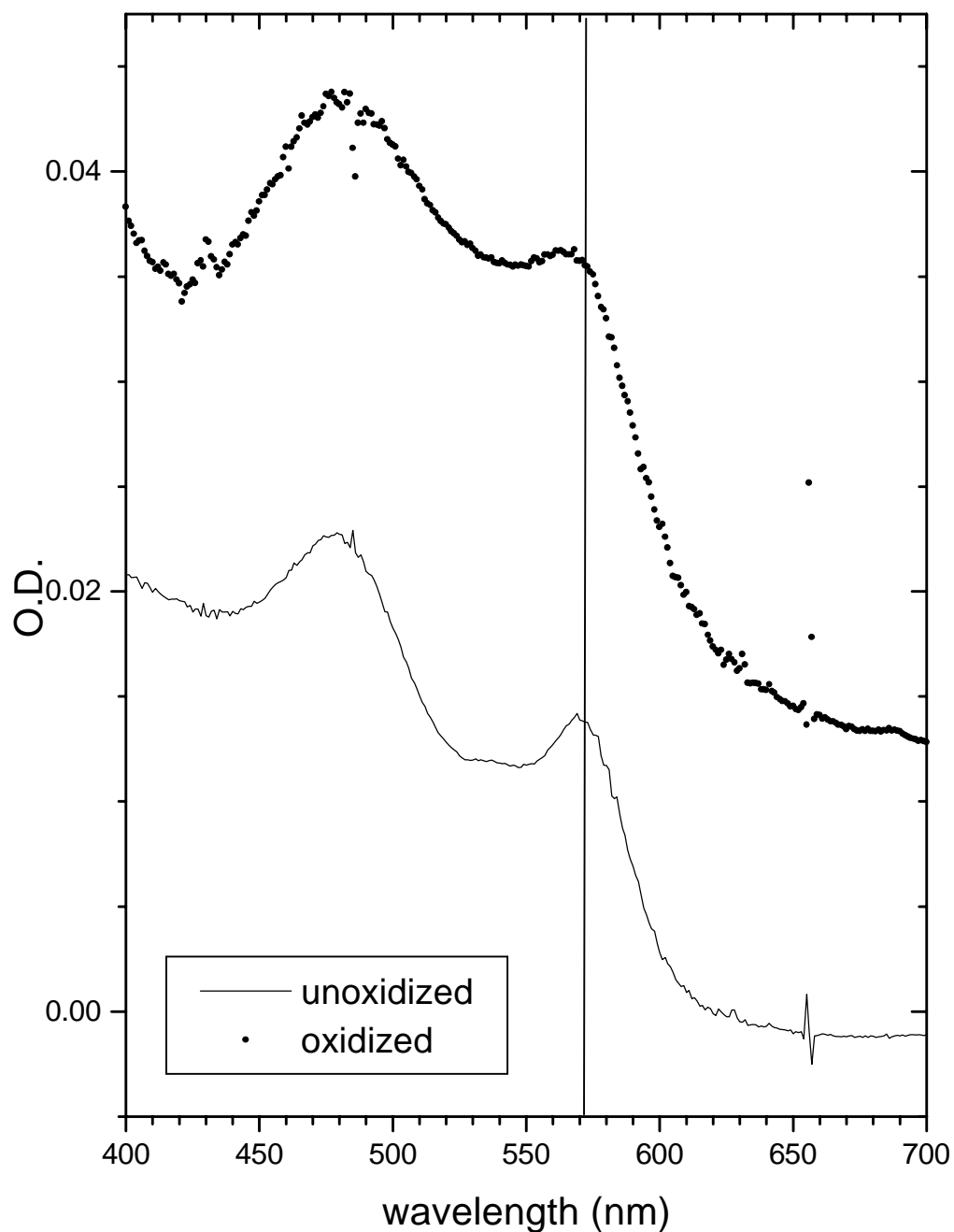


Figure 8-4 Optical absorption of unoxidized (line) and oxidized (dots) CdSe nanocrystals deposited onto dithiol/ITO slides. The main absorption feature at 570nm shifts to higher energy (15nm) and broadens slightly for the oxidized sample.

From UV-visible absorption spectroscopy one can determine the size of the unreacted CdSe in the particles. The spectra for two samples, before and after oxidation, are

shown in Figure 4. As the particles are oxidized, the absorption peak retains its spectral features but shifts to higher energy and broadens slightly. The fact that the absorption feature retains its quality indicates that the particles still contain a crystalline CdSe domain upon oxidation. Figure 5 shows the peak maximum (left axis) and inferred nanocrystal diameter in Å (right axis) from the absorption spectra for a single sample of particles 37 Å in diameter. The total decrease in diameter is ~ 4 Å, corresponding to approximately one atomic layer on the surface. Thus in the time interval for the oxidation experiment, the nanocrystals oxidize only on the surface. This result confirms a model obtained in earlier experiments [12, 13]. In order to analyze properly the oxidation data for rate constants, the intensity of the XPS signal must be corrected for the surface. The percentage of the XPS signal that is due to the interior of the particle is determined using an attenuation calculation [12, 23] and subtracted from the Se 3d curve. Figure 6 shows the data corrected in this manner (circles, Se 3d; squares, oxidized Se; evaporated Se, triangles).

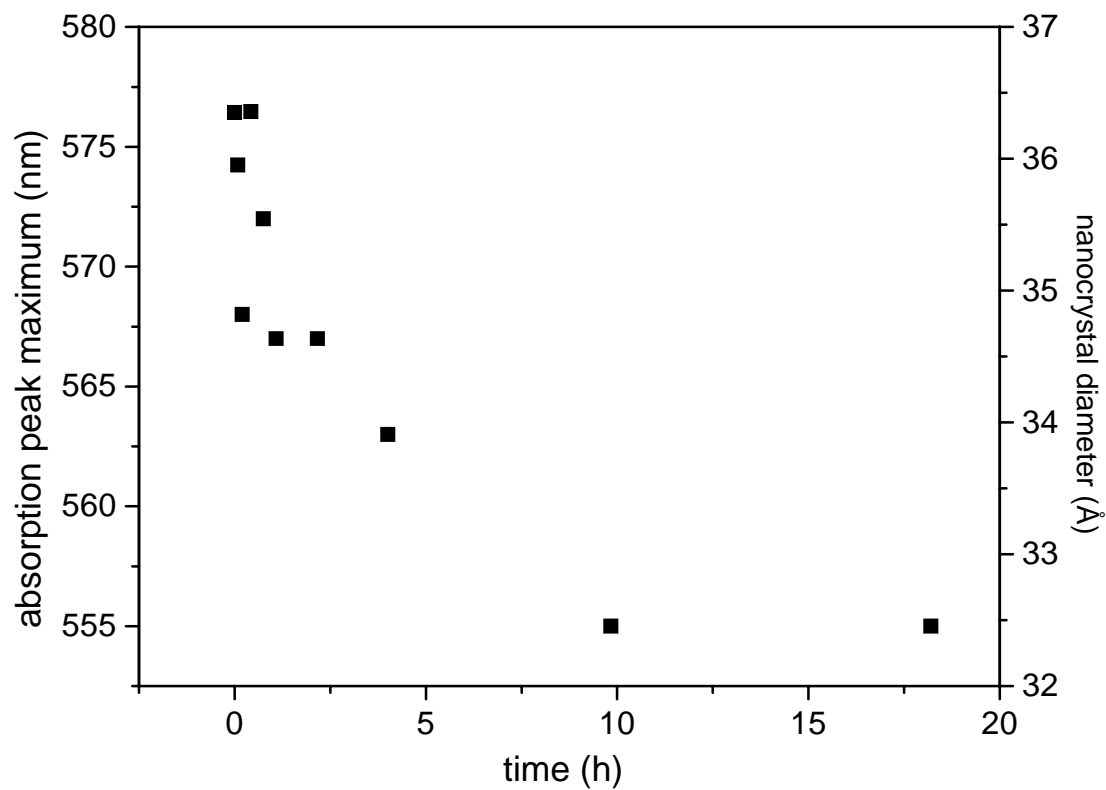


Figure 8-5 UV/visible absorption peak maximum (left axis) as a function of oxidation time. The mean diameter of the nanocrystal that is inferred from the absorption peak is also indicated (right axis). This is an indication that the CdSe domain is getting smaller upon oxidation due to the formation of an oxide layer on the surface.

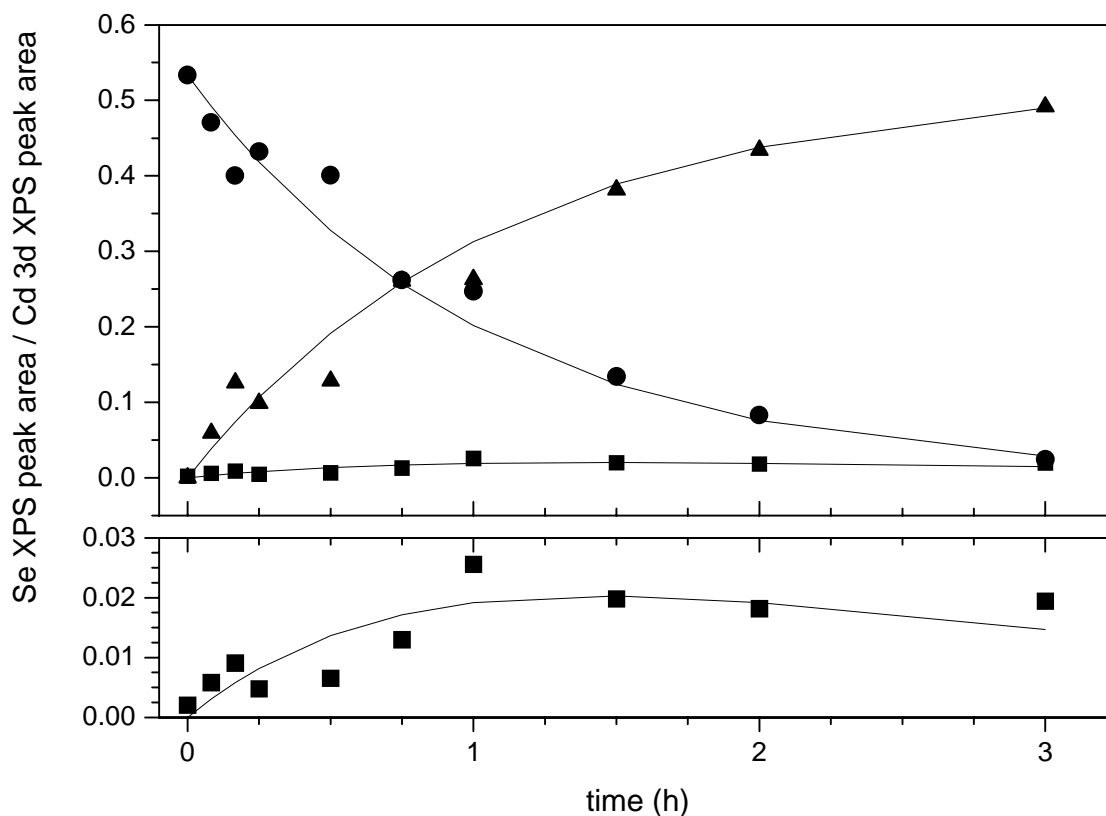
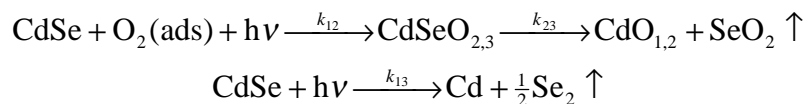


Figure 8-6 Se 3d peak areas (circles) corrected for the amount of Se on the surface of the nanocrystal. The dotted lines are fits assuming the set of rate equations described in the text. The lower spectrum is a close-up of the Se oxide time trace and its fit.

8.3.1 Model

The functional form for the time trace can be fit if one assumes the set of reactions



XPS measurements of oxidized CdSe (0001) [24] have shown that the stoichiometry of the oxidized form of CdSe is $\text{CdSeO}_{2,3}$. Earlier EELS measurements [20, 21] deduce the formation of SeO_2 from $\text{CdSeO}_{2,3}$ vapor, due to its high vapor pressure (2×10^{-10} torr at room temperature) and low heat of formation of (-225 kJ/mol).

The kinetics of vaporization of bulk CdSe surfaces has been previously studied [10]. The evolution of Cd (g) and Se₂ (g) was observed. The rate limiting step in the evaporation process was determined to be a charge transfer process in which the atoms on the surface are converted to their neutral states before desorption.

These reactions were confirmed in the nanocrystals. CdSe particles without the presence of light or oxygen at high temperatures do not oxidize to form CdSeO_{2,3}. The assistance of oxygen in the k₂₃ reaction was ruled out by oxidizing nanocrystals to form a detectable amount of CdSeO_{2,3}, and then changing the atmosphere in the flow tube to 100% N₂ in the presence of light. The amount of CdSeO_{2,3} was then measured by XPS and determined to have decreased due to the formation of SeO₂ (g). The loss of SeO₂ without the assistance of O₂ (g) or light was also confirmed by the TPD measurements, which were performed in a vacuum chamber. The possibility of the k₁₃ reaction was determined by heating the nanocrystals in 100% O₂ in the dark. No CdSeO_{2,3} peak was detectable in XPS but the amount of Se in the CdSe form decreased. This can be attributed to the formation of Se₂ (g). Separate mass spectroscopic experiments confirmed the formation of Se (g), Se₂ (g), and SeO₂ (g), and Cd (g).

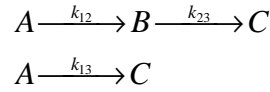
The rates of formation of CdSe, CdSeO_{2,3}, and Se in the evaporated form can be written as

$$\begin{aligned}\frac{d\text{CdSe}}{dt} &= -k'_{12}[\text{CdSe}] - k'_{13}[\text{CdSe}] \\ \frac{d\text{CdSeO}_{2,3}}{dt} &= k'_{12}[\text{CdSe}] - k_{23}[\text{CdSeO}_{2,3}] \\ \frac{d(\text{SeO}_2 + \text{Se}_2)}{dt} &= k_{13}[\text{CdSe}] + k_{23}[\text{CdSeO}_{2,3}]\end{aligned}$$

in which the reactions are first order. The k' indicates that the oxygen and/or light dependence are folded into the rate constant. The solutions for this set of differential

equations can be obtained in a straightforward manner using an eigenvalue equation [25].

For the set of reactions:



the functional forms for the rates of A, B, C are

$$\begin{aligned} A(t) &= A_0 \exp(-(k_{12} + k_{13})t) \\ B(t) &= A_0 \left(\frac{k_{12}}{(k_{23} - k_{12} - k_{13})} \exp(-(k_{12} + k_{13})t) - \frac{k_{12}}{(k_{23} - k_{12} - k_{13})} \exp(-k_{23}t) \right) \\ C(t) &= A_0 \left(\frac{-(k_{23} - k_{12})}{(k_{23} - k_{12} - k_{13})} \exp(-(k_{12} + k_{13})t) + \frac{k_{12}}{(k_{23} - k_{12} - k_{13})} \exp(-k_{23}t) + 1 \right) \end{aligned}$$

The time traces were then fit to these functional forms, yielding values for the rate constants. In fitting the rate data to these equations, we are assuming that the reactions at the surface are not hindered due to diffusion of the atoms through the surface layers. We do not take into account incongruent evaporation explicitly, which may not affect the rate constants due to the finite size of the particles. The values for k_{12} and k_{13} were obtained in this manner, but due to experimental scatter it was not possible to accurately obtain the k_{23} rate constants by fitting the data. These parameters are determined separately in the TPD experiments. Figure 6 shows the fits to the corrected data (lines). The inset shows a close-up of the Se oxide data and its fit. Due to the fact that XPS cannot detect the evaporated products, the evaporated Se is a sum of Se_2 (g) and SeO_2 (g). Activation energies (E_a) for each of the reactions can be extracted via the Arrhenius equation. Plotting $\ln k$ versus $1/T$ yields a straight line with a slope of the activation energy. A sample plot of k_{13} for a 28Å diameter nanocrystal and its linear fit is shown in Figure 7.

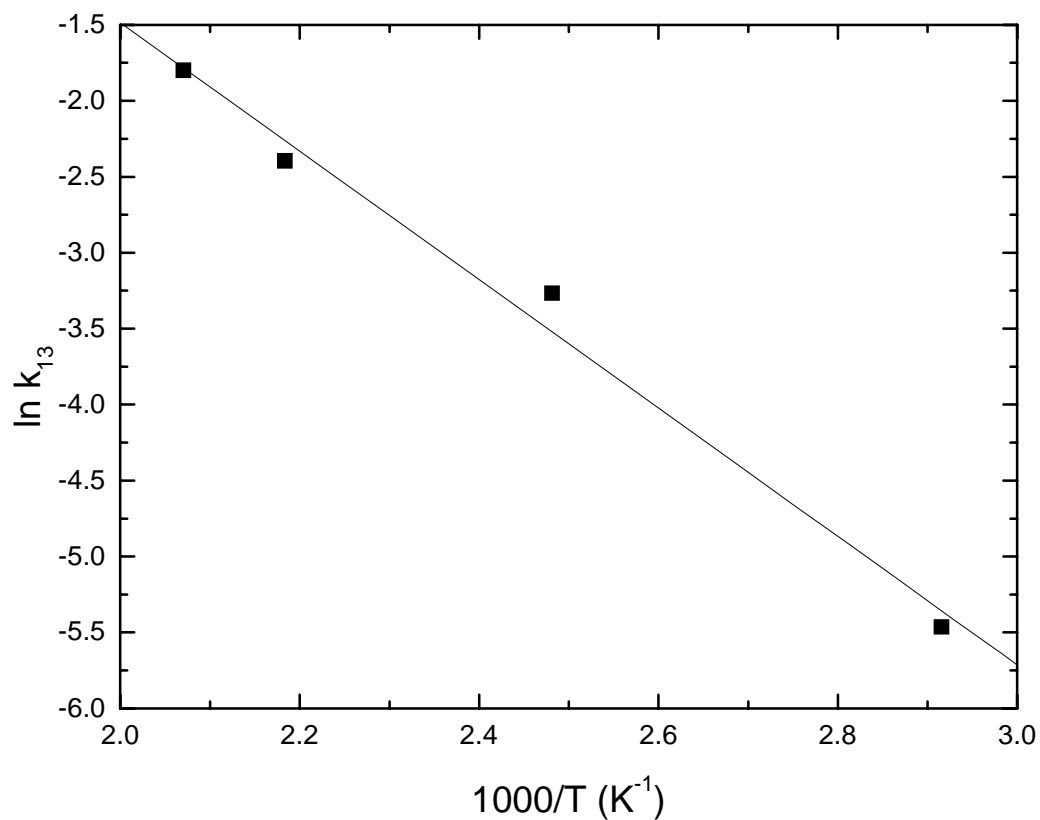


Figure 8-7 Arrhenius plot for k_{13} for a 28Å diameter nanocrystal. A fit to a straight line is included.

8.3.2 Determination of the rate law

The form of the rate law was determined from the dependence of the rate constants on the concentration of oxygen or intensity of light. For example, plotting $\ln k'$ vs. \ln (light intensity) yields the order of the reaction with respect to light. The order for oxygen in the k_{12} reaction was determined to be 0.27 ± 0.05 and found to be negligible (~ 0.04) in the k_{13} reaction, confirming that the k_{13} reaction proceeds without the assistance of O_2 . The order for the k_{12} reaction was determined to be 0.37 ± 0.11 and for the k_{13} reaction 0.27 ± 0.01 .

8.3.3 Interpretation of activation energies

Figure 8 is a plot of the activation energy as a function of nanocrystal diameter for the k_{12} (circles) and k_{13} (squares) reactions. The activation energy for the formation of $\text{CdSeO}_{2.3}$ decreases from 24 kJ/mol to 3 kJ/mol with decreasing diameter. The size dependence of the activation energy can be explained in terms of surface to volume ratio. The general trend can be interpreted simply as a result of surface curvature. Higher surface curvature results in a greater number of lower coordination sites and consequently activation energy for oxidation is expected to be lower. The activation energy varies roughly as $1/R$, as expected for a simple model dependent upon surface to volume ratios (Figure 9).

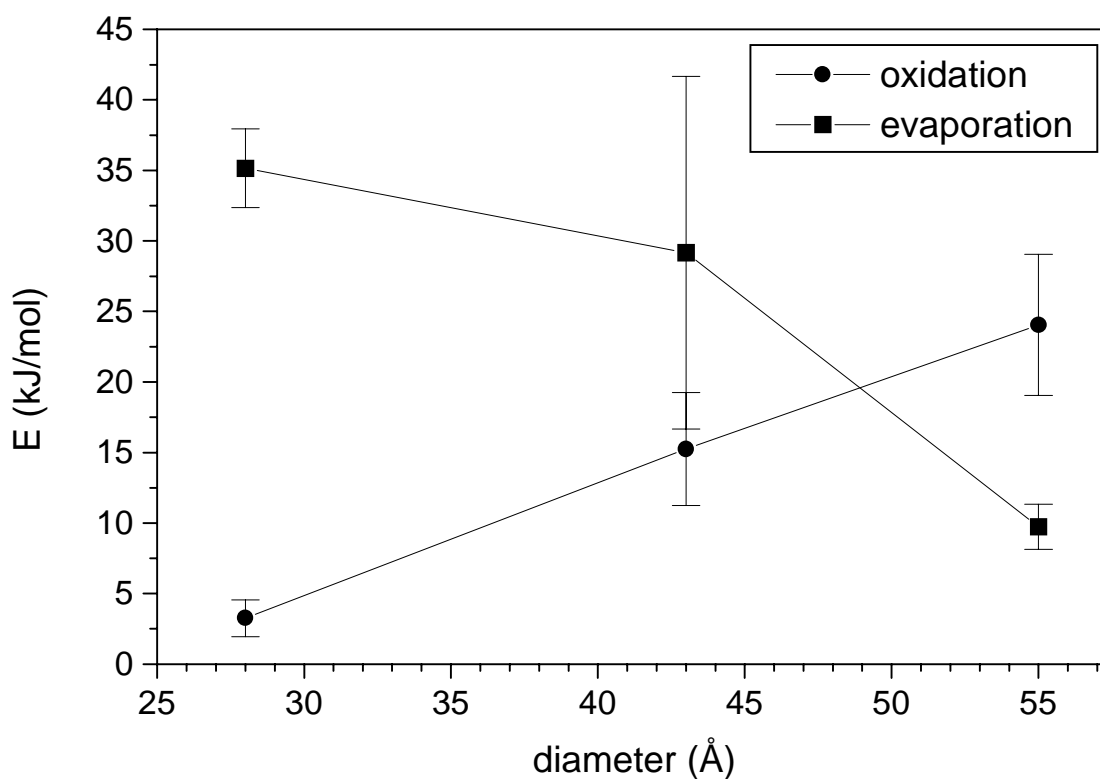


Figure 8-8 Activation energies (kJ/mol) for the oxidation (k_{12} , circles) and evaporation (k_{13} , squares) reactions vs. the nanocrystal diameter (Å).

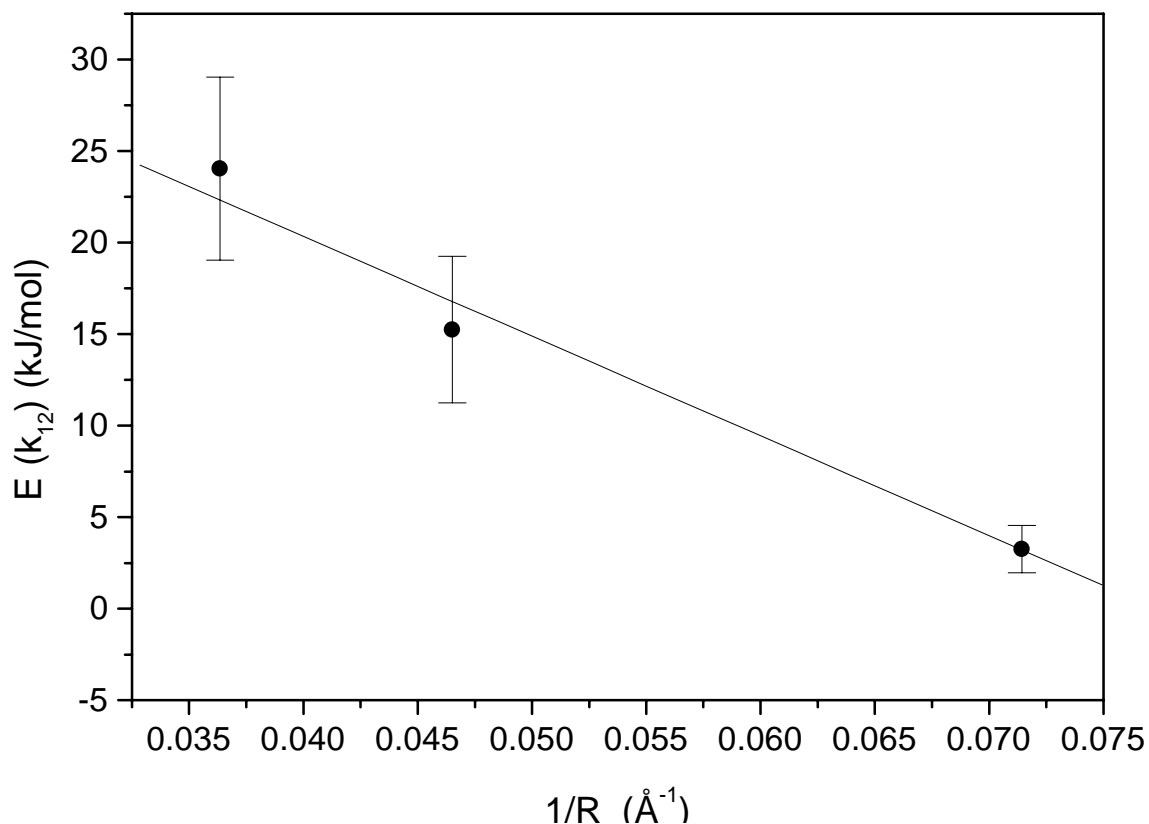


Figure 8-9 Activation energy for the oxidation (k_{12}) reaction as a function of $1/\text{radius}$. The fit to a straight line is also shown.

In addition, previous studies utilizing resistivity measurements of oxidation on polycrystalline CdSe films have shown that a greater change in resistivity (corresponding to more oxidation) results from the oxidation of films with an excess of Cd [26]. The Se:Cd ratios in the nanocrystals can be determined by accounting for the attenuation of the photoelectron intensity [12]. The atomic ratios of Se:Cd for three sizes of unreacted nanocrystals is shown in Table 1. Due to surface stabilization by the electron-donating ligand TOPO in synthesis, there is an excess of surface Cd in all of the nanocrystal samples. The stoichiometry approaches the value of 1 as the size is increased. Therefore, in terms of stoichiometry, the trend in the activation energies obtained for the k_{13} reaction agrees with those obtained for bulk CdSe films.

Table 8-1 Atomic Se:Cd ratio for three sizes of unoxidized nanocrystals obtained from XPS intensities.

| Diameter (Å) | Atomic Cd:Se ratio |
|--------------|--------------------|
| 28 | 1.26 |
| 43 | 1.04 |
| 55 | 1.02 |

In addition to oxidation, two evaporation processes occur: the evaporation of Se_2 from CdSe and the evaporation of SeO_2 from $\text{CdSeO}_{2,3}$. The activation energy for the evaporation of Se_2 from $\text{CdSeO}_{2,3}$ increases from 9.7 kJ/mol to 35 kJ/mol as the size of the nanocrystal is decreased (Figure 8). These values are considerably lower than that for the evaporation of Se_2 from bulk CdSe (0001), 234 kJ/mol [10]. The size dependence of the activation energy can be interpreted in terms of stoichiometry. It has been observed in the bulk measurement that excess Cd on the surface of bulk CdSe crystals decreases the evaporation rate, implying a higher activation energy. The decreasing atomic Se:Cd ratios as a function of decreasing nanocrystal size (Table 1) confirm the trend in the activation energy for the evaporation of Se_2 .

8.3.4 Interpretation of Arrhenius parameters

Arrhenius parameters, A , are also obtainable from the from the Arrhenius plots. The Arrhenius parameter for the oxidation reaction is shown in Figure 10, the evaporation reaction in Figure 11. The A parameter shows a strong size dependence, changing from nearly 0 to 60 mW for the oxidation reaction (k_{12}) and decreasing over three orders of magnitude (from ~ 1000 to nearly 0) for the evaporation reaction (k_{13}). However, the

Arrhenius parameter is obtained from a \ln function, and the uncertainty in the Arrhenius plots is magnified by the \ln dependence.

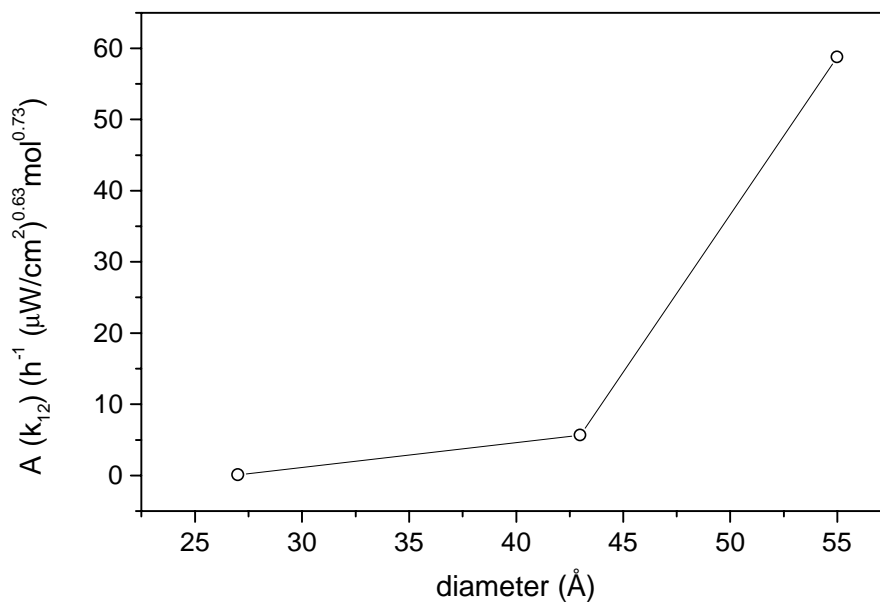


Figure 8-10 Arrhenius parameter for the k_{12} reaction as a function of nanocrystal size.

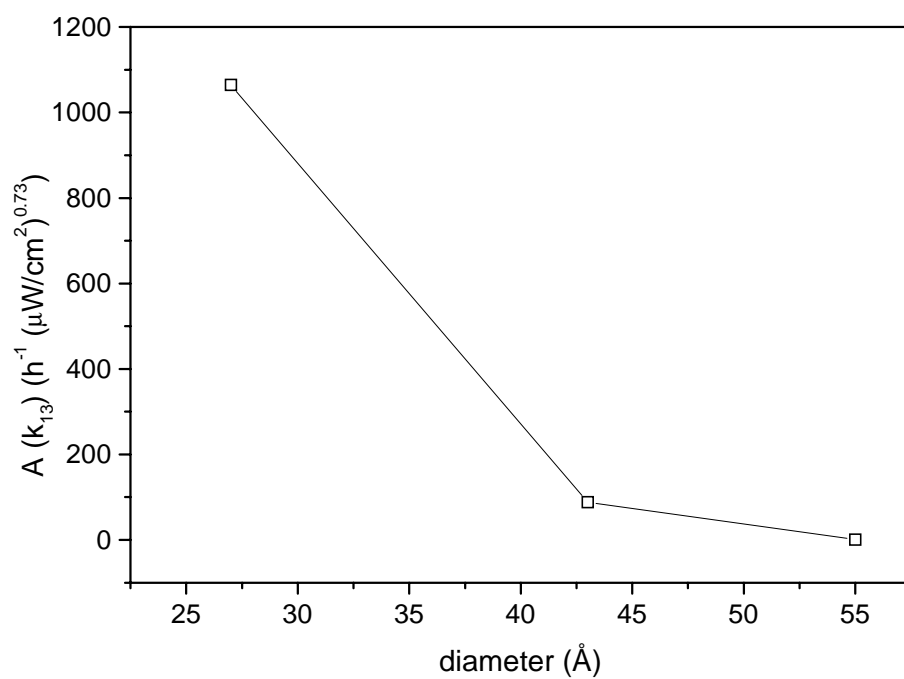


Figure 8-11 Arrhenius parameter for the k_{13} reaction as a function of nanocrystal size.

8.3.5 TPD

The evaporation of SeO_2 from oxidized CdSe particles is independent of stoichiometry and thus can be evaluated to study size dependent properties. In order to obtain the kinetic parameters of the k_{23} reaction separately from the k_{13} reaction, the evaporation of SeO_2 from the particles was measured by thermal desorption spectroscopy. As aforementioned, the evaporation of SeO_2 from oxidized CdSe particles is independent of Cd:Se ratios, and hence a scaling law for this process would not be complicated by the change in stoichiometry of the nanocrystals as a function of size.

The advantage of TPD is that the activation energy and Arrhenius parameters can be determined from a reaction without having to do a series of reactions at different temperatures. The temperature is ramped, and peaks in the pressure of a given mass occur at a certain temperature depending on its activation energy. The dependence of E and A on the ramping rate is

$$\frac{E}{RT_p^2} = \frac{A}{\beta} \exp\left(-\frac{E}{RT_p^2}\right)$$

where E is activation energy, A is Arrhenius parameter, T_p is temperature of TPD maximum, and β is ramping rate of the temperature in $^\circ\text{C} / \text{sec}$. The desorption is run at least twice with different ramping rates, β_1 and β_2 , which results in a temperature maximum at T_1 and T_2 , respectively. From two equations and two sets of unknowns one can then solve for E and A:

$$E = \frac{RT_1T_2}{(T_1 - T_2)} \ln\left(\frac{T_2^2 \beta_1}{T_1^2 \beta_2}\right)$$

in units of R's units (J/mol K). For Arrhenius parameter

$$A = \frac{T_2}{T_1} \frac{\beta_1}{(T_1 - T_2)} \ln M \left(M^{\frac{N}{R\eta_1}} \right)$$

A is in units of β ($^{\circ}\text{C}$ or K/sec). Note that since A again has a power dependence on T_1 , its calculated value has a much larger uncertainty than E.

In a TPD experiment the partial pressure of SeO_2 is plotted as a function of temperature. Identification of the mass peaks was achieved by measuring the standards of SeO_2 (powder). Oxidation of the Se was confirmed by XPS. The static mass spectrum of pure SeO_2 and oxidized bulk CdSe is shown in Figures 12 and 13. The peak at 112 amu is the SeO_2 peak monitored in the TPD experiments. Cd also has a peak at 112 amu; another Cd peak was monitored (which is not coincident with SeO_2 or Se) and showed no temperature dependence. Thus, any temperature dependence was attributed to the SeO_2 desorption.

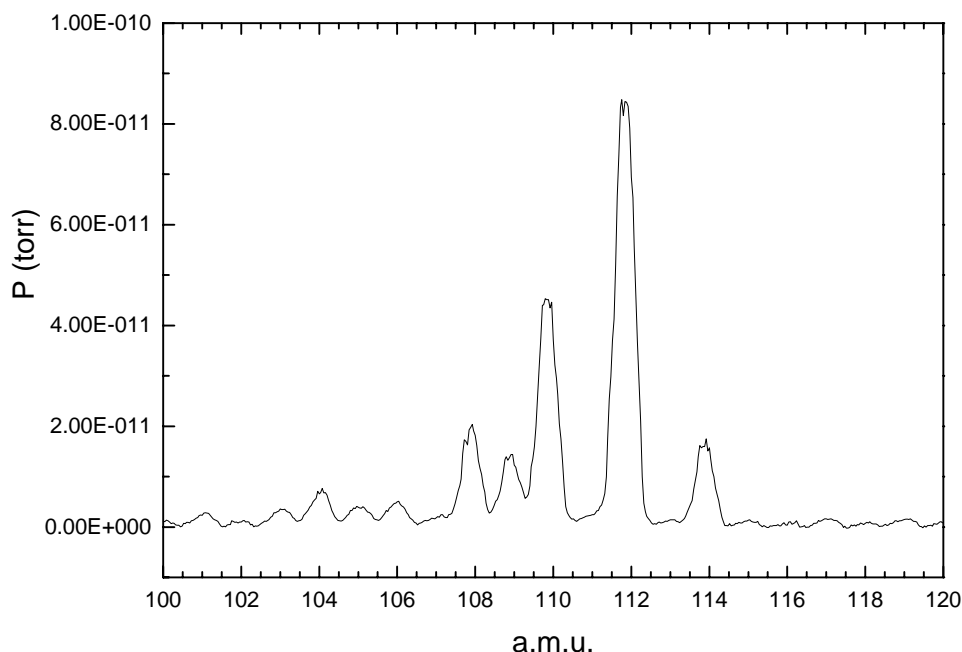


Figure 8-12 Static mass spectrum of SeO_2 . The peak at 112 amu is the one monitored in the TPD experiments as a function of temperature.

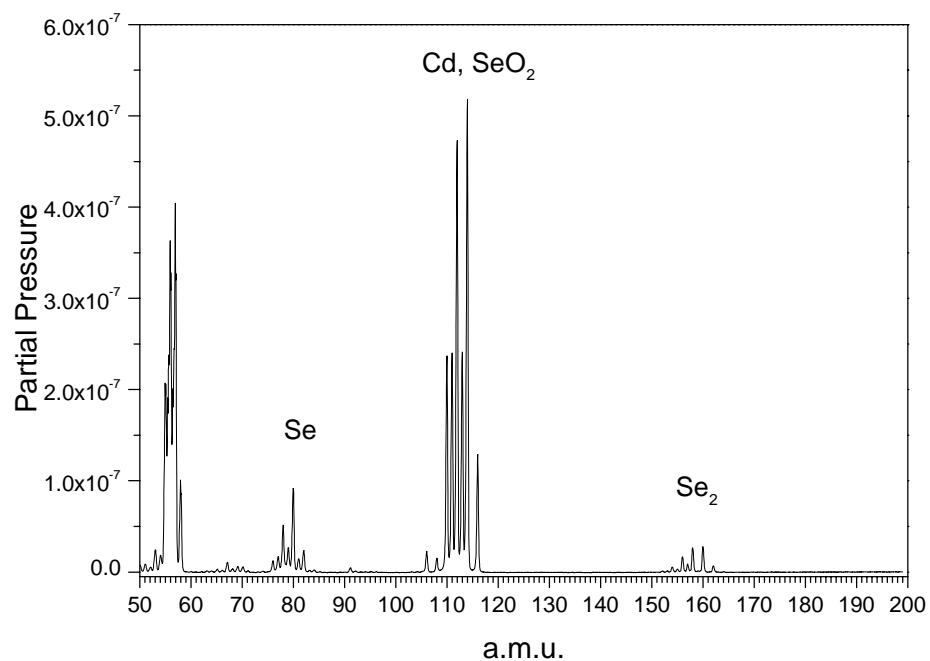


Figure 8-13 Static mass spectrum of oxidized bulk CdSe at 600°C. The peaks from 109-118 are a convolution of SeO₂ and Cd peaks. However, the peak at 112 is a dominant SeO₂ peak.

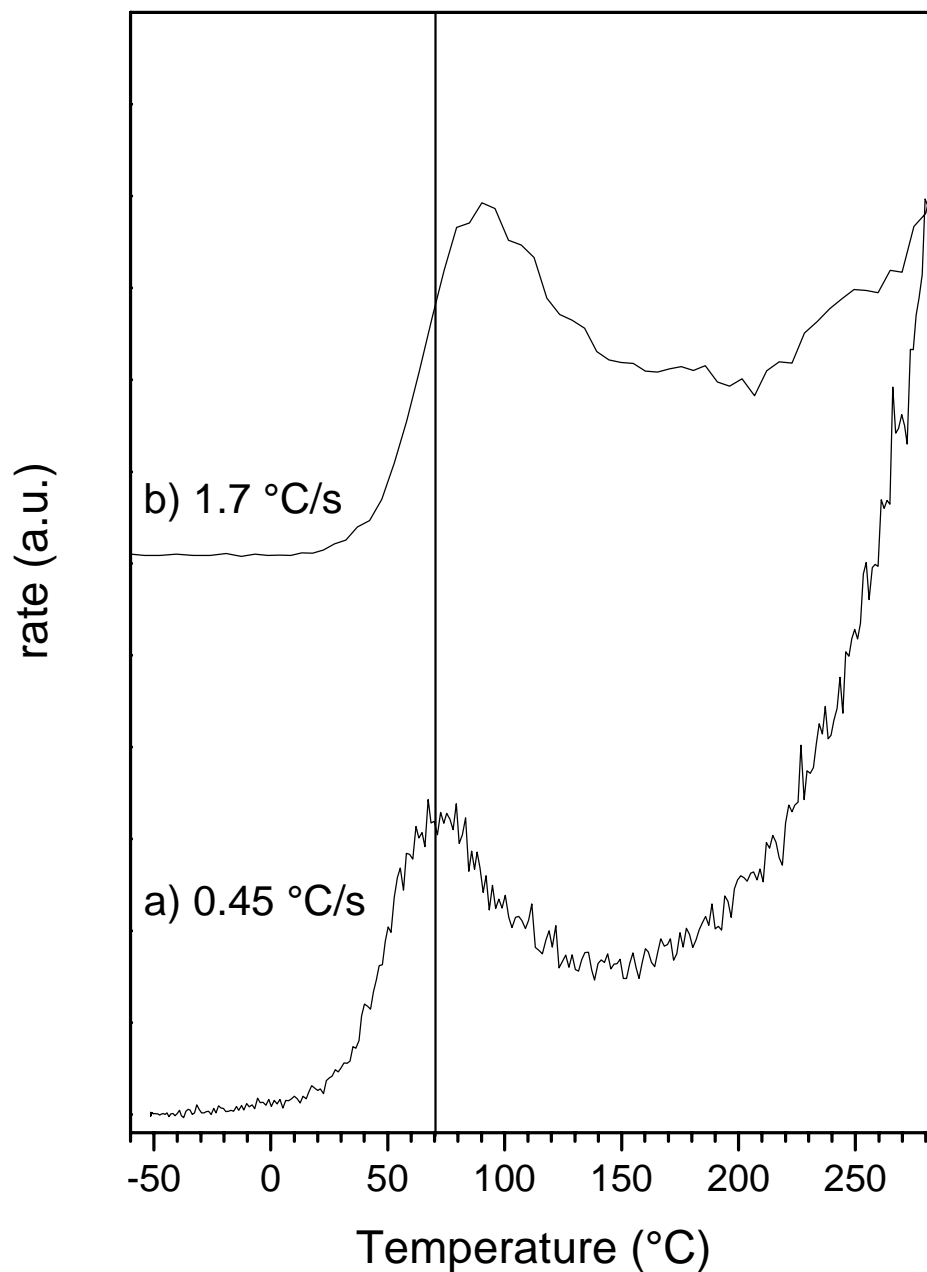


Figure 8-14 Sample TPD spectra for the desorption of SeO_2 (mass detected = 112 amu) from a nanocrystal 35\AA in diameter. (a) temperature ramping rate of 0.45°C/sec (b) rate of 1.7°C/sec .

The TPD spectra, Figure 14, shows a peak due to the desorption of SeO_2 in the 70-130°C range, the position depending on the temperature ramping rate and amount of SeO_2 in the sample. From the peak shape and position, the activation energy and Arrhenius pre-

exponential for the k_{23} reaction can be determined [27, 28]. The activation energy of desorption can be calculated from TPD spectra by several methods. The best results were achieved by utilizing the form of the equation as

$$\frac{d[\text{SeO}_2]}{dt} = A[\text{SeO}_2]^x \exp(-E/RT)$$

or

$$\ln\left(\frac{d[\text{SeO}_2]}{dt}\right) = \ln A + x \ln[\text{SeO}_2] - \frac{E}{RT}$$

where A is the Arrhenius pre-exponential for the desorption reaction, E is the activation energy of desorption, and x the order of the reaction. If a plot of $\ln(d\text{SeO}_2/dt)$ vs. $1/T$ is constructed for the first rise of the desorption peak, the slope of the line yields the activation energy. An example of this plot is shown in Figure 15.

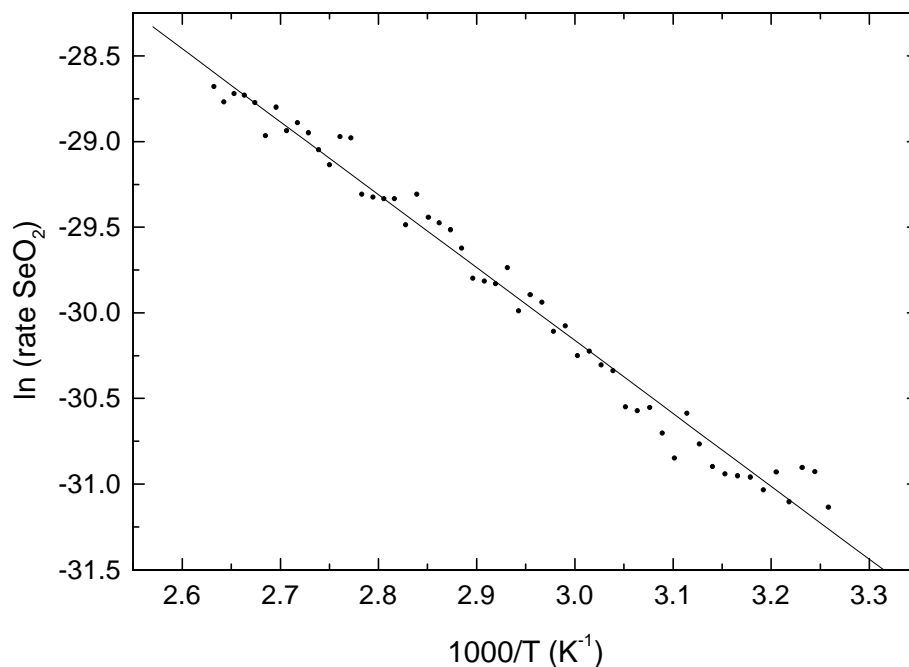


Figure 8-15 Plot of $\ln d(\text{SeO}_2)/dt$ vs. $1/T \text{ (K}^{-1}\text{)}$ for a TPD run of 55Å diameter particles for temperature ramping rate of 0.4°C/sec. The plot shows a fit to a straight line, the slope of which is the activation energy.

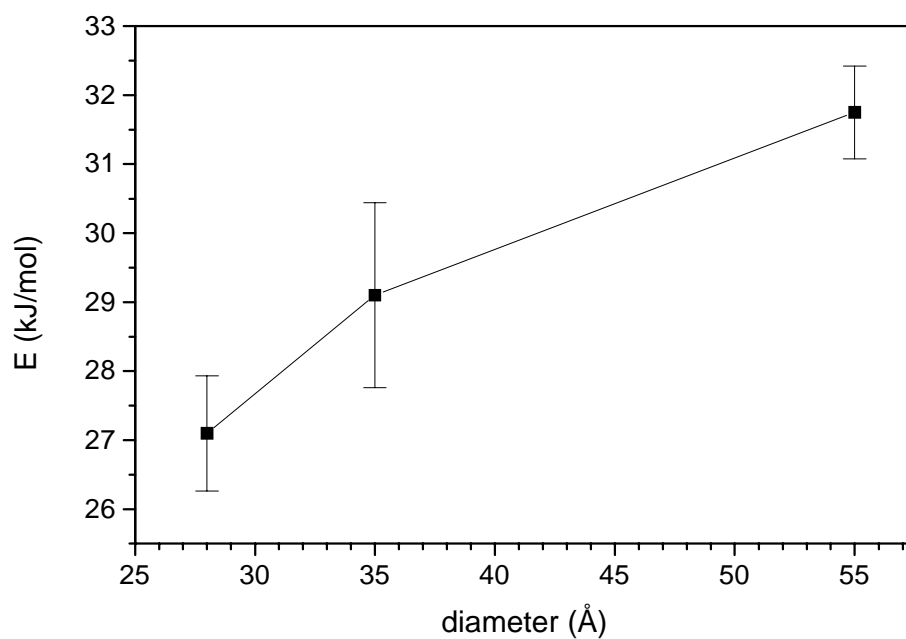


Figure 8-16 Activation energy for the k_{23} reaction vs. nanocrystal diameter determined by TPD.

The values obtained for the activation energy for three sizes of nanocrystals are plotted in Figure 16. The values of the activation energy show a trend towards lower values as the size of the nanocrystal is decreased. The size trend can be fit to a $1/R$ dependence (Figure 17), which describes the surface to volume ratio for a sphere. The plot also includes a fit to a straight line. Again, this can be explained by the larger number of surface sites that have lower coordination numbers than the sites on the interior of the crystal. Arrhenius parameters could not be reasonably determined within the resolution of the experiment.

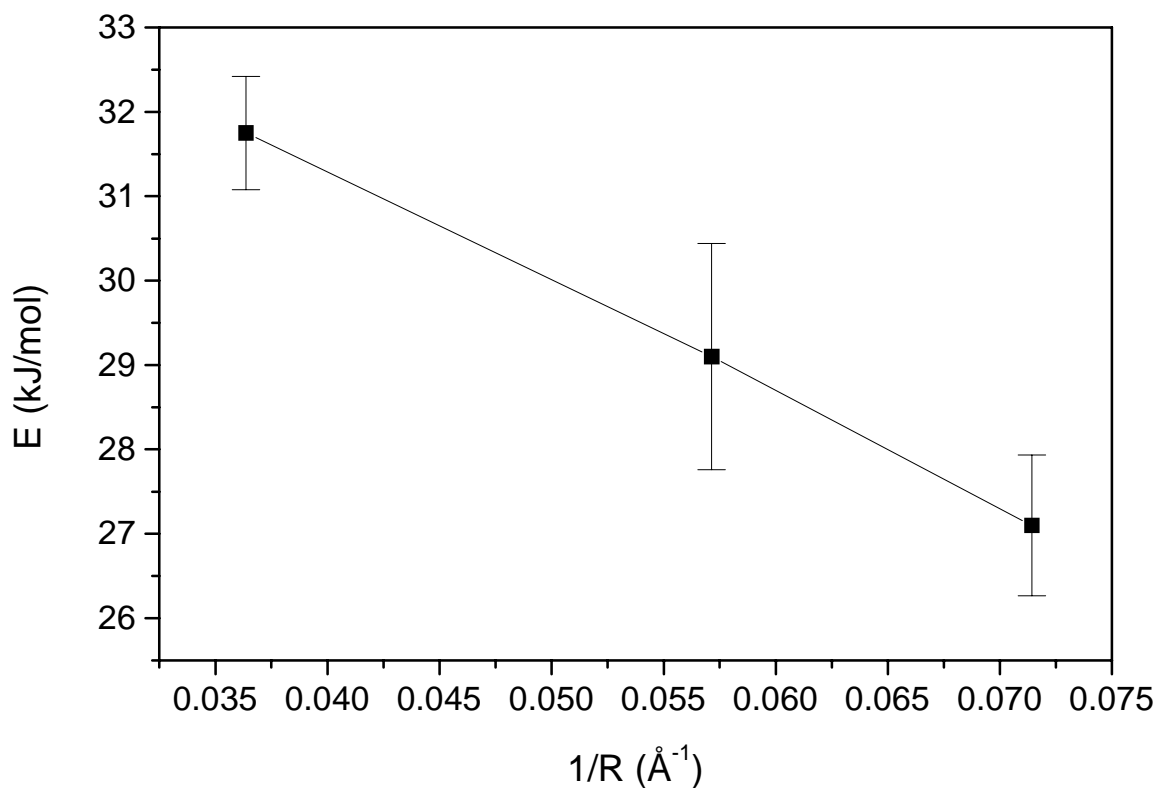


Figure 8-17 Activation energy for the k_{23} reaction vs. $1/\text{nanocrystal radius}$. The plot includes a fit to a straight line.

8.3.5.1 Reaction order of the k_{23} reaction

Studies of evaporation of atomic sodium from supported sodium clusters with average sizes ranging from 100\AA - 1500\AA have shown that the order of the reaction for

evaporation is less than the expected value of 1 due to preferential evaporation from surface and perimeter sites [29]. The measured order of the evaporation reaction was 0.79 ± 0.08 . Fractional orders of desorption were also measured in H on Zn (0001) surfaces, where the H atoms form islands due to lateral interactions [30]. Island formation results in H atoms at the edge sites that desorb more easily than the H atoms in the center. It would be interesting to determine the reaction order of the desorption of SeO_2 from CdSe nanocrystals to see if it is fractional. Such information would support the presence of low coordination sites on the nanocrystal surface. The following section describes the data analysis used to obtain the reaction order, which utilizes the analysis of the TPD data on sodium clusters as a guide [29]. The order of the evaporation of SeO_2 from CdSe clusters can be obtained from the rate equation:

$$\frac{d[\text{SeO}_2]}{dt} = k[\text{SeO}_2]^x$$

or the more useful form:

$$\ln\left(\frac{d[\text{SeO}_2]}{dt}\right) = \ln k + x \ln[\text{SeO}_2]$$

where x is the reaction order. Thus, a plot of $\ln (d\text{SeO}_2/dt)$ vs. $\ln \text{SeO}_2$ yields a straight line of slope x . The value for x obtained was 0.89 ± 0.14 . An estimate of the reaction order that takes into account the surface and edge sites can be calculated if one assumes that

$$n_{\text{surface}} = n_{\text{total}}^{x_{\text{surface}}}$$

$$n_{\text{perimeter}} = n_{\text{total}}^{x_{\text{perimeter}}}$$

and

$$n_{\text{surface}} + n_{\text{perimeter}} = n_{\text{total}}$$

where n_{surface} and $n_{\text{perimeter}}$ are the number of atoms on the surface or perimeter of the crystal surface, respectively [29]. The orders for the reactions of surface and perimeter desorption can be calculated by

$$x_{\text{surface}} = \frac{\ln(n_{\text{surface}})}{\ln(n_{\text{total}})}$$

$$x_{\text{perimeter}} = \frac{\ln(n_{\text{perimeter}})}{\ln(n_{\text{total}})}$$

By constructing reasonable models of the nanocrystals and counting the number of edge and surface sites, one can calculate how many atoms are on the surface and edges of the crystal, and hence the reaction order expected for the evaporation reaction. The values obtained by assuming roughly spherical crystals and counting only Se atoms on the surface and edges are summarized in Table 2. The reaction order shows a weak size dependence in the 28-55 Å range. The calculated values were obtained by assuming that all Se atoms on surface and edge sites are oxidized. Overall, the calculated values are less than the measured reaction orders, which is probably due to the fact that the amount of Se atoms that can oxidize is underestimated. However, the observed reaction order is certainly fractional, supporting the model of sites with lower coordination number on the nanocrystal surface.

Table 8-2 Desorption orders.

| Diameter (Å) | measured desorption order $\langle x_{\text{meas}} \rangle$ | calculated desorption order, x_{calc} |
|-----------------|---|--|
| 28 | 0.94±0.21 | 0.8172 |
| 35 | 0.94±0.12 | 0.8049 |
| 55 | 0.85±0.19 | 0.784 |

8.4 Summary

We have studied the oxidation and evaporation kinetics of CdSe nanocrystals. A consecutive-parallel reaction scheme has been determined in which CdSe in the presence of light reacts with oxygen to form $\text{CdSeO}_{2,3}$. Evaporation of SeO_2 from $\text{CdSeO}_{2,3}$ occurs along with the evaporation of Se_2 directly from CdSe.

Table 8-3 Summary of rate constants and activation energies as a function of nanocrystal size.

| Diameter (\AA) | k_{12} 70°C | k_{12} 130°C | k_{12} 185°C | k_{12} 210°C |
|---------------------------|---------------|----------------|----------------|----------------|
| 28 | 0.0315 | 0.045 | 0.0428 | 0.045 |
| 43 | 0.0246 | 0.0738 | 0.0861 | |
| 55 | 0.0149 | 0.0332 | | 0.1728 |

| Diameter (\AA) | k_{13} 70°C | k_{13} 130°C | k_{13} 185°C | k_{13} 210°C |
|---------------------------|---------------|----------------|----------------|----------------|
| 28 | 0.0042 | 0.0382 | 0.0912 | 0.1654 |
| 43 | 0.004 | 0.0079 | 0.0554 | |
| 55 | 0.0413 | 0.0596 | | 0.1114 |

| Diameter (\AA) | $E(k_{12})$ kJ/mol | $E(k_{13})$ kJ/mol | $E(k_{23})$ kJ/mol |
|---------------------------|-----------------------|-----------------------|-----------------------|
| 28 | 3.26 ± 1.3 | 35.15 ± 2.8 | 27.1 ± 0.84 |
| 35 | | | 29.1 ± 1.34 |
| 43 | 15.25 ± 4 | 29.17 ± 12 | |
| 55 | 24.04 ± 5 | 9.74 ± 1.6 | 31.75 ± 0.67 |

From the activation energies for these reactions the size dependence of stability has been determined. Larger nanocrystals are more resistant to decomposition via oxidation and desorption of SeO_2 due to the facilitated reaction of oxygen with surfaces of high curvature. Although it is difficult to test the validity of scaling laws with three sizes of nanocrystals, the general trends can be approximated. The activation energy of the oxidation of CdSe to $\text{CdSeO}_{2,3}$ and for the evaporation of SeO_2 from $\text{CdSeO}_{2,3}$ depends on size as approximately $1/R$, which agrees with the surface to volume ratio for a sphere. The fractional reaction order for the evaporation of SeO_2 also suggests preferential desorption from corners and

edges on the crystal surface. A scaling law for the evaporation of Se_2 from CdSe could not be clearly extracted since the process depends on particle stoichiometry.

The stoichiometric ratio of Cd:Se has opposite effects: it facilitates the oxidation of CdSe to $\text{CdSeO}_{2,3}$ but hinders the evaporation of Se_2 from CdSe. As a result, smaller particles are more resistant to Se_2 evaporation due their inherent excess of Cd. It is postulated that the nanocrystals most stable to oxidation and evaporation would be as large as possible and have a stoichiometric ratio that would balance the effects of oxidation and evaporation. The large change in the pre-exponential cannot be explained in terms of surface curvature.

From the rate constants for these reactions the stability of nanocrystals in oxygen and light can be estimated. 1 monolayer of an unprotected 28\AA nanocrystal stored in a 20mL vial of air under solar irradiation would completely react in approximately 7 hours.

These experiments measure quantitatively the size dependent reactivity of CdSe nanocrystals with light and oxygen, which is relevant for quantifying their stability in ambient conditions. It is apparent that more sizes need to be measured to construct scaling laws for reactivity; however, the data suggests that the activation energy should follow size dependent behavior in agreement with spherical surface to volume ratios.

Although the results shown here are not of high precision and unsuitable for investigating scaling laws, they illustrate how traditional surface science techniques can be applied to non-planar, finite surfaces to get quantitative information. The following chapter will show another case in which a bulk technique, x-ray absorption spectroscopy, will be adapted to obtain structural information about nanocrystal surfaces.

8.5 References

- [1] V. L. Colvin, M. C. Schlamp, and A. P. Alivisatos, *Nature* **370**, 354 (1994).
- [2] N. C. Greenham, X. Peng, and A. P. Alivisatos, *Phys. Rev. B* **54**, 17628 (1996).
- [3] B. O. Dabbousi, M. G. Bawendi, O. Onitsuka, and M. F. Rubner, *Appl. Phys. Lett.* **66**, 1316 (1995).
- [4] M. C. Schlamp, X. Peng, and A. P. Alivisatos, *J. Appl. Phys.* **82**, 5837 (1997).
- [5] Y. H. Wang, N., *J. Lumin.* **vol.70**, 48.
- [6] E. K. Parks, L. Zhu, J. Ho, and S. J. Riley, *J. Chem. Phys.* **102**, 7377 (1995).
- [7] S. A. Mitchell, L. Lian, D. M. Rayner, and P. A. Hackett, *J. Chem. Phys.* **103**, 5539 (1995).
- [8] O. Bjorneholm, F. Federmann, F. Fossing, and T. Moller, *Phys. Rev. Lett.* **74**, 3017 (1995).
- [9] J. Jortner, *Z. Phys. D* **24**, 247 (1992).
- [10] G. A. Somorjai, *Progress in Solid State Chemistry* **4**, 1 (1967).
- [11] C. Y. Lou and G. A. Somorjai, *J. Chem. Phys.* **55** (1971).
- [12] J. E. Bowen Katari, V. L. Colvin, and A. P. Alivisatos, *J. Phys. Chem.* **98**, 4109 (1994).
- [13] A. A. Guzelian, J. E. B. Katari, A. V. Kadavanich, U. Banin *et al.*, *J. Phys. Chem.* **100**, 7212 (1996).
- [14] J. J. Shiang, A. V. Kadavanich, R. K. Grubbs, and A. P. Alivisatos, *J. Phys. Chem.* **99**, 17417 (1995).
- [15] X. Peng, J. Wickham, and A. P. Alivisatos, *J. Am. Chem. Soc.* **120**, 5343 (1998).
- [16] C. B. Murray, D. J. Norris, and M. G. Bawendi, *J. Am. Chem. Soc.* **115**, 8706 (1993).

- [17] X. Peng, M. C. Schlamp, A. V. Kadavanich, and A. P. Alivisatos, J. Am. Chem. Soc. **119**, 7019 (1997).
- [18] B. O. Dabbousi, J. Rodriguez-Viejo, F. V. Mikulec, J. R. Heine *et al.*, J. Phys. Chem. B **101**, 9463 (1997).
- [19] J. F. Moulder, W. F. Stickle, P. E. Sobol, and K. D. Bomben, *Handbook of X-ray Photoelectron Spectroscopy* (Physical Electronics, Inc., Eden Prairie, 1995).
- [20] A. Ebina, K. Asano, Y. Suda, and T. Takahashi, J. Vac. Sci. Tech. **17**, 1074 (1980).
- [21] A. Ebina, K. Asano, and T. Takahashi, Phys. Rev. B **22**, 1980 (1980).
- [22] G. A. Somorjai, J. Phys. Chem. Solids **24**, 175 (1963).
- [23] J. Bowen Katari, 1994, Chemistry, University of California at Berkeley, Thesis.
- [24] D. P. Masson, D. J. Lockwood, and M. J. Graham, J. Appl. Phys. **82**, 1632 (1997).
- [25] A. A. Frost and R. G. Pearson, *Kinetics and Mechanisms* (John Wiley & Sons, Inc., New York, 1953).
- [26] F. Raoult, B. Fortin, A. Quemerais, G. Rosse *et al.*, J. Phys. Chem. Solids **53**, 723 (1992).
- [27] P. A. Redhead, Vacuum **12**, 203 (1962).
- [28] G. Carter, Vacuum **12**, 245 (1962).
- [29] M. Vollmer and F. Träger, Surf. Sci. **187**, 445 (1987).
- [30] L. Chan and G. L. Griffin, Surf. Sci. **145**, 185 (1984).

9 SURFACE STRUCTURE OF SEMICONDUCTOR NANOCRYSTALS STUDIED BY XANES

9.1 Introduction

The advent of colloidal methods to prepare high quality inorganic nanocrystals has led to an increasing number of studies of size dependent scaling laws [1]. Due to the finite size of nanocrystals, the structure and composition of their surface may have particular importance for their chemical and physical properties. For instance, nanocrystal growth and manipulation relies heavily on their surface chemistry [2]. The thermodynamic phase diagrams of nanocrystals are strongly modified from those of the bulk materials by the surface energies [3]. The electronic structure of semiconductor nanocrystals is influenced by surface states which lie within the band gap but are thought to be eliminated by surface reconstruction [4]. Because measuring the properties of nanocrystal surfaces has proven to be difficult, it has been previously ignored or approximated as a defect. Thus, for any picture of the physical properties of nanocrystals to be complete, the structure of the surface must be determined.

9.1.1 Surface reconstructions for bulk

The presence of surface reconstructions in nanocrystals have been postulated theoretically for many years but have not been directly measured. For bulk solids, surface reconstructions have been well characterized for well-defined surfaces by a variety of techniques. Therefore, the surface structure is known for several types of bulk solids for different crystallographic faces and adsorbate systems [5], even in cases where the symmetry has deviated considerably from bulk geometry.

9.1.1.1 Peierls distortion

The driving force behind a surface reconstruction is the lowering of a total energy as a result of a distortion in the system. Surface reconstructions are a two dimensional analog of a Peierls distortion, which occurs in 1-dimensional systems when it can lower its symmetry in order to decrease its total energy [6, 7]. It is the infinite case of a Jahn-Teller distortion. In order to understand the basis for distortion, consider the 1-D case of polyacetylene (Figure 1). The energy levels for a chain of n 1 electron atoms with a periodicity a is given by

$$E_j = \alpha + 2\beta \cos(2j\pi/n)$$

where j is an index that has the values of

$$j = 0, \pm 1, \pm 2, \pm 3, \dots$$

and α is the Coulomb integral given by

$$\alpha = \langle \phi_1 | H | \phi_1 \rangle$$

and β is the interaction integral given by

$$\beta = \langle \phi_1 | H | \phi_2 \rangle.$$

The energy levels can be written in a more useful form by adopting the index k which is defined by

$$k = 2j\pi/na$$

The form for the energy levels then becomes

$$E_j = \alpha + 2\beta \cos(2j\pi/n)$$

k is a useful index as it is the crystal momentum. The diagram for the energy levels, or band, is shown in Figure 1 as a plot of E vs k . The energy levels are plotted in the

reduced zone scheme, which can be simply as folding the bands back on itself. If one fills the bands with all the available electrons (n of them), the bands are filled exactly to the half point on the diagram.

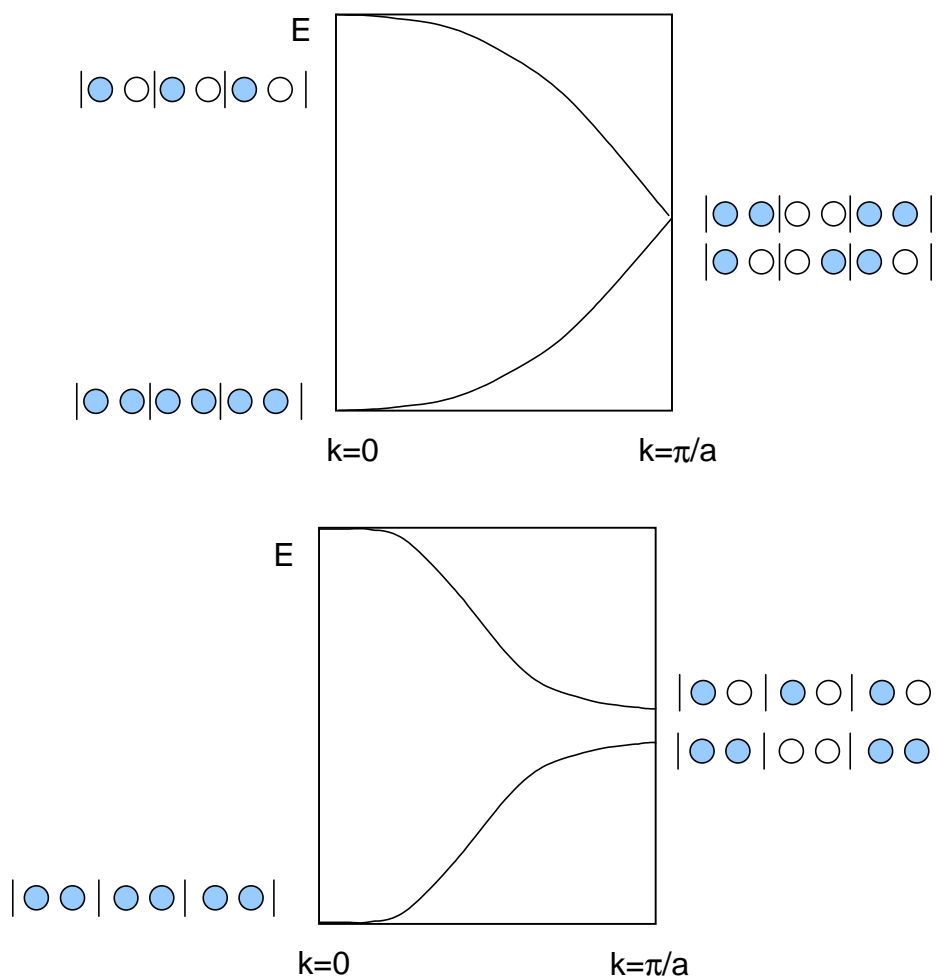


Figure 9-1. The bands for an infinitely long chain in the symmetric (undistorted) and asymmetric (distorted) form constructed from the frontier orbitals. The distortion is a Peierls distortion, which introduces a gap at the band edge (at $k=\pi/a$). The undistorted form is a metal, while the distorted form is a semiconductor.

Polyacetylene has the possibility of being metallic if the π electrons are fully delocalized or insulating if the π electrons occupy alternate bonds. If one draws the bands for the fully delocalized case, where the atoms are evenly spaced, the orbitals at $k = \pi/a$ are degenerate. In the alternating bond length cases, the distortion doubles the size of the

primitive unit cell. The states at π/a are no longer degenerate because one band is stabilized by becoming more bonding and the other destabilized by becoming more antibonding in character. Because of this stabilization /destabilization an energy gap results. Upon filling the bands with electrons, the lower band is fully occupied and the upper band is completely empty, so the system is insulating and the total energy of the system is lower than the metallic case.

A semiconductor surface in some way is analogous to the polyacetylene example. Atoms on the surface do not have a full set of nearest neighbors and thus have dangling bonds. A surface in its unreconstructed form is a metal since these dangling bonds are partially filled. These metallic states, or surface states, lie in the gap of the semiconductor. However, if the surface can reconstruct, it converts to a semiconducting system, completely filling or emptying the orbitals. This results in the removal of the states in the gap of the semiconductor and lowers the total energy. The shifting of states in the gap to the bulk bands have been observed theoretically [8, 9]. Surface reconstructions cannot be described in such simple terms as a Peierls distortion, which is a strictly 1-D effect; however, the concept of a system distorting to lower its total energy still applies. There are numerous examples of solids undergoing complicated rearrangements, and it seems difficult to construct a general set of rules as to how surfaces reconstruct. Nevertheless, recently there has been an endeavor to generalize the behavior of surface reconstructions. [5, 10]

The determination of nanocrystal surface structure has proven to be particularly difficult. It is unclear how the surface atoms would rearrange in a spherical particle to lower the total energy. Long range mechanical restoring forces, which can play a determining role in bulk surface reconstructions, will be markedly different in nanocrystals. Strain effects which are negligible for infinite 2D planes may be substantial for a nanocrystal. The

presence of surface reconstructions on a nanocrystal is plausible, yet it is believed that the surface structure is quite complex in that it influences the crystal lattice throughout the entire particle. Thus, how surface atoms reconstruct to accommodate large surface area in a finite sized, organic surfactant capped particle cannot easily be anticipated [11].

Techniques such as transmission electron microscopy (TEM) and powder x-ray diffraction (XRD) yield much information about the shape of the nanocrystal and the long-range order of the atoms [12-14]. These techniques show that the interior of the nanocrystals is crystalline and defect free, manifesting itself as single nucleation events observed in structural phase transitions [15]. Furthermore, TEM indicates that CdSe nanocrystals are faceted [13] and from TEMs with shape information one can deduce which planes are present on the surface of a nanocrystal. However, the structural rearrangements at the faces are not discernible from the images. Powder x-ray diffraction has been used extensively to model the structure of the nanocrystals, and it is possible to obtain fits of XRD patterns by assuming bulk lattice parameters [14]. However, the information content in XRD patterns is limited, particularly with respect to aperiodic parts of the nanocrystal such as the surface. For example, fits of XRD powder patterns can be obtained with or without surface reconstructions in the model (insert figure of xrd fits here). This is not surprising as both XRD and TEM are diffraction techniques, which get their information from scattering over multiple lattice planes and in principle insensitive to short periodicities such as at the surface. Consequently, apart from a few cases in which single crystal x-ray diffraction patterns of small nanocrystals could be recorded [16], almost no information about the surface structure of nanocrystals is available.

Techniques that have been extremely effective in determining the structure of reconstructions in bulk surfaces are difficult to implement on nanocrystals. Scanning

tunneling microscopy (STM) in combination with low energy electron diffraction (LEED) and energy minimization calculations have been used successfully to determine the geometry of complicated structures such as the 7×7 reconstruction of the Si (111) surface. However, STM uses a tip of curvature on the order of that of the nanocrystal, hence imaging with atomic resolution is difficult. Only in a few cases has it been successful in imaging atoms on the surfaces of free-standing objects with high curvature such as carbon nanotubes [17, 18]. LEED requires crystalline orientation of the nanocrystals over large length scales ($\sim 1000 \mu\text{m}^2$), which has not been achievable in two dimensions. However, there has been recent progress in both of these endeavors [19, 20] which indicates that these techniques will soon be able to image nanocrystal surfaces. Z-contrast TEM imaging of CdSe nanocrystals has also shown the possibility of assembling a three-dimensional image of a single nanocrystal, including the surface atoms [21].

Another technique which has not yet been implemented on nanocrystals that is quite promising for determining surface structure is photoelectron diffraction (XPD or PED). A photoelectron from an atom is scattered off nearby atoms and interferes with the original outgoing wave, modulating the photoelectron intensity. The modulations are extremely sensitive to the structural environment of the atom from which the photoelectron originates. Measuring the interference pattern is achieved by mapping the photoelectron intensity as a function of angle in 2π space. From these maps in conjunction with calculations bond distances and angles can be deduced. It is element specific due to the fact that a core electron is examined. However, as it is a diffraction experiment, it demands crystallization of the sample but due to the finite mean free path of the electron it requires only short range order. Furthermore, since it is a type of photoelectron spectroscopy, electron contact must be made to the sample, so two-dimensional crystallization on metallic substrates is required.

This technique may seem to be an excessively involved method to obtain information about bond distances, but in fact it is this very phenomenon of photoelectron interference patterns that will allow one to understand structural disorder in nanocrystals.

9.1.2 X-ray absorption as a structural probe

A technique with the potential to measure structural disorder including surface atom configurations in nanocrystals is x-ray absorption spectroscopy (XAS). The phenomenon which occurs in XAS is similar to that of XPD: the cross section of an absorbing atom in XAS depends on the scattering of the generated photoelectron wave from neighboring atoms, thereby including information about the local structure around the absorber (Figure 2) [22]. Modulations in the absorption coefficient result from the interference pattern between the outgoing (black) and backscattered waves (purple), which can be translated into information about the distance between the absorber and scatterer with a precision of a few hundredths of an Ångström. Due to the local nature of this process, XAS does not rely on any long-range order in a sample, in contrast to diffraction techniques. It is also much simpler to employ than diffraction: instead of an electron detector and careful sample orientation control, all that is required is a method to monitor absorption. This can be achieved by measuring transmitted intensity (Beer's Law) or by measuring the current from the sample, enabling the study of samples too thick for transmission [23]. It has been used extensively to investigate the local structure in the interior and at the surface of a variety of solid-state materials, in liquids, gases and molecular beam clusters [24]. Also, EXAFS (extended x-ray absorption fine structure) has proven to be a valuable tool to investigate surface induced changes in nanocrystals [25].

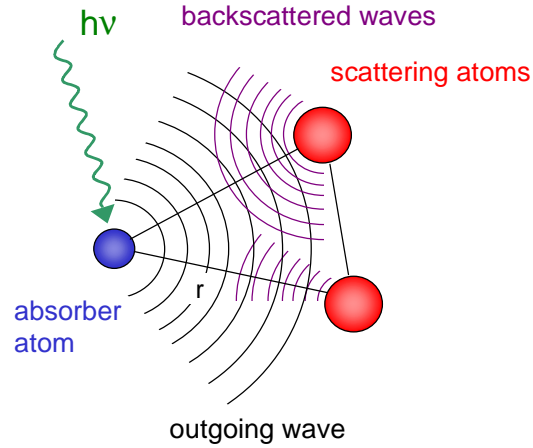


Figure 9-2. Schematic for a XANES process. Upon absorption of a photon (green), an atom (blue) emits a photoelectron wave (black). The interference pattern between the outgoing photoelectron wave and backscattered waves (purple) is sensitive to the position (r) of the scattering atoms (red) relative to the absorber.

The absorption coefficient of a material is written as

$$\alpha(E) = \alpha_0(E) \left[1 + \chi_2(E) + \sum_{n=3} \chi_n(E) \right]$$

where α_0 is the atomic absorption coefficient, and χ is the modulations in the absorption coefficient in the system. χ_2 is the fractional change in the absorption coefficient for the case of single scattering events, or when only one backscattered wave results. The sum over the higher order χ_n is the modulation of the absorption coefficient due to the multiple scattering events, or when a backscattered wave scatters off another neighboring atom, producing a second backscattering wave, and so on. In order to understand how structural information from these modulations, let us examine the functional form of χ_2 . It can be described as a function of k (the momentum) as

$$\chi(k) = \sum_j \frac{N_j}{kR_j^2} f(k) \exp\left(-\frac{\Gamma R_j}{k}\right) \exp(-2\sigma^2 k^2) \sin(2kR_j + \phi_j)$$

The sum is over the j th coordination shell, which has N_j atoms in it. $f(k)$ is the amplitude of the backscattered wave originating from a neighboring atom j which is at a distance R_j from the absorber. The $\sin(2kR_j + \phi_j)$ describes the interference term producing modulations in the absorption cross section where ϕ_j is the phase shift, which depends on the nature of the absorber and the scatterer atoms. There is also the term $\exp(-\Gamma R_j/k)$ which contains Γ , the inelastic mean free path of the photoelectron. Γ describes the exponential decay of the photoelectron wavefunction amplitude, and is loosely defined as the length by which the amplitude decreases by $1/e$. The damping of the fine structure from the inelastic mean free path limits a region around the absorber in which the atoms contribute to the oscillations. The $\exp(-2\sigma^2 k^2)$ is a Debye-Waller term describing the damping of the signal due to the atomic vibrations.

Structural information about the local environment around the absorber is contained in the $f(k) \cdot \sin(2kR_j + \phi_j)$ term, which denotes the scattering paths. If one knows $f(k) \cdot \sin(2kR_j + \phi_j)$ and for a given absorber and backscatterer combination, one can deduce from χ and thus the absorption spectrum N_j and R_j , the number of scatterers at a given distance from the absorber. Therefore, the absorption spectrum contains structural information in the form of a radial distribution function ($N_j(R_j)$). However, the effects that occur in the limits of low and high electron kinetic energy are very different, and one must consider these two limits.

9.1.3 EXAFS vs. XANES

A schematic of an absorption edge is shown in Figure 3, which the high and low energy regimes indicated. If the photoelectron kinetic energy is high ($>100\text{eV}$), it is only weakly scattered by neighboring atoms. This part of the spectrum is dominated by single scattering events. This can be seen by the weak oscillations in the absorption spectrum at energies far above the absorption edge. The spectrum can be directly inverted to obtain a radial distribution function. In practice, this involves truncating the spectrum at the multiple scattering regime, subtracting an atomic background, and fourier transforming the spectrum to real space. What results is bond length information which is atom specific and exact down to 1% of a bond length. Not surprisingly, EXAFS has proven to be a technique key to obtaining structural data of systems.

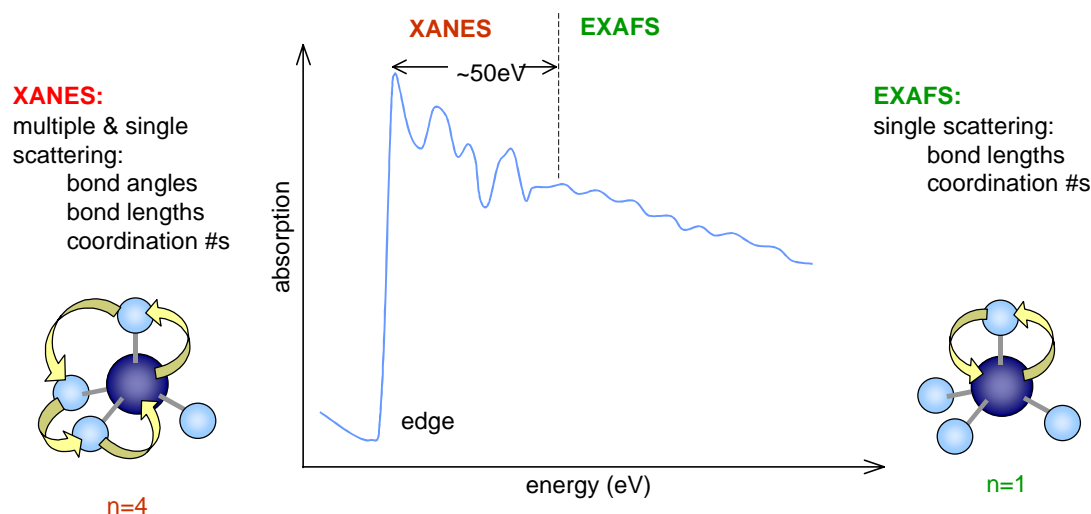


Figure 9-3. Cartoon of an absorption spectrum above the edge, delineating the XANES and EXAFS regions. A photoelectron is ejected from the absorber atom (dark blue) and is scattered off neighboring atoms (light blue). Its scattering path is denoted as the yellow arrows.

Whereas EXAFS mainly probes the radial arrangement of neighboring atoms with respect to the absorbing atom, the spectrum within 50 eV above the absorption edge (x-ray absorption near edge structure, XANES) is sensitive to the relative arrangement of multiple

atoms due to the increased contribution of multiple scattering effects. The absorption spectrum near the edge is much more strongly affected by scattering and thus has a more intricate structure in contrast to the weak, periodic oscillations far above the edge. In principle, one can extract from XANES spectra more complex information such as bond angles instead of an averaged pair distribution function [22]. Information about the relative positions of three or more atoms is only possible through forward focussing effects, or when the atoms are arranged collinearly [26]. Therefore, XANES is in theory more amenable to the modeling of complex structural rearrangements in nanocrystals than EXAFS.

The multiple scattering description of the near edge part of the spectrum is a recent development. In the past the near edge part of the absorption spectrum had been either treated by band structure theory (as the density of unoccupied states) or ignored due to its complex nature. However, in the 1980's it was shown that XANES could be treated as a real-space effect like EXAFS and that the spectrum could yield structural information as well. In fact, the multiple scattering picture reduces exactly to the band structure description. XANES offers an experimental advantage over EXAFS in that the near edge region of the spectrum has larger amplitude oscillations, allowing the measurement of dilute samples. In addition, the decay of the absorption coefficient at high energies above the absorption edge also makes using EXAFS oscillations over a large range difficult.

However, because the processes in XANES are much more complicated, it is not as simple as EXAFS to get structural information from a spectrum. Instead of directly inverting the spectrum, one must make educated guesses at the structure and then simulate them. Because all scattering paths must be taken into account, the computing time is considerably greater than in the single scattering case, making the data analysis a much more tedious and time-consuming process.

9.2 Experiment

CdSe and InAs nanocrystals with a mean diameter ranging from 17-80 Å were synthesized according to literature methods [2, 27]. The particles are capped with tri-*n*-octylphosphine oxide (TOPO) and tri-*n*-octylphosphine (TOP) in the case of CdSe and InAs, respectively. High-resolution TEM show crystalline, well separated CdSe and InAs particles with wurtzite and zincblende lattice fringes, respectively, in agreement with corresponding XRD patterns.

Because the absorption as a function of photon energy is the desired quantity, XANES experiments must be performed at a synchrotron. The XANES spectra of the $M_{4,5}$ edge at 405eV (Cd) and 445eV (In) were measured at the Advanced Light Source Synchrotron, Berkeley on beamline 6.3.2. The insertion device at 6.3.2 is a bend magnet, with a monochromator with no entrance slit for improved flux. High photon intensity is key as the signal from nanocrystals is typically very low in comparison to bulk. Possible energy ranges from 50eV to 1300eV, with an ultimate resolution of 7000 (E/ Δ E). For the edges observed here, the exit slits on the monochromator were set to 20 μ m, which corresponds to a beam resolution of 100meV. The photon energy was calibrated to the F 1s line in MgF₂ (690eV).

The absorption was monitored by measuring sample current (total yield) since transmission experiments require accurate characterization of sample thickness, which is not trivial for monolayers of nanocrystals. Transmission also requires suitable substrates that are optically transparent in the energy regime of interest and also are physically sturdy. For total yield experiments, the nanocrystals must be electrically accessible. Sub-monolayers of particles were deposited onto HF etched Si wafers from toluene solutions. Electrical contact was facilitated by rubbing Ga on the backs of the Si substrates, which then had Al foil folded

around them to hold them in place. The Al foil was glued onto a glass slide so that the sample could be mounted into the endstation without grounding it. Current was measured from an alligator clip attached to the Al foil (Figure 4).

Scans for each core for a series of nanocrystals and bulk were taken within a single beam fill so as to eliminate changes in energy calibration between fills. The linewidth for the 3d core level of both In and Cd is estimated at $\sim 300\text{meV}$ [28] which is the limiting factor in the resolution of the experiment. Samples that had been exposed to synchrotron radiation had shown no change in their optical absorption spectra, indicating that the sample did not degrade in the beam.

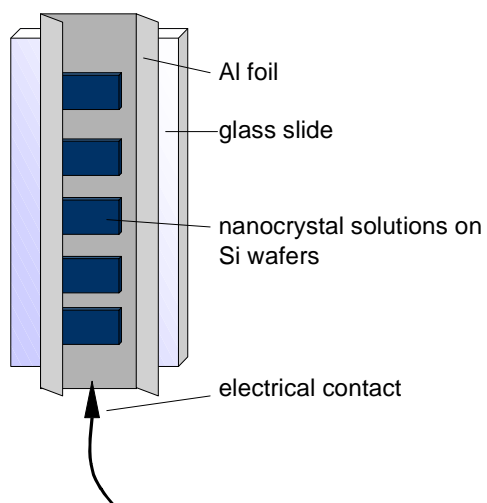


Figure 9-4 Sample block for x-ray absorption measurements.

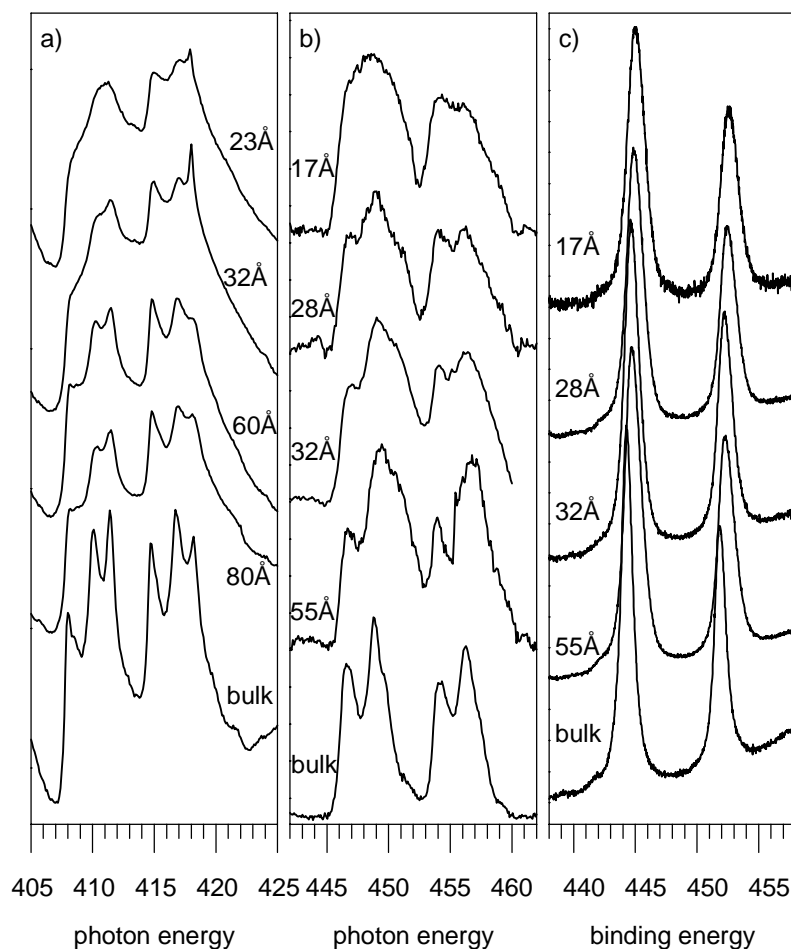


Figure 9-5. XANES spectra for the Cd (a) and In (b) $M_{4,5}$ edge for a series of nanocrystals. Bulk spectra are also included. (c) is the XPS spectra of the In 3d core for InAs nanocrystals.

Figure 5 shows the absorption onset at the a) Cd and b) In $M_{4,5}$ edges as a function of size of CdSe and InAs nanocrystals as well as the respective bulk spectrum (bottom). The 3d core in both atoms is spin orbit split by 6.76 eV and 7.6 eV, respectively, leading to a superposition of the M_4 and M_5 edge spectra. The bulk solids show relatively sharp spectral features. As the size of the particle decreases, the features broaden significantly to the point that for the smallest particle (17 Å for InAs) no splitting within the M_4 or M_5 edge spectra is visible anymore.

By using literature values for the energy of the core level relative to the conduction band minimum [29], the In and Cd M_3 and M_4 absorption spectra can be plotted relative to the conduction band minimum. Figure 6 shows the M_3 (red) and M_4 (blue) transitions plotted relative to the CB minimum for InAs and CdSe. Due to dipole selection rules the M_3 edge maps the s density of unoccupied states because it originates from the 3p core level and the $M_{4,5}$ maps the p density of unoccupied states. From the data it is clear that the bottom of the conduction band in CdSe and InAs is mainly derived from the 5s-states of the cation. It is also apparent that the In and Cd $M_{4,5}$ transition is *not* an excitation into states located at the conduction band edge but into higher p-bands that are 2-6eV above the conduction band minimum. Therefore, the $M_{4,5}$ transition is less sensitive to quantum confinement effects, which will be discussed later.

The qualitative shape of the spectral features in the cation M_3 and M_4 edges were confirmed by comparison to band structures of the bulk materials. Figure 6 also shows a qualitative sketch of the conduction bands in InAs and CdSe. The density of states at a given energy, $N(E)$, is given by $(dE/dk)^{-1}$, or qualitatively, areas of flat bands give peaks in the CBDOS. Rough peak assignments are shown in Figure 6 (dotted lines). From the spectra it is evident that the s and p bands overlap less in energy and are not as broad for CdSe than InAs. This is due to decreased s-p mixing in CdSe. For a more ionic material, the amount of mixing between s and p states decreases, so the bands are more separated in energy and narrower. A qualitative sketch for the covalent case (Si, Ge) is also shown, where s-p mixing is the greatest since all atoms are equivalent.

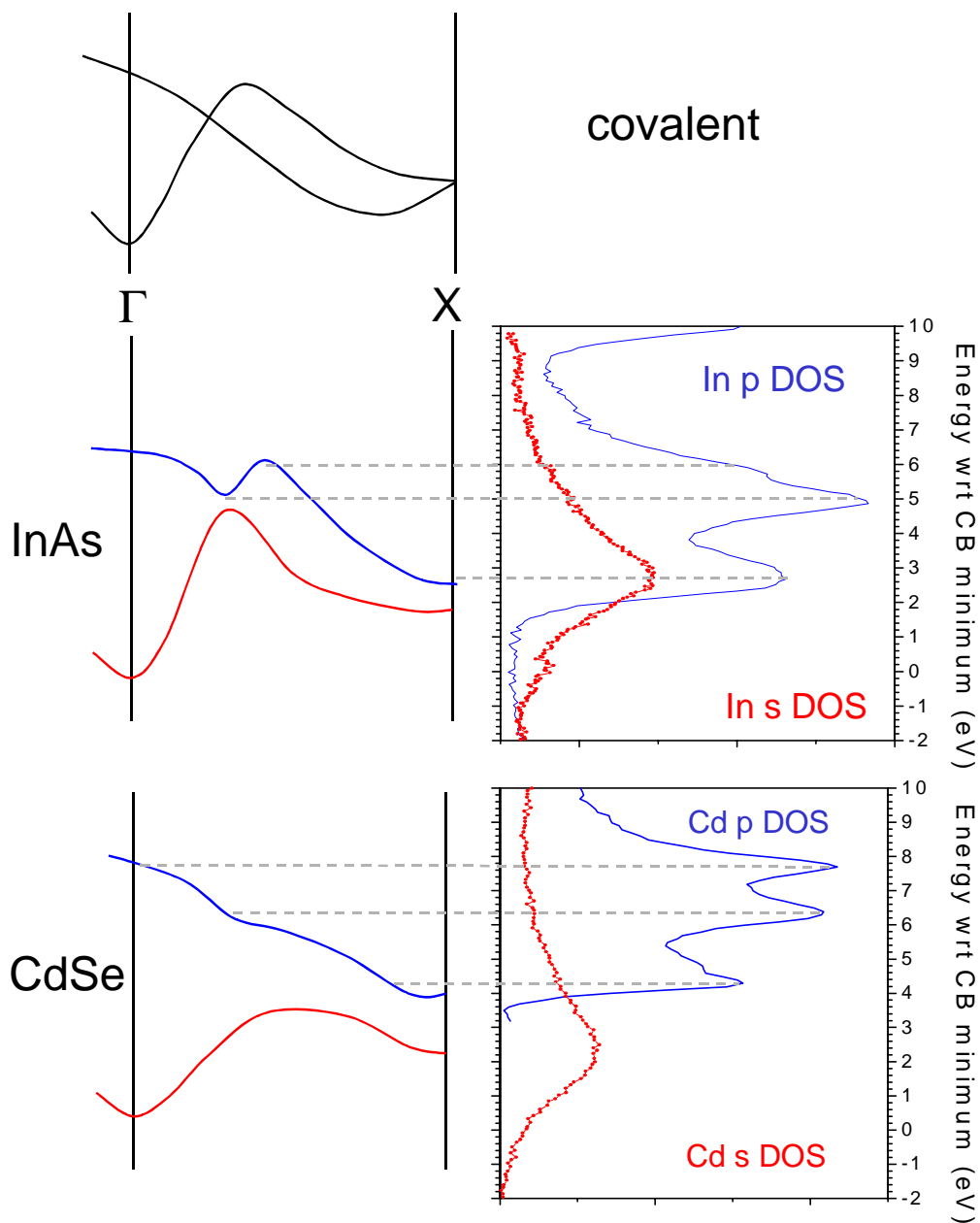


Figure 9-6 Schematic for the s and p bands in semiconductors of increasing ionicity. Peaks in the absorption spectrum correspond to flat features in the band dispersion. As the ionicity of the material increases, the energy separation due to s and p DOS increases due to decreased s-p mixing.

9.2.1.1 3p (M_3) absorption

The size dependent broadening was not observed for any other absorption edges that were measurable by this beamline. Figures 7 and 8 show the Cd $3p_{3/2}$ and In $3p_{3/2}$

absorption spectra for a series of CdSe and InAs nanocrystals. The only size dependent effect is exhibited as a shifting of the absorption edge to higher energy as the size of the particle is decreased. This is due to quantum size effects as the M_3 absorption edge probes the bottom of the conduction band. Using the effective mass approximation, the conduction band is expected to shift roughly $1/2$ the shift of the optical absorption energy since the effective mass of the electron and the hole are equal in InAs. The magnitude of the conduction band shift is in rough agreement with this estimation. The edge of the conduction band is taken as the intersection of the lines extrapolated through the background and the absorption onset, shown in Figure 9. However, it is difficult to extract the shift quantitatively as the background is quite sensitive to environmental effects such as sample charging and beam flux, and often changes from scan to scan. Figure 10 shows the quantitative amount of the absorption edge shift.

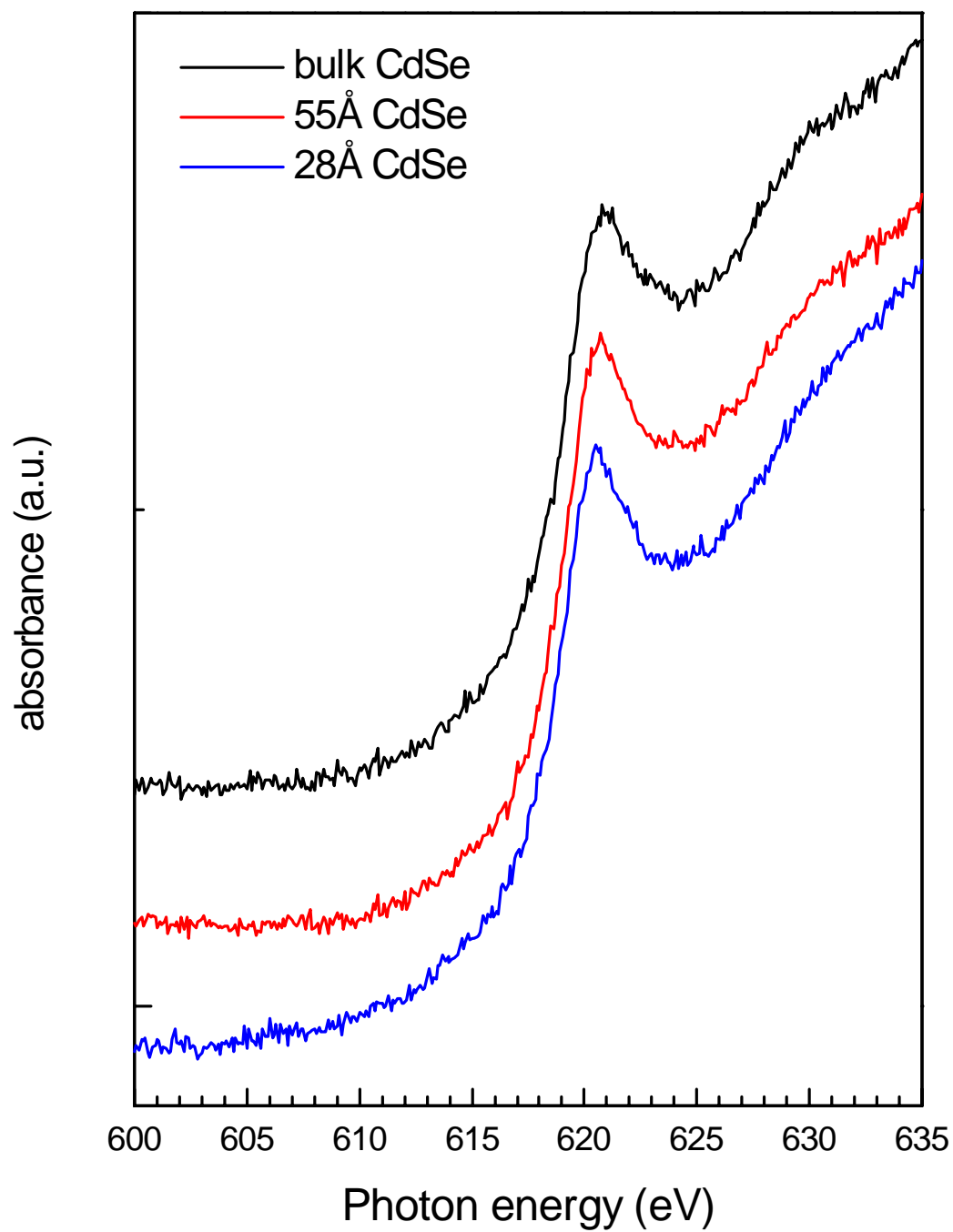


Figure 9-7 Cd 3p absorption edge for bulk and two sizes of CdSe nanocrystals.

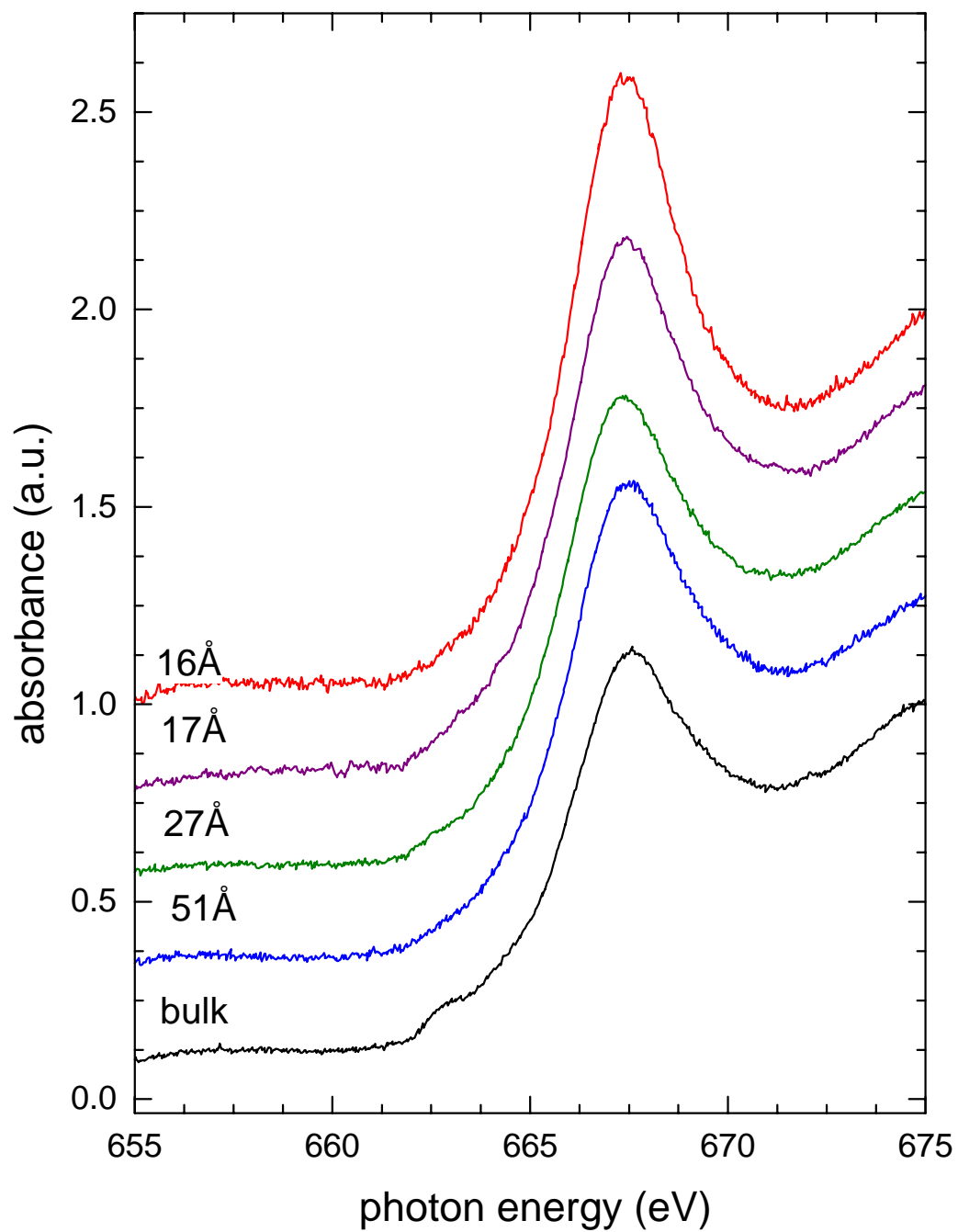


Figure 9-8 In 3p absorption for InAs bulk and nanocrystals.

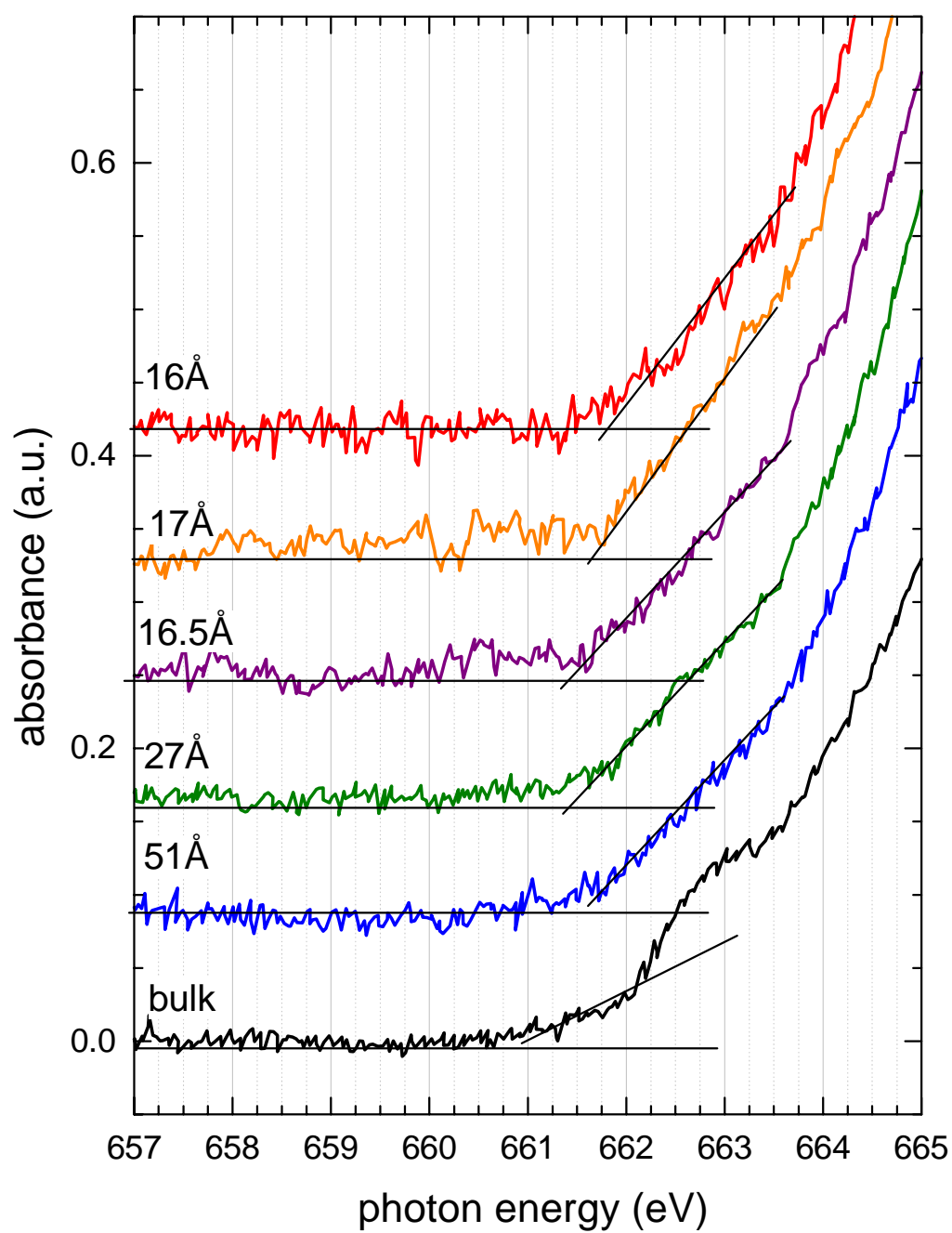


Figure 9-9 In 3p absorption edge for bulk and several sizes of nanocrystals.

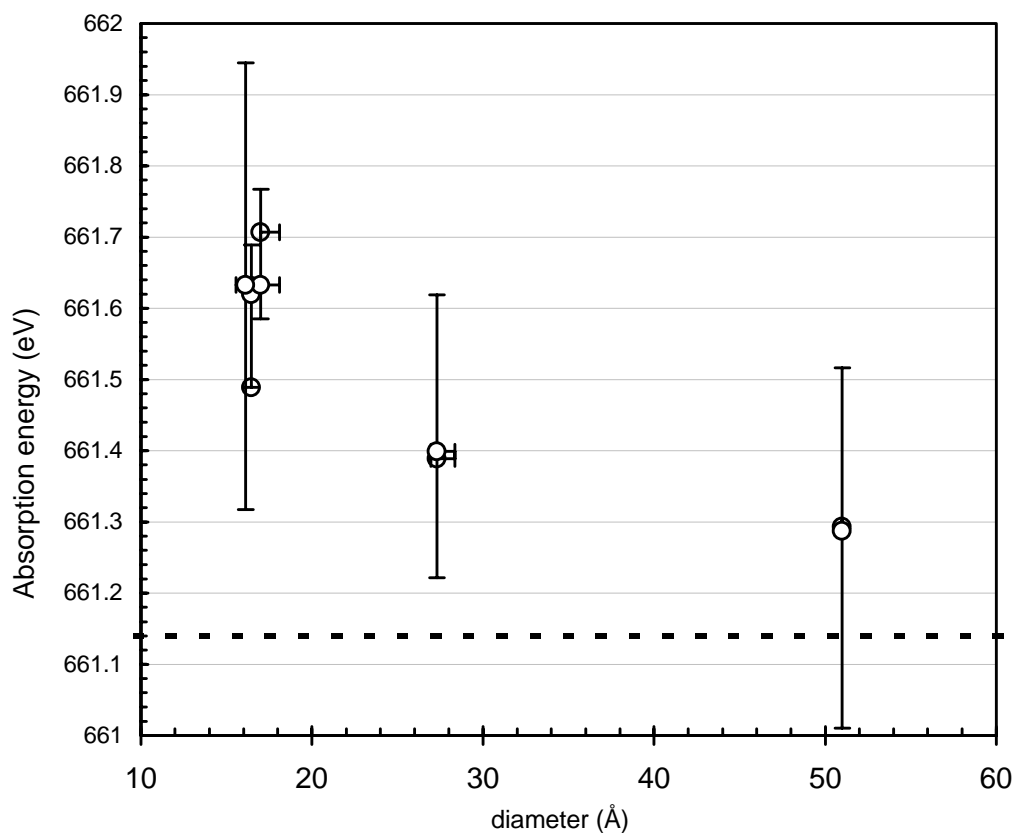


Figure 9-10 Edge shift of In 3p absorption edge as function of nanocrystal size. The dotted line is the bulk value.

9.2.1.2 XPS

In order to make sure that the broadening of the XANES spectra is due to the unoccupied states and not the core, the cores were examined by XPS (figure 5, right panel). Previous experiments on a synchrotron show that the Cd 3d levels do not show any size dependence measurable down to a resolution of 150meV. However, the In 3d core levels show a slight size-dependent shift to higher binding energy and an increase in linewidth observable on a conventional XPS spectrometer with a Mg $K\alpha$ anode. This shift has been well characterized in metal clusters and is attributed to decreased core-hole screening in nanocrystals [30]. In principle, the final state of XPS that is measured in the core level is

not the same as the final state of an absorption process. The final state of XPS is an ionized system, whereas in XAS the final system is neutral (electron in an unoccupied state, hole on a core). Therefore, comparing the final states of XAS and XPS is not strictly correct. The observed size dependent effects in XPS are a convolution of properties intrinsic to the nanocrystal as well as the final state in the photoemission process. However, the magnitude of the combined initial and final state effects (0.5eV) is negligible compared to the effects seen in the XANES spectra. Therefore, the smearing of the XANES spectrum is due predominantly to the nature of the unoccupied states (the environment of the photoelectron in the crystal) and not the core level from which the electron is ejected.

9.3 Discussion

9.3.1 FEFF7 Simulations

To gain a qualitative understanding of this data, we have undertaken simulations of the In $M_{4,5}$ edge absorption spectra using a multiple scattering model recently extended for XANES spectra, FEFF7 [31]. Scattering potentials are constructed by averaging the electron density around each unique atom in the Mattheiss prescription using muffin tin potentials. Scattering paths are constructed from the atomic configurations. Finally, the atomic absorption coefficient is calculated by propagating the electron waves through the scattering paths. FEFF7 is largely a real-space EXAFS simulation package, though it is one of the first to allow for multiple scattering calculations.

For proper calculation of the near edge spectrum the following options in FEFF7 were utilized. A sample input file is shown with a description of file input parameters in Figure 11. The input file consists of “cards” which specify options that the user wishes to use in the calculation.

First, the option to calculate the low energy part of the spectrum was turned on (the XANES card). The order of the scattering path could be set by the NLEG card, which can have a maximum value of 8 where 2 is for single scattering. To reproduce XANES spectra, multiple scattering must be accounted for. Therefore, all generated scattering paths are used in the calculation, with no cutoff for low-amplitude paths. This is done by using the CRITERIA 0 0 card. The two zeroes specify no cutoffs for both circular and plane waves. The option for using different types of scattering potentials is in the EXCHANGE card. The first index gives the code for the potential to use, while the second and third number give the real and imaginary energies, which give the shifts and the broadening. Good agreement with the bulk experimental spectrum was achieved when a ground state or a Dirac-Hara potential was used. The experimental broadening included in the calculation is defined as $\text{vri} = 100\text{meV}$. Lifetime of the core hole is given by $0.2 + \text{vri}$, which is thus 0.3eV , in agreement with the measured core line broadening due to lifetime in In [28]. Finally, FEFF7 sets a limit for the length of the longest scattering path with the RMAX card. The RMAX that was used in all of the calculations was 12\AA , which was determined to be the minimum length possible; for a bulk absorption spectrum, the spectra for longer RMAX values looked the same as for $\text{RMAX} = 12\text{\AA}$. Identities of the atoms are assigned by the IPOT card, which requires only an atomic number to identify the atom. Potentials for different atomic sites can be distinguished from one another by tagging them with distinct potential indices, where an index of 0 indicates the absorbing atom and must be unique.


```

TITLE    indium arsenide - zinc blende

HOLE 9   1.0      In M4 edge, s0^2=1.0

*          mphase,mpath,mfeff,mchi
CONTROL   1      1      1      1
PRINT     1      0      0      0

RMAX      12

CRITERIA  0 0
*NLEG      8

POTENTIALS
*   ipot    z   label
      0    49   In
      1    33   As
      2    49   In
      3    49   InS
      4    33   AsS

XANES
CORRECTIONS 5 0.1
EXCHANGE 2 5 0.1

ATOMS
0.00000    0.00000    0.00000    2   In    0.00000
-1.51500    1.51500   -1.51500    1   As    2.62406
1.51500    1.51500    1.51500    1   As    2.62406
1.51500   -1.51500   -1.51500    1   As    2.62406
-1.51500   -1.51500    1.51500    1   As    2.62406
3.03000    3.03000    0.00000    2   In    4.28507
-3.03000   -3.03000    0.00000    2   In    4.28507

END

```

Figure 9-11 Sample input file for FEFF7 showing all the cards employed in the simulations for InAs nanocrystals. The positions of all the atom are abbreviated, showing only 7 atoms.

The InAs nanoparticles are modeled as roughly spherical with an excess of In atoms at the surface, in accordance with results from XPS [32, 33]. In the simulations, the two outermost layers of In and As atoms are distinguished from those in the interior of the particle by calculation of their muffin-tin potential separately [34]. Those are the potentials with the tags of InS and AsS. Because all of the atoms in the nanocrystal give different absorption spectra, the calculation is performed for each In atom in the nanocrystal and the

resulting spectra are averaged; a 17Å nanocrystal has 55 In atoms, so 55 absorption spectra were calculated and averaged. The absolute energy of the simulated spectra was shifted to match the data at the first spectral feature of bulk (446.5eV).

Figure 12 shows simulations (lines) and spectra (dots) of a) InAs bulk, as well as b) 28Å (441 atoms) and c) 17Å (99 atoms) diameter InAs nanocrystals with the same lattice parameters as in bulk. In agreement with experiment, the simulated bulk spectrum shows features at 446.5eV and 449eV, though it introduces a broad peak around 460eV that is not seen in the experiment. The other systematic problem that occurs with the simulation is that the signal does not approach zero before the absorption edge. It is thought that the simulation truncates the absorption spectrum on the low energy side, though the reason for this is unclear. Although the theoretical simulation do not reproduce the experimental results for bulk, examination of the two features allows for a qualitative evaluation of the simulation. Reproduction of the bulk Cd M₄ absorption edge in CdSe was of poorer quality and was not performed for the nanocrystals.

For the InAs nanocrystals, the simulation predicts similar results with a slight broadening of the features at 446.5 eV and 449 eV. However, this broadening is much smaller than observed in the experimental data. Apparently, if the nanocrystal has uniform bulk bond lengths throughout, then the broadening of the spectra in smaller particles is not reproduced. Thus, the observed broadening does not arise simply from the finite number of coherent scatterers, as it does in the case of XRD.

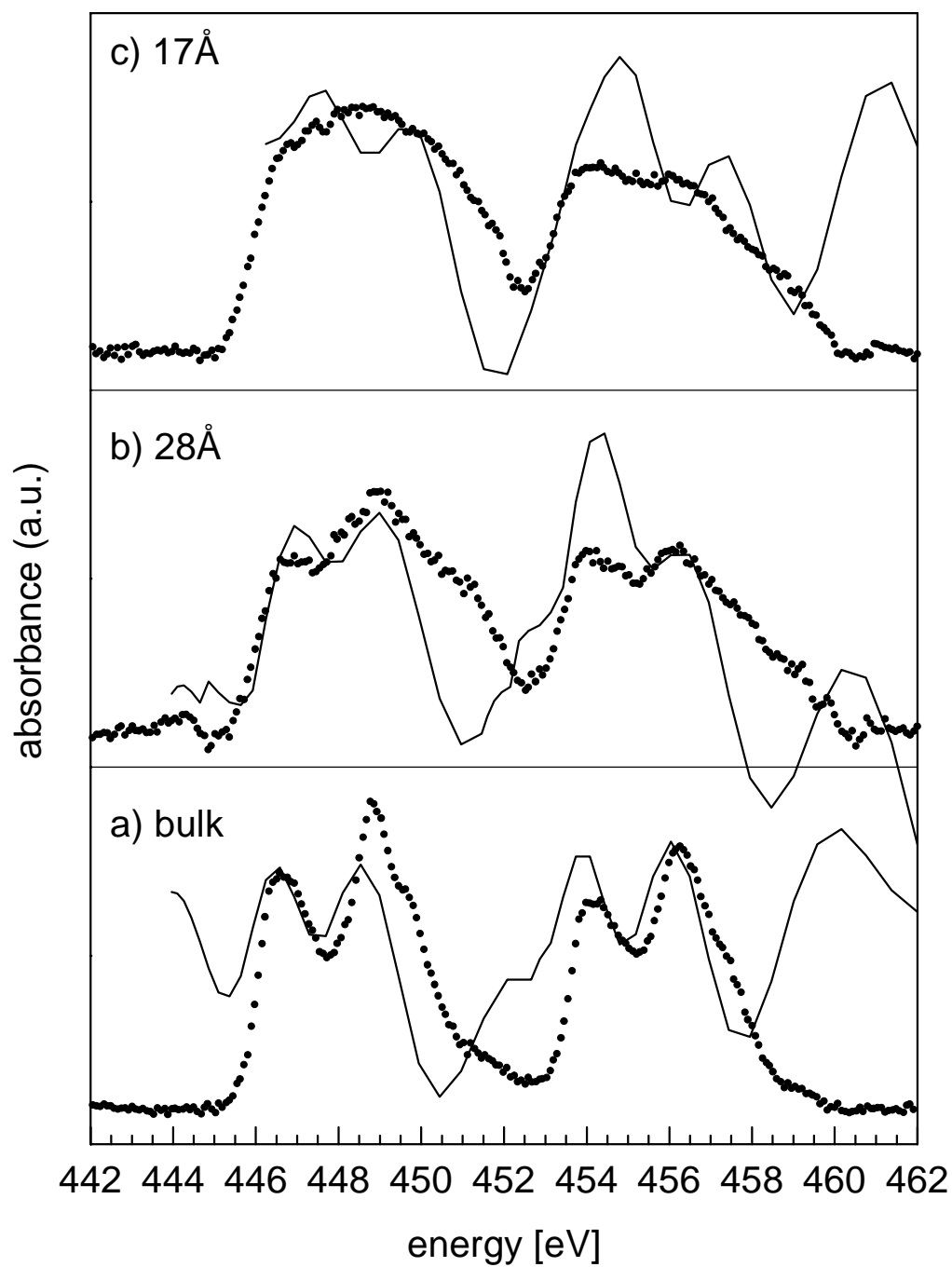


Figure 9-12 Experimental data (dots) and FEFF7 simulations (lines) for bulk and a 17Å and 28Å diameter InAs nanocrystal with bulk lattice parameters throughout.

9.3.2 Bulk reconstruction as model

A broadening of the XANES spectra is due to a distribution in the scattering paths in the crystal. Including a surface reconstruction in the models for the XANES simulations would introduce different bond lengths within a nanocrystal with respect to the bulk material. This in turn increases the number of distinct photoelectron scattering paths, which would possibly yield a broadening of the XANES spectra in the simulations. Therefore, we look to the example of the reconstructions in bulk semiconductors.

The surface reconstruction that has been the most well characterized for compound semiconductors is the “bond rotation” of both the nonpolar (110) face of zincblende both III-V and and the $(10\bar{1}0)$ surface of (II-VI) wurtzite semiconductors[35]. Figure 13 shows a sketch of this reconstruction. LEED experiments as well as energy minimization (tight binding) calculations [36] [8, 9] confirm this structure. In this reconstruction the cation is retracted into the solid and the anion is pushed outwards. This rearrangement is a result of the charge transfer from the Ga orbital to the As orbital, leaving the former completely empty and the latter filled. In terms of VSEPR theory, the three fold coordinated group III cation (In, Ga) would like to be trigonal planar, so it moves into the surface to achieve this. The three fold coordinated group V anion (As, P) tends toward a pyramidal symmetry, so it moves out of the surface. In the picture of molecular the cation becomes sp^2 hybridized and the anion s^2p^3 hybridized. This results in a semiconducting state and a lower total energy. Band structure calculations of this reconstruction show the removal of states in the gap. [8, 9] The anion-cation bond length stays the same due to the simultaneous change in the pyramidal angle and the tilt angle. The rearrangement at the surface ($\Delta_{1\perp}$) is $\sim 0.7\text{\AA}$ but persists for only a few layers, and by the second layer the atomic displacements ($\Delta_{1\perp}$) are small ($\leq 0.1\text{\AA}$).

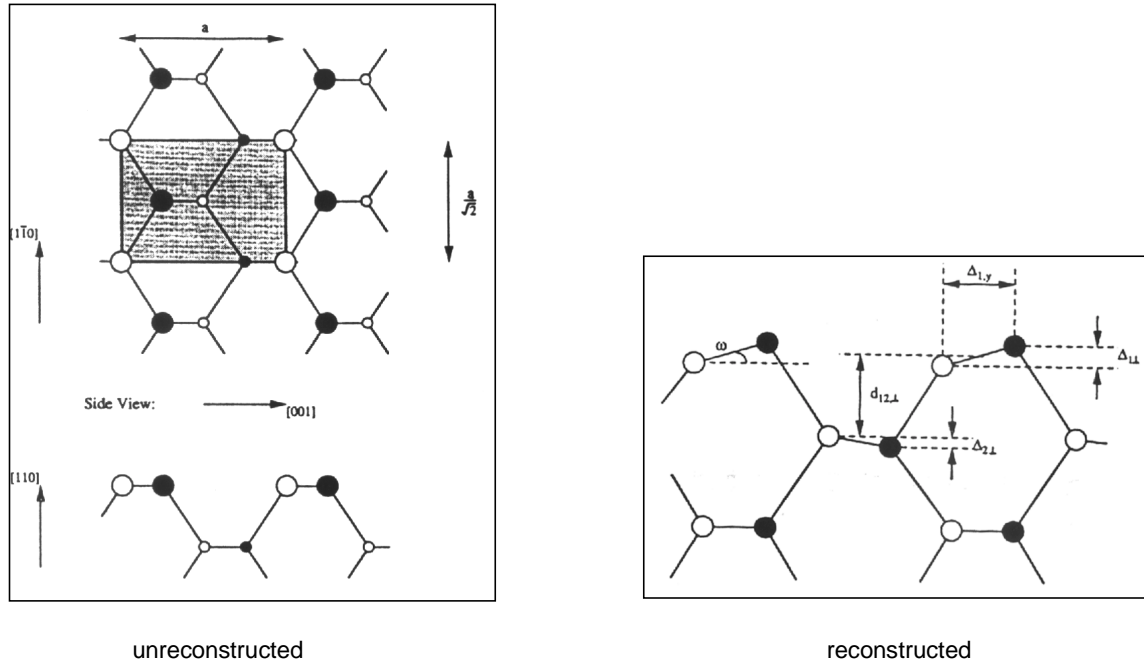


Figure 9-13 The bond rotation surface reconstruction for bulk III-V (110) face.

The reconstruction in the nanocrystal that we simulate is modeled after this rearrangement. We assume a radially symmetric relaxation of the outermost In layer by -0.85\AA (inwards) and the As layer just beneath it by $+0.39\text{\AA}$ (outwards). As a first order approximation this is done with radial symmetry and only the first cation and anion layers are moved. A model of this reconstruction is shown in Figure 15. This rearrangement in spherical 17\AA and 28\AA InAs nanocrystals (Figure 14) produces a broadening of the simulated spectrum comparable to the experiment, as the splitting between the peaks within the M_4 and M_5 edges disappears.

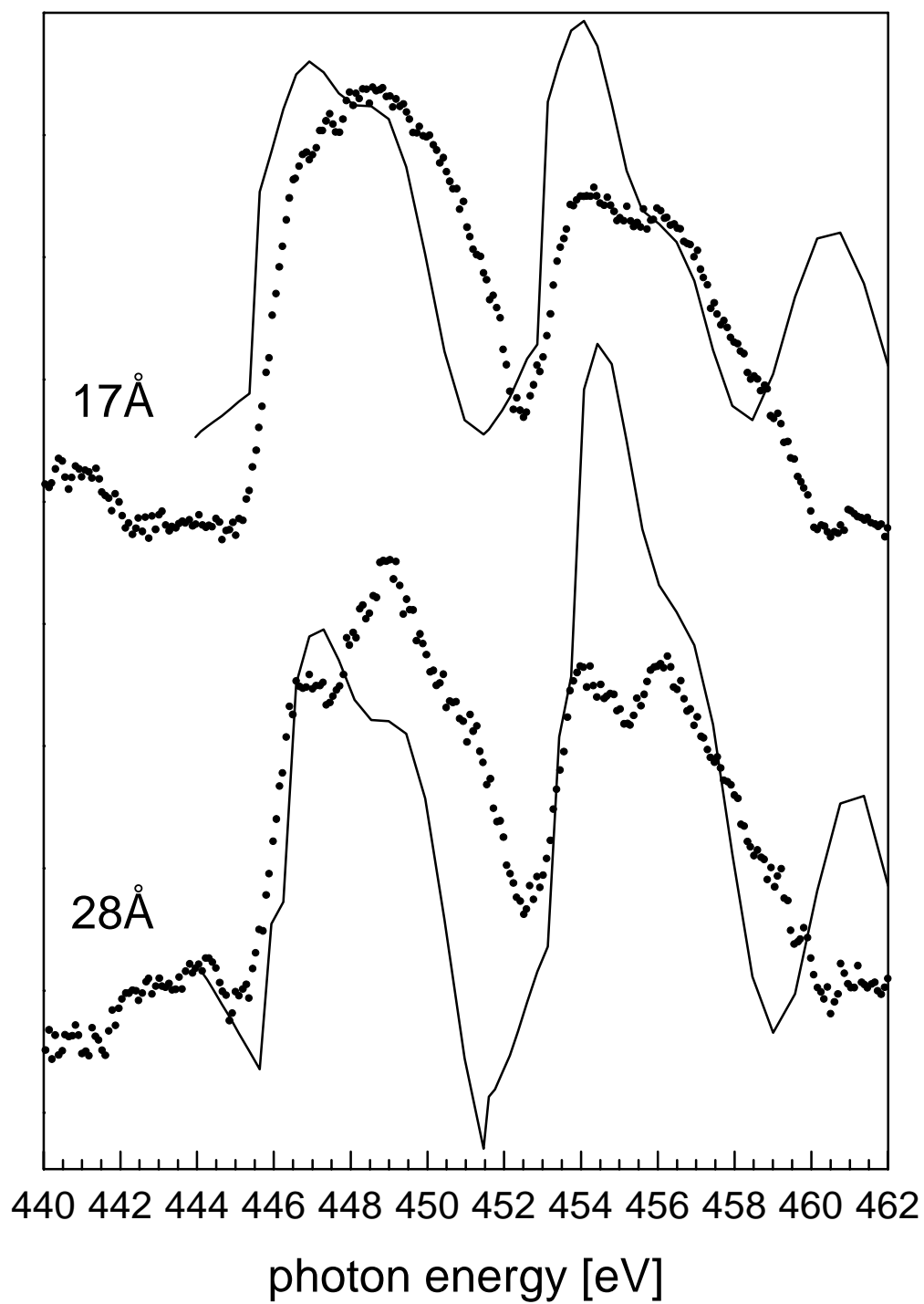


Figure 9-14 Experimental data (dots) and simulations (lines) of a 17Å nanocrystal (top) and a 28Å nanocrystal (bottom) with a surface reconstruction of the outermost layers.

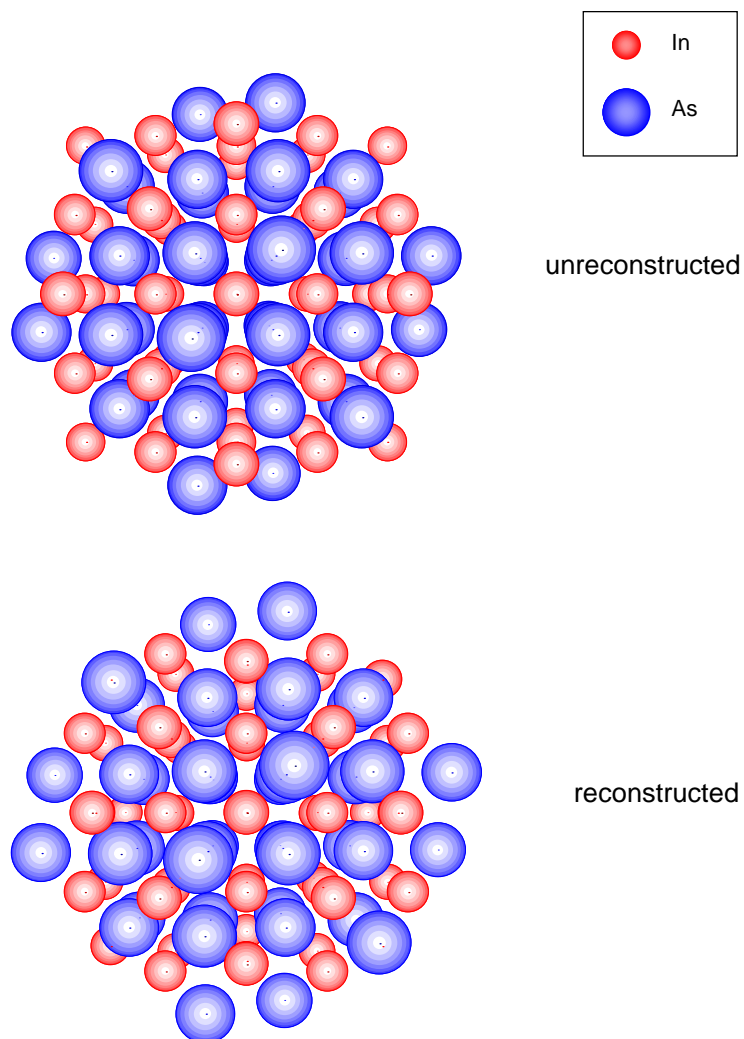


Figure 9-15 Picture of an unreconstructed and reconstructed 17Å InAs nanocrystal used in the FEFF simulations.

In nanocrystals this surface relaxation changes the bond lengths at the outermost surface layers. Figure 16 is a plot of the number of As nearest neighbors for an In atom as a function of distance for an unreconstructed nanocrystal (black) and a reconstructed nanocrystal (red). The unreconstructed curve has single peaks at 2.62Å, 5.02Å, and 6.6Å corresponding to the 1st, 2nd, and 3rd coordination shells. For the reconstructed nanocrystal, additional low intensity peaks occur above and below the bulk values for the In-As distances. These peaks give a distribution around the bulk value, indicating that the InAs bond length is changed in the model of the reconstruction. However, the average value is the same as in

the bulk-like lattice. The values for the InAs bond lengths can be grouped into distributions, as the dotted line suggests, and averaged. Table 1 shows the values of the average bond distance in the unreconstructed nanocrystal compared to the bulk values. For the 1st and 2nd coordination shells, the bond length is the same. However, a slight deviation occurs for the 3rd coordination shell (0.9 Å longer in the nanocrystal). This may be the result of the increasing difficulty to distinguish coordination shells as the distance increases.

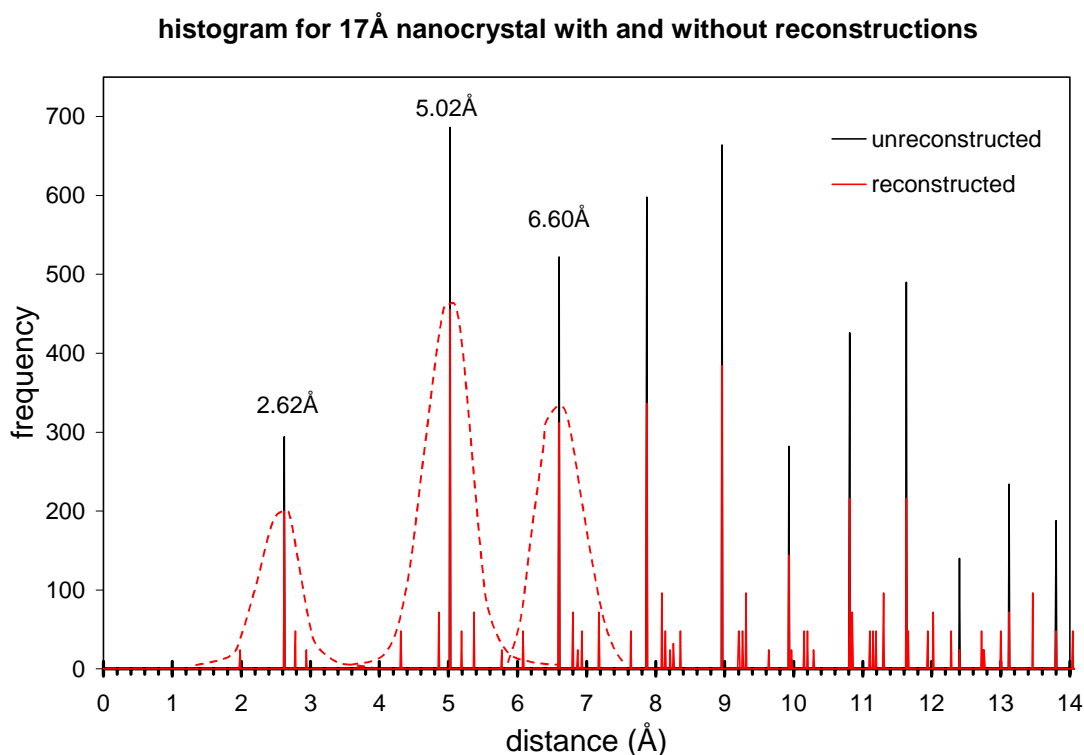


Figure 9-16. Number of atoms as a function of distance for In-As separations. The black lines are for a nanocrystal with bulk lattice parameters. The red lines are for a nanocrystal with a surface reconstruction in the first layers.

Table 9-1 Values for the histogram for the nanocrystal with bulk lattice parameters (right column) and of a nanocrystal with a surface reconstruction, averaged.

| d | freq | r avg nc (Å) | r avg, bulk (Å) |
|------|------|--------------|-----------------|
| 1.98 | 24 | | |
| 2.62 | 200 | | |
| 2.78 | 48 | | |
| 2.94 | 24 | 2.62 | 2.62 |
| 4.31 | 48 | | |
| 4.86 | 72 | | |
| 5.02 | 456 | | |
| 5.19 | 48 | | |
| 5.37 | 72 | | |
| 5.77 | 24 | 5.028 | 5.02 |
| 6.08 | 48 | | |
| 6.6 | 312 | | |
| 6.8 | 72 | | |
| 6.87 | 24 | | |
| 6.93 | 48 | | |
| 7.18 | 72 | 6.6929167 | 6.6 |

However, the experimental broadening may not only be due to a structural rearrangement of exclusively the two outermost layers as assumed in the simulations. It is very probable that bond lengths and angles deviate from the idealized bulk values throughout the whole particle, with the largest displacements occurring at the surface. Tight-binding calculations which minimize the total energy by moving all the atoms in the nanocrystal show that the perturbations are indeed similar to bulk reconstructions and are the largest on the surface[37, 38]. But lacking an appropriate model to account for internal rearrangements, we only state here that the observed broadening of XANES spectra can be related to structural disorder within the nanocrystals, which is believed to be largely due to atomic displacements at the surface.

One question is how does a surface reconstruction show up in an x-ray diffraction pattern? We can simulate the pattern for a reconstructed particle. It has been shown that the x-ray diffraction pattern are best fit with the inclusion of stacking faults in the simulation. An experimental powder pattern for 28Å InAs nanocrystals is shown in Figure 17 along the

fits using an unreconstructed and reconstructed particle both with the requisite number of stacking faults. The difference between the simulation for the particle with a reconstruction and without a reconstruction is slight, which is expected since x-ray diffraction is a bulk sensitive measurement.

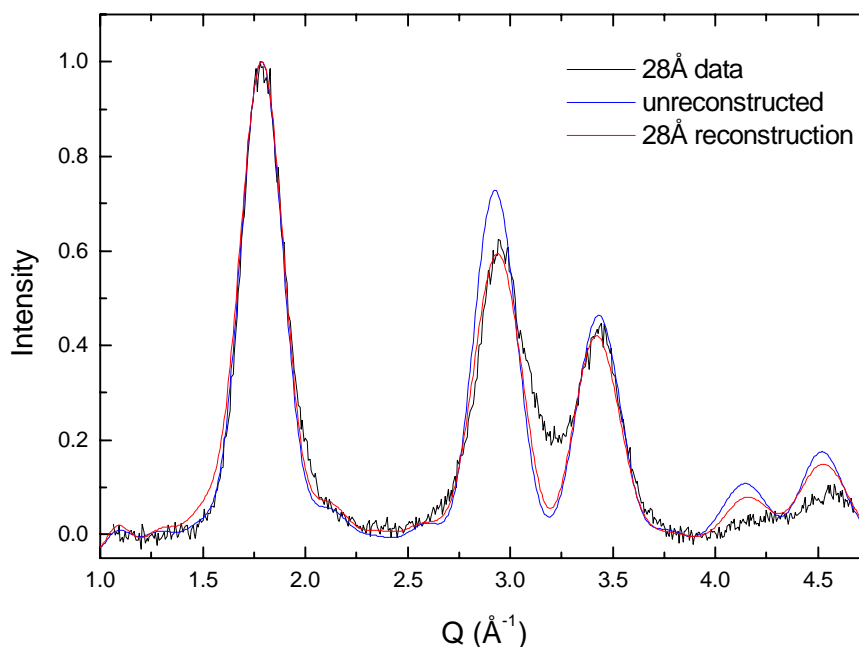


Figure 9-1 X-ray diffraction data (black) and simulations for a unreconstructed (blue) and reconstructed (red) particle. The simulated spectra show no marked differences.

9.3.3 Other possibilities for broadening

Other possible structural sources for the broadening effects have been systematically studied and excluded. We simulated spectra for an unreconstructed 17Å nanocrystal with a) a capping of the outermost In layer with P atoms and b) a slightly elliptical shape, shown in Figure 18. The surface capping with P atoms models the experimental situation that the outermost In layer is covered by a disordered layer of ligands (TOP) as confirmed by XPS [32, 33].

Since scattering scales as Z^2 , where Z is the atomic number, the P atoms at the surface contribute weakly to the spectrum compared to As or In atoms. A slightly elliptical particle shape (aspect ratio 1.1) which is evident from TEM and XRD results [13, 39] increases the number of scattering paths due to the symmetry reduction from a sphere, and should in principle lead to a broadening of the XANES spectra. However, this contribution is negligible compared to the experimental result.

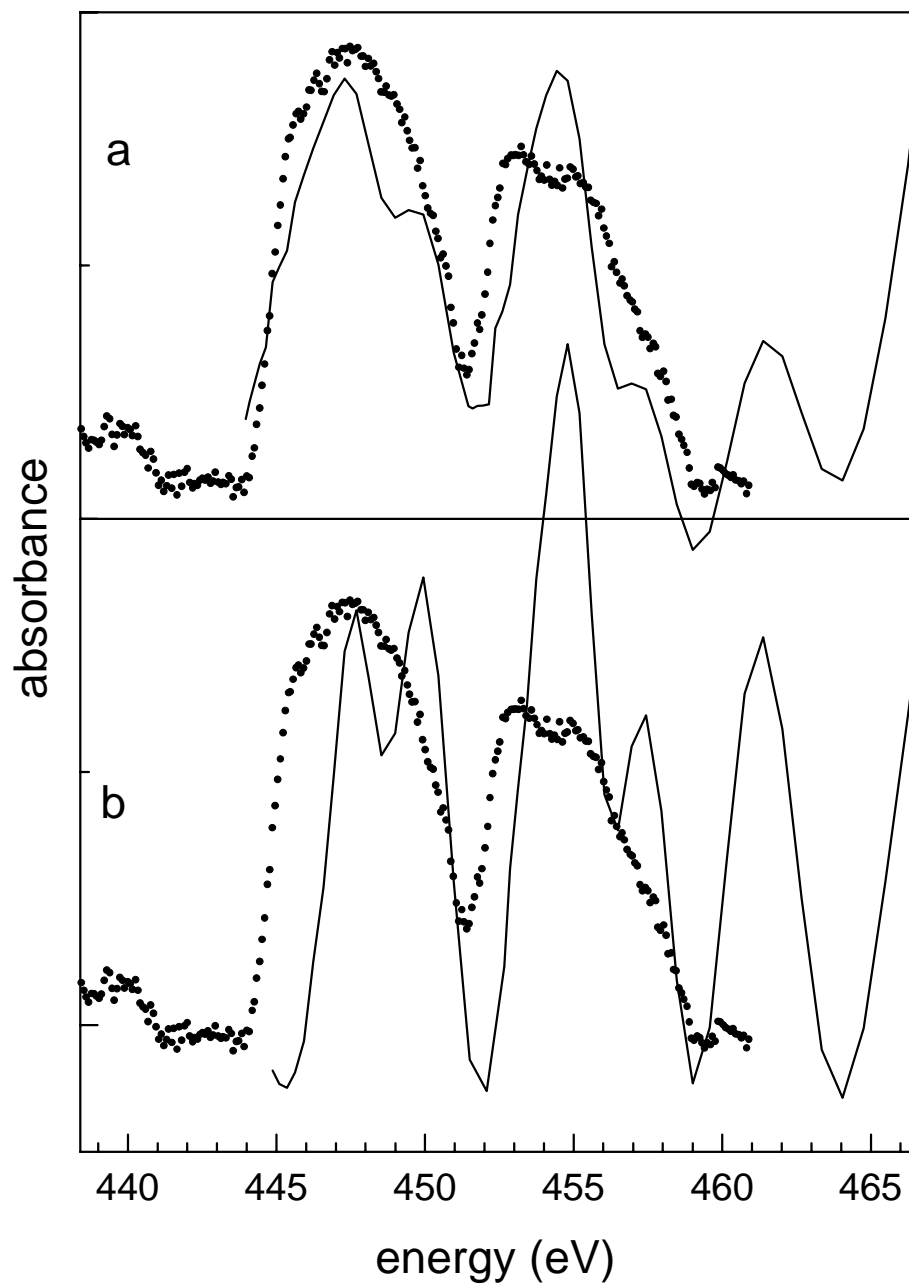


Figure 9-18 Simulations of a 17Å InAs nanocrystal with (a) an amorphous layer of P on the surface and (b) with an aspect ratio of 1.1 in comparison with the experimental data (dots)

9.3.4 Quantum confinement effects

The other non-structural cause of size dependent broadening are quantum size effects, which would exhibit itself as a change in the band structure and thus as a change in the absorption spectrum. Because FEFF7 is a real space calculation, it does not take into consideration quantum confinement. How these higher energy XANES features evolve as a function of size has not been calculated. Clearly, if we are to determine whether the size effects in the XANES broadening are due to structural properties or strictly electronic structure, higher order calculations are necessary to elucidate the electronic structure as a function of size.

However, we can estimate the effects of quantum confinement in a simplistic way to see the effect on the spectra. The effects are approximated as a conduction band energy shift convoluted with a size distribution. The question is whether a size distribution convoluted with band edge shifts could result in a broadened spectrum. XAS of Si nanocrystals show that the bulk experimental spectrum convoluted with a conduction band shift produces a spectrum similar to the one obtained for nanocrystals [40]. We adopt this model and estimate the broadening due to a size distribution and an energy shift due for the smallest size nanocrystal (17Å) for which the effects should be the largest. Since the $M_{4,5}$ transition is into higher energy p bands, ΔE_{CB} is not known. It is approximated by using the shifts for the lowest energy band (s bands), obtained from the optical excitation energy ΔE_{opt} . ΔE_{opt} measured by UV-Vis is fit to a $1/R$ polynomial describing the size dependence. As the effective masses of the hole and electron in InAs bulk are identical ($m_e = m_h = 0.026$), we assume ΔE_{CB} and the valence band shift (ΔE_{VB}) contribute equally to ΔE_{opt} in InAs nanocrystals. From the particle size distribution determined by TEM (10 %), a width in

ΔE_{CB} of 100 meV is calculated for 17 Å InAs nanocrystals. Since the curvature of the p bands is lower than in the s bands (Figure 19), this overestimates the effects of quantum confinement and subsequently the size distribution effect on the x-ray spectra.

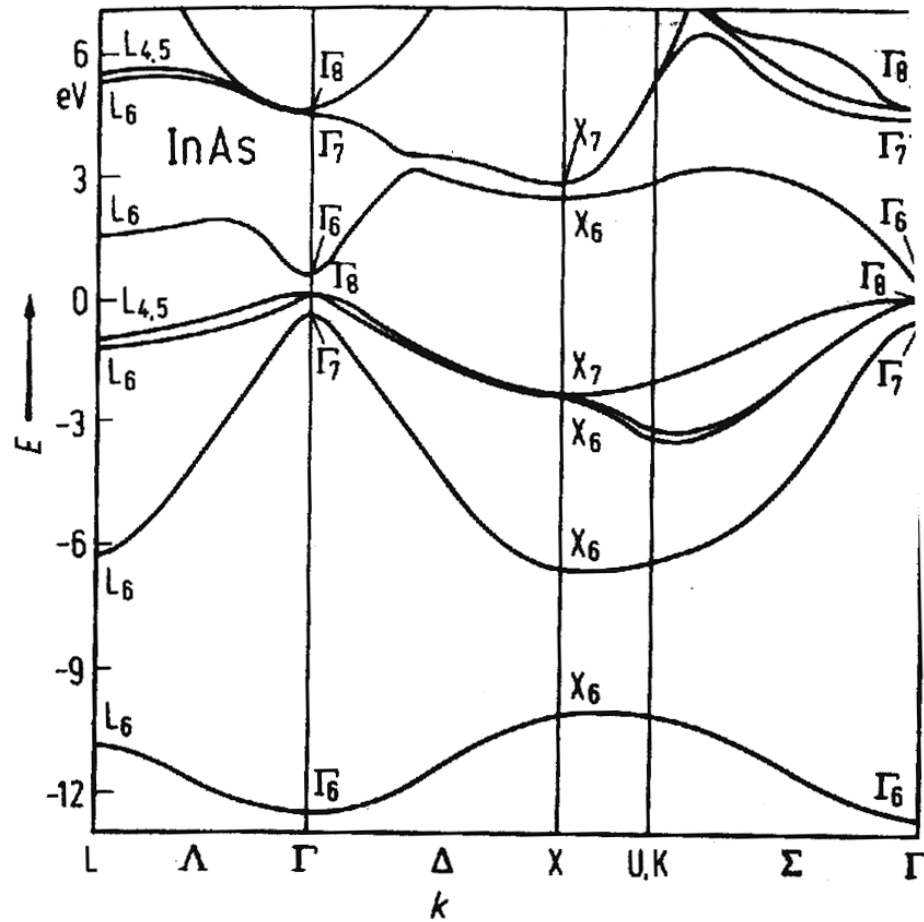


Figure 9-19 Band structure for bulk InAs. The s band which constitutes the lowest energy conduction band is labeled Γ_6 . The bands that are probed by the XANES $M_{4,5}$ transition are the bands labeled Γ_7 and Γ_8 and have lower curvature.

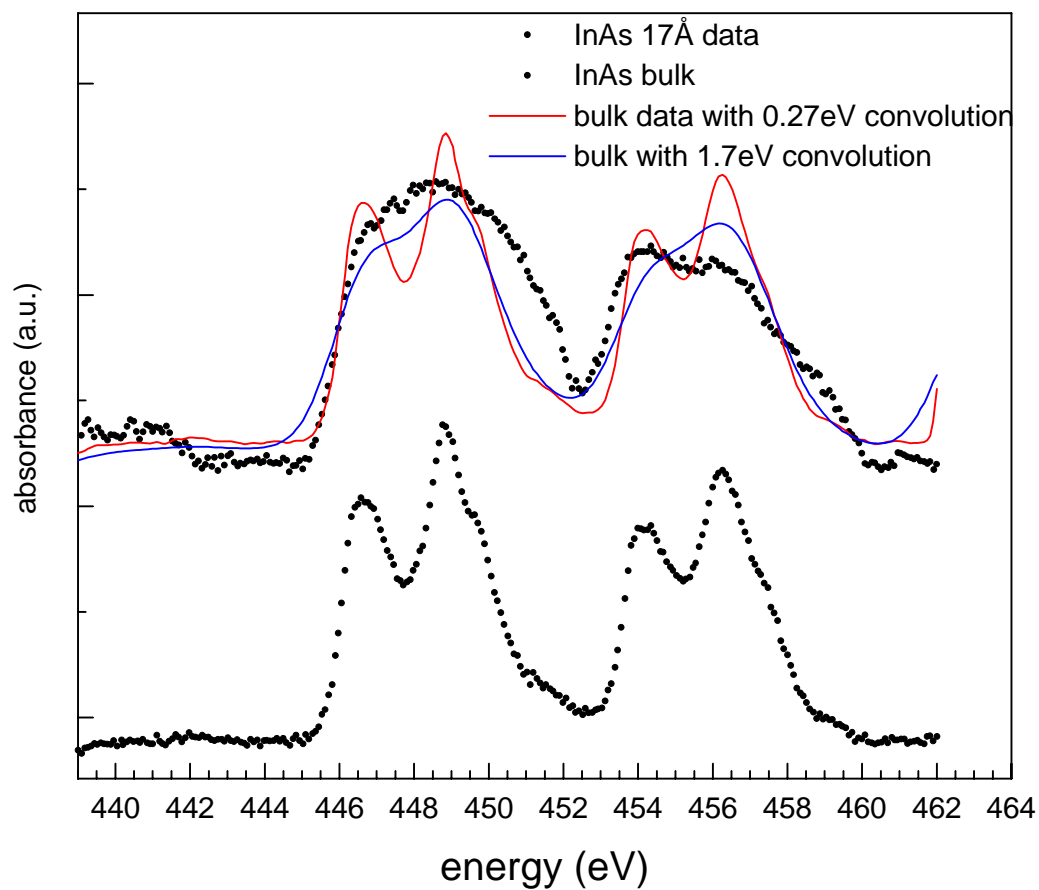


Figure 9-20 Simulations of quantum confinement convoluted with a size distribution. The bulk experimental data (dots, bottom) are convoluted with a Gaussian of 0.27 eV (red line) and compared to the 17 Å experimental data. The bulk data is also convoluted with a Gaussian of 1.7 eV in width.

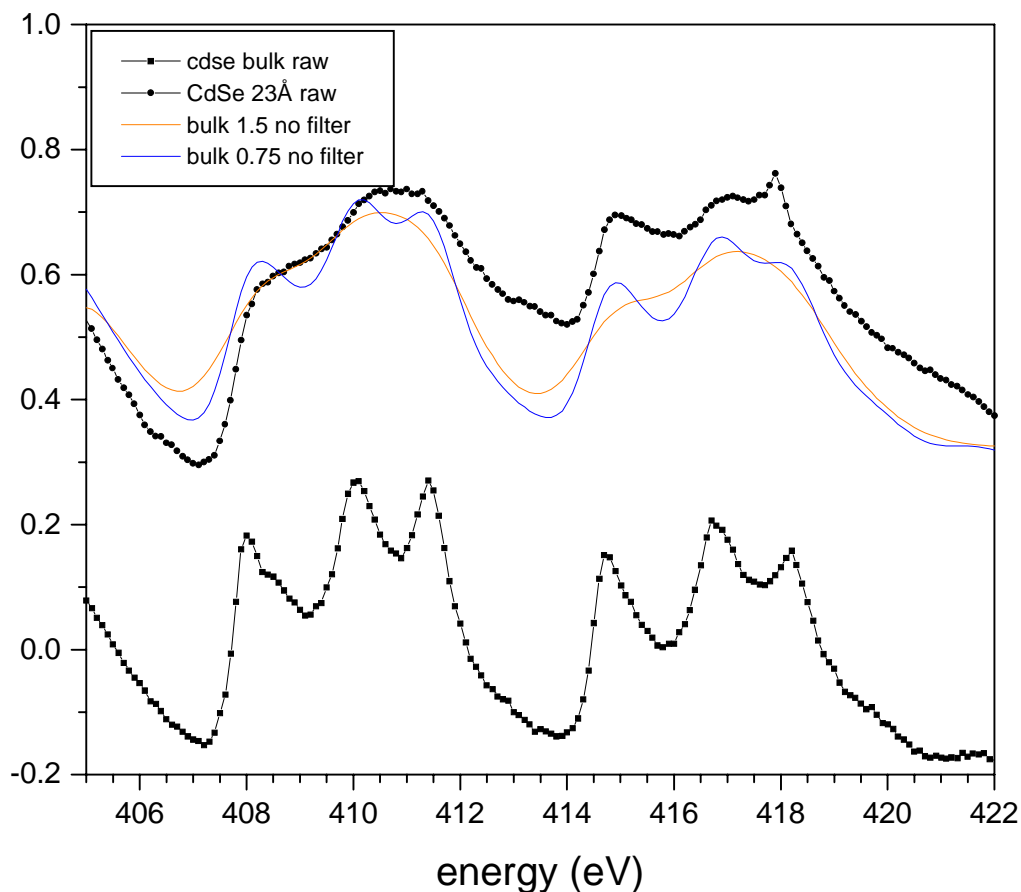


Figure 9-21 Simulations of quantum confinement convoluted with a size distribution for CdSe.

This calculation results in a Gaussian of a width of 100 meV representing the conduction band shifts (ΔE_{CB}) corresponding to the size distribution [41]. If this Gaussian is convoluted with the bulk experimental spectrum, the result shows a minor amount of broadening of the spectrum relative to the 17Å spectrum. In order to reproduce the experimental broadening of the 17Å InAs nanocrystal, the bulk spectrum must be convoluted with a Gaussian of at least 1.7eV in width; for a 23Å CdSe nanocrystal the bulk must be convoluted with a Gaussian of 1.5eV in width. The convolutions for both the InAs and CdSe bulk spectra are shown in Figures 20 and 21 for the convolution of a symmetric Gaussian with the bulk spectra.

Therefore, we conclude that structural disorder in InAs and CdSe nanocrystals is the major factor in the broadening of the XANES spectra at the In and Cd $M_{4,5}$ edge as seen from the simulations including a bulk-like surface reconstruction in Figure 14. However, until more definitive theoretical investigations of these states are performed, the effects of quantum confinement cannot be strictly ruled out.

9.4 Core shell particles

Comparison between the XANES spectra of nanocrystals of different sizes and surface stabilizations might provide more information about the nature of the reconstruction. For example, the nanocrystals can be stripped of their surfactant, and epitaxial shells of related semiconductors can be grown onto the cores (e.g. InAs coated with CdS or CdSe). These surface modifications will provide additional checks on the complex surface reconstructions of semiconductor nanocrystals.

One can test the surface reconstruction model by measuring the XANES spectrum for core-shell materials. Epitaxial growth of a shell onto the nanocrystal surface to make a core-shell system would in principle remove any surface reconstructions. It has been observed by TEM and luminescence and absorption that the core-shell system have no dangling bonds at the interface. [42-44] If the shell material does not contain the elements of the interior, then the cores are independent. InAs/CdSe is an appropriate system since the lattice mismatch between bulk InAs and bulk zincblende CdSe is expected to be nearly zero ($a_{\text{InAs}} = 6.06\text{\AA}$, $a_{\text{CdSe}} = 6.052\text{\AA}$). Furthermore, because of the chemical difference between the core and shell, it is straightforward to distinguish the core and shell absorption spectra.

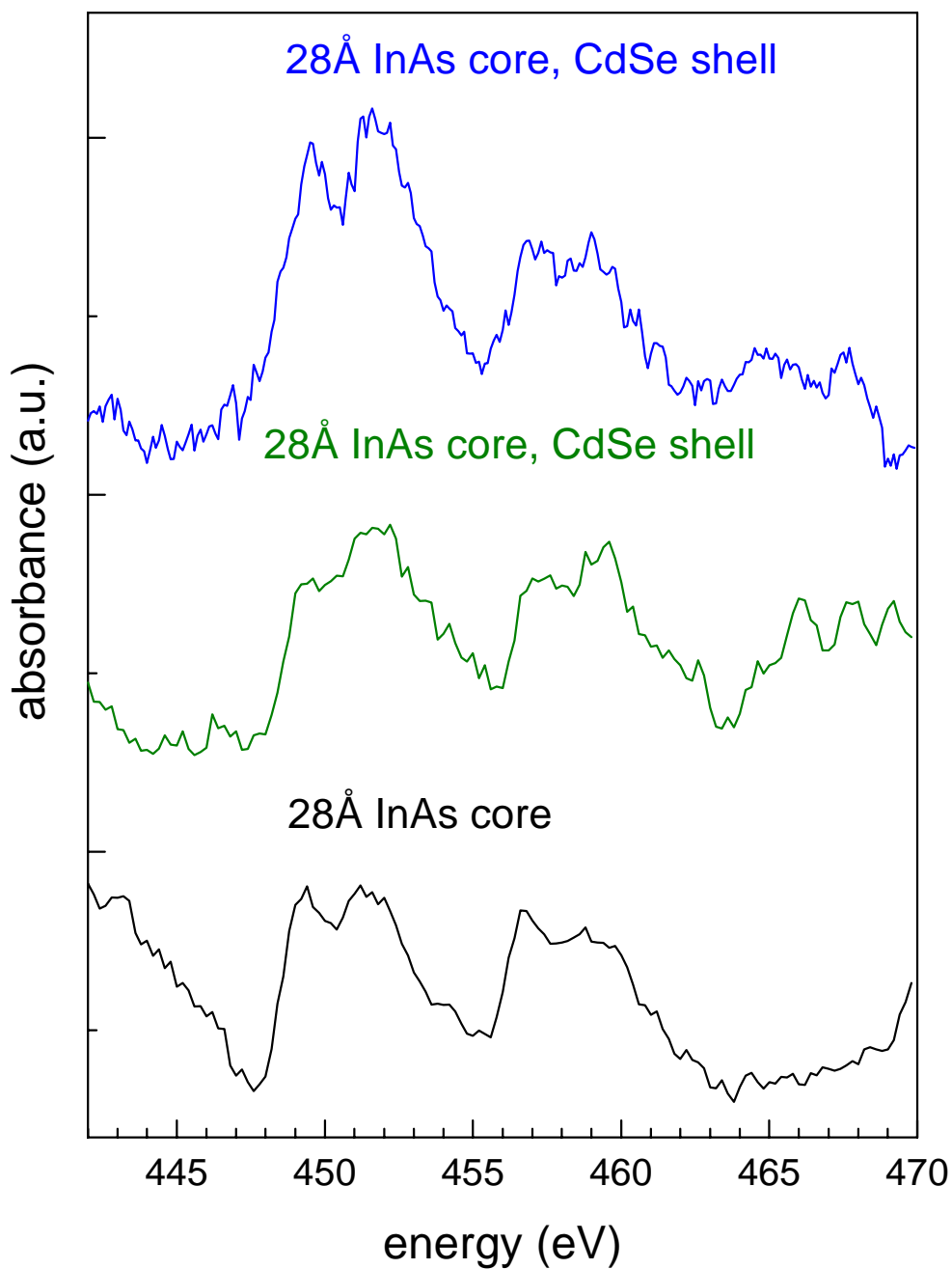


Figure 9-22 In $M_{4,5}$ XANES spectra of a 28Å diameter InAs nanocrystal and a InAs/CdSe core shell nanocrystal in which the core is also 28Å. The core-shell spectra have different beamline parameters in their acquisition, which can change how broad the features appear in comparison to the core-only spectrum.

Preliminary experiments have been performed on InAs/CdSe. Core shell particles were synthesized as described in Chapter 2. The absorption spectra were measured at

beamline 8.0, which is an undulator beam at the ALS capable of higher fluxes (give number). Electron detection was measured by both sample current as well as by a channeltron next to the sample in the chamber. Fluorescence yield detection gave very low signal.

Figure 22 shows the In $M_{4,5}$ spectra for a core-shell sample and the corresponding core of the same size (28Å). The spectrum for the core-shell is not as broad as for the core. However, the experimental details of the measurement still need to be optimized. Further experiments on core-shell systems are will be carried out in the future. In addition to studying surface reconstructions, core-shells provide an interesting system to study the structural effects of strain. Because of the curvature of the surface, the strain in the system is not easily predictable and XANES analysis may provide information about how the strain is dispersed in heteroepitaxy of non-planar surfaces.

9.5 Evaluation of results

Quantitative agreement of the simulations with the experiment needs to be met in order to be able to properly model the surface structure. As aforementioned, the FEFF7 multiple scattering model relies on muffin-tin potentials which are too simplistic. The use of self-consistently calculated potentials may afford better agreement with experimental results, and has been included in a new version of the FEFF code, FEFF8 [45]. Also, approximations used by FEFF7 have only been thoroughly tested for bulk materials which might have to be altered for nanocrystals. For instance, deviations of the electron inelastic mean free path in nanocrystals from the bulk value have been discussed for Al nanoparticles [46]. The mean free path has been shown theoretically to be dependent on crystallographic direction, which is not accounted for in a spherical description. [47]

The results presented here are some of the first experiments which probe the structure of the nanocrystal surface. However, the experiments are preliminary, and the information out of it is not quantitative yet. Despite the poor agreement of the simulations, the experimental results show the potential for yielding structural information about nanocrystals. As aforementioned, the reconstruction assumed in the simulations is modeled after bulk reconstructions, but it represents a step towards modeling the surface structure.

In addition, using the multiple scattering regime of the x-ray absorption spectrum as a probe of geometric structure of surfaces is a relatively new procedure. It has shown encouraging results so far for a variety of systems for bulk crystals and surfaces. Perhaps in the future analysis of XANES spectra will be developed to the point that it can be used routinely to extract complicated structural information. Until then, the determination of surface structure in nanocrystals remains to be a challenging problem.

9.6 References

- [1] H. Weller, *Angew. Chem., Int. Ed. Engl.* **35**, 1079 (1996); S. Empedocles and M. Bawendi, *Science* **278**, 2114 (1997); T. G. Schaaff, *et al.*, *J. Phys. Chem. B* **101**, 7885 (1997); J. R. Heath and J. J. Shiang, *Chem. Soc. Rev.* **27**, 65 (1998).
- [2] X. Peng, J. Wickham, and A. P. Alivisatos, *J. Am. Chem. Soc.* **120**, 5343 (1998).
- [3] J. M. McHale, A. Auroux, A. J. Perrotta, and A. Navrotsky, *Science* **277**, 788 (1997); S. H. Tolbert and A. P. Alivisatos, *J. Chem. Phys.* **102**, 4642 (1995).
- [4] N. A. Hill and K. B. Whaley, *J. Chem. Phys.* **100**, 2831 (1994).
- [5] C. B. Duke, *Chem. Rev.* **96**, 1237 (1996).
- [6] R. Hoffmann, *Solids and Surfaces: A Chemist's View on Bonding in Extended Structures* (VCH Publishers, New York, 1988).
- [7] J. K. Burdett, *Chemical Bonding in solids* (Oxford University Press, New York, 1995).
- [8] J. L. A. Alves, J. Hebenstreit, and M. Scheffler, *Phys. Rev. B* **44**, 6188 (1991).
- [9] Y. R. Wang and C. B. Duke, *Phys. Rev. B* **37**, 6417 (1988).
- [10] G. P. Srivastava, *Rep. Prog. Phys.* **60**, 561 (1997).
- [11] However, the growth of quantum dots by molecular beam epitaxy and metal -organic chemical vapor deposition is determined by long range mechanical forces. In this case, surface effects are well understood to the point where a high degree of growth control is possible. D. Bimberg, M. Grundmann, and N. N. Ledentsov, *Mater. Res. Bull.* **23**, 31 (1998).
- [12] A. R. Kortan, R. Hull, R. L. Opila, M. G. Bawendi *et al.*, *J. Am. Chem. Soc.* **112**, 1327 (1990); X. Peng, *et al.*, *J. Am. Chem. Soc.* **119**, 7019 (1997); C. L. Cleveland, *et al.*, *Phys. Rev. Lett.* **79**, 1873 (1997).

- [13] J. J. Shiang, A. V. Kadavanich, R. K. Grubbs, and A. P. Alivisatos, *J. Phys. Chem.* **99**, 17417 (1995).
- [14] C. B. Murray, D. J. Norris, and M. G. Bawendi, *J. Am. Chem. Soc.* **115**, 8706 (1993).
- [15] C.-C. Chen, A. B. Herhold, C. S. Johnson, and A. P. Alivisatos, *Science* **276**, 398 (1997).
- [16] H. Krautscheid, D. Fenske, G. Baum, and M. Semmelmann, *Angew. Chem., Int. Ed. Engl.* **32**, 1303 (1993); N. Herron, *et al.*, *Science* **259**, 1426 (1993); T. Vossmeier, *et al.*, *Science* **267**, 1476 (1995); T. Vossmeier, *et al.*, *J. Am. Chem. Soc.* **117**, 12881 (1995).
- [17] T. W. Odom, J.-L. Huang, P. Kim, and C. M. Lieber, *Nature* **391**, 62 (1988).
- [18] J. W. G. Wildoer, L. C. Venema, A. G. Rinzler, R. E. Smalley *et al.*, *Nature* **391**, 59 (1998).
- [19] B. A. Korgel and D. Fitzmaurice, *Phys. Rev. Lett.* **80**, 3531 (1990).
- [20] P. C. Ohara, D. V. Leff, J. R. Heath, and W. Gelbart, *Phys. Rev. Lett.* **75**, 3466 (1995).
- [21] A. K. Kadavanich and S. J. Rosenthal, 1999, personal communication.
- [22] A. Bianconi, in *X-ray Absorption: Principles, Applications, Techniques of EXAFS, SEXAFS, XANES*, edited by D. C. Koningsberger and R. Prins (Wiley, New York, 1988), p. 573.
- [23] A. Erbil, G. S. Cargill III, R. Frahm, and R. F. Boehme, *Phys. Rev. B* **37**, 2450 (1988).
- [24] in *Proceedings of the 9th International Conference on X-Ray Absorption Fine Structure in Grenoble, France*, 1996, *J. Phys. IV (Paris)* **7**, (1997).

- [25] J. Rockenberger, L. Tröger, A. Kornowski, T. Vossmeier *et al.*, J. Phys. Chem. B **101**, 2691 (1997); J. Rockenberger, *et al.*, J. Chem. Phys. **108**, 7807 (1998); T. Shido and R. Prins, J. Phys. Chem. B **102**, 8426 (1998).
- [26] C. S. Fadley, in *Synchrotron Radiation Research: Advances in Surface and Interface Science*, edited by R. Z. Bachrach (Plenum Press, New York, 1992), Vol. Volume 1: Techniques, p. 421.
- [27] A. A. Guzelian, U. Banin, A. V. Kadavanich, X. Peng *et al.*, Appl. Phys. Lett. **69**, 1432 (1996).
- [28] N. Mårtensson and R. Nyholm, Phys. Rev. B **24**, 7121 (1981).
- [29] L.-W. Wang and A. Zunger, Phys. Rev. B **53**, 9579 (1996).
- [30] S. B. Diczio and G. K. Wertheim, Comments Solid State Phys. **11**, 203 (1985).
- [31] S. I. Zabinsky, J. J. Rehr, A. Ankudinov, R. C. Albers *et al.*, Phys. Rev. B **52**, 2995 (1995).
- [32] J. E. Bowen Katari, V. L. Colvin, and A. P. Alivisatos, J. Phys. Chem. **98**, 4109 (1994).
- [33] A. A. Guzelian, J. E. B. Katari, A. V. Kadavanich, U. Banin *et al.*, J. Phys. Chem. **100**, 7212 (1996).
- [34] D. Bazin, D. Sayers, J. J. Rehr, and C. Mottet, J. Phys. Chem. **101**, 5332 (1997).
- [35] T. N. Horsky, G. R. Brandes, K. F. Canter, C. B. Duke *et al.*, Phys. Rev. B **46**, 7011 (1992).
- [36] C. B. Duke, J. Vac. Sci. Tech. B **1**, 732 (1993).
- [37] S. Pokrant and K. B. Whaley, European Physical Journal D **6**, 255 (1999).
- [38] K. Leung and K. B. Whaley, J. Chem. Phys. **110**, 11012 (1999).

- [39] D. J. Norris, A. L. Efros, M. Rosen, and M. G. Bawendi, Phys. Rev. B **53**, 16347 (1996).
- [40] T. van Buuren, private communication.
- [41] T. van Buuren, T. Tiedje, Y. Gao, J. R. Dahn *et al.*, Appl. Phys. Lett. **60**, 3013 (1992).
- [42] M. A. Hines and P. Guyot-Sionnest, J. Phys. Chem. **100**, 468 (1996).
- [43] X. Peng, M. C. Schlamp, A. V. Kadavanich, and A. P. Alivisatos, J. Am. Chem. Soc. **119**, 7019 (1997).
- [44] B. O. Dabbousi, J. Rodriguez-Viejo, F. V. Mikulec, J. R. Heine *et al.*, J. Phys. Chem. B **101**, 9463 (1997).
- [45] A. L. Ankudinov, B. Ravel, J. J. Rehr, and S. D. Conradson, Phys. Rev. B **50**, 7565 (1998).
- [46] J. Zhao and P. A. Montano, Phys. Rev. B **40**, 3401 (1989).
- [47] A. Kuzmin, J. Phys: Condens. Matter **6**, 5761 (1994); M. Bader *et al.*, Phys. Rev. Lett. **57**, 3273 (1986); J. Zhao and P. A. Montano, Phys. Rev. B **40**, 3401 (1989).